10/4-11-90 JS ①

DIRECT NUMERICAL SIMULATIONS OF A PLANE COMPRESSIBLE WAKE: STABILITY, VORTICITY DYNAMICS, AND TOPOLOGY

By

Jacqueline H. Chen, Brian J. Cantwell
and Nagi N. Mansour

Prepared with the support of the
U.S. Department of Energy
Under Contract DE-AC04-76DP00789

Report No. TF-46

Thermosciences Division
Department of Mechanical Engineering
Stanford University
Stanford, California 94305

November 1989

SAND90-8201

DIRECT NUMERICAL SIMULATIONS OF A PLANE COMPRESSIBLE WAKE: STABILITY, VORTICITY DYNAMICS, AND TOPOLOGY

SAND--90-8201

DE90 007934

by

Jacqueline H. Chen, Brian J. Cantwell,
and Nagi N. Mansour

Prepared with the support of the
U. S. Department of Energy
under Contract DE-AC04-76DP00789

Report No. TF-46

Thermosciences Division
Department of Mechanical Engineering
Stanford University
Stanford, California 94305

November 1989

MASTER

ABSTRACT

Recent interest in supersonic combustion and problems of transatmospheric flight has prompted renewed research efforts in laminar-turbulent free shear flow transition. In the present work, linear stability theory and direct numerical simulations are used to study the effect of Mach number on the linear, nonlinear, and three-dimensional aspects of transition in a plane compressible wake. Direct numerical simulations are also used to study the sensitivity of a compressible wake to (1) phase effects and (2) two- and three-dimensional subharmonics.

A linear stability analysis shows that the influence of increasing Mach number is stabilizing, resulting in reduced growth rates for both antisymmetric and symmetric modes of the wake. This reduction is due to baroclinic and dilatational effects as revealed from the linear eigenfunctions. For both low and high Mach numbers, the least stable wave is a two-dimensional antisymmetric mode aligned with the streamwise direction.

Direct numerical simulations of a temporally-evolving wake were performed using a spectral collocation method. The results of two-dimensional simulations show that, for high Mach numbers, the same mechanisms responsible for the reduced growth rates from linear stability theory are also responsible for the delay in the roll-up of vortices. Two-dimensional simulations were also performed to study the effect of phase angle between a fundamental and its subharmonic on the development of a subharmonic in a low Mach number wake.

Three-dimensional simulations were performed to study the effect of phase angle between a fundamental and a pair of oblique waves on the development of the large-scale structures in a wake. Depending upon the phase angle, vortex loops may or may not form due to the interaction of the streamwise and spanwise vortices. Staggered "peak-valley-splitting" vortices, which have been observed in boundary-layers and incompressible wakes, develop if the simulations are forced with a pair of oblique subharmonic waves.

Finally, the topology of the computed velocity, vorticity, and pressure gradient fields is determined using a generalized three-dimensional critical point theory.

ACKNOWLEDGMENTS

The authors gratefully acknowledge the contributions of their colleagues at Stanford University and at NASA-Ames Research Center. Professors W. Reynolds and G. Mungal provided many useful suggestions throughout this work and carefully reviewed the manuscript. Dr. N. Sandham and Mr. Greg Blaisdell offered many stimulating discussions concerning compressible flow and numerical methods. At NASA-Ames Research Center, we wish to thank Drs. J. Buell, R. Moser, M. Rogers, S. Lele, and K. Shariff for their insights. During the initial stages of this work, Dr. L. Mack at the Jet Propulsion Laboratory provided invaluable assistance with his boundary layer stability codes.

Financial support was provided under the Doctoral Study Program [†] at Sandia National Laboratories, and computing resources were provided by ACF and NAS at NASA-Ames Research Center. Special thanks go to Dr. C. Robinson and Dr. C. Hartwig for their assistance and encouragement.

[†] U.S. Department of Energy contract DE-AC04-76DP00789.

CONTENTS

LIST OF FIGURES

Figure *Page*

Figure *Page*

NOMENCLATURE

Roman Symbols

a	Cain mapping stretching parameter, section 2.3
A	5×5 matrix for linear stability eigenvalue problem, equation (2.3.2)
A, a_{ij}	3×3 matrix containing deformation tensor of a vector field, equation (6.2.1)
$\grave{\mathbf{b}}_{\mathbf{2D}}$	Linear eigenfunction vector of 2D mode, $\grave{b}_{2D} = [\grave{u}_1, \grave{u}_2, \grave{\rho}, \grave{T}]_{2D}$
$\grave{\mathbf{b}}_{\mathbf{2DS}}$	Linear eigenfunction vector of 2D subharmonic mode, $\grave{b}_{2DS} = [\grave{u}_1, \grave{u}_2, \grave{\rho}, \grave{T}]_{2DS}$
$\grave{\mathbf{b}}_{\mathbf{3D}}$	Linear eigenfunction vector of 3D mode, $\grave{b}_{3D} = [\grave{u}_1, \grave{u}_2, \grave{u}_3, \grave{\rho}, \grave{T}]_{3D}$
$\bar{\mathbf{b}}_{\mathbf{3D}}$	Mean flow vector, $\bar{b}_{3D} = [\bar{u}_1, \bar{u}_2, \bar{u}_3, \bar{\rho}, \bar{T}]_{3D}$
$\tilde{\mathbf{b}}_{\mathbf{3D}}$	Linear disturbance vector, $\tilde{b}_{3D} = [\tilde{u}_1, \tilde{u}_2, \tilde{u}_3, \tilde{\rho}, \tilde{T}]_{3D}$
$\mathbf{b}$	Flow field vector, $[u_1, u_2, u_3, \rho, T]$
b_i	Initial half-width of the wake
c	Sound speed
c	Complex phase speed, $c_{ph} + ic_i$
c_{ph}	Phase speed of linear disturbances, ω_r/α
c_1	Constant in definition of mean velocity, equation (2.1.1)
CFL	Courant-Friedrichs-Lewy number, section 3.4.3
D	Derivative operator in x_2
e	Internal energy
E	Kinetic energy of each mode, equation (3.6.1)
$\mathbf{E}$	Fluxes in x_1, equation (3.1.16)
E_T	Total energy, equation (3.1.6)
E_α	Spectral energy at α, x_2, x_3, equation (4.1.5.1)
$E_{\alpha,\beta}$	Spectral energy at α, x_2, β, equation (5.5.1)
f	Arbitrary function
$\mathbf{F}$	Fluxes in x_2, equation (3.1.17)
G	Variable for shooting method, equation (2.3.10)
$\mathbf{G}$	Fluxes in x_3, equation (3.1.18)
h'	Metric for Cain mapping, section 2.3
k_1, k_2, k_3	Wave numbers in the x_1, x_2, x_3, section 3.4.1

k	Thermal conductivity, equation (3.1.12)
L_1, L_2, L_3	Length of computational box in x_1, x_2, x_3 directions
M	Freestream Mach number, $M = u_{1o}/c_o$
M_2, M_3	Drawer size in x_2 and x_3, section 3.5
M_r	Relative Mach number, $M_r = \Delta u_c M$
N_1, N_2, N_3	Number of Fourier modes in x_1, x_2, x_3 directions
N	Number of collocation points in x_2 for matrix eigenvalue problem, section 2.3
p	Pressure
P, p_{ij}	Matrix containing spectral derivative operator, equation (2.3.7)
P	Matrix invariant for critical point theory, equation (6.2.2)
P	Complex mode shape used in linear growth rate comparisons
Pr	Prandtl number, $\mu^* c_p{}^* / k^*$
q_1, q_2, q_3	Heat flux in the x_1, x_2, x_3 directions
Q	Matrix invariant for critical point theory, equation (6.3.2)
r_1, r_2	Inner and outer radius of limit cycle, section 6.3.2
R	Matrix invariant for critical point theory, equation (6.2.4)
$\mathbf{R}$	Right-hand side of equations (3.1.14–3.1.18)
Re	Reynolds number, $\rho u_{1o} b_i / \mu_o$
Re_c	Critical Reynolds number
$\mathbf{s}$	Dependent variables in direct simulations $[\rho, \rho u_1, \rho u_2, \rho u_3, E_T]$
S_{ij}	Strain rate tensor
t	Time
T	Temperature
u_1, u_2, u_3	Velocity in x_1, x_2, x_3 directions
U_c	Convective velocity of eddies
u_c	Wake centerline velocity
u_d	$(u_{1o} - u_1)/\Delta u_c$
u_{1rms}	Root mean square velocity fluctuation
x_1, x_2, x_3	Streamwise, transverse, and spanwise directions
$\mathbf{v}^c$	Arbitrary vector field evaluated at critical point, section 6.2

Greek Symbols

α	Streamwise wave number

$\alpha_1, \alpha_2, \alpha_3$	Coefficients for third-order Runge-Kutta scheme, equation (3.4.3.2)
β	Spanwise wave number
$\beta_1, \beta_2, \beta_3$	Coefficients for third-order Runge-Kutta scheme, equation (3.4.3.2)
γ	Ratio of specific heats, c_p/c_v
δ_{ij}	Kronecker delta
Δt	Time step
Δu_c	Initial velocity difference between freestream and wake centerline
$\Delta x_1, \Delta x_2, \Delta x_3$	Grid spacing in the x_1, x_2, x_3 directions
ϵ_{2D}	Initial amplitude of a 2D fundamental mode
ϵ_{2DS}	Initial amplitude of a 2D subharmonic mode
ϵ_{3D}	Initial amplitude of a 3D mode
ζ	k/ρ
θ	Angle of linear disturbance, $\theta = \tan^{-1}(\beta/\alpha)$
Θ	Relative phase angle between a fundamental and a 3D mode
λ	Complex eigenvalue in CFL condition, equation (3.4.3.5)
λ_c	Convective part of λ
λ_d	Diffusive part of λ
μ	Dynamic viscosity
ξ	Transformed computational coordinate in Cain mapping, section 2.3
ρ	Density
σ	Index to indicate fundamental or subharmonic, equation (3.3.1)
τ_{ij}	Shear stress tensor
ϕ	Relative phase angle between a fundamental, α, and its subharmonic, $\alpha/2$
χ	Dependent variable for shooting method, equation (2.3.8)
χ_r	Real part of χ
χ_i	Imaginary part of χ
ψ	μ/Re
ω	Complex eigenvalue from linear stability
ω_r	Real part of complex eigenvalue, frequency
ω_i	Imaginary part of complex eigenvalue, growth rate
$\omega_1, \omega_2, \omega_3$	Vorticity components in x_1, x_2, and x_3 directions
$\boldsymbol{\omega}$	Vorticity vector field

Ancilliary Symbols

$\hat{()}$	Fourier-transformed quantity
$\grave{()}$	Linear eigenfunction, function only of x_2
$\tilde{()}$	Disturbance quantity
$\bar{()}$	Mean quantity
$()_o$	Freestream quantity
$()^*$	Dimensional quantity
$()^c$	Evaluated at critical point
$()$	Total flow, (sum of mean and disturbances)
$()'$	Differentiation in x_2
$()^\dagger$	Complex conjugate
$\lvert()\rvert$	Magnitude

CHAPTER 1

INTRODUCTION

Recent interest in supersonic combustion and problems of transatmospheric flight has prompted renewed research efforts in laminar-turbulent free shear flow transition. The transition problem in a supersonic wake has been a subject of considerable interest over the years. In the 1960s, the location of transition was obtained primarily from hot-wire fluctuation and mean flow measurements combined with interpretations of schlieren photographs and shadowgraphs. In a schlieren photograph (Kendall [1963]) of a Mach 3.2 wake behind a splitter plate forced at its natural frequency, the visible onset of transition occurs several plate lengths downstream of the trailing edge of the plate, suggesting that compressible wakes are more stable than incompressible wakes (see Figure 1-1). The initial instability results in the formation of two rows of staggered vortices in which the large-scale structures that develop are similar to those observed in incompressible wakes; this suggests that there are similarities in the nonlinear development of flat-plate wakes at both high and low Mach numbers. This photograph raises several important questions. Why are supersonic wakes more stable than incompressible wakes? What organized motion results from the initial instability? What similarities does this motion have with incompressible wakes and are there ways to control it? We attempt to provide definitive answers to these questions by performing both a linear stability analysis and two- and three-dimensional direct numerical simulations of a plane compressible wake.

1.1 Background

Currently, our knowledge of the large-scale motion which results from a Kelvin-Helmholtz instability comes largely from experimental studies of incompressible wakes. In this section, some of the results for incompressible wakes are reviewed, along with previous theoretical and experimental results concerning linear growth rates in compressible wakes, and previous incompressible and compressible numerical simulations of free shear flows.

1.1.1 *The Incompressible Wake*

Significant inroads have been made toward understanding transition in incompressible wake flows over the past fifty years. There now exists considerable theoretical (*e.g.* Sato & Kuriki [1961], Mattingly & Criminalie [1972]) and experimental (*e.g.* Sato & Kuriki [1961], Sato & Onda [1970], Sato & Saito [1975]) work leading to a fairly comprehensive picture of the primary stage of transition. This primary stage consists of a Kelvin-Helmholtz instability which results in the development of strong spanwise vortices of alternating sign: the famous two-dimensional Kármán vortex street. This flow pattern manifests itself as a series of vortex centres connected by saddle points in a frame of reference moving with the spanwise vortices (Cantwell & Coles [1983]).

Secondary stages of incompressible transition leading to 3D structures and turbulent breakdown are not as well understood. Early measurements by Townsend [1956] and Grant [1958] of time-averaged velocity correlations in the far wake of a cylinder suggest the presence of 3D structures. These structures were thought to consist of counter-rotating streamwise vortex pairs, later called the double roller eddy by Townsend [1979]. This description of the streamwise vortex pairs was further elaborated on by Payne & Lumley [1967] and Mumford [1983].

There still remains a great deal of uncertainty concerning the instantaneous nature of the streamwise structures and their origin. Based on Grant's interpretation of two counterrotating vortices whose axes are normal to the plane of the wake, and spanwise vortices whose axes are parallel to the plane of the wake, Roshko [1976] conjectured that the 3D structures may be time-averaged superposition of vortex loops, formed by the "pinching off and joining together of vortices from the opposite sides of the street." This formation of vortex loops is possible for wakes and jets, since their mean flow contains two rows of vortices of opposite sign, but not for a mixing layer which contains only one row of vortices of the same sign.

In a reacting flow visualization experiment examining wakes and mixing layers behind a three-dimensionally perturbed splitter plate, Breidenthal [1980] showed that there is a fundamental difference between flows which contain one sign of mean vorticity (mixing layers) and those that contain two (wakes). He observed that the mixing layer rapidly relaxes to its usual two-dimensional structure, while the wake forms closed vortex loops which persist for a long distance downstream without any appreciable spanwise growth.

From inviscid vortex dynamics computations and experimental interface flow visualization, Meiburg & Lasheras [1988] surmised that the inviscid mechanism of vortex stretching is responsible for the formation of counter-rotating pairs of streamwise vortices which superimpose onto the spanwise vortices resulting in the formation of vortex loops, in agreement with Roshko's earlier hypothesis. They showed that if the initial orientation of the periodic perturbation is horizontal, the three-dimensional wake develops into an array of vortex loops which are staggered 180 degrees out-of-phase in the streamwise direction. On the other hand, if the initial orientation of the periodic perturbation is vertical, the three-dimensional wake develops into an array of vortex loops which are aligned in the streamwise direction.

Cimbala, Nagib & Roshko [1988] also observed organized 3D structures in the wake of a cylinder. By placing a smoke wire on one side of the wake centerline, they were able to observe hairpin-like vortices, with successive vortices 180 degrees out-of-phase in the streamwise direction. They suggested that the three-dimensional structures may be a result of a secondary instability based on the interaction of spanwise oblique disturbances with the two-dimensional vortex street. They speculated that this secondary instability may be similar to Pierrehumbert & Widnall's [1982] parametric subharmonic resonance in mixing layers, or to Herbert's [1983] "H-type" instability in channel flows.

Loop-like structures also appear in photographs of forced coflowing wakes and jets taken by Perry, Lim & Chong [1980]. By applying critical point theory to instantaneous velocity vector fields surrounding the vortex loops, they obtained a qualitative description of the three-dimensional flow and related it to their smoke patterns. Their smoke patterns for neutrally buoyant double-sided wakes are quite similar to the photographs of Breidenthal. They described the process of entrainment of irrotational fluid based on the deduced topology of the velocity vector field.

In spite of the volume of experimental, theoretical and numerical work that exists for wakes, a detailed understanding of the underlying mechanism that initiates three-dimensional behavior in wakes and the resultant structure is still missing. Do the structures consist of closed vortex loops or hairpin vortices? How are they connected? Are they aligned or staggered? These are among many questions which still need to be answered.

1.1.2 *The Compressible Wake*

Early attempts at understanding transition in both incompressible and compressible wakes came largely from linear stability theory. Lees & Lin [1946] determined that compressible wakes are inviscidly unstable due to the presence of an inflexion point in the profile of the density-vorticity product. Based on this result, Lees & Gold [1966] speculated that, at least qualitatively, compressible wake transition is similar to low-speed wake transition. They studied the inviscid stability characteristics of compressible, planar, and axisymmetric wake flows and found that a heated wake is more stable than a cool one if the relative Mach number (between the freestream and the wake centerline) is less than the critical Mach number. Their study covered a limited range of relative Mach numbers and temperature defects, and was restricted to two-dimensional disturbances. They did not consider the amplification of three-dimensional waves which Groppengiesser [1970] later found to be important at high Mach numbers for compressible mixing layers.

Experimental measurements of growth rates in the linear regime at supersonic speeds were obtained by Kendall [1962] for a forced wake behind a flat plate at Mach 3.7, by Behrens [1968] for the far wake of cylinders at Mach 6, by Behrens & Lewis [1971] for the wake of a wedge at Mach 4, and by Behrens & Ko [1971] for the wake of a flat plate at Mach 6. Behrens & Ko [1971] found that at Mach 6, the amplitude distributions of the velocity fluctuations across the wake at the fundamental and first harmonic are qualitatively similar to Roshko's [1954] incompressible cylinder far wake measurements. Furthermore, they compared their frequency spectra with Roshko's and found that certain resemblances existed. In both cases, off the wake centerline, there exist peaks in the frequency spectrum where the amplitude of the fundamental frequency is largest, while at the wake centerline, there are peaks at the first harmonic frequency. The main difference between their fluctuation spectra and Roshko's is that the peaks for the Mach 6 wake are broadband waves whereas for Roshko's incompressible wake, the peaks are discrete monochromatic waves. They speculated that these differences would cause the nonlinear vortical motion of the high-speed wake to deviate from the double row of discrete vortices seen in the incompressible wake.

More recently Gasperas [1989] applied viscous linear compressible stability theory and the e^N method to a Mach 3 and Mach 6 flat plate wake to predict the transition location. The e^N method (Smith [1956] and Van Ingen [1965]) bridges the nonlinear processes between linear stability results and the onset of fully developed turbulence. It consists of using stability theory to compute the total growth of the disturbances up to a point where transition is observed. The ratio of the final to initial amplitudes at that location is e^N. Gasperas found that the N-factors for wakes are in the same range as those for attached shear layers (N between 6 and 8). While he showed that increasing the freestream Mach number stabilizes the wake, in agreement with Lees & Gold, he did not consider the influence of oblique disturbance waves on the growth rates.

1.1.3 *Direct Numerical Simulations of Free Shear Flows*

Since the early 1970's, direct numerical simulations of the time-dependent three-dimensional Navier-Stokes equations have been used to study transition and turbulence in free shear flows. In this approach all the significant scales of turbulence are computed without using any turbulence models. In order to resolve the wide range of turbulent scales, highly accurate numerical methods are required. The main disadvantage with direct numerical simulations is that they are limited to low Reynolds numbers due to available computational resolution. The difficulty is that a large number of grid points are needed to resolve both the largest and smallest eddies in a flow. For example, the number of grid points required in a free shear layer is proportional to $Re_\delta^{3/4}$, where Re_δ is the Reynolds number of a free shear layer based on the width and velocity difference driving the shear layer (Mansour, Ferziger & Reynolds [1978]).

The incompressible free shear flow simulations to date are primarily of mixing layers and jets, while wakes have received less attention. There have been even fewer simulations of compressible free shear flows due to their more stringent computational demands. In fact, prior to 1989, no literature on compressible wake simulations existed. Mansour *et al.* [1978] addressed the evolution of the incompressible time-developing mixing layer. They showed, in agreement with Winant & Browand [1974], that the vortex pairing mechanism is responsible for growth in the mixing layer. Riley & Metcalfe [1980a], Patnaik, Sherman & Corcos [1976], Metcalfe, Orszag *et al.* [1987] are among others who have simulated the mixing layer. One of few wake simulations performed was by Riley & Metcalfe [1980b] of a turbulent axisymmetric wake.

Compared to our knowledge of incompressible flows, an understanding of transition for compressible free shear flows is still evolving. Numerically, this is largely due to the added complexity of having to solve a coupled velocity-temperature field. Furthermore, viscous and thermal transport coefficients depend upon the instantaneous local temperature. This leads to a significant increase in the number of parameters which needs to be considered in comparison with incompressible flows and poses even greater numerical restrictions as to the range of Reynolds numbers for which the flow field can be adequately resolved. Current research is heavily focused on the effects of compressibility on mixing phenomenon in compressible free shear layers. Toward this end, Lele [1989] simulated a two-dimensional spatially- and temporally-developing mixing layer and found that compressibility effects alter the behavior of large-scale structures. He attributed the reduction in growth rate of the mixing layer to dilatational effects. He also tested and confirmed the validity of the convective Mach number concept which Bogdanoff [1982] and Papamoschou & Roshko [1986] developed for a mixing layer.

From a linear stability analysis and direct simulations of a time-developing compressible mixing layer, Sandham & Reynolds [1989a,b] showed that oblique waves are dominant above a convective Mach number of 0.6, leading to the formation of three-dimensional structures at high Mach numbers. This is contrary to low-speed mixing layers, where the structure is primarily two-dimensional. Sandham & Reynolds [1989a] attributed the reduced growth rates at high convective Mach numbers to strong baroclinic and dilatational effects.

1.2 Outline of Present Work

In the present work, the influence of compressibility on the mechanisms governing the linear, nonlinear, and three-dimensional stages of transition in a supersonic wake is investigated. A description of the three-dimensional topology of a compressible wake from critical point theory is used to provide a concise, unambiguous representation of the computed flow fields. Finally, the effect of a relative phase lag between a fundamental and its subharmonic is investigated as a possible means of controlling the evolution of a wake.

In Chapter 2, results from a linear stability analysis provide physical insights for the observed reduction in growth rate at high Mach numbers. A newly-developed hybrid algorithm, which combines a direct spectral method with a shooting method, is used to solve the compressible inviscid linear disturbance equations. Growth rates for both antisymmetric and symmetric modes of two-dimensional and oblique waves are computed for a wide range of Mach numbers between 0.01 and 7.0. Linear eigenfunctions of the velocity components, temperature, and density are computed and are later employed as initial conditions in the direct simulations.

In Chapter 3, a new spectral collocation method for solving the compressible Navier-Stokes equations for a parallel mean free shear flow with periodic freestream boundary conditions is described. The method combines Fourier expansions of spatial derivatives of the dependent variables with an explicit time-advancement algorithm.

In Chapter 4, results obtained from two-dimensional direct simulations for two different problems are described. First, results concerning the effect of compressibility on the linear and nonlinear evolution of the flow field are discussed. An explanation for the observed reduction in growth rate is offered based on the behavior of several compressible vorticity source terms. Second, the effect of varying the relative phase difference between a fundamental and its subharmonic is explored as one possible means of controlling the evolution of a wake.

In Chapter 5, results obtained from three-dimensional direct simulations are used to explore the response of a compressible plane wake to various three-dimensional disturbances. The disturbances consist of unstable two-dimensional and oblique modes obtained from a linear stability analysis. First, the sensitivity of a low Mach number wake to (1) a phase difference imposed between a fundamental and a pair of oblique waves, and (2) the streamwise wavelength of the oblique waves is determined. Second, the effect of Mach number on the evolution of three-dimensional large-scale motions is determined. The vorticity dynamics of the flow are studied in detail and the developed temperature, density, and pressure fields are presented.

In Chapter 6, the evolution of the topology of the velocity, vorticity, and pressure gradient fields is presented and compared with the results of Chapter 5. Instantaneous streamlines, vortex lines, and pressure gradient vectors are computed from the three-dimensional flow fields obtained from the simulations. A generalized three-dimensional critical point theory is employed to classify the critical points in the flow. The topology of the initial three-dimensional disturbance field is determined and compared with the morphology of the developed wake.

In Chapter 7, conclusions are stated and possible avenues for future work are suggested.

1.3 Summary of Results

Linear Stability. From a three-dimensional compressible inviscid linear stability analysis, the influence of increasing Mach number is found to be stabilizing, resulting in reduced growth rates for both antisymmetric and symmetric modes of the wake. The least stable wave at all Mach numbers corresponds to an antisymmetric wave aligned with the streamwise direction. This implies that the initial roll-up of vortices for both low and high Mach number wakes will be inherently two-dimensional, and that any subsequent three-dimensional motion must be the result of secondary instabilities. Linear eigenfunctions are used to construct several compressible vorticity source terms in the linearized vorticity equation. Baroclinic and dilatational effects, which prevent the roll-up of spanwise vortices, are found to be primarily responsible for the reduction in growth rate at high Mach numbers.

Two-Dimensional Simulations–Nonlinear Compressibility Effects. From two-dimensional direct simulations, it is shown that the primary influence of increasing Mach number is to delay the onset of nonlinear roll-up of vortices. The actual roll-up process is remarkably similar to its incompressible counterpart. The delay is due to the much lower linear amplification rates of these disturbances at high Mach numbers. Due to large density gradients present in the flow at high Mach number, the baroclinic torques become significant and prevent vorticity from being advected into the cores of the rollers. Dilatational effects are also important, particularly in the saddle region, assisting the baroclinic torques in inhibiting the roll-up.

Two-Dimensional Simulations–Flow Control. Using the results from two-dimensional simulations, one possible means of controlling the evolution of a wake is investigated by varying the relative phase difference between a fundamental and its subharmonic. The results of these simulations show the asymmetric development of the subharmonic on either side of the wake for relative phase angles between 0 and $\pi/2$. For the limiting cases of 0 and $\pi/2$, pairing is observed on only one side of the wake, and for angles in between, on both sides. However, there is no angle for which pairing can occur at the same rate on both sides of the wake. This is a result of the staggered arrangement that the fundamental vortices assume after the fundamental saturates.

Three-Dimensional Simulations. The development of the three-dimensional motion is explained in terms of the morphology of the large-scale structures and the topology of velocity, vorticity, and pressure gradient vector fields.

Three-Dimensional Morphological Description. The morphology of a compressible wake is described by contour plots of vorticity components, magnitude of vorticity, and vorticity stretching terms at various stages in their development. These plots show the development of a pair of counterrotating streamwise vortices in the saddle point region on either side of the wake which are aligned with the diverging separatrix. Initially the diverging separatrix connects spanwise vortices of a similar sense of rotation. In other words, the initial stages of the wake appear as two separate mixing layers. As the vorticity in the alleyway is entrained into the two layers, the two sides begin to behave as a single wake in which the diverging separatrix connects spanwise vortices of alternating sign. The intensification and stretching of the streamwise vorticity in the mean strain field of the spanwise vortices eventually leads to the development of vortex loops inclined along the principal axis of positive strain, depending upon the initial phase difference between the fundamental and a pair of oblique waves. From oblique subharmonic simulations, vortical structures develop which exhibit a staggered "peak-valley-splitting" arrangement similar to the "H-type" secondary instability found in boundary layers and channel flows. There is, however, no evidence of any oblique pairings in the simulations.

Three-Dimensional Topological Description The topology of the velocity, vorticity, and pressure gradient vector fields complements the interpretation of the three-dimensional motion provided by the morphology of the vorticity field. The initial topology of the wake is found to be equivalent to two staggered mixing layers. After the fluid in the alleyway is entrained into the mixing layers, the topology bifurcates such that the saddle points connect opposite sides of the wake. This interpretation is consistent with the temporal evolution of the streamwise vorticity in the saddle point region. From the velocity field, the topology of a two-dimensional compressible wake is found to consist of stable foci and saddle points while the topology of a three-dimensional compressible wake is found to consist of spanwise alternating stretching and contracting foci points and saddle points. Moreover, limit cycles are found to exist in between the focus points in the spanwise direction.

From a critical point analysis of the vorticity field, the topology of the vorticity field is found to consist of no-flow through centers connected by saddle points. Vortex loops form as a result of the interaction of the streamwise vorticity with the spanwise vortices. In addition to the vorticity field, the pressure gradient field is studied because it indicates, neglecting viscous forces, the acceleration direction of a fluid particle. The pressure gradient vector field is found to consist of nodes coinciding with the spanwise vortex centres and saddle points connecting the centres.

CHAPTER 2

LINEAR STABILITY THEORY

In this chapter, the response of a compressible plane wake to two-dimensional and three-dimensional disturbances is investigated using linear stability theory. The linearized compressible inviscid disturbance equations are solved, using a new hybrid algorithm, to find the growth rates and eigenfunctions of these disturbances for freestream Mach numbers ranging from the incompressible limit to a supersonic value of 7. From the growth rates, the least stable disturbance (mode) is determined; it is anticipated that this mode will initiate nonlinear roll-up of large-scale structures in the wake. The growth rate is found to always decrease with increasing Mach number and, from the eigenfunctions, terms in the linearized vorticity equation are constructed which offer a physical explanation of this reduction. The eigenfunctions also provide initial conditions for the direct simulations described in subsequent chapters.

Note: In this chapter, the mean flow and disturbances are normalized by the appropriate physical scales. Velocities are normalized by the freestream velocity (u_{1o}). Length scales are normalized by the initial half width of the wake (b_i), temperature and density are normalized by their freestream values (T_o, ρ_o), and pressure is normalized by p_o.

2.1 Mean Flow

Consider the linear stability of a compressible parallel plane wake moving in the streamwise (x_1) direction with variations in the transverse direction (x_2). It is assumed that the laminar mean flow for a wake, on which the stability analysis is based, consists of Gaussian profiles of velocity and temperature. The Gaussian profile is a good approximation for the far-wake region behind a body. In this region the mean velocity ($\overline{u}_1$) is given by

$$\overline{u}_1 = 1 - \Delta u_c e^{-c_1 x_2^2} \qquad (2.1.1)$$

where Δu_c is the velocity deficit at the wake centerline, c_1 is a scaling factor, and x_2 is the distance from the centerline (the transverse coordinate). The factor c_1 is chosen to be 0.69 in order to make the initial wake halfwidth (b_i) equal to 1.0 *

The mean temperature ($\overline{T}$) is obtained from the mean velocity ($\overline{u}_1$) by assuming that the mean flow for a perfect gas satisfies the steady boundary-layer equations, that the Prandtl number of the flow is 1.0, and that the ratio of specific heats (γ) is constant. For these conditions, irrespective of the form of the viscosity and thermal conductivity, the mean temperature depends only on the mean velocity. This approach was first used by Crocco [1932] and Busemann [1931] to study the compressible boundary layer over a flat plate. The total enthalphy equation takes on the following form

$$\overline{\rho}\,\overline{u}_1\frac{\partial \bar{H}}{\partial x_1} + \overline{\rho}\,\overline{u}_2\frac{\partial \bar{H}}{\partial x_2} = \frac{d}{dx_2}\left(\frac{\mu}{Pr}\frac{\partial \bar{H}}{\partial x_2}\right) \tag{2.1.2}$$

which admits the solution

$$\bar{H} = \bar{h} + \overline{u}_1^2 = \text{constant}. \tag{2.1.3}$$

Setting $\bar{H} = \bar{H}_o$ and substituting $\bar{h} = c_p\overline{T}$ into equation (2.1.3), the relation between temperature and velocity is obtained

$$\overline{T} = 1 + 0.5M^2(\gamma - 1)(1 - \overline{u}_1^2). \tag{2.1.4}$$

Figure 2-1 shows the mean velocity profile, which does not depend on Mach number, for a velocity deficit of 0.692. Figure 2-2 shows several mean temperature profiles for the same velocity deficit and freestream Mach numbers ranging from 1 to 7. In the next section, the compressible, inviscid linear disturbance equations are derived for a plane compressible wake.

2.2 Derivation of the Linearized Inviscid Disturbance Equations

Lees & Lin [1946] showed that inviscid compressible free shear flows are more unstable than their viscous counterparts because a point of inflection exists in the profile of the density vorticity product. Therefore, since the growth rate of the most unstable mode is of interest, the inviscid compressible disturbance equations are solved. The

---

* Sato & Kuriki [1961] considered $\Delta u_c = 0.692$ in their experiments; here we consider values ranging from 0.692 to 1.

starting point for a linear stability analysis is the equations of continuity, momentum, and energy in Cartesian coordinates for a perfect gas. Neglecting molecular diffusion, these equations are given in the nondimensional form

$$\frac{\partial \rho}{\partial t} + \frac{\partial(\rho u_j)}{\partial x_j} = 0$$

$$\frac{\partial \rho u_i}{\partial t} + \frac{\partial(\rho u_i u_j)}{\partial x_j} = -\frac{1}{\gamma M^2}\frac{\partial p}{\partial x_i}$$

$$\rho\frac{\partial T}{\partial t} + \rho u_j \frac{\partial T}{\partial x_j} = -(\gamma - 1) p \frac{\partial u_j}{\partial x_j}. \tag{2.2.1}$$

Any inviscid flow, perturbed or unperturbed, satisfies equation (2.2.1). By representing the total flow as the sum of its mean and fluctuating parts, the stability of the mean flow subjected to time-varying disturbances can be studied. Superposed on the mean are fluctuations in the velocity components, density, and temperature, so that

$$\mathbf{b} = \bar{\mathbf{b}} + \tilde{\mathbf{b}}, \tag{2.2.2}$$

where $\mathbf{b} = [u_1, u_2, u_3, \rho, T]$ is the total flow vector, $\bar{\mathbf{b}} = [\overline{u}_1, \overline{u}_2, \overline{u}_3, \bar{\rho}, \bar{T}]$ is its mean part, and $\tilde{\mathrm{b}} = [\tilde{u_1}, \tilde{u_2}, \tilde{u_3}, \tilde{\rho}, \tilde{T}]$ is its fluctuating part. Substituting equation (2.2.2) into equation (2.2.1), subtracting the mean part from equation (2.2.1) since it satisfies the steady boundary layer equations, and linearizing the disturbances, the disturbance equations become a system of partial differential equations

$$\frac{\partial \tilde{\rho}}{\partial t} + \overline{\rho}(\frac{\partial \tilde{u}_i}{\partial x_i}) + \overline{u}_1 \frac{\partial \tilde{\rho}}{\partial x_1} + \tilde{u}_2 \frac{\partial \overline{\rho}}{\partial x_2} = 0$$

$$\overline{\rho}\frac{\partial \tilde{u}_i}{\partial t} + \overline{u}_i \frac{\partial \tilde{\rho}}{\partial t} + \overline{\rho}\,\overline{u}_i \frac{\partial \tilde{u}_j}{\partial x_j} + \overline{u}_j \overline{\rho} \frac{\partial \tilde{u}_i}{\partial x_j} + \tilde{u}_j \overline{\rho} \frac{\partial \overline{u}_i}{\partial x_j} + \overline{u}_j \overline{u}_i \frac{\partial \tilde{\rho}}{\partial x_j} + \tilde{u}_j \overline{u}_i \frac{\partial \overline{\rho}}{\partial x_j} = -\frac{1}{\gamma M^2}\frac{\partial \tilde{p}}{\partial x_i}$$

$$\overline{\rho}\frac{\partial \tilde{T}}{\partial t} + \overline{\rho}\,\overline{u}_j \frac{\partial \tilde{T}}{\partial x_j} + \overline{\rho}\tilde{u}_j \frac{\partial \overline{T}}{\partial x_j} = -(\gamma - 1)(\bar{p}\frac{\partial \tilde{u}_j}{\partial x_j}). \tag{2.2.3}$$

If the disturbances are further assumed to behave as travelling waves, then in nondimensional form they are given as

$$\tilde{\mathrm{b}} = \grave{\mathbf{b}}_{3\mathrm{D}} e^{i(\alpha x_1 + \beta x_3 - \omega t)} \tag{2.2.4}$$

where $\grave{\mathbf{b}}_{3\mathrm{D}} = \left[\grave{u}_1, \grave{u}_2, \grave{u}_3, \grave{\rho}, \grave{T}\right]$ is a vector of complex eigenfunctions dependent only on the transverse direction (x_2), α is the streamwise wave number, β is the spanwise wave number, and ω is the frequency. In the most general case, the amplitude, $\grave{\mathbf{b}}_{3\mathrm{D}}$, the streamwise and spanwise wave numbers, α and β, and the frequency, ω, in equation (2.2.4) can be complex. Since temporal instabilities are considered, α and β are real quantities, while $\omega = \omega_r + i\omega_i$ is complex. The imaginary part of ω represents the growth rate of the disturbance, the real part its frequency. Disturbances are amplified when ω_i is positive, damped when ω_i is negative, and are neutrally stable when ω_i is zero. The angle the disturbance makes with the streamwise direction is given by

$$\theta = \tan^{-1}(\beta/\alpha). \tag{2.2.5}$$

By substituting equation (2.2.4) into equation (2.2.3), the system of partial differential equations in equation (2.2.3) is reduced to a system of ordinary differential equations in x_2 for the amplitudes of the disturbances

$$\begin{gathered}
i\grave{\rho}(\alpha\overline{u}_1 - \omega) + \grave{u}_2\overline{\rho}' + \overline{\rho}[i(\alpha\grave{u}_1 + \beta\grave{u}_3) + D\grave{u}_2] = 0 \\
\overline{\rho}[i(\alpha\overline{u}_1 - \omega)\grave{u}_1 + \overline{u}_1'\grave{u}_2] = -\frac{i\alpha}{\gamma M^2}\grave{p} \\
i\overline{\rho}(\alpha\overline{u}_1 - \omega)\grave{u}_2 = -\frac{D\grave{p}}{\gamma M^2} \\
i\overline{\rho}(\alpha\overline{u}_1 - \omega)\grave{u}_3 = -\frac{i\beta\grave{p}}{\gamma M^2} \\
\overline{\rho}[i(\alpha\overline{u}_1 - \omega)\grave{T} + \grave{u}_2\grave{T}'] = -(\gamma - 1)[i(\alpha\grave{u}_1 + \beta\grave{u}_3) + D\grave{u}_2].
\end{gathered} \tag{2.2.6}$$

Here D is the differentiation operator d/dx_2 and $'$ denotes known derivatives of the mean with respect to x_2. An equation for $\grave{p}$, the pressure disturbance, is obtained from the linearized perfect gas equation of state

$$\grave{p} = \grave{\rho}\overline{T} + \overline{\rho}\grave{T}. \tag{2.2.7}$$

According to equation (2.2.4), disturbances can either grow or decay exponentially away from the shear layer as $x_2 \to \pm\infty$. Only the decaying disturbances are physically meaningful; therefore, the boundary condition

$$\text{as } x_2 \rightarrow \pm\infty \qquad \grave{\mathbf{b}} \rightarrow 0 \tag{2.2.8}$$

is imposed. With the governing amplitude equations (2.2.6) in x_2, and the homogeneous boundary conditions (2.2.8), the following eigenvalue problem is defined: *for a given α and β, the eigenvalues, ω_r and ω_i, are to be determined such that the eigenfunctions of equation (2.2.6), $\grave{\mathbf{b}}$, satisfy the boundary conditions (2.2.8).*

2.3 Solution of the Eigenvalue Problem

Two possible approaches to solving equations (2.2.6) are direct spectral methods and shooting methods. Direct spectral methods capture all of the unstable modes, whereas conventional shooting methods can only solve for a single mode at a time. However, direct spectral methods converge slowly as weakly amplified disturbances approach the neutral singular point (Leibovich & Lele [1985]). Shooting methods are required since symmetric disturbances at all wave numbers are weakly amplified at high Mach numbers resulting in slow convergence in a direct method. Shooting methods, however, require a reasonable initial guess for the eigenvalues. The drawbacks of both methods are overcome by a hybrid approach; the inviscid linear disturbance equations are solved with a direct spectral method to obtain an initial estimate of the eigenvalues for a shooting method.

Direct Spectral Method. In the direct spectral method used here, $\grave{p}$ is eliminated from the momentum equations in (2.2.6) by substituting the linearized equation of state (2.2.7) into equations (2.2.6). The resultant disturbance equations are then cast as a 5 × 5 matrix eigenvalue problem

$$A\grave{\mathbf{b}}_{\mathbf{3d}} = \omega\grave{\mathbf{b}}_{\mathbf{3d}}, \tag{2.3.1}$$

where

$$\mathrm{A} = \begin{bmatrix} \alpha\overline{u}_1 & \alpha\overline{\rho} & -i(\overline{\rho}' + \overline{\rho}D) & \overline{\rho}\beta & 0 \\ \frac{\alpha\overline{T}}{\overline{\rho}\gamma M^2} & \alpha\overline{u}_1 & -i\overline{u}_1' & 0 & \frac{\alpha}{\gamma M^2} \\ \frac{-i(\overline{T}'+\overline{T}D)}{\overline{\rho}\gamma M^2} & 0 & \alpha\overline{u}_1 & 0 & \frac{-i(\overline{\rho}'+\overline{\rho}D)}{\overline{\rho}\gamma M^2} \\ \frac{\beta\overline{T}}{\overline{\rho}\gamma M^2} & 0 & 0 & \alpha\overline{u}_1 & \frac{\beta}{\gamma M^2} \\ 0 & \frac{(\gamma-1)\alpha}{\overline{\rho}} & -i(\overline{T}' + \overline{T}(\gamma-1)D) & \overline{T}\beta(\gamma-1) & \alpha\overline{u}_1 \end{bmatrix}. \tag{2.3.2}$$

For a temporal instability $\grave{\mathbf{b}}_{\mathbf{3d}} = [\grave{\rho}, \grave{u}_1, \grave{u}_2, \grave{u}_3, \grave{T}]$ are the unknown eigenfunctions, and ω is the unknown complex eigenvalue. The matrix A contains terms involving derivatives of known mean quantities denoted by $'$ as well as derivatives of unknown eigenfunctions denoted by D. The mean velocity, temperature, and density profiles are differentiated in x_2 using a spectral mapping developed by Cain, Ferziger & Reynolds [1981, 1984]. This scheme maps an infinite domain onto a finite computational domain in which the mapping function for a wake is given as

$$x_2 = h(\xi) = -a\cot(\pi\xi) \qquad (0 \leq \xi < 1) \quad (-\infty \leq x_2 \leq \infty), \tag{2.3.3}$$

where a is a grid stretching parameter. The first derivative operator for a wake is given by

$$\left.\frac{\partial f}{\partial x_2}\right|_j = \frac{1}{a}\sum_{n=-N/2+1}^{N/2-1}\left[in\hat{f}_n - \frac{i}{2}(n-1)\hat{f}_{n-1} - \frac{i}{2}(n+1)\hat{f}_{n+1}\right]e^{i2\pi n\xi_j}, \tag{2.3.4}$$

where $\hat{f}_n$ is a complex Fourier coefficient

$$\hat{f}_n = \frac{1}{N}\sum_{j=0}^{N-1} f(\xi_j)e^{-i2\pi n\xi_j}. \tag{2.3.5}$$

Here, a new differentiation operator is developed, which casts the derivatives of the unknown eigenfunctions as a product of an $N \times N$ matrix P whose elements are given by p_{lj} with the unknown eigenfunctions, $\grave{\mathbf{b}}_{\mathbf{3d}}$, where N is the number of collocation points in x_2. For instance, the derivative of a function $f(x_2)$ is expressed as

$$(Df)_\ell = \sum_{j=0}^{N-1} p_{\ell j} f(\xi_j). \tag{2.3.6}$$

Substituting equation (2.3.5) into equation (2.3.4), applying the definition for a geometric series and simplifying, the matrix elements p_{lj} in equation (2.3.6) become, for $j \neq l$

$$\mathrm{p}_{\ell j} = \frac{1}{a}\left\{\frac{[1-\cos(2\pi\xi_j)]}{2}(-1)^{\ell-j}\cot\left[\frac{\pi(\ell-j)}{N}\right] - \frac{\sin(2\pi\xi_j)}{N}\right.$$
$$\left.\frac{\sin[\frac{N-1}{N}\pi(\ell-j)]}{\sin[\frac{\pi(\ell-j)}{N}]}\right\} \tag{2.3.7a}$$

and for $j = l$

$$\mathrm{p}_{\ell j} = -\frac{1}{a}\left\{\frac{\sin(2\pi\xi_j)(N-1)}{N}\right\}. \tag{2.3.7b}$$

The linear disturbance equations are solved at N collocation points resulting in a $5N \times 5N$ matrix, which can be solved by a standard library routine to determine all of the eigenvalues and eigenvectors for a given set of parameters. The parameters include the freestream Mach number, the mean velocity and mean temperature profiles and their first derivatives, the streamwise and spanwise wave numbers, and the ratio of specific heats.

Shooting Method. The shooting method employed here is a generalization of a method developed by Groppengiesser [1970] for compressible plane mixing layers. Sandham [1989c] extended the method of Groppengiesser to plane compressible free shear flows for both temporal and spatial stability problems. The essence of the method is the reduction of the system of five linear disturbance equations (2.2.6) to one nonlinear first-order equation of the Riccati type, by introducing a new variable χ defined as

$$\chi = \chi_r + i\chi_i = \frac{i\alpha\grave{p}}{\gamma M^2 \grave{u}_2}. \tag{2.3.8}$$

The advantage of the χ transformation is that numerically, neutral supersonic disturbances remain regular in the critical layer, whereas they become singular in $\grave{u}_2$, which is the variable solved for normally. The first-order equation in χ is

$$\frac{d\chi}{dx_2} = \frac{\alpha^2(\overline{u}_1 - \frac{\omega}{\alpha})}{\overline{T}} - \frac{\chi(G\chi + \overline{u}_1{}')}{(\overline{u}_1 - \frac{\omega}{\alpha})}, \tag{2.3.9}$$

where

$$G = \frac{\overline{T}(\alpha^2 + \beta^2)}{\alpha^2} - \frac{M^2(\alpha\overline{u}_1 - \omega)^2}{\alpha^2}. \tag{2.3.10}$$

In the freestream, $\overline{u}_1'$ is zero and $\grave{p}$ and $\grave{u}_2$ decay at the same exponential rate. Therefore, χ must approach a constant value in the freestream since it is formed from the ratio of $\grave{p}$ and $\grave{u}_2$. Setting $\frac{d\chi}{dx_2}$ and $\overline{u}_1'$ to zero at infinity in equation (2.3.9) yields the following boundary condition for χ

$$\chi(x_2 = \pm\infty) = \frac{\alpha(\overline{u}_1 - \omega/\alpha)}{\sqrt{G\overline{T}}}. \tag{2.3.11}$$

Specifying the mean flow, α and β, and providing an initial estimate for ω, equation (2.3.9) is integrated from $x_2 = \pm\infty$ to the centerline of the flow, $x_2 = 0$, where χ from both sides of the integration is matched. The eigenvalue ω is iterated upon using a Newton-Raphson scheme until convergence to a specified tolerance (10^{-7}) is reached. To approximate the freestream, integrations are started ten initial half widths away from the wake centerline. At this distance, the eigenfunctions have decayed to 10^{-5}. For the symmetric mode of the wake, $\grave{u}_2 = 0$ at $x_2 = 0$, and χ approaches infinity according to equation (2.3.9). Therefore, for this mode, the variable $1/\chi$ is integrated from infinity to $x_2 = 0$ rather than the variable χ.

The eigenfunctions are then obtained by integrating equations for $\grave{p}$ and $\grave{u}_2$ from the centerline out to the freestream. The details of the method are described in Sandham [1989c] and Groppengiesser [1970]. Sandham & Reynolds [1989a] used this approach to study the effect of Mach number on the stability of a compressible plane mixing layer.

2.4 Verification

Linear growth rates obtained from the direct and shooting methods were checked against each other. These comparisons are shown in Figure 2-3 at several different Mach numbers. Both methods are able to capture the most unstable mode. However, the spectral method has difficulty converging at high wave numbers where the disturbances are weakly amplified.

Comparisons are also made between the shooting method and measurements of an incompressible wake (Sato & Kuriki [1961]). The phase velocity for the two methods is shown in Figure 2-4 where the agreement is quite good. Finally, the magnitude of the $\hat{u}_1$ eigenfunction, obtained from the shooting method, is compared with the results of Sato & Kuriki [1961] in Figure 2-5.

2.5 Results

The method described in the previous section was used to compute growth rates for antisymmetric and symmetric modes of two-dimensional and oblique waves in a plane compressible wake for freestream Mach numbers ranging from 0.01 to 7. The centerline velocity deficit was assumed to be 0.692 for all cases to match Sato & Kuriki [1961].

The influence of increasing Mach number on the growth rate of two-dimensional antisymmetric and symmetric modes is shown in Figures 2-6 and 2-7. Both modes are damped with increasing Mach number. The maximum growth rate for a given Mach number shifts to longer wavelength, lower frequency disturbances with increasing Mach number. At $M = 3$ the growth rate of the most unstable antisymmetric mode is 57% of the incompressible growth rate. In agreement with Lees & Gold [1966], the antisymmetric mode is found to be considerably more amplified than the symmetric mode for the range of Mach numbers considered. While the antisymmetric mode continues to be amplified at high Mach numbers, the symmetric mode is completely damped for two-dimensional disturbances above $M = 2$. Figures 2-8 and 2-9 show the frequency of the most unstable two-dimensional antisymmetric and symmetric modes as a function of Mach number.

The effect of obliquity on the growth rate of antisymmetric and symmetric modes is shown in Figures 2-10 and 2-11. For nearly incompressible flow ($M = 0.01$), the most unstable wave for both antisymmetric and symmetric modes corresponds to a two-dimensional wave as required by Squire's theorem (Squire [1933]). For the antisymmetric mode, even as the Mach number increases, the most unstable wave remains a two-dimensional wave, *i.e.* $\theta = 0$. The effect of increasing obliquity at all Mach numbers is a reduction in the growth rate. The symmetric mode behaves differently from the antisymmetric mode at high Mach numbers. For the symmetric mode, above $M = 1.2$, three-dimensional waves of increasing obliquity are more amplified than two-dimensional waves.

Figure 2-12 shows a comparison of the growth rates of the most unstable three-dimensional antisymmetric and symmetric modes for Mach numbers ranging from 0.01 to 7. Note, that for both modes there is a substantial reduction in growth rate with increasing Mach number. As the Mach number increases from the incompressible limit, the most unstable antisymmetric mode remains a two-dimensional wave oriented in the streamwise direction. However, for $M > 1.2$, the most unstable symmetric mode becomes more oblique at higher Mach numbers, *e.g.* at $M = 3$, the most unstable symmetric mode is an oblique wave at $\theta = 60$ degrees. (θ is indicated only for the symmetric mode since $\theta = 0$ corresponds to the most unstable antisymmetric mode.)

In summary, for $0.01 < M < 7$, the two-dimensional antisymmetric mode is always significantly more amplified than the symmetric oblique mode. This implies that the first nonlinear structures to develop from the disturbances will be two-dimensional for both incompressible and compressible wakes. This contrasts with mixing layers, where the dominant waves are three-dimensional for convective Mach numbers above 0.6 (Sandham [1989a, 1989b]).

2.6 Eigenfunctions

Since the two-dimensional antisymmetric mode initiates instability in the wake, it is worthwhile to examine its linear eigenfunctions $\grave{u}_1$, $\grave{u}_2$, $\grave{\rho}$, and $\grave{T}$. These eigenfunctions are shown in Figures 2-13 to 2-15, normalized by the peak value of the largest eigenfunction, for $M = 0.01$, $M = 3$, and $M = 7$. Note that $\grave{u}_1$, $\grave{\rho}$, and $\grave{T}$ are antisymmetric about the wake centerline, while $\grave{u}_2$ is symmetric. The shape of $\grave{u}_1$ agrees qualitatively with measurements by Sato & Kuriki [1961] for an incompressible wake behind a flat plate. The shape is characterized by twin peaks centered below and above the wake centerline. While the shapes of the velocity, temperature, and density eigenfunctions are qualitatively the same for the Mach numbers considered ($0.01 < M < 7$), the temperature and density eigenfunctions become more important as the Mach number increases. For example, for $M = 3$, the temperature eigenfunction is five times larger than the streamwise velocity eigenfunction. The temperature, density, and pressure disturbances are proportional to M^2. Therefore, for a given velocity fluctuation, the relative importance of the temperature and density eigenfunctions increases with increasing Mach number.

While the eigenfunctions are employed in subsequent chapters as initial conditions in direct simulations, they are interesting in their own right. In particular, they are used to construct various terms in the linearized vorticity equation which can be compared with the nonlinear development of these same terms computed from direct simulations. The inviscid vorticity equation for ω_3 is

$$\begin{aligned}\frac{D(\omega_3)}{Dt} = &-\omega_3\left(\frac{\partial u_1}{\partial x_1}+\frac{\partial u_2}{\partial x_2}\right)\\ &+\frac{1}{\rho^2}\left(\frac{\partial p}{\partial x_1}\frac{\partial \rho}{\partial x_2}-\frac{\partial \rho}{\partial x_1}\frac{\partial p}{\partial x_2}\right),\end{aligned} \tag{2.6.1}$$

where the two terms on the right-hand side of equation (2.6.1) are compressible vorticity source terms. The first term is the product of spanwise vorticity and the divergence of the velocity field, representing fluid compression and expansion. The second term is the baroclinic torque, produced by pressure and density gradient vectors which have a non-zero cross product.

Contour plots of the pressure, density, spanwise vorticity, baroclinic and dilatational terms formed from these linear eigenfunctions are shown in Figure 2-16. The vorticity and density are assumed to be composed of the mean flow plus disturbances which have been artificially amplified by 50%. This is to bring out the structure in the flow which would otherwise be dominated by the mean flow. The vorticity contour plot shows that in each layer two elementary vortices will rotate around each other to form a larger vortex. The pressure and density contour plots show that the minima will be located where the vortex centres will form and the maxima will be located in between the centres where the saddle points will form. Because the pressure vector forms a non-zero cross product with the density in the saddle point region, baroclinic torques are created. They prevent the elementary vortices from rolling up, even in the linear region of the flow. Baroclinic torques become more significant at higher Mach numbers because the density and pressure gradients are proportional to M^2. Similarly, the product of dilatation and vorticity is negative in exactly those regions where the vorticity is positive, cancelling the vorticity which is trying to roll-up. We believe it is these compressible vorticity source terms, which originate from linear stability theory, that may possibly account for the reduction in growth observed by Kendall [1962] for a compressible wake.

CHAPTER 3

MATHEMATICAL FORMULATION AND NUMERICAL METHODOLOGY

In this chapter, a new algorithm is presented for solving the three-dimensional compressible Navier-Stokes equations on a domain typical for time-developing plane wake and jet flows. The domain is homogeneous in the streamwise (x_1) and spanwise (x_3) directions, and is doubly infinite in the normal direction (x_2) where a mapped Fourier method is used. Motivated by a desire to study the evolution of a wake, a spectral collocation method combining Fourier methods with a higher-order accurate time integration scheme was developed. Before the details of the numerical method are presented, a mathematical formulation of the time-developing compressible wake flow is given. The equations and the numerical algorithms put forth in this chapter form the basis for the 2D and 3D simulation codes used to perform the studies described in subsequent chapters.

Note: All equations presented in this chapter have been nondimensionalized by characteristic physical scales as follows:

$$x_1 = \frac{x_1^*}{b_i} \qquad x_2 = \frac{x_2^*}{b_i} \qquad x_3 = \frac{x_3^*}{b_i} \qquad t = \frac{t^*}{b_i/u_{1o}}$$

$$u_1 = \frac{u_1^*}{u_{1o}} \qquad u_2 = \frac{u_2^*}{u_{1o}} \qquad u_3 = \frac{u_3^*}{u_{1o}} \qquad \mu = \frac{\mu^*}{\mu_{1o}}$$

$$\rho = \frac{\rho^*}{\rho_o} \qquad p = \frac{p^*}{\rho_o {u_{1o}}^2} \qquad T = \frac{T^*}{T_o} \qquad e = \frac{e^*}{{u_{1o}}^2}$$

where the asterisk denotes dimensional quantities. All length scales have been normalized by the initial half-width of the wake, b_i; all velocities by the freestream velocity, u_{1o}; pressure by $\rho_o {u_{1o}}^2$; internal energy by ${u_{1o}}^2$; and all other quantities by their respective freestream values.

3.1 Governing Equations

While linear theory predicts the growth rate and frequency of disturbances when their amplitude is small relative to the mean flow, it does not provide information about nonlinear interaction between different modes when the amplitudes of the disturbances become large. Therefore, to investigate the nonlinear evolution of these disturbances, direct numerical simulations of the compressible Navier-Stokes equations were performed. As in linear stability theory, the mean flow was assumed to be parallel so that the wake could develop temporally as opposed to spatially. In the temporal reference frame, the observer moves with the large eddies in the flow as they move downstream. The temporal evolution is related to the spatial evolution by the Taylor hypothesis

$$x_1 = U_c t \tag{3.1.1}$$

where U_c is the speed at which the large eddies are convected. Consider the computational domain for a temporal wake, shown in Figure 3-1, with a Cartesian coordinate system oriented with x_1 in the mean flow direction, x_2 in the major gradient direction, and x_3 in the spanwise direction. The flow is homogeneous in x_1 and x_3 so periodic boundary conditions can be applied in those two directions. The major gradient direction (x_2) is doubly infinite with freestream boundary conditions applied at $x_2 = \pm\infty$. The laminar mean velocity and temperature profiles are the same as those employed in the linear stability analysis (equations (2.1.1) and (2.1.4)). The choice of the computational box size, L_1 and L_3, was determined from linear stability theory and has to be large enough to support the growth of the longest wave

$$L_1 = 2\pi n/\alpha, \qquad L_3 = 2\pi n/\beta \tag{3.1.2}$$

where n is the number of multiples of the fundamental wavelength. For example, in the pairing simulations $n = 2$. The wave number of the fundamental, α, corresponds to the most unstable wave predicted from linear stability theory. The spanwise wave number β corresponds to an amplified oblique wave oriented between 30 and 50 degrees with respect to the streamwise direction.

In the direct simulations of the temporally-evolving wake, the following equations governing the conservation of mass, momentum, and energy for a compressible Newtonian fluid were solved without incorporating any turbulence models:

$$\frac{\partial \rho}{\partial t} + \frac{\partial(\rho u_i)}{\partial x_i} = 0 \tag{3.1.3}$$

$$\frac{\partial(\rho u_i)}{\partial t} + \frac{\partial(\rho u_i u_j)}{\partial x_j} = -\frac{\partial p}{\partial x_i} + \frac{\partial \tau_{ij}}{\partial x_j} \qquad (i = 1,2,3) \tag{3.1.4}$$

$$\frac{\partial E_T}{\partial t} + \frac{\partial (E_T u_j)}{\partial x_j} = -\frac{\partial (p u_j)}{\partial x_j} + \frac{\partial (u_i \tau_{ij})}{\partial x_j} - \frac{\partial q_j}{\partial x_j} \tag{3.1.5}$$

where the dependent variables are denoted by the vector $\mathbf{s} = [\rho, \rho u_1, \rho u_2, \rho u_3, E_T]$. The total energy, E_T, consists of the sum of the kinetic and internal energies of the flow

$$E_T = \rho(e + \frac{u_i u_i}{2}) = \frac{p}{(\gamma - 1)} + \frac{\rho u_i u_i}{2}. \tag{3.1.6}$$

Assuming constant specific heats, the perfect gas equation of state is

$$p = (\gamma - 1)\rho e \tag{3.1.7}$$

or

$$T = \frac{\gamma M^2 p}{\rho}. \tag{3.1.8}$$

The components of the shear-stress tensor which appear in the momentum and energy equations are

$$\tau_{ij} = \frac{\mu}{Re}\left[\left(\frac{\partial u_i}{\partial x_j} + \frac{\partial u_j}{\partial x_i}\right) - \frac{2}{3}\delta_{ij}\frac{\partial u_k}{\partial x_k}\right] \qquad (i, j = 1, 2, 3) \tag{3.1.9}$$

where Re is the Reynolds number

$$Re = \frac{\rho_o u_{10} b_i}{\mu_o}. \tag{3.1.10}$$

The nondimensional temperature dependent dynamic viscosity was approximated by a power law for dilute gases (White [1974])

$$\mu = T^n \tag{3.1.11}$$

where $n = 2/3$ for air. By assuming a unity Prandtl number and constant specific heats, the thermal conductivity is proportional to the dynamic viscosity

$$k = \frac{\mu}{(\gamma - 1)M^2 Re Pr} \tag{3.1.12}$$

and the heat flux vector is given by

$$q_j = -k\frac{\partial T}{\partial x_j}. \tag{3.1.13}$$

The governing equations were solved in conservation law form to insure that physically conserved quantities, mass, momentum, and energy, are also numerically conserved. Equations (3.1.3–3.1.5) are cast in conservation law form and written in a compact vector notation in which spatial derivatives appear only on the right-hand side of each of the equations (Anderson, Tannehill & Fletcher [1984])

$$\frac{\partial \mathbf{s}}{\partial t} = -\left[\frac{\partial \mathbf{E}}{\partial x_1} + \frac{\partial \mathbf{F}}{\partial x_2} + \frac{\partial \mathbf{G}}{\partial x_3}\right], \tag{3.1.14}$$

where

$$\mathbf{s} = \begin{bmatrix} \rho \\ \rho u \\ \rho v \\ \rho w \\ E_T \end{bmatrix}, \tag{3.1.15}$$

$$\mathbf{E} = \begin{bmatrix} \rho u_1 \\ \rho u_1^2 + p - \tau_{11} \\ \rho u_1 u_2 - \tau_{12} \\ \rho u_1 u_3 - \tau_{13} \\ (E_T + p)u_1 - u_1\tau_{11} - u_2\tau_{12} - u_3\tau_{13} + q_1 \end{bmatrix}, \tag{3.1.16}$$

$$\mathbf{F} = \begin{bmatrix} \rho u_2 \\ \rho u_1 u_2 - \tau_{12} \\ \rho u_2^2 + p - \tau_{22} \\ \rho u_2 u_3 - \tau_{23} \\ (E_T + p)u_2 - u_1\tau_{12} - u_2\tau_{22} - u_3\tau_{23} + q_2 \end{bmatrix}, \tag{3.1.17}$$

$$\mathbf{G} = \begin{bmatrix} \rho u_3 \\ \rho u_1 u_3 - \tau_{13} \\ \rho u_2 u_3 - \tau_{23} \\ \rho u_3^2 + p - \tau_{33} \\ (E_T + p)u_3 - u_1\tau_{13} - u_2\tau_{23} - u_3\tau_{33} + q_3 \end{bmatrix}. \tag{3.1.18}$$

This form of the equations is useful in understanding the time advancement scheme described in section 3.4.3.

3.2 Boundary Conditions

Periodic boundary conditions are imposed in the streamwise (x_1) and spanwise (x_3) directions for the time-developing wake

$$\mathbf{s}(x_1, x_2, x_3) = \mathbf{s}(x_1 + L_1, x_2, x_3) \tag{3.2.1}$$

$$\mathrm{s}(x_1, x_2, x_3) = \mathrm{s}(x_1, x_2, x_3 + L_3). \tag{3.2.2}$$

The boundary conditions imposed in the transverse direction (x_2) are that the disturbances must decay to zero outside of the vortical region in the freestream

$$\frac{\partial \mathrm{s}}{\partial x_2}(x_1, x_2, x_3)\Big|_{x_2=\pm\infty} = 0. \tag{3.2.3}$$

3.3 Initial Conditions

The initial conditions in the time-developing wake consist of linear eigenfunctions obtained from the linear stability calculations described in Chapter 2 superimposed on the laminar mean flow. The most unstable 2D Kelvin-Helmholtz mode, together with its first subharmonic (used in pairing simulations described in Chapter 4), and a pair of equal and opposite oblique 3D modes (used in 3D simulations described in Chapter 5), are superimposed on the mean velocity, temperature, and density profiles at the beginning of a simulation

$$\begin{aligned} \mathrm{b}(x_1, x_2, x_3, 0) = \overline{\mathrm{b}}(x_2) + \mathrm{Real}\Big[& \epsilon_{2\mathrm{D}} \grave{\mathrm{b}}_{2\mathrm{D}}(x_2) e^{i(\alpha x_1 + \Theta)} \\ & + \epsilon_{2\mathrm{DS}} \grave{\mathrm{b}}_{2\mathrm{DS}}(x_2) e^{i(\alpha x_1/2 + \phi)} \\ & + \frac{1}{2}\epsilon_{3\mathrm{D}} \grave{\mathrm{b}}_{3\mathrm{D}}(x_2) e^{i(\sigma\alpha x_1 + \beta x_3)} \\ & + \frac{1}{2}\epsilon_{3\mathrm{D}} \grave{\mathrm{b}}_{3\mathrm{D}}(x_2) e^{i(\sigma\alpha x_1 - \beta x_3)}\Big], \end{aligned} \tag{3.3.1}$$

where $\grave{\mathrm{b}}_{2\mathrm{D}}$ and $\grave{\mathrm{b}}_{2\mathrm{DS}}$ are the eigenfunctions of the two-dimensional modes corresponding to the streamwise wave numbers α and $\alpha/2$; $\grave{\mathrm{b}}_{3\mathrm{D}}$ is the eigenfunction of the oblique modes corresponding to the streamwise and spanwise wave numbers, α and β. The parameter σ is either 1.0 and 0.5 depending on whether a three-dimensional fundamental instability or a three-dimensional subharmonic instability is studied, respectively. The relative phase angle between the fundamental and the oblique waves, denoted by Θ, was varied between 0 and $\pi/2$. The relative phase angle between the subharmonic and fundamental modes, denoted by ϕ, also was varied between 0 and $\pi/2$. The amplitudes of the fluctuations, $\epsilon_{2\mathrm{D}}$, $\epsilon_{2\mathrm{DS}}$, and $\epsilon_{3\mathrm{D}}$, were chosen to be 1–2% of the maximum freestream value.

3.4 Numerical Method

The details of the numerical methods used are described in this section. The choice of method was motivated by a need to resolve the relevant spatial scales of motion for an unsteady transitional flow. Therefore, it was necessary for the numerical method to be spatially as well as temporally accurate. Since the domain is periodic in the streamwise (x_1) and spanwise (x_3) directions, spatial derivatives in those directions were approximated spectrally. It is well known that spectral methods give the most accurate differentiation with the fewest number of grid points. Furthermore, it is relatively inexpensive to compute discrete Fast Fourier Transforms (using the method of Cooley, Lewis & Welch [1970]) in those directions. In the major gradient direction (x_2), a mapping procedure was employed which allowed the use of a spectral method for computing derivatives in the transformed coordinate system. Higher-order derivatives or cross derivatives were obtained by successive first-order differentiation, thereby eliminating the need for complex Fourier transforms in the second or third direction.

An explicit time integration method was employed since the wake is an advection-dominated flow. Furthermore, explicit methods are easier and less expensive to implement than implicit methods. Incompressible equations are usually advanced in Fourier space. For compressible flows, it is much more efficient to advance the solution in physical space, because the compressible equations contain many more products than the incompressible equations. The disadvantage of taking products in physical space is that aliasing errors occur if the spatial resolution is inadequate. Therefore, the simulations must be overresolved.

3.4.1 *Approximation of Streamwise and Spanwise Derivatives*

Since periodic boundary conditions were invoked in the streamwise (x_1) and spanwise (x_3) directions, a discrete Fourier expansion was used to represent spatial derivatives in those directions. For example, in the streamwise direction, an arbitrary function $f(x_1)$ can be expressed as

$$f(x_{1j}) = \sum_{n=-N_1/2}^{N_1/2-1} \hat{f}_n e^{ik_{1n}x_{1j}} \qquad (3.4.1.1)$$

where the derivative of f is analytical

$$\frac{df}{dx_1}(x_{1j}) = \sum_{n=-N_1/2}^{N_1/2-1} ik_{1n}\hat{f}_n e^{ik_{1n}x_{1j}}. \tag{3.4.1.2}$$

In equations (3.4.1.1) and (3.4.1.2), $\hat{f}_n$ is the complex Fourier coefficient at a streamwise wave number $k_{1n} = 2\pi n/L_1$. The j^{th} grid point in the x_1 direction is defined as $x_{1j} = j\Delta x_1$, where $\Delta x_1 = L_1/N_1$. Each derivative requires a forward transform to compute the Fourier coefficient, $\hat{f}_n$,

$$\hat{f}_n = \frac{1}{N_1}\sum_{j=0}^{N_1-1} f(x_{1j})e^{-ik_{1n}x_{1j}} \tag{3.4.1.3}$$

which is then multiplied by ik_{1n} before the inverse transform is taken. Derivatives in the spanwise direction were obtained in a similar manner.

Second-order derivatives and cross derivatives which appear in the viscous stress tensor in the momentum and energy equations were obtained by successive first-order differentiation.

3.4.2 *Approximation of Transverse Spatial Derivatives*

In the transverse direction (x_2), the boundary conditions are applied at infinity. Some means of handling boundary conditions infinitely far away is required. One approach is to apply freestream boundary conditions at a large but finite distance away from the vortical region. By so doing, the boundary conditions imply unphysical image solutions which can cause errors in the computation. Alternatively, the image flows are kept infinitely far away by employing a procedure developed by Cain *et al.* [1981, 1984]. This procedure maps the doubly infinite extent of the x_2 direction onto an interval of finite extent in the computational coordinate ξ. In the transformed coordinate system, a spectral method is then used to compute derivatives.

Metrics appear in the transformed derivative of a function $f(x_2)$ under a mapping to a new coordinate system, where $1/h'$ is the metric

$$\frac{df}{dx_2} = \frac{df}{d\xi}\frac{d\xi}{dx_2} = \frac{df}{d\xi}\frac{1}{h'}. \tag{3.4.2.1}$$

In the transformed coordinate system, the derivatives are represented by a discrete Fourier transform in which the grids are uniformly spaced

$$\frac{df}{d\xi}(\xi_j) = \sum_{n=-N_2/2}^{N_2/2-1} ik_{2n}\hat{f}_n e^{ik_{2n}\xi_j} \qquad (3.4.2.2)$$

where $k_{2n} = 2\pi n$ and $-N_2/2 \leq n \leq N_2/2 - 1$. However, if $\frac{df}{d\xi}$ is represented spectrally and then multiplied by an analytic metric, aliasing errors occur. This is especially true if the metric is also represented by a Fourier series expansion with the same wave number range as the function itself. Cain tried to avoid aliasing problems inherent in the differentiation operator by devising a mapping function whose metric is represented completely by only a few Fourier modes with wave numbers which are small in comparison with those of the function, f, itself. The cotangent function is a suitable mapping function for this reason, and moreover, it clusters points in the vortical region where higher resolution is required

$$x_2 = h(\xi) = -a\cot(\pi\xi) \qquad (0 \leq \xi < 1) \quad (-\infty \leq x_2 \leq \infty). \qquad (3.4.2.3)$$

The product of the metric and $\frac{df}{d\xi}$ is carried out in Fourier space to avoid aliasing errors. Here we present only the first derivative operator for a wake since the details of the mapping are explained in Cain *et al.* [1981, 1984]

$$\left.\frac{df}{dx_2}\right|_{x_{2j}} = \frac{1}{a}\sum_{n=-N_2/2+1}^{N_2/2-1}\left[in\hat{f}_n - \frac{i(n-1)}{2}\hat{f}_{n-1} - \frac{i(n+1)}{2}\hat{f}_{n+1}\right]e^{ik_{2n}\xi_j} \qquad (3.4.2.4)$$

where modes with a magnitude greater than $N/2-1$ are truncated to prevent aliasing. The second derivative of f with respect to x_2 is obtained by applying equation (3.4.2.4) to the first derivative of f.

In the mapped coordinate ξ, the boundary conditions at $x_2 = \pm\infty$ are periodic since the wake is symmetric about the centerline, $x_2 = 0$, and since the disturbances are required to vanish in the freestream. The periodic boundary conditions at $x_2 = \pm\infty$ are not satisfied by the metric defined by the Cain mapping. This is due to the truncation of terms in the Fourier series which are greater than the magnitude of $N_2/2 - 1$. In order for the boundary conditions to be satisfied at the edge of the domain, all derivatives with respect to x_2 must be zero at $\zeta_j = 1$, that is

$$
\begin{aligned}
\frac{df}{dx_2}\Big|_{\zeta_j=1} &= 0 \\
&= \frac{1}{a}\sum_{n=0}^{N_2/2-1} \hat{f}'_n + c.c. \\
&= \frac{1}{a}\sum_{n=0}^{N_2/2-2} [-\frac{in}{2} + in - \frac{in}{2}]\hat{f}_n \\
&+ \frac{1}{a}[-\frac{i}{2}(\frac{N_2}{2}-1) + i(\frac{N_2}{2}-1)]\hat{f}_{N_2/2-1} + c.c.
\end{aligned}
\tag{3.4.2.5}
$$

In equation (3.4.2.5), the coefficients of $\hat{f}_n$ between $0 \leq n \leq N_2/2 - 1$ must be zero for any arbitrary value of $\hat{f}_n$ in order for $\frac{df}{dx_2}\big|_{\zeta_j=1} = 0$. In the first term on the right-hand side of equation (3.4.2.5), the coefficients of $\hat{f}_n$ for $0 \leq n \leq N_2/2 - 2$ are zero since the Fourier coefficients of the metric cancel each other out. However, since the Fourier series for $\frac{df}{dx_2}$ is truncated at $N_2/2 - 1$, the metric at $n = N_2/2 - 1$ is incomplete. Therefore, in the second term on the right-hand side of equation (3.4.2.5) the coefficient of $\hat{f}_{N_2/2-1}$ does not sum to zero, and the boundary condition at infinity is not satisfied. The Cain mapping algorithm was modified to insure that derivatives of the dependent variables are zero at the edge of the domain by setting to zero the individual terms of the Fourier coefficient for $\hat{f}_{N_2/2-1}$. The effect of truncating the energy contained in this mode is negligible since the energy contained in the wave number, $n = N_2/2 - 1$, is very small compared with that contained in lower wave numbers.

Therefore, the modified first derivative operator becomes

$$
\begin{aligned}
\frac{df}{dx_2}\Big|_{x_{2j}} = \frac{1}{a}\Big[&\sum_{n=0}^{N_2/2-3} \{in\hat{f}_n - \frac{i(n-1)}{2}\hat{f}_{n-1} - \frac{i(n+1)}{2}\hat{f}_{n+1}\}e^{i2\pi n\xi_j} \\
&+ \{i(\frac{N_2}{2}-2)\hat{f}_{\frac{N_2}{2}-2} - \frac{i}{2}(\frac{N_2}{2}-3)\hat{f}_{\frac{N_2}{2}-3}\}e^{i2\pi(\frac{N_2}{2}-2)\xi_j} \\
&- \{\frac{i}{2}(\frac{N_2}{2}-2)\hat{f}_{\frac{N_2}{2}-2}\}e^{i2\pi(\frac{N_2}{2}-1)\xi_j}\Big] + c.c.
\end{aligned}
\tag{3.4.2.6}
$$

The stretching parameter, a, was selected to adequately resolve the initial eigenfunctions, and to allow maximum resolution in the spreading wake. Typical values of a are between 8.3 and 12.3 for a wake. This allocates over 50% of the collocation points to the vortical region of the flow. Furthermore, since the gradients in the dependent variables are likely to be similar in all directions after the vortices have rolled-up, the spatial resolution requirements will be similar in all three directions. Therefore, the grid spacing was taken to be the same in all three directions, *i.e.* $\Delta x_1 = \Delta x_{2_{min}} = \Delta x_3$.

3.4.3 *Time Advancement*

Numerical simulations of transition in compressible free shear flows require a considerable amount of spatial resolution to resolve the different scales of motion. Using a spectral collocation method, a large number of ODE's needs to be solved, of up to 10^7 equations for a 128^3 simulation. The large number of equations is a result of the coupling between the temperature and velocity fields for compressible flows. A total of nineteen words per grid point are needed: five for the dependent variables, five for the terms on the right-hand side of equations (2.1.13-2.1.18), and nine for forming intermediate quantities. For a 128^3 simulation this amounts to 39.8 million words of storage. Furthermore, temporal accuracy is needed to capture the unsteady nature of transition characterized by unsteady vorticity and strain rate fields. Given these constraints, it was desirable to employ a minimal-storage, higher-order accurate time advancement method such as Wray's [1988] "compact" third-order Runge-Kutta scheme. This scheme is compact in the sense that it requires only two storage locations per dependent variable at a given grid point compared with traditional third-order Runge-Kutta methods which require three storage locations. At a given time, the two storage locations contain the dependent variable, $\mathbf{s_i}$, and the right-hand side of the governing equations (2.1.13-2.1.18), $\mathbf{R_i}$.

A brief description of the implementation of Wray's algorithm is given here. Third-order accuracy was obtained by simultaneous computation and storage overlaying of $\mathbf{R_i}$ and $\mathbf{s_i}$ at each of the three substeps. At each substep, a new right-hand side was formed in memory location SDATA (see Table 3.1). This was accomplished by taking a prescribed linear combination of the dependent variable and the right-hand side, both evaluated at the previous substep, while simultaneously overwriting the previous contents in memory location S2DATA with a prescribed linear combination of the previous dependent variable and right-hand side.

The solution of the Navier-Stokes equations was considered in the following vector form

$$\frac{d\mathbf{s}}{dt} = \mathbf{R}(\mathbf{s}, t) \tag{3.4.3.1}$$

where $\mathbf{s}$ contains the dependent variables and $\mathbf{R}$ contains the right-hand sides of equations (2.1.13-2.1.18). The contents of the two memory locations following each substep are shown below in Table 3.1.

TABLE 3.1 CONTENTS OF SDATA AND S2DATA FOR EACH SUBSTEP

Time	**SDATA storage location**	**S2DATA storage location**
t^n	$\mathbf{R}(\mathbf{s}^n, t^n)$	$\mathbf{s}^n$
$t' = t^n + \beta_1 \Delta t$	$\mathbf{r}' = \alpha_1 \Delta t \mathbf{R}(\mathbf{s}^n, t^n) + \mathbf{s}^n$	$\mathbf{s}' = \beta_1 \Delta t \mathbf{R}(\mathbf{s}^n, t^n) + \mathbf{s}^n$
$t'' = t' + (\alpha_2 + \beta_1)\Delta_t$	$\mathbf{r}'' = \alpha_2 \Delta t \mathbf{R}(\mathbf{r}', t') + \mathbf{s}'$	$\mathbf{s}'' = \beta_2 \Delta t \mathbf{R}(\mathbf{s}', t') + \mathbf{s}'$
$t^{n+1} = t^n + \Delta t$	$\mathbf{r}^{n+1} = \alpha_3 \Delta t \mathbf{R}(\mathbf{r}'', t'') + \mathbf{s}''$	$\mathbf{s}^{n+1} = \beta_3 \Delta t \mathbf{R}(\mathbf{s}'', t'') + \mathbf{s}''$

The coefficients α_i, and β_i in Table 3.1 were chosen to obtain third-order accuracy and are given as follows:

$$\begin{array}{lll} \alpha_1 = 2/3, & \alpha_2 = 5/12, & \alpha_3 = 3/5, \\ \beta_1 = 1/4, & \beta_2 = 3/20, & \beta_1 = 3/5. \end{array} \tag{3.4.3.2}$$

Since Runge-Kutta is an explicit method, there are stability restrictions. These restrictions are based on a Courant number determined by solving the following model advection/diffusion equation (Blaisdell [1989]):

$$\frac{\partial \phi}{\partial t} + u_i \frac{\partial \phi}{\partial x_i} = \zeta \frac{\partial^2 \phi}{\partial x_i \partial x_i}, \tag{3.4.3.3}$$

where $\zeta = \mu/\rho((\gamma - 1)M^2 RePr)$ and summation over i from 1 to 3 is assumed. Taking the Fourier transform of equation (3.4.3.3), the following ordinary differential equation for $\hat{\phi}$ is obtained

$$\frac{\partial \hat{\phi}}{\partial t} = \lambda \hat{\phi}, \tag{3.4.3.4}$$

where the complex eigenvalue, λ is given by

$$\lambda = \{-ik_i u_i - \alpha k_i k_i\}. \tag{3.4.3.5}$$

The complex eigenvalue, λ, is the sum of a diffusive part

$$\lambda_d = -\alpha k_i k_i \tag{3.4.3.6}$$

and a convective part

$$\lambda_c = -ik_i u_i. \tag{3.4.3.7}$$

Since $|\lambda_d + \lambda_c| \leq |\lambda_d| + |\lambda_c|$, the maximum timestep is bounded by $|\lambda_d|_{max} + |\lambda_c|_{max}$. Therefore the timestep, Δt, is obtained from

$$\Delta t \leq \frac{\mathrm{CFL}}{|\lambda_d|_{max} + |\lambda_c|_{max}}, \tag{3.4.3.8}$$

where CFL is the numerical stability requirement by Courant, Friedrichs & Lewy [1928]. For linear equations, third-order Runge-Kutta methods are stable for CFL numbers less than $\sqrt{3}$. The maximum eigenvalue, λ_d and λ_c, is obtained at the highest wave number in each direction

$$k_i = \frac{\pi}{\Delta x_i} \qquad (i = 1, 2, 3) \tag{3.4.3.9}$$

and at the maximum velocity

$$u_i = c + |u_i| \qquad (i = 1, 2, 3) \tag{3.4.3.10}$$

where c is the sound speed. Substituting equations (3.4.3.9) and (3.4.3.10) into equations (3.4.3.6) and (3.4.3.7) and (3.4.3.8), the timestep is obtained as

$$\Delta t = \frac{\mathrm{CFL}}{|\lambda_d|_{max} + |\lambda_c|_{max}} \tag{3.4.3.11a}$$

where the convection-dominated terms are given by

$$|\lambda_c|_{max} = \pi \left(\frac{|u_1|}{\Delta x_1} + \frac{|u_2|}{\Delta x_2} + \frac{|u_3|}{\Delta x_3} \right) + \pi c \left(\frac{1}{\Delta x_1^2} + \frac{1}{\Delta x_2^2} + \frac{1}{\Delta x_3^2} \right)^{1/2} \tag{3.4.3.11b}$$

and the viscous diffusion-dominated terms are given by

$$|\lambda_d|_{max} = \pi^2 \frac{\mu}{\rho(\gamma - 1)M^2 RePr} \left(\frac{1}{\Delta x_1^2} + \frac{1}{\Delta x_2^2} + \frac{1}{\Delta x_3^2} \right). \tag{3.4.3.11c}$$

The Courant number was fixed at 1.7 and the timestep, Δt, was updated after each time step (3 substeps per time step).

3.5 Code Implementation and Data Management

If there was enough memory on the Cray-XMP, the structure of the code would be straightforward. It would involve time advancing the right-hand side of equations

(3.1.14-3.1.18) according to the third-order Runge-Kutta method. The difficulty is that there are only 2 million 64 bit words (2 MW) of central memory available on the Cray-XMP while 30MW of memory are required for a 128 × 128 × 128 simulation. Therefore, a data management scheme was needed to efficiently load portions of the data field from a secondary storage device into central memory when the data is used to perform a computation. The solid-state storage device (SSD), which can store up to 32 MW, was chosen over disk-based mass storage because of its much faster access times. To reduce storage requirements on the SSD, all data fields were packed from 64-bit words to 32-bit words. While packing reduced the precision by two, all computations were actually done with 64-bit precision. Some difficulties arose due to packing the data in which round-off error was accumulating in the terms on the right-hand side of equations (3.1.14-3.1.18). For all other wave numbers besides the "oddball" †, the round-off error was eventually dampened by viscosity. However, there is no mechanism for removing round-off error which enters the "oddball" wave number; this energy accumulates and aliases back into the lower wave numbers through the nonlinear terms. The error associated with the oddball manifests itself as two-delta wave oscillations in the solution which grow and affect the solution. This problem was overcome by zeroing out the contribution of the oddball wave number in the right-hand side of equations (3.1.14-3.1.18) after each substep. The algorithm employed was developed by Blaisdell [1989] and a description of its implementation is given in the Appendix.

The computations and database were carefully structured to use the SSD effectively. The code is structured in horizontal and vertical passes through the data in order to optimize the manner in which Fourier transforms are taken. All the data to be transformed must simultaneously reside in core memory. For example, in PASS2 where x_1 and x_2 derivatives are taken, all $x_1 - x_2$ planes of data for a given x_3 grid must be loaded into core. Several x_3 grid points of $x_1 - x_2$ planes of information can fit into core at the same time. The data is arranged in "drawers" comprised of data for all values x_1, a few values of x_2 (M_2), and a few values of x_3 (M_3). Therefore, to load a particular $x_1 - x_2$ plane of data into core, a column of M_2 drawers of data are read in for a given constant x_3. Likewise, for Fourier transforms taken in a $x_1 - x_3$

---

† The oddball wave number refers to the highest wave number in each direction, where modes range from $\frac{-N_i}{2} + 1, ..., \frac{N_i}{2} - 1, \frac{N_i}{2}$, and $k_i = \frac{N_i}{2}$ is the oddball. The derivatives at this wave number are undefined since the corresponding wave number at $k_i = -\frac{N_i}{2}$ does not exist for an even transform. Therefore, the derivative of this wave number is set to zero.

plane, a row of M_3 drawers of data are read in for a given value of x_2. Typically, several x_2 planes ($M_2 = 4$) of $x_1 - x_3$ data or x_3 planes ($M_3 = 4$) of $x_1 - x_2$ data can fit into core together. In the time advancement subroutine the solution is advanced drawer-by-drawer since no spatial derivatives are taken. This concept of opening and closing drawers of data as they are needed in each of the the passes and in the time advancement module is illustrated in Figure 3-2.

Each substep of the time advancement code consists of three passes through the data denoted by PASS1, PASS2, and PASS3. PASS1 and PASS3 are horizontal passes through the data in which the computations are performed in $x_1 - x_3$ planes corresponding to a given x_2. Similarly, PASS2 is a vertical pass through the data in which the computations are performed in $x_1 - x_2$ planes corresponding to a given x_3. There are three main databases. The primary database, SDATA, contains the right-hand side of equations (3.1.14-3.1.18) at each substep, the database S2DATA contains the dependent variables at each substep, and the database WORKDATA contains intermediate quantities needed to form the right-hand side from one pass to the next. The information in WORKDATA is read in at the beginning of a pass, overwritten with new information in the course of forming the terms on the right-hand sides of equations (3.1.14-3.1.18), and stored for the next pass. The code was written in VECTORAL, a computing language written by Wray [1984] which facilitates vectorization and data management. Table 3.2 lists the order the computations are performed in each pass through the data.

TABLE 3.2 CODE STRUCTURE AND DATA MANAGEMENT

PASS1

1) Unpack SDATA.
2) Filter energy in oddball wave number.
3) Compute $\partial u_1/\partial x_3$, $\partial u_2/\partial x_3$, $\partial u_3/\partial x_3$.
4) Compute time step.
5) Pack WORKAREA.

PASS2

1) Unpack SDATA and WORKAREA.
2) Compute μ.

3) Compute κ.
4) Compute components of stress tensor.
5) Compute $\partial T/\partial x_1$, $\partial T/\partial x_2$.
6) Form partial right-hand side of total energy equation

$$-[\partial E_5/\partial x_1 + \partial F_5/\partial x_2].$$

7) Form partial right-hand side of momentum equations

$$-[\partial E_i/\partial x_1 + \partial F_i/\partial x_2]$$

where $i = 2, 3, 4$.
8) Form total energy flux in x_3 direction G_5.
9) Form momentum flux in x_3 direction G_2, G_3, G_4.
10) Form partial right-hand side for continuity equation

$$-[\partial \rho u_1/\partial x_1 + \partial \rho u_2/\partial x_2].$$

11) Pack partial right-hand side of governing equations into SDATA. Pack G_2, G_3, G_4, G_5 into WORKAREA.

PASS3

1) Unpack SDATA and WORKAREA.
2) Form remainder of right-hand side for energy equation

$$-[\partial E_5/\partial x_1 + \partial F_5/\partial x_2 + \partial G_5/\partial x_3].$$

3) Form remainder of right-hand side for momentum equations

$$-[\partial E_i/\partial x_1 + \partial F_i/\partial x_2 + \partial G_i/\partial x_3]$$

where $i = 2, 3, 4$.
4) Form remainder of right-hand side for continuity equation

$$-[\partial \rho u_1/\partial x_1 + \partial \rho u_2/\partial x_2 + \partial \rho u_3/\partial x_3].$$

5) Pack completed right-hand side into SDATA.

3.6 Resolution Check (Aliasing Errors)

In incompressible flows, where the governing equations contain only double products of the dependent variables, some sort of dealiasing is always applied (Rogallo [1981]). However, in compressible flows, where the governing equations contain triple products of the dependent variables, variable fluid properties, and divisions, it is not practical to dealias the solution. Alternatively, for compressible flows the solution is overresolved to minimize aliasing errors. To ensure the solution is well-resolved, the energy spectra in x_1 and x_3 is monitored at several stages in a simulation. This was accomplished by computing the kinetic energy of each mode given by

$$E(x_2) = \left|\hat{u}_i(\alpha, x_2, \beta)\right|^2 \tag{3.6.1}$$

where summation over i from 1 to 3 is implied and $\hat{u}_i(\alpha, x_2, \beta)$ is the Fourier transform of $u_i(x_1, x_2, x_3)$ in the $x_1 - x_3$ plane. Figures 3-3a and 3-3b illustrate the distribution of kinetic energy of the various modes for a 3D simulation performed at a Mach number of 3 at two different times in the simulation. The energy of each mode on one side of the wake, and also at the centerline was examined. The energy is displayed on a logarithmic scale in which only energy above a certain floor level is displayed ($1.0 \cdot 10^{-08}$ or $1.0 \cdot 10^{-12}$). Note that the distribution of energy in Figure 3-3a is such that all the wave numbers are well-resolved, *i.e.* there is no build up of energy at the high wave numbers and there is a cascade of energy from the low wave numbers to high wave numbers. This spectra is representative of a well-resolved simulation. In contrast, Figure 3-3b illustrates a poorly-resolved simulation in which energy contained in the high wave number modes has aliased back into the domain, causing an accumulation of energy at the high wave numbers. Note the hump in the energy spectra at $k_1 = 11$. The energy spectra was monitored during the course of a simulation and additional modes were included if the resolution became marginal. This was accomplished by transforming the data into wave space, adding more Fourier modes, and transforming back to physical space with the increased number of modes.

3.7 Code Verification

In this section, tests performed to validate the direct simulation codes are described. One of the main difficulties with validating a compressible code is that there are not many analytical solutions to check the code against. The two tests available for compressible codes are (1) linear growth rate check, and (2) diffusion check. The structure of the two-dimensional code is identical to the three-dimensional code. Therefore, only the three-dimensional code was verified. In the first test, the numerical simulation results were compared with the exact solution of the incompressible laminar wake. The purpose of this test was to make sure the time advance and diffusion portions of the code were working properly. In the second test, linear growth rates obtained from numerical simulations at several different Reynolds numbers were compared with those computed from an inviscid linear stability analysis. This test provided the minimum Reynolds number at a given Mach number below which the least stable inviscid wave would be damped.

3.7.1 *Incompressible Laminar Wake*

For parallel flow, the governing equations for a two-dimensional, incompressible, time-developing far wake reduce to a diffusion equation

$$\frac{\partial u_d}{\partial t} = \psi \frac{\partial^2 u_d}{\partial x_2^2} \qquad (3.7.1.1)$$

where $\psi = \mu/\rho Re$ and $u_d = u_{1o}(1 - u_1)/\Delta u_c$. The boundary conditions imposed in this problem are

$$\lim_{x_2 \to \infty} u_d(x_2, t) = 0 \qquad (3.7.1.2)$$

$$u_d'(0, t) = 0. \qquad (3.7.1.3)$$

The problem was solved for $\mu/\rho Re = 100$ using the following number of grid points in each direction

$$N_1 = 128, N_2 = 128, N_3 = 4.$$

The stretching parameter in the Cain mapping, a, was set to 8.3 and the initial temperature, density, and pressure were assumed to be uniform. The mean velocity is given by equation (2.1.1) where the velocity deficit at the centerline was assumed to be 1.0. The computation was run for 200 time steps from $t = 0$ to $t = 1.48$ at which time the numerical solution was compared with the analytical solution,

$$u_d(x_2,t) = \frac{\beta}{\sqrt{t}} e^{-x_2^2/4\psi t}. \tag{3.7.1.4}$$

The comparison is shown in Figure 3-4 at $t = 1.48$. The excellent agreement indicates that the time advance and diffusion portions of the code work properly.

3.7.2 *Linear Growth Rate*

As another test of the accuracy of the code, linear growth rates were computed by direct simulation of the Navier-Stokes equations and then compared against those computed from linear stability theory. The direct simulation was forced with the most unstable eigenfunctions predicted from linear stability theory. To insure the absence of nonlinear interactions, the initial amplitude of the fluctuations was taken as 0.01% of the maximum freestream value. The simulations were performed for $1 <= M <= 3$ at $Re = 1500$, where viscous effects are small so that comparisons could be made with inviscid stability calculations. Since the modes grow independently of each other in the linear limit, very few modes are required; the simulations were performed with $N_1 = 16$, $N_2 = 128$, and $N_3 = 4$. The stretching parameter, a, was set to 8.3. The growth rate was obtained by assuming each mode in the spectral decomposition of the dependent variables can be represented by a travelling wave

$$\hat{u}_1(\alpha, x_2, t) = P(\alpha, x_2) e^{-i\alpha ct} \tag{3.7.2.1}$$

where c is the complex wave speed, and P is the complex mode shape.

Taking the natural log of both sides of equation (3.7.2.1) and separating the real and imaginary parts, the growth rate is obtained

$$\text{Real}[\ln(\hat{u}_1(\alpha, x_2, t))] = \ln|P| + \alpha c_i t \tag{3.7.2.2}$$

where the growth rate, αc_i, is given by the time rate of change of the real part of the natural log of the Fourier coefficients of the dependent variable at a given x_2 location in the wake.

Comparisons of the growth rates computed by the two methods are shown in Figure 3-5 for the most unstable two-dimensional wave at $M = 1$, 2, and 3 for $\Delta u_c = 0.692$. The growth rate is given by the slopes of the curves. The initial deviation from the correct growth rate for $M = 1$ is a result of the error associated with fitting the eigenfunctions with a spline onto the computational grid in the direct simulation.

After the initial transient diminishes (by $t = 15$), the growth rate computed from direct numerical simulation is within 1% of the linear stability prediction.

Since the actual simulations are performed at finite Reynolds numbers, the growth rates will be lower than the inviscid growth rates. Below a critical Reynolds number, the growth rates are stable and the flow will remain laminar. Therefore, the simulations must be performed above the critical Reynolds number in order for the flow to become unstable. In Figure 3-6, the influence of Reynolds number on the growth rates is shown for $M = 1$ and $M = 3$. Note the stabilizing influence of viscosity for both cases. Note also that the critical Reynolds number increases as the Mach number increases ($Re_c = 50$ for $M = 1$ and $Re_c = 100$ for $M = 3$).

CHAPTER 4

RESULTS OF TWO-DIMENSIONAL SIMULATIONS

Two-dimensional direct simulations, based on the formulation and numerical methodology described in the previous chapter, were used to study two different problems. The results of these simulations are presented in this chapter. First, the influence of Mach number on the nonlinear development of a compressible wake is investigated. The simulations were forced initially with the eigenfunctions of the fastest growing mode predicted from linear stability theory. The results of the simulations show the same physical mechanism responsible for the reduced linear growth rates is also responsible for the slow nonlinear roll-up of spanwise vortices at high Mach numbers. Second, the effect of varying the relative phase angle between a fundamental and its subharmonic is explored as one possible means of controlling the evolution of a wake. The asymmetric development of the subharmonic is discussed for three limiting angles.

4.1 Influence of Mach number on the Evolution of Large-Scale Structures

Beyond the region of exponential growth where the disturbances are governed by linearized Navier-Stokes equations, the Kelvin-Helmholtz instability leads to the nonlinear roll-up of spanwise vortices of alternating sign, the so-called Kármán vortex street. This vortex street consists of regions of recirculating spanwise vorticity connected by saddle points. Direct simulations were performed at several Mach numbers to determine the effect of compressibility on the development of spanwise vortices in the the vortex street. In similar studies by Sandham [1989c] and Lele [1989], compressibility issues concerning mixing layers are addressed.

To illustrate the effect of Mach number, the results of two simulations are described, one at $M = 1$, $Re = 600$, and the other at $M = 3$, $Re = 600$. An explanation is offered for the reduction in growth rate at high Mach number based on information drawn from contour plots of the baroclinic and dilatational source terms in the vorticity equation for a compressible flow.

4.1.1 *Physical and Numerical Parameters*

The simulations performed at $M = 1$ and $M = 3$ are selected as representative cases to illustrate the effect of Mach number. A more appropriate measure of compressibility is the relative Mach number, M_r, which is based on the velocity deficit at the wake centerline and the freestream sound speed. For an initial velocity deficit of 0.692, the relative Mach number at $M = 3$ is $M_r = 2.076$ which is supersonic, while the relative Mach number at $M = 1$ is $M_r = 0.692$, which is subsonic. Note that the freestream Mach number remains constant as the wake evolves downstream, while the relative Mach number decreases since the velocity deficit decreases. Therefore, compressibility has its largest influence near the trailing edge of the plate and loses its influence as the wake develops downstream. Unlike the laboratory wake which develops downstream, the numerically simulated wake develops temporally. The simulations were performed at $Re = 600$ to insure that the disturbances predicted from an inviscid linear stability analysis would be amplified. The governing equations, boundary conditions, and numerical techniques detailed in Chapter 3 were employed in these simulations. The computational domain was discretized into 64 modes in x_1, and 128 modes in x_2. The Cain stretching parameter, a, was chosen to be 8.3 so that $\Delta x_1 = \Delta x_{2min}$. The length of the box in the streamwise direction was selected to support the growth of the least stable fundamental mode. The CFL number was taken to be 1.7.

4.1.2 *Initial Conditions*

For the time-developing wake, initial conditions need to be prescribed. The initial conditions consist of the mean flow, described in Chapter 2, forced with the least stable two-dimensional eigenfunctions, $\grave{\mathrm{b}}_{2\mathrm{D}}$, of the inviscid laminar wake

$$\mathrm{b}(x_1, x_2, 0) = \overline{\mathrm{b}}(x_2) + \mathrm{Real}\left[\epsilon_{2\mathrm{D}}\grave{\mathrm{b}}_{2\mathrm{D}}(x_2)e^{i\alpha x_1}\right]. \tag{4.1.2.1}$$

Since the eigenfunctions are complex-valued, only the real parts are retained to ensure that the resulting disturbances are real-valued. For these simulations, the amplitudes of the eigenfunctions, $\epsilon_{2\mathrm{D}}$, were assumed to be 2.0% of the maximum freestream value. These eigenfunctions were shown earlier in Figures 2-13 through 2-15.

4.1.3 *Evolution of the Temperature Field*

The evolution of the temperature field for $M = 1$, $Re = 300$ is shown in Figure 4-1. At low Mach numbers the temperature and velocity fields are weakly coupled so the temperature behaves almost like a passive scalar. Therefore, the temperature (or density) field can be compared to flow visualization experiments. Initially, the temperature field is Gaussian, with the maximum temperature located near the wake centerline, $x_2 = 0$. Note that as the wake rolls-up due to the initial instability, strong temperature gradients develop near the saddle point region on either side of the wake. These gradients lie along the diverging separatrix of the saddle point which becomes steeper as the wake evolves. Initially, the maximum temperature is located at the wake centerline. As the wake rolls-up the maximum temperature shifts to the saddle points on either side of the wake. The temperature field at $M = 3$ behaves like the lower Mach number case with the gradients aligned along the saddle point. The primary difference between the two cases is that the peak temperature is much greater for $M = 3$ even after the fundamental has saturated. The maximum temperature for $M = 3$ is $2.0T_o$ at $t = 96$, while for $M = 1$ is only $1.1T_o$ at $t = 40$.

4.1.4 *Mean Velocity and Temperature Fields*

The mean velocity and temperature fields are shown in Figure 4-2 at several times. Each curve was obtained by averaging the data in the homogeneous direction x_1 at a given instant in time. In Figure 4-2a, note that the streamwise velocity deficit decreases rapidly during the linear stage of development even at $Re = 600$ where viscous effects are small. While the mean velocity profile remains nearly Gaussian even in the nonlinear roll-up stages, the temperature deficit shown in Figure 4-2b changes character at $t = 86$. The initially Gaussian mean temperature profile exhibits two peaks on either side of the wake centerline. The location of these peaks is in the vicinity of the saddle points on either side of the wake shown in Figure 4-1. This behavior is consistent with the results of Antonia, Browne & Bisset [1987] who measured the temperature variance for a heated far wake of a cylinder and found that the peak temperature variance lies along the diverging separatrix of the saddle point. Since both the velocity and temperature deficits relax very quickly, we expect that strong compressibility effects will appear early in the simulations. Late in the simulation, the wake should behave more like its incompressible counterpart.

4.1.5 *Energy spectra*

The time history of the modal energy of the fundamental is shown in Figure 4-3 for $M = 3$ and $M = 1$, where the total energy of this mode is defined by

$$E_\alpha = \int_{-\infty}^{\infty} \hat{u}_i(\alpha, x_2)\hat{u}_i^\dagger(\alpha, x_2)dx_2. \tag{4.1.5.1}$$

Here summation over i from 1 to 2 is implied, $\hat{u}_i(\alpha, x_2)$ denotes the Fourier transform of $u_i(x_1, x_2)$, and † denotes the complex conjugate. For both Mach numbers, the fundamental initially increases exponentially, followed by a period of slower nonlinear growth, and finally by a period of saturation and decay. The duration of the region of exponential growth for $M = 3$ is almost twice that of $M = 1$. This is consistent with the much lower growth rate at $M = 3$ predicted from linear stability theory. Note that the spanwise vortices roll-up and saturate at $t = 80$ for $M = 3$ compared with $t = 40$ for $M = 1$. Furthermore, for $M = 3$ the fundamental saturates at a lower level than for $M = 1$ since the mean flow, which supplies energy to the fundamental, is less energetic at later times. From the energy spectra, it is noted that except for an initial delay in the roll-up process due to the reduced linear growth rates experienced at higher Mach numbers, the nonlinear development of the compressible wake is similar to its incompressible counterpart.

4.1.6 *Turbulence Intensities*

The onset of nonlinearity in both compressible and incompressible wakes is characterized by the same phenomenon. For the two cases simulated, the nonlinear interaction of the disturbances produces higher harmonics, particularly at the first harmonic corresponding to twice the frequency of the fundamental. This can be seen in distributions of the r.m.s velocity fluctuation, $u_{1_{\text{rms}}}$, for $M = 3$ shown in Figure 4-4 at linear and nonlinear stages in the development. In the linear stage of development ($t = 32.4$), the distribution is characterized by two peaks in the r.m.s. velocity fluctuation centered above and below the wake centerline. In the nonlinear stage of development ($t = 86.0$), the distribution has grown and is characterized by the appearance of higher harmonic components at the wake centerline. The first harmonic is primarily responsible for the large fluctuation at the wake centerline at later times as shown in Figure 4-5 by its distribution in the linear and nonlinear regions. At

$t = 32.4$, the first harmonic is negligible compared with the fundamental mode. However, at $t = 86.0$, the first harmonic develops three peaks centered below, above, and at the wake centerline.

The emergence of the first harmonic in the nonlinear region bears qualitative resemblance to measurements of $u_{1_{\mathrm{rms}}}$ in an incompressible wake behind a flat plate (Sato & Kuriki [1961]). The main difference is that, for higher Mach numbers, the saturation of the fundamental occurs at much later times in the development due to much lower linear growth rates.

4.1.7 *The "Culprit" – Baroclinic and Dilatational Effects*

Insights into the mechanisms causing the decreased growth rate at $M = 3$ were obtained by examining contour plots of the terms which appear in the inviscid compressible vorticity equation

$$\begin{aligned}\frac{\partial \omega_3}{\partial t} + U_c \frac{\partial \omega_3}{\partial x_1} = -(u_1 - U_c)\frac{\partial \omega_3}{\partial x_1} - u_2 \frac{\partial \omega_3}{\partial x_2} - \omega_3 \left(\frac{\partial u_1}{\partial x_1} + \frac{\partial u_2}{\partial x_2}\right) \\ + \frac{1}{\rho^2}\left(\frac{\partial p}{\partial x_1}\frac{\partial \rho}{\partial x_2} - \frac{\partial \rho}{\partial x_1}\frac{\partial p}{\partial x_2}\right).\end{aligned} \tag{4.1.7.1}$$

Here, the rate of change of spanwise vorticity is defined in a frame of reference moving with the vortex centres, U_c. The rate of change of spanwise vorticity is the net result of the terms on the right-hand side of equation (4.1.7.1): (1) the first two terms are the vorticity advected relative to the observer, (2) the third term is the product of dilatation and vorticity representing fluid compression or expansion, and (3) the fourth term is the baroclinic torque. In an incompressible two-dimensional flow, there is no vorticity production mechanism and advection is solely responsible for the roll-up of the vortices. However, in a compressible two-dimensional flow, in addition to advection, dilatational and baroclinic vorticity source terms exist which redistribute vorticity in the flow. Therefore, it is the net effect of all three terms which determines the rate at which the vortices roll-up. Contour plots at $M = 3$ of spanwise vorticity, pressure, density, baroclinic torques, and the dilatational term are shown in Figures 4-6 to 4-10 for linear ($t = 32$), nonlinear ($t = 68$ and $t = 86$), and saturated ($t = 96$) stages in their development. Contour plots of the vorticity advection term in a frame of reference moving with the vortex centres are shown in

Figure 4-11 for the nonlinear stage of development. In Figure 4-11, the solid and broken lines represent counterclockwise and clockwise senses of rotation, respectively.

The roll-up of vorticity is shown in Figure 4-6. As the linear disturbances grow, the vorticity in each layer rolls-up nonlinearly resulting in a Kármán vortex street by $t = 86$. In the absence of any vorticity source terms, the roll-up is a result of advection of vorticity from the saddle region to the cores along the diverging separatrix of the saddle as shown in Figure 4-12. This is a different topology than for a mixing layer in which fluid is advected from both upstream and downstream of the saddle point.

The primary effect of compressibility is to delay the roll-up of vortices and to redistribute the vorticity in the core. At high Mach number, this arises mainly due to the misalignment of the pressure and density gradients in the saddle point region. In Figure 4-8 note that strong density gradients exist along the diverging separatrix in the saddle region. These gradients are perpendicular to pressure gradients which are positive upstream of the saddle and negative downstream of the saddle (Figure 4-7). Therefore, baroclinic torques arise which oppose the advection of vorticity upstream of the saddle and enhance the advection downstream of the saddle (Figure 4-9). Similarly, dilatational effects caused by strong temperature gradients across the diverging separatrix of the saddle point also annihilate vorticity upstream of the saddle point (Figure 4-10). The combined effect of the baroclinic and dilatational terms is to prevent vorticity from the opposite side of the wake from being advected into the vortex core (Figure 4-12). Together, the baroclinic torque and dilatational term represent 15–20% of the vorticity advection in a frame of reference moving with the vortex centres. Therefore, at high Mach numbers where density and temperature gradients are significant, the growth rate of the vortices is reduced, since fluid entrainment from the opposite side of the wake is inhibited. Note that these source terms are present even in the linear stages of development preventing the formation of vortices. These effects also account for the reduced linear growth rates predicted from linear theory at high Mach numbers.

In summary, the two-dimensional simulations show that the physical mechanism responsible for the observed reduction in growth rate of compressible wakes (Kendall [1962]) is the same in both linear and nonlinear regimes. Linear theory not only predicts lower growth rates at high Mach numbers; it also provides an explanation for why they are reduced. The eigensolutions used to produce baroclinic torques and dilatational terms, described in Chapter 2, contain important information about the physics of the flow. In particular, these terms prevent vorticity in the saddle region from rolling-up. Moreover, this effect is more pronounced at high Mach number where density gradients become larger.

4.2 Influence of Relative Phase Angle on Forced Subharmonic Perturbations

As a means of controlling transition, the effect of varying the relative phase difference between a fundamental and its subharmonic is determined from 2D direct numerical simulations of a low Mach number wake ($M = 1$).

4.2.1 *Initial Conditions*

In two-dimensional pairing simulations, the mean profiles, $\bar{\mathrm{b}}$, were forced with the eigenfunctions of the least stable two-dimensional mode, $\grave{\mathrm{b}}_{2\mathrm{D}}$, and with the eigenfunctions of its subharmonic, $\grave{\mathrm{b}}_{2\mathrm{DS}}$

$$\begin{aligned} \mathrm{b}(x_1, x_2, x_3, 0) = \bar{\mathrm{b}}(x_2) + \mathrm{Real}\Big[&\epsilon_{2\mathrm{D}}\grave{\mathrm{b}}_{2\mathrm{D}}(x_2)e^{i\alpha x_1} \\ &+ \epsilon_{2\mathrm{DS}}\grave{\mathrm{b}}_{2\mathrm{DS}}(x_2)e^{i(\alpha x_1/2+\phi)}\Big]. \end{aligned} \tag{4.2.1.1}$$

The phase angle of the subharmonic relative to the fundamental, ϕ, was taken to be 0, $\pi/4$, and $\pi/2$. Initially, the amplitudes of both modes, $\epsilon_{2\mathrm{D}}$ and $\epsilon_{2\mathrm{DS}}$ were made equal to 2.0% of the maximum freestream value.

4.2.2 *Background*

In a mixing layer, there are two families of relative phase angles between the subharmonic and the fundamental mode which are of particular importance (Patnaik, Sherman & Corcos [1976].) These angles correspond to even and odd multiples of $\pi/2$. If the relative phase angle is an odd multiple of $\pi/2$, the subharmonic will alternately displace the vortices up and down while keeping their same strength. This results in their rotation about each other which eventually leads to their pairing. If the relative phase angle is an even multiple of $\pi/2$, the subharmonic will alternately strengthen and weaken the vortices without moving their centres. This leads to shredding of the weaker vortices in the strain field of the stronger ones.

The wake differs from the mixing layer in that it has two layers of vorticity with an opposite sense of rotation. Therefore, a vortex in one layer is influenced by its neighboring vortices in the same row as well as by counterrotating vortices in the opposing layer. Meiburg [1987] considered the wake as two separate rows of vortices (*i.e.* two mixing layers of opposite sign), each subjected to separate subharmonic perturbations. From inviscid vortex dynamics considerations, he showed that by varying the relative phase angle between a fundamental and subharmonic in each layer an unsymmetrical development of the subharmonic can occur.

4.2.3 *Results of Subharmonic Forcing*

In the present work, instead of treating the wake as two mixing layers in which each layer is subject to its own subharmonic disturbance, the entire mean wake profile was perturbed with its fundamental and subharmonic modes as determined from a linear stability analysis. Therefore, the relative phase angle was held constant throughout the wake. The time evolution of the pairing process for relative phase angles of 0, $\pi/4$, and $\pi/2$ is shown in contour plots of spanwise vorticity and temperature in Figures 4-13 to 4-15. Initially, the fundamental mode experiences a greater amplification than the subharmonic mode. Then the fundamental mode rolls-up and saturates, forming a staggered vortex street by $t = 49$. Subsequently, the subharmonic mode dominates, and for ϕ equal to 0 and $\pi/2$ (Figures 4-13 and 4-15), two fundamental vortices in either the upper or lower layer rotate around each other and finally pair. For ϕ equal to $\pi/4$ (Figure 4-14), two vortices in both the upper and lower layers rotate around each other and pairing occurs in both layers. Note that while the spanwise vorticity contours clearly indicate the occurrence of pairing, it is less apparent in the accompanying temperature contour plots. Therefore, it would be difficult to tell from experimental visualizations based on smoke, dye, or schlieren methods whether increases in scale in the wake are due to hydrodynamic instabilities or whether they are due to pairing events such as shown here. Determining the cause would require additional frequency spectra.

The observed asymmetry in the subharmonic development can be explained qualitatively from inviscid vortex dynamics considerations. The influence of the fundamental mode on the mean flow is to generate two staggered rows of vortices forming a Kármán vortex street. To first approximation, this can be thought of as a quasi-steady state which is then perturbed by a subharmonic disturbance, since the growth rate of the subharmonic is initially slower than the fundamental. Three different possible routes for pairing were identified depending on the initial relative phase angle between the subharmonic and fundamental modes.

In the first case (Figure 4-16a), the phase angle is an odd multiple of $\pi/2$. The solid line represents the fundamental forcing which produces an alternating vortex street indicated by the clockwise and counterclockwise arrows. The dashed line represents the subharmonic forcing which is shifted $\pi/2$ from point A. In the upper layer the vortices are shifted up and down from their equilibrium positions (as indicated by the arrows) by the subharmonic, and, due to the induced differential velocity, rotate about each other in a clockwise manner. In the lower layer, the vortices are not displaced from their original positions since the zeros of the subharmonic coincide with the centres of the vortices. This results in the vortices being alternately shredded and strengthened by the strain field. In Figure 4-16a the vortex at point B in the lower row is being shredded while the vortex at C is being strengthened.

In the second case (Figure 4-16b), the relative phase angle is an even multiple of $\pi/2$. By the same arguments used for the first case, this leads to vortices which are shredded and strengthened in the upper layer, and which rotate about each other in a counterclockwise manner and pair in the lower layer. Therefore, the vortices in Figures 4-13 and 4-15 are exact mirror images of each other.

In the third case (Figure 4-16c), the relative phase angle is between 0 and $\pi/2$. Here, both layers will rotate about each other and pair since the zeros of the subharmonic do not coincide with the fundamental vortices. Thus, pairing occurs on both sides of the wake for angles between 0 and $\pi/2$. However, there is no angle for which the subharmonic development occurs at the same rate for both sides of the wake due to the staggered arrangement of the fundamental vortices. The behavior of the vortices described by these arguments is consistent with the observations of the subharmonic development for the three cases. Any relative phase angle can be characterized by one of these three limiting cases.

From the temperature contours shown in Figures 4-13b to 4-15b, note that the introduction of a subharmonic causes the width of the wake to double (20 times the initial half-width), compared with the width at the time of fundamental saturation (10 times the initial half-width). The doubling of the wake width occurs regardless of the relative phase angle between the fundamental and subharmonic. Also note that after pairing has occurred, the temperature gradients still lie along the diverging separatrix of the saddle point on each side of the wake.

The time-history of the streamwise kinetic energy of the disturbances of the fundamental and subharmonic modes is shown in Figure 4-17 for relative phase angles of 0, $\pi/4$, and $\pi/2$. It is seen that the fundamental grows exponentially initially and then rolls-up, saturates, and decays. After the fundamental has saturated, the subharmonic takes over until it also saturates at which time pairing occurs. Note that the peaks in the fundamental and subharmonic development occur at the same time for all three phase differences. The subharmonic for $\phi = \pi/4$ saturates at a slightly higher level than for $\phi = 0$ or $\phi = \pi/2$. Also, note that there is no difference in the development of either the fundamental or subharmonic for $\phi = 0$ and $\phi = \pi/2$; by integrating the energy across the entire width of the wake, information concerning the asymmetry in the pairing process is removed.

In summary, it was determined that pairing does occur in a wake if the subharmonic is forced; this results in a doubling of the width of the wake. Relative phase angles of 0 and $\pi/2$ lead to pairings in the lower and upper halves of the wake, respectively, while angles in between lead to pairings on both sides of the wake. Moreover, there is no angle ϕ for which pairing can occur at the same rate on both sides of the wake due to the staggered nature of the fundamental mode. Finally, in addition to temperature or density fields, frequency spectra are needed to tell whether pairing or hydrodynamic instabilities account for the change in scale observed in the far wake.

CHAPTER 5

THREE-DIMENSIONAL MORPHOLOGICAL DESCRIPTION

In this chapter, three-dimensional simulations based on the formulation and numerical methodology described in Chapter 3 are used to study the morphology of a perturbed compressible plane wake. The three-dimensional perturbations consist of unstable two-dimensional and oblique modes obtained from the linear stability analysis described in Chapter 2. Specifically, the sensitivity of the morphology of a wake to (1) the relative phase angle between a fundamental and a pair of oblique modes, (2) the streamwise wavelength of the oblique modes, and (3) Mach number is examined. The vorticity dynamics and energy spectra of the flow are studied in detail at various stages in the evolution.

5.1 Motivation and Objectives

In Chapter 4 it was determined that the Kelvin-Helmholtz instability results in the formation of two rows of alternating vortices for both incompressible as well as compressible wakes. Beyond this initial instability, however, there still remains a great deal of uncertainty concerning the nature of the subsequent three-dimensional motions which develop in a wake.

Dating back to the work of Townsend [1956] and Grant [1958], there have been numerous observations of three-dimensionality in a wake. Based on time-averaged correlations in the far wake of a cylinder, Townsend [1956] and Grant [1958] deduced that spanwise variations in a wake may be pairs of counter-rotating streamwise vortices. However, it is difficult to extract details about a dynamically varying flow from time-averaged measurements made at only a few stationary points in the flow.

More recent experiments involving smoke visualization or diffusion-controlled reactions (Breidenthal [1980], Perry & Lim [1978], Antonia, Browne & Bisset [1987], Cimbala, Nagib & Roshko [1988], and Meiburg and Lasheras [1988]) have begun to shed some light on detailed features of the three-dimensional flow. Although direct measurements of vorticity or strain rates are still unavailable, these instantaneous distributions of smoke or dye do indicate that there exist spanwise variations in the large-scale motions of a far wake of either a cylinder or plate. Two dominant types of motion can be inferred from photographs of these visualizations.

The first of these motions are vortex loops which appear as regions in the far wake of a cylinder that are marked by heavy concentrations of dye (Antonia, Browne & Bisset [1987]). These regions resemble three-dimensional bulges which are comprised of clusters of vortex loops. These vortex loops are inclined at approximately ±45 deg with respect to the wake centerline and the tips of the bulges have a tendency to curl over in the direction of the centerline. Roshko [1976] had conjectured that the topology of a wake may in fact be a vortex loop, with the sides of the loop consisting of the counter-rotating streamwise vortices which Grant [1958] had earlier alluded to, and the top and bottom consisting of oppositely-signed spanwise vortices. Figure 5-1 illustrates the interaction of the streamwise vortices with the spanwise vortices to form closed loops. The exact manner in which these vortex loops originate, the way in which the streamwise and spanwise vortices interact with each other, and the way in which they evolve are issues which are still unresolved.

The second of these motions is a "honeycomb" structure of which an example is shown in Figure 5-2 which is a plan view of a far wake of a cylinder in which the smoke wire was placed on one side of the wake (Cimbala, Nagib & Roshko [1988]). Note that in the upper right-hand corner of the photograph, there are hairpin-like vortices similar to those observed in boundary layers. These hairpin vortices are 180 degrees out-of-phase with the preceding vortices in the streamwise direction. This staggered peak-valley-splitting arrangement, also known as the "H-type" secondary instability in boundary layer and channel flows, may be responsible for the structures Cimbala observed in a wake. This secondary instability could arise from the interaction of a pair of oblique subharmonic modes with a Kármán vortex street in which the streamwise wave number associated with the oblique modes is half that of the fundamental.

Our objective is to determine under what set of initial conditions does the formation of vortex loops or staggered hairpin vortices occur, how do they develop, what parameters influence their development, and what influence, if any, does Mach number have on the morphology of the three-dimensional structures?

To provide a definitive answer to these questions, the sensitivity of a wake subjected to various three-dimensional disturbances was explored via direct numerical simulations. In particular, the sensitivity of the large-scale structures to (1) the relative phase angle between the fundamental and oblique modes, and (2) the streamwise wavelength of the oblique modes was considered. Recent mixing layer simulations (Riley, Mourad, Moser & Rogers [1988]) show that the resultant large-scale structure in an incompressible mixing layer is very sensitive to the initial relative phase angle between a fundamental and a pair of oblique modes. Their results show that the presence of vorticity in the braid region in the developed state of a mixing layer is largely dependent upon the initial presence of streamwise vorticity in the stagnation region. We also wish to determine whether relative phase angles can similarly be used to control the evolution of a wake. In addition to phase effects, the streamwise wavelength of the three-dimensional disturbances has been found to be important in secondary stability problems associated with channel flows (Herbert [1983]). If the streamwise wavelength of the three-dimensional wave is the same as for the fundamental, then "peak-valley" lambda vortices develop which are aligned in the streamwise direction (x_1). On the other hand, if the streamwise wavelength is twice that of the fundamental then a staggered pattern develops. Conceptually, these two different patterns are illustrated in Figure 5-3. We also wish to consider whether oblique subharmonic disturbances can account for the staggered vortices that Cimbala observed in an incompressible wake.

5.2 The Three-Dimensional Initial Forcing: Mean Flow and Disturbances

If the mean flow is excited by a low level of broadband noise, then the first disturbance to emerge would be the mode corresponding to $(\alpha, 0)$, where α is the wave number associated with the least stable linear stability mode. From two-dimensional simulations, this mode was shown to be responsible for the initial roll-up of the spanwise vortices and for the generation of higher harmonics. In this chapter, three-dimensional disturbances are considered in which a pair of oblique modes at equal and opposite angles are superimposed on the fundamental and the laminar mean

$$\begin{aligned}\mathbf{b}(x_1, x_2, x_3, 0) = \overline{\mathbf{b}}(x_2) + \mathrm{Real}\Big[&\epsilon_{2\mathrm{D}}\grave{\mathbf{b}}_{2\mathrm{D}}(x_2)e^{i(\alpha x_1 + \Theta)} \\ &+ \epsilon_{3\mathrm{D}}\grave{\mathbf{b}}_{3\mathrm{D}}(x_2)e^{i(l\alpha x_1 + \beta x_3)} + \epsilon_{3\mathrm{D}}\grave{\mathbf{b}}_{3\mathrm{D}}(x_2)e^{i(l\alpha x_1 - \beta x_3)}\Big].\end{aligned} \tag{5.2.1}$$

In the nomenclature used here, the oblique modes are denoted by $(\alpha, \pm\beta)$ where β is the spanwise wave number. Three-dimensional modes corresponding to the fundamental (α, β) and subharmonic $(\alpha/2, \beta)$ families of disturbances are considered where $l = 1$ corresponds to the fundamental and $l = 1/2$ corresponds to the subharmonic. The oblique subharmonic instability is analogous to the "helical pairing" mode for a row of Stuart vortices (Pierrehumbert & Widnall [1982]). The shapes of the disturbances were provided by the complex linear eigenfunctions, $\grave{\mathbf{b}}_{2\mathrm{D}}(x_2)$ and $\grave{\mathbf{b}}_{3\mathrm{D}}(x_2)$. Although the eigenfunctions are complex-valued, only the real parts are used to ensure that the resulting disturbances are real-valued. The phase difference between the two-dimensional and three-dimensional disturbances is denoted by Θ. The two-dimensional disturbances are in-phase with the three-dimensional disturbances for $\Theta = 0$ and out-of-phase for $\Theta = \pi/2$. In addition to the phase, the amplitudes of the eigenfunctions, $\epsilon_{2\mathrm{D}}$ and $\epsilon_{3\mathrm{D}}$, need to be specified. Here, they are assumed to be 5.0% of the maximum freestream value.

5.3 Physical and Numerical Parameters for 3D Simulations

To illustrate the different three-dimensional motions which evolve from these prescribed initial conditions, the following discussion will focus on four of the many simulations that were performed. The first two simulations were performed at $Re = 300$ and $M = 1$. The third simulation was performed at $Re = 100$ and $M = 1$, and the fourth simulation was performed at $Re = 300$ and $M = 3$. The first two simulations address the effect of phase on the evolution of large-scale motions in a wake. In the first simulation, the oblique modes $(\alpha, \pm\beta)$ are in phase with the fundamental $(\alpha, 0)$. In the second simulation the oblique modes $(\alpha, \pm\beta)$ are 90 degrees out-of-phase with the fundamental $(\alpha, 0)$. In the third simulation the influence of a three-dimensional subharmonic on the development of a wake is addressed in which the oblique modes $(\alpha/2, \pm\beta)$ are in-phase with the fundamental $(\alpha, 0)$. Finally, in the fourth simulation the effect of Mach number is studied in which the oblique modes $(\alpha, \pm\beta)$ are in phase with the fundamental. The parameters for each of these four simulations are summarized in Table 5.1.

In the remaining sections of this chapter, the results of these four simulations are presented. Cases 1 and 2 are compared in section 5.5, Case 3 is considered in section 5.6, and Case 4 is considered in section 5.7. To aid in the understanding of

TABLE 5.1 SUMMARY OF PARAMETERS FOR 3D SIMULATIONS

Case	α	β	l	Θ	Re	M	M_r
1	0.750	0.433	1	0	300	1	0.692
2	0.750	0.433	1	90	300	1	0.692
3	0.750	0.433	0.5	0	300	1	0.692
4	0.570	0.433	1	0	300	3	2.076

the complicated three-dimensional motions which evolve from these initial conditions, contour plots of various quantities are presented at several stages in the evolution. The interaction of the two-dimensional fundamental mode with the oblique modes is explained by monitoring the history of their modal energies along with instantaneous two-dimensional energy spectra. The vorticity dynamics and temperature field are studied to gain some insight into the evolution of three-dimensional large-scale motions.

Note: In the following discussion, both three-dimensional perspective plots and two-dimensional contour plots of various quantities are presented. There are five planes in the flow field which are of particular interest and will be referred to frequently. The locations of these five planes are shown in Figure 5-4 in a perspective plot of the vorticity norm, $\sqrt{\omega_i \omega_i}$, at a time when the fundamental mode has saturated. The first two planes correspond to spanwise slices (A-A and B-B) which are located midway between the peak in streamwise vorticity. In these two planes of symmetry, the streamwise vorticity is zero. These are the only planes of symmetry in the spanwise direction due to the initial orientation of the oblique waves and to the spanwise periodic boundary conditions. The third plane also corresponds to a spanwise slice (C-C) which passes through the maximum streamwise vorticity in the saddle region. The fourth plane corresponds to a transverse slice (D-D) which passes through the saddle point region and the roller in the top half of the wake. Finally, the fifth plane corresponds to a streamwise slice (E-E) which passes through the streamwise location where the vorticity of the roller in the top half of the wake is a maximum.

5.4 Morphology of the Initial Disturbance Field

The morphology of the initial disturbance field is worth examining since much of the phenomena observed later in the nonlinear stages in the development of the compressible three-dimensional wake can be traced back to the structure of the initial disturbance field comprised of linear eigenfunctions and the Gaussian mean.

Since the fastest growing modes for both low and high Mach number wakes are antisymmetric (Chen, Cantwell, & Mansour [1989a]), the streamwise and spanwise components of the velocity disturbance field along with the temperature, density, and pressure disturbances are all antisymmetric. The only symmetric eigenfunction is the transverse component of the velocity field. Therefore, the initial streamwise vorticity field (ω_1) is symmetric about the wake centerline ($x_2 = 0$), while the initial pressure (p) and spanwise vorticity (ω_3) fields are antisymmetric about $x_2 = 0$. The initial pressure and streamwise vorticity fields are shown in Figure 5-5.

From two-dimensional simulations, it is noted that the pressure maximum serves as a good marker of regions of high strain rates associated with the saddle points and the pressure minimum serves as a good marker of rotational flow associated with the cores of the spanwise vortices. If pressure is employed as a similar marker for a three-dimensional field, the high strain rates delineated by the pressure maxima, will stretch the streamwise vorticity initially present at that location. Therefore, the streamwise vorticity in the saddle region will alternate in sign in the streamwise direction as shown in Figure 5-6. Due to the pair of oblique disturbances imposed, the streamwise vorticity pattern in the spanwise direction (x_3) will also alternate in sign. This accounts for the counterrotating pairs of streamwise vortices in the developed wake.

The prescribed initial conditions offer the possibility of forming vortex loops. Due to the initial mean vorticity field, the spanwise vortices which develop have a clockwise sense of rotation in the upper half of the wake and a counterclockwise sense of rotation in the lower half of the wake. Moreover, since they eventually roll-up in regions corresponding to the minima in pressure, two staggered rows of spanwise vortices are created. Vortex loops can form if a pair of counterrotating streamwise vortices in the spanwise direction interacts with a pair of alternating spanwise vortices to form a continuous loop. Subsequent loops in the streamwise direction x_1 will be aligned in the spanwise direction (x_3) since the initial streamwise vorticity field alternates in the streamwise direction. If the initial disturbances consisted of streamwise vortices instead of oblique waves, then successive loops in the streamwise direction would be staggered 180 degrees apart (Buell & Mansour [1989]).

5.5 Effect of Phase Lag

To illustrate the effect of phase on the development of three-dimensional motions, results from Cases 1 and 2 are compared.

The modal energy history of the fundamental and oblique modes is shown in Figure 5-7 for both simulations. The modal energy is defined as

$$E_{\alpha,\beta} = \int_{-\infty}^{\infty} \hat{u}_i(\alpha, x_2, \beta)\hat{u}_i^{\dagger}(\alpha, x_2, \beta)dx_2 \tag{5.5.1}$$

where summation over i from 1 to 3 is implied, $\hat{u}_i(\alpha, x_2, \beta)$ denotes the Fourier transform of $u_i(x_1, x_2, x_3)$ in the (x_1-x_3) plane, and † denotes the complex conjugate.

In both simulations, the fundamental first grows exponentially at the same rate predicted by linear stability theory, then grows more slowly as the spanwise vortices roll-up nonlinearly, and finally saturates at the same convective time, $t = 49$. The fundamental saturates at a higher energy level (0.1) for Case 1 compared with (0.08) for Case 2. In Case 1, the oblique modes first grow exponentially; this is followed by a period when their energies level off and actually decrease slightly during the fundamental roll-up and saturation, and by a second period of exponential growth on the newly rolled-up base state. In contrast, the oblique modes for Case 2 experience a longer initial exponential growth period saturating at a higher energy level than for Case 1. Furthermore, the oblique modes for Case 2 are not unstable to the rolled-up fundamental base state. The oblique modes saturate at $t = 64$ for both simulations. In Case 1, the mean flow is more efficient at feeding energy to the fundamental than it is for Case 2. The opposite is true for the oblique modes.

Instantaneous two-dimensional energy spectra for Case 1 is shown in Figure 5-8 and is representative of both simulations. Initially, only three modes are excited corresponding to the fundamental and the two oblique modes. The energy spectra corresponding to the wake centerline ($x_2 = 0$) and to one side of the wake ($x_2 = 2$) is shown in Figures 5-8b,c at a time when the fundamental has saturated. Note that the generation of higher harmonics occurs at approximately the same rate in both the streamwise and spanwise directions. This is an indication that velocity gradients in the streamwise and spanwise directions are of the same order of magnitude. Additionally, note that the simulation is well resolved in both the streamwise and spanwise directions.

The two-dimensional and three-dimensional saturated states of the vorticity field are shown in contour plots of the vorticity norm, $\sqrt{\omega_i \omega_i}$ (Figure 5-9). Two streamwise periods and one spanwise period are shown in these perspective plots. The contour level was chosen to bring out both the vorticity found in the saddle region as well as the vorticity in the vortex cores. The peak vorticity is located in the vortex cores, while the streamwise vorticity in the saddle region is approximately 40% of the peak value.

For both simulations, the initially perturbed vorticity field rolls-up into two rows of staggered vortices as vorticity is advected from the saddle region into the cores of the spanwise vortices. The spanwise vortices become progressively more deformed in the spanwise direction as they roll-up, due to their own self-induction caused by their curvature. At a time when the fundamental has saturated, note that this deformation occurs primarily in the (x_3-x_2) plane for Case 1 and in the (x_1-x_3) plane for Case 2 (Figure 5-9a,c). As the spanwise vortices evolve beyond the saturated fundamental state, their self-induction causes them to rotate in a direction opposite to the rotation of the vorticity. Note, that at a time when the oblique modes have saturated, this retrograde rotation has moved the plane of the deformation in each simulation by $\pi/2$. The self-induction mechanism observed here was originally suggested by Hama [1963] as a possible mechanism for the amplification of three-dimensional small disturbances in the presence of background shear.

In addition to the spanwise vortices, note that there exists counter-rotating pairs of streamwise vorticity downstream of the saddle region on each side of the wake. This vorticity is inclined along the principal axis of positive strain and, due to the strain field generated by the spanwise vortices, is stretched around the downstream spanwise roller. The streamwise vorticity is stretched around the downstream vortex first because the saddle points connecting oppositely-signed spanwise vorticity are closer to the downstream vortex. Due to intense stretching, the streamwise vorticity in the saddles is six times larger than its initial value of 0.06 when the fundamental saturates. After the fundamental saturates, the vorticity in the saddle region winds itself into the vortex cores for Case 1, while remaining in the saddle region for Case 2.

This difference in behavior of the streamwise vorticity in the saddle region can be explained in terms of the streamwise location of the maximum strain rate relative to the streamwise vorticity extrema illustrated in Figure 5-10. Again the pressure maximum is used to mark the regions of maximum strain rate near the saddle point located in between the spanwise rollers. Contour plots of the pressure and streamwise vorticity fields for the two simulations are shown in Figure 5-11 early in the simulation ($t = 30$) before the 2D wave has saturated. Note, that if the streamwise vorticity extrema are out-of-phase with the pressure maxima (Case 1), then streamwise vorticity is not fixed or "pinned-down" at the saddle point where the high strain rates can stretch the vorticity equally on both sides of the saddle point. Instead, the streamwise vorticity located downstream of the saddle point is stretched and eventually advected into the vortex cores. The streamwise vorticity upstream of the saddle is merely advected into the vortex core of the adjacent upstream roller. In contrast, if the streamwise vorticity extrema are in-phase with the pressure maxima (Case 2), then streamwise vorticity is stretched equally on both sides of the saddle point, and remains there until viscous dissipation eventually balances the vortex stretching in that region. To better illustrate the alignment of the pressure and streamwise vorticity fields, a plan view (D-D) of the pressure and the streamwise vorticity fields is shown in Figure 5-12 at $t = 49$. Note the alignment of the pressure maxima with the streamwise vorticity in the saddle region, and the alignment of the the pressure minima with the streamwise vorticity in the vortex cores.

There are several things to note about the developed streamwise vorticity field in the saddle point region which are best described in a perspective view of the streamwise vorticity, along with the side, plan, and end views shown in Figure 5-13. (The streamwise vorticity for Case 1 is similar to Case 2 at a time when the fundamental saturates; therefore, only the streamwise vorticity for Case 2 is shown.) There are several things to note about the developed streamwise vorticity field in the saddle point region. First, at a given spanwise location (C-C), streamwise vorticity alternates in sign in the streamwise direction as a result of the initial conditions described earlier in section 5.4. Second, in a plane perpendicular to the streamwise direction, the velocity induced by neighboring streamwise vortices tends to rotate the flattened vortices about their centers as shown in Figure 5-13d. This is similar to the dynamics associated with the streamwise vorticity in a mixing layer originally studied by Lin & Corcos [1984], and more recently by Rogers & Moser [1989]. The vorticity in the saddle region is flattened due to the strain field of the spanwise rollers. The vorticity in the saddle region did not collapse, however, due to the low Reynolds number considered here.

For both simulations, the streamwise vorticity in the saddle region is stretched by the plane strain field generated by the spanwise rollers. During the early development of the streamwise vortices, the strain field connects spanwise rollers of the same sign forming two staggered mixing layers shown in Figure 5-14a. Subsequently, the topology changes such that the strain field connects spanwise rollers of opposite sign as shown in Figure 5-14b. Note that the streamwise vorticity in both topologies is aligned with the diverging separatrix of the saddle point.

For the three-dimensional wake simulated, the principal source of streamwise vorticity is due to vortex stretching terms in the vorticity equation

$$\frac{D(\omega_1)}{Dt} = (S_{11}\omega_1 + S_{12}\omega_2 + S_{13}\omega_3) + \text{viscous terms} \tag{5.5.2}$$

where S_{11}, S_{12}, and S_{13} are components of the strain rate tensor. These terms are concentrated in the saddle point region during the early stages of development, and in the cores of the spanwise rollers in the later stages of development after the fundamental has saturated. Contour plots of these stretching terms for Case 1 are shown in Figures 5-15 and 5-16 at $t = 30$ and at $t = 64$. At $t = 30$, note that the intensification of the streamwise vorticity in the saddle point region is due to the plane strain generated by the rollers, $S_{11}\omega_1$ and $S_{12}\omega_2$. At $t = 64$, the streamwise vorticity in the saddle region for Case 1 has largely been advected into the spanwise rollers and the predominant concentration of streamwise vorticity now resides inside the rollers. The increase in circulation of the streamwise vorticity inside the rollers is mainly due to the spanwise distortion of the spanwise rollers in which ω_3 is converted to ω_1 through the term $S_{13}\omega_3$. This term is shown in Figure 5-16d. Note, that there is very little streamwise vorticity produced in the saddle point region at $t = 64$ and that very complicated vortex stretching mechanisms occur inside the rollers.

Shown in Figure 5-17 are streamwise (x_3–x_2) cuts of ω_1 and S_{33} at $t = 64$. Note that in addition to the remainder of the streamwise vorticity in the saddle region, the distortion of the rollers produces a quadrupole of streamwise vorticity inside the rollers. This quadrupole of vorticity produces large negative strain rates in the spanwise cores, corresponding to vortex suppression regions in between the streamwise vortices (denoted by the symbol "C" in Figure 5-17b). Weaker regions of ω_3 enhancement corresponding to positive strain rates are found on either side of the suppression regions. Perspective plots of the vortex stretching term, $S_{33}\omega_3$, are shown in Figures 5-18a and 5-19a and ω_3 is shown in Figures 5-18b and 5-19b. A spanwise cut of $S_{33}\omega_3$ and ω_3 is shown in Figure 5-20. As a result of the strong negative strain rate S_{33}, spanwise vorticity is removed in the center of the core leaving behind a concentration of vorticity on the perimeter of the roller resembling a "hoop" at $x_3 = 0$ (Chen, Mansour & Cantwell [1989b]). Similar "hoop-like" structures have been predicted in simulations of time-developing 3D incompressible mixing layers (Rogers & Moser [1989]), and in spatially-developing simulations of 3D incompressible wakes (Buell & Mansour [1989]).

Scalar pressure, density, and temperature fields. Experimentally, heat or smoke is often injected into the flow to track the vorticity. At low Mach numbers, density behaves like a passive scalar. A spanwise cut (C-C) of the density and pressure fields for Case 1 is shown in Figure 5-21, and perspective plots of the vorticity norm, pressure minima, and density minima for Cases 1 and 2 are shown in Figures 5-22 and 5-23, respectively. The pressure and density minima were found to consistently track the vortical regions in the flow located in the rollers. Note that a pressure minima does not exist in the saddle region since the streamwise vorticity in the saddle region did not collapse.

Based on the developed temperature field shown in Figure 5-24, the peak temperatures do not appear to track the vortical regions in the flow concentrated inside the rollers. Instead, the peak temperatures mark the fluid in the saddle region. Note that the peak temperatures are located on either side of the wake centerline downstream of the saddle point and are aligned along the diverging separatrix of the saddle point. The peak temperatures are denoted by the symbol "H". The location of the peak temperatures varies in the spanwise direction with the peak at one spanwise location (A-A) positioned downstream of the peak at the next spanwise location (B-B). This variation may be the result of different advection rates along the spanwise direction.

5.6 Effect of Oblique Subharmonic Modes

In this section, the effect of a pair of oblique subharmonic modes on the large-scale vortical motion is determined. It is of interest whether the staggered hairpin vortices shown in the upper right-hand corner of Figure 5-2 can be reproduced by numerical simulations. Case 3 was performed at $M = 1$, $\Delta u_c = 0.692$, and at $Re = 100$. The streamwise wave number of the oblique modes was taken to be half that of the fundamental, and the oblique modes were assumed to be inclined at ±50 deg relative to the streamwise direction. The relative phase angle between the fundamental and subharmonic was assumed to be 0.

The spectral energy evolution for the fundamental and oblique subharmonic modes is shown in Figure 5-25. Note that the fundamental mode first grows exponentially, then grows more slowly as the spanwise vortices roll-up nonlinearly, and finally saturates at a convective time of $t = 40$. The oblique subharmonic modes first grow exponentially; this is followed by a period when their energies level off and actually decrease slightly during the fundamental roll-up and saturation, and by a second period of growth on the new base state. However, the oblique subharmonic modes are much less energetic than the fundamental mode, and unlike the two-dimensional subharmonic described in Chapter 4, never surpass the energy of the fundamental.

The instantaneous two-dimensional energy spectra for Case 3 is shown in Figure 5-26. Initially, only three modes are excited corresponding to the fundamental and the two oblique subharmonic modes. The energy spectra corresponding to the wake centerline ($x_2 = 0$) and to one side of the wake ($x_2 = 2$) are shown in Figures 5-26b,c at a time when the oblique modes have saturated. Note that the higher harmonics are produced primarily in the streamwise direction. Also note that the resolution is more than adequate in both the streamwise and spanwise directions.

Unlike the two-dimensional subharmonic, the oblique subharmonic instability does not lead to "helical" pairing as proposed by Pierrehumbert & Widnall [1982] for a row of Stuart vortices. The large-scale 3D vortical motions that develop are conceptualized in Figure 5-27. Only the vortical structures on the top side of the wake are shown. The structures on the opposite side of the wake are staggered by half a period in the streamwise direction and have an opposite sense of rotation. A perspective view of the computed vorticity magnitude and pressure are shown in Figure 5-28. As in Case 1 and Case 2, spanwise variations in the rollers occur due to their self-induced motion caused by their initial curvature. Note, however, that the instability develops differently on opposite sides of the wake; the curvature of the rollers on the upper side of the wake is greater than it is for the lower side. On the upper side of the wake, note that the tips of successive vortices in the streamwise direction are not aligned, but are 180 degrees out-of-phase with the previous vortex.

A cut through the lifted portion of the vortices corresponding to a plan view (A-A) reveals structures similar to those observed by Cimbala, *et al.* [1988]. Contour plots of the spanwise vorticity, pressure, and streamwise vorticity are shown in Figure 5-29 at $t = 60$ corresponding to the plan view (D-D). Two periods in the streamwise and spanwise directions are shown. Successive spanwise vortices are shifted by 180 degrees on each side of the wake. Note that the pressure minima consistently marks the location of the spanwise vortices.

Similar to the two-dimensional subharmonic, the oblique subharmonic evolves differently on opposite sides of the wake. Evidence of this is shown in contour plots (Figure 5-30) of the spanwise (ω_3), streamwise (ω_1), and transverse vorticity components at a time when the fundamental has saturated. Note that the streamwise and transverse vorticity is much stronger on the top half of the wake. This is quite different from the behavior of the streamwise vorticity for Cases 1 and 2 for an oblique fundamental, where opposite sides of the wake evolve in a similar manner.

5.7 Effect of Mach Number

Comparing Cases 1 and 4 illustrates the effect of Mach number on the development of large-scale motions. Comparisons of the modal energy evolution between Case 1 and Case 4 are shown in Figure 5-31. Note that qualitatively, the fundamental and oblique modes for the two simulations are similar. The primary difference is that the growth rates for Case 4 are much lower than for Case 1 leading to much longer saturation times. The fundamental mode for Case 4 saturates at $t = 120$ compared to $t = 49$ for Case 1. The vorticity norm is shown in Figure 5-32 at a time when the three-dimensional waves have saturated. Similar to the low Mach number wake, streamwise vorticity is stretched in the saddle region along the diverging separatrix, connecting alternating spanwise vortices.

Since the fundamental roll-up for this simulation is delayed as a result of the lower linear growth rates, the streamwise vorticity which develops is much weaker and more diffuse than for Case 1. The ratio of the peak streamwise vorticity to the peak vorticity norm is 20% for Case 4 compared with 40% for Case 1. Since the strain from the weak spanwise rollers is not capable of producing strong streamwise vorticity in between the rollers, vortex loops are less likely to form at high Mach numbers.

CHAPTER 6

THREE-DIMENSIONAL TOPOLOGICAL DESCRIPTION

In this chapter, the topology of a low Mach number wake is determined using a generalized three-dimensional critical point theory applied to the velocity, vorticity, and pressure gradient fields. Instantaneous streamlines, vortex lines, and pressure gradient vectors are computed based on the three-dimensional flow fields obtained from direct numerical simulations. The critical points are classified and displayed in state diagrams in the space of the invariants of the gradient tensor of the vector field under consideration. Finally, the topology of the initial velocity field is compared with the morphology of a developed wake.

6.1 Motivation and Background

In Chapter 5, the morphology of a wake was described based on its vorticity, pressure, and temperature fields. In this chapter, the topology of the velocity, vorticity, and pressure gradient fields is determined from instantaneous streamlines, vortex lines, and pressure gradient vectors. A three-dimensional generalized critical point theory (Chong, Perry & Cantwell [1989]) is applied to several of these fields to determine the critical points in the flow. The merits and drawbacks associated with each of these different fields is discussed. The critical points are then presented on P–Q and Q–R state diagrams in the space of invariants of the gradient tensor of the vector field.

A description of the three-dimensional topology from critical point theory provides a concise framework for interpreting the voluminous amount of numerical data that results from a three-dimensional simulation. The critical points are points in the flow where a vector field, such as velocity, vorticity, or pressure gradient, is indeterminate. Put another way, the norm of the vector field at the critical points is zero. Recently, Chong, Perry & Cantwell [1989] devised a generalized approach for the classification of three-dimensional flow patterns for incompressible as well as compressible flows. This approach is based on the determination of three matrix invariants (P, Q, and R) of the local gradient tensor of a continuous vector field evaluated at the critical points. These invariants represent topologically distinct regions of the flow and offer a concise way of summarizing complicated flow patterns.

Previous studies concerning the topology of wakes and jets have relied on two-dimensional phase plane methods applied to velocity fields obtained from hot-wire anemometry measurements (Perry & Lim [1978], Cantwell & Coles [1983], Perry & Tan [1984], and Perry & Steiner [1987b]). Based on these methods and conjectured sectional streamline patterns, some of the flow patterns in a wake have been deduced. In Cantwell & Coles [1983] the topology of a 2D incompressible wake was found to consist of centres connected to saddle points on both sides of the wake in which the centroids of the vortices were used to define an appropriate frame of reference. Based on sectional streamline patterns there is some evidence that "limit cycles" can exist in 3D wakes (Perry & Tan [1984] and Perry & Steiner [1987a]). "Limit cycles" are bifurcation lines which have closed on themselves. Based on the presence of both focus points spiraling inward and focus points spiraling outward, Perry & Steiner [1987a] surmised that regions of vortex stretching and vortex compression can coexist in a three-dimensional wake. The vorticity and strain rate fields described in Chapter 5 also indicate the presence of localized regions of vortex compression alternating with localized regions of vortex stretching inside the spanwise rollers. The strong compression regions are attributed to large negative strain rates generated by a quadrupole of streamwise vorticity located inside the spanwise rollers. The large negative strain rates result in the formation of "hoop-like" vorticity structures.

In the present work, the topology of the velocity, vorticity, and pressure gradient fields is determined by identifying and classifying the critical points in the simulated flows. The derivatives of the velocity, vorticity, and pressure gradient fields are obtained from spectral differentiation of the computed velocity, vorticity, and pressure gradient fields.

The advantage of the vorticity field over the velocity field is that vorticity is invariant with respect to the reference frame of the observer. Furthermore, for compressible flow, the vorticity field is solenoidal whereas the velocity field is not. This eliminates one of the matrix invariants, P, which is zero for solenoidal fields. Therefore, the topology of the three-dimensional vorticity field is completely determined by computing the two invariants, Q and R, for each critical point. Smoke patterns for double-sided wakes (Perry, Lim & Chong [1980] and Antonia, Browne & Bisset [1987]) show the presence of a series of vortex loops. Here, the evolution of vortex lines in a wake was computed where the vortex lines were initially aligned with the spanwise direction, x_3. Based upon the developed vortex line pattern, the critical points in the flow were determined for the vorticity field and displayed on a $Q - R$ state plane.

A quantity which has not received much attention is the pressure gradient field. In an inviscid flow, the pressure gradient is equivalent to the negative of the acceleration field. The pressure gradient field is unique because the gradient tensor of this field, $\partial^2 p/\partial x_i \partial x_j$, always has real eigenvalues with orthogonal eigenvectors. The pressure gradient vectors were computed and the critical points of this field were identified.

6.2 Method

The instantaneous streamlines, vortex lines, and pressure gradient lines are obtained by integrating the velocity, vorticity, and pressure gradient vector fields using a second-order Adams-Bashforth scheme (Walatka & Buning [1989]). A recently developed generalized three-dimensional method for classifying the critical points was employed, the details of which are given in Chong, Perry & Cantwell [1989]. The critical points for each vector field are located by searching for the zeros of the corresponding vector field. Computationally, these zeros correspond to the minima of the norm of the computed quantity. Since pockets of irrotational fluid border rotational fluid, care must be taken in retaining only the zeros of the vorticity field inside the rotational region of flow. Once the grid points associated with the zeros are found, the vector field, denoted by $\mathbf{v}$ is expanded in a Taylor series about the critical point $\mathbf{v^c} = (v_1^c, v_2^c, v_3^c)$:

$$\begin{bmatrix} dv_1/d\tau \\ dv_2/d\tau \\ dv_3/d\tau \end{bmatrix} = \begin{bmatrix} a_{11} & a_{12} & a_{13} \\ a_{21} & a_{22} & a_{23} \\ a_{31} & a_{32} & a_{33} \end{bmatrix} \begin{bmatrix} v_1 - v_1^c \\ v_2 - v_2^c \\ v_3 - v_1^c \end{bmatrix} . \qquad (6.2.1)$$

If the matrix A, whose elements are a_{ij}, corresponds to the velocity gradient tensor, then τ parameterizes the position of a fluid particle along an instantaneous streamline. If $\mathbf{v} = \boldsymbol{\omega}$ then the coefficients are $a_{ij} = \partial\omega_i/\partial x_j$. If $\mathbf{v} = \partial p/\partial x_j$ then the coefficients are $a_{ij} = \partial^2 p/\partial x_i \partial x_j$.

The derivatives of each of the vector fields are computed spectrally and evaluated at each critical point. The matrix invariants P, Q, and R of A are then evaluated where

$$P = -\text{trace}[A] = -(a_{11} + a_{22} + a_{33}), \tag{6.2.2}$$

$$Q = \frac{1}{2}[P^2 - \text{trace}[A^2]] = \begin{vmatrix} a_{11} & a_{12} \\ a_{21} & a_{22} \end{vmatrix} + \begin{vmatrix} a_{11} & a_{13} \\ a_{31} & a_{33} \end{vmatrix} + \begin{vmatrix} a_{22} & a_{23} \\ a_{32} & a_{33} \end{vmatrix}, \tag{6.2.3}$$

and

$$R = -\det[A] = \begin{vmatrix} a_{11} & a_{12} & a_{13} \\ a_{21} & a_{22} & a_{23} \\ a_{31} & a_{32} & a_{33} \end{vmatrix}. \tag{6.2.4}$$

The following equation defines a surface in phase space which divides the real and complex solutions of equation (6.2.1):

$$27R^2 + (4P^3 - 18PQ)R + (4Q^3 - P^2Q^2) = 0. \tag{6.2.5}$$

Once P, Q, and R are evaluated according to equations (6.2.2)–(6.2.4), their position in phase space relative to the surface defined by equation (6.2.5) is found by solving the following cubic equation

$$Q^3 - (\frac{1}{4}P^2)Q^2 - (\frac{9}{2}PR)Q + (P^3R + \frac{27}{4}R^2) = 0. \tag{6.2.6}$$

The roots of equation (6.2.6), Q, are determined by substituting in the invariants P and R at each critical point into equation (6.2.6). The location of the critical points relative to this surface can be displayed on a $Q - R$ phase diagram, and the critical points are then classified according to Chong, Perry & Cantwell [1989].

6.3 Velocity Field

In this section, the results of the first simulation ($M = 1$, $Re = 300$) in Chapter 5 are used to illustrate the topological features in a wake. First, however, the flow pattern for a two-dimensional wake is studied so as to provide a baseline case against which to compare the three-dimensional results.

6.3.1 *2D streamline pattern*

The two matrix invariants of the velocity gradient tensor, P and Q, were found at $t = 0$ and are displayed in a phase diagram (Figure 6-1). The critical points in the flow consist of two stable foci ($P > 0$) and two saddle points ($P < 0$). Note that one of the saddle points lies very close to the axis, $P = 0$, while the other saddle point lies well below the axis. Ideally, the saddle points on both sides of the wake should be identical since the wake is symmetric. However, since the critical points are evaluated at the grid points, there is some variation in the invariants P, Q, and R. Refining the mesh should minimize this problem. In fact, any prior knowledge of symmetries in the flow can be used to determine whether there is adequate resolution to identify the critical points. In an incompressible flow, the foci in Figure 6-1 would become centres since the velocity field is solenoidal. Centres ($P = 0$) can not exist in this flow since the velocity field is not solenoidal at $M = 1$ and the density field is unsteady. In physical space, the relation of the foci and saddle points is shown in a plot of the instantaneous streamlines obtained by integrating particle tracks with the velocity field frozen (Figure 6-2a). The initial position of the particle tracks was chosen to be in the vicinity of the critical points. The observer was assumed to move at the phase speed of the 2D linear disturbances, $c_{ph} = 0.71$, obtained from a linear stability analysis. In Figure 6-2a, the saddle points, representing regions of high strain rates, connect foci on the same side of the wake during the early stages of development. This is in contrast to the topology of the developed wake where the saddle points connect foci on opposite sides of the wake (Figure 6-2b). To verify that there is no interaction between the two sides of the wake initially, the streamlines were all initialized in the streamwise direction in a region known as the "alleyway" near the centerline of the wake where fluid is moving upstream. The streamlines originating in the upper side of the alleyway all wound up in the upper side of the wake, whereas, those originating in the lower side of the alleyway, all wound up in the lower side of the wake. Therefore, the wake behaves initially as two independent mixing layers in which fluid in the spanwise rollers is entrained from both the freestream and from the slower moving fluid located in the alleyway. Eventually the fluid in the alleyway will become depleted as it is entrained into the rollers, and at this point, the topology must bifurcate in order for mass to be conserved.

The instantaneous streamlines at a time after the fundamental has saturated ($t = 40$) are shown in Figure 6-2b. Note that the saddle points connect both sides of the wake and the fluid initially in the alleyway has collapsed to a line dividing the two sides of the wake. Note, however, that the saddle points in Figure 6-2b appear distorted in the sense that the converging separatrices do not converge to the same point. This type of dislocated saddle has been documented by Perry, Lim & Chong [1980] in coflowing wakes and jets and also by Patnaik, Sherman & Corcos [1976] in mixing layers. In the inviscid limit, a distorted regular saddle would become a dislocated saddle, comprised of two half-saddles, separating two discontinuous vortex sheets. However, if the saddle region is enlarged as shown in Figure 6-2c, note that what appears as a dislocated saddle in a global sense is really a regular saddle point. Finally, in the developed wake fluid in the spanwise rollers is entrained from the freestream and from the opposite side of the wake.

6.3.2 *3D streamline pattern*

The instantaneous streamline pattern for the 3D case is shown at $t = 0$ in Figure 6-3 and at $t = 0$ and at $t = 25$ in Figure 6-4. As in the 2D case, the observer is initially assumed to move at the phase speed of the disturbances, and then, after the spanwise vortices have rolled-up, to move with the centroids of the rollers. For the case studied here, the phase speed for the 2D and 3D disturbances is the same, $c_{ph} = 0.71$. At $t = 0$, the streamlines are initialized in the two spanwise planes of symmetry, $x_3 = 0$ and $x_3 = L_3/2$. Note that in both planes, there are foci and saddle points connecting foci on the same side of the wake, similar to the 2D case (Figures 6-3 and 6-4). However, the foci at $x_3 = 0$ are spiraling in a direction opposite to the foci at $x_3 = L_3/2$. The direction of the foci is determined by examining velocity vectors projected onto these two planes shown in Figure 6-5. Note that in both planes the velocity vectors are moving in a clockwise direction in the top half of the wake and in a counterclockwise direction in the bottom half of the wake. Therefore, the foci in Figure 6-4 are spiraling outward at $x_3 = 0$ and inward at $x_3 = L_3/2$ corresponding to unstable and stable focus points, respectively. In Figures 6-3 and 6-4, at the center of each focus point, there are streamlines that leave the symmetry plane and connect the foci at $x_3 = 0$ and $x_3 = L_3/2$ on the same side of the wake. In Figure 6-3, these connections resemble a Chinese handcuff toy. In two dimensions, these connections do not exist and there is no flow in the spanwise direction. However, in three dimensions, the foci become stretching focus points alternating with compressing focus points with flow in between the symmetry planes in the spanwise direction.

In Figure 6-4b, the streamlines at $t = 25$ are initialized in the symmetry planes, $x_3 = 0$ and $x_3 = L_3/2$, and a similar pattern of oppositely spiraling foci appear. Note that the connections between the symmetry planes still exist. However, the saddle points at $x_3 = 0$ now connect foci on opposite sides of the wake, whereas the saddle points at $x_3 = L_3/2$ still connect foci on the same side of the wake. This is an indication that the wake rolls-up at different rates along the span (x_3).

If the streamlines are initialized between the planes of symmetry, then a "limit cycle" emerges as shown in Figure 6-6. Along the inner radius (r_1) the streamlines are spiraling toward $x_3 = 0$ in a helical manner; as they approach $x_3 = 0$ they return toward $x_3 = L_3/2$ on the outer radius r_2 where $r_2 > r_1$, forming a closed cylindrical cell.

Based on the streamline patterns at $t = 0$ and $t = 25$, there appear to be three different types of critical points in the flow: 1) compressing unstable foci at $x_3 = 0$, 2) stretching stable foci at $x_3 = L_3/2$, and 3) saddle points connecting the foci in each plane. The three invariants of the velocity gradient tensor were computed, and the critical points classified. These critical points are displayed on a P-Q diagram shown in Figure 6-7. They correspond to compressing unstable foci (Figure 6-7a) and stretching stable foci (Figure 6-7b). The topology of the initial velocity field indicates that there are spanwise regions of localized vorticity compression alternating with regions of vortex stretching in what will eventually develop into the spanwise rollers. In the next section, a comparison of the vorticity and strain rate fields described in Chapter 5 with the initial streamline pattern indicates that some of the nonlinear aspects of the wake are topologically equivalent to the initial linear behavior.

6.3.3 *Comparison of Vorticity and Velocity Fields*

During the early stages of roll-up the behavior of the streamwise vorticity in the saddle region is consistent with the initial 3D streamline pattern as shown in Figure 5-14a. Note that the streamwise vorticity is stretched by the strain field generated by spanwise vorticity of the same sign. The streamwise vorticity at $t = 18$ resembles the "ribs" seen in mixing layers. At a subsequent time $t = 40$ shown in Figure 5-14b, a comparison of the streamline pattern and the streamwise vorticity indicates that the strain field is between adjacent spanwise rollers of opposite sign. This indicates that the topology has changed such that the saddle points now connect foci on opposite sides of the wake.

While vortex stretching accounts for the intensification of the streamwise vorticity in the saddle point region, it also plays a significant role in the development of the spanwise rollers. Spanwise alternating regions of localized vortex compression and stretching were found to exist near the center of the spanwise rollers during the nonlinear stages. Strong negative strain rates at $x_3 = 0$ result in vortex compression removing spanwise vorticity (ω_3) in the center of an otherwise uniform roller. The vortex stretching term responsible for the production of spanwise vorticity, $S_{33}\omega_3$, along with ω_3 were shown in Figures 5-18 and 5-19. The existence of stretching stable foci (at $x_3 = L_3/2$) and compressing unstable foci (at $x_3 = 0$) in the initial topology of the velocity field may explain the spanwise nonuniformity in the developed rollers.

6.4 Vorticity Field

Instantaneous vortex lines are shown in Figure 6-8 at several stages in the three-dimensional development of a $M = 1$, $Re = 100$ wake in which $\Theta = \pi/2$. The vortex lines were obtained by integrating particle tracks for an instantaneous vorticity field. Initially, the particle tracks were all oriented in the spanwise direction, x_3. In Chapter 5, it was shown that as the spanwise vorticity rolls-up it creates a strain field, first between spanwise vortices of the same sign, and later between spanwise vortices of opposite sign, which reaches a maximum at the saddle points. This strain field amplifies the vorticity in the saddle point region subjecting it to intense vortex stretching. The streamwise vorticity becomes aligned along the principal axis of positive strain, and eventually wraps around the spanwise rollers downstream and upstream of the saddle point. The interaction of the counterrotating streamwise vorticity in the saddle region with the oppositely-rotating spanwise vortices results in the formation of closed vortex loops by $t = 81$. These loops are in planes inclined along the principal axis of positive strain, and successive loops in x_1 have an opposite sense of circulation due to the initial conditions. Similar structures of interconnected vortex loops have appeared in flow visualizations of forced wakes (Breidenthal [1980]) and of unforced wakes (Perry, Lim & Chong [1980] and Antonia, Browne & Bisset [1988]). Figure 6-9 shows two views of vortex loops at a late stage in the development corresponding to a higher Reynolds number simulation, $Re = 300$ and $M = 1$, at a time when the oblique waves have saturated ($t = 64$). The vorticity has formed a series of disk-like loops similar to the lower Reynolds number case. Note that successive loops are connected by a helical structure resembling a "Slinky" toy.

The critical points for the vorticity field are found by searching for the zeros of the vorticity norm. Critical points were found at the center of each of the vortex loops and, based on the invariants Q and R, were found to consist of "no-flow through centres". These critical points correspond to the points plotted above the $Q = 0$ axis of the Q–R diagram shown in Figure 6-10. Numerically, the critical points are actually critical regions within one or two grid points of each other. Therefore, there is a slight amount of scatter in the values of the invariants. The remaining critical point located below the $Q = 0$ axis corresponds to a saddle point which lies outside of the loop and between adjacent loops where the sense of circulation changes sign between adjacent loops. Only one saddle point was found. This may be due to the nature of the vorticity field which is flat over an extended region close to the boundary between the rotational and irrotational fluid. Therefore, the gradient of the vorticity field is very small there and it is very difficult, if not impossible, to distinguish some of the critical points.

6.5 Pressure Gradient Field

The pressure gradient vectors corresponding to a $M = 1$, $Re = 300$ simulation are shown in Figure 6-11. The spanwise cut shown in Figure 6-11a corresponds to the location of maximum streamwise vorticity, and the spanwise cut shown in Figure 6-11b corresponds to a spanwise symmetry plane where the streamwise vorticity is zero. Aside from the variation in strength of the pressure gradients, the topology at these two planes is the same. The topology of this field consists of nodes and saddle points. The nodes exist at the centers of the spanwise rollers and are connected by saddle points located slightly above and below the wake centerline ($x_2 = 0$). While the critical points are easily identified inside the wake, near the freestream the pressure gradient becomes degenerate.

An attempt was made to integrate the pressure gradient vectors. However, near the saddle point region of the velocity field, the integration scheme encountered difficulties since the pressure gradients are very small. Therefore, any critical points associated with the streamwise vorticity there were not discernable. Improvements in the algorithm are needed so that critical points near degenerate regions in the flow can still be distinguished.

CHAPTER 7

CONCLUSIONS

7.1 Concluding Remarks

In the present work it was demonstrated that linear stability theory combined with direct simulations in both two and three dimensions is an effective way to study transition in a compressible plane wake. A large portion of this work was devoted to the development of algorithms for solving unsteady compressible free shear flows, since very few direct simulations of compressible free shear flows existed at the outset of this work. First, a hybrid approach for solving the linearized inviscid compressible disturbance equations was developed. In this approach, the inviscid disturbance equations are solved with a direct spectral method to obtain an initial estimate of the eigenvalues for a shooting method. In principle a direct method should capture all of the unstable modes. However, at high Mach numbers the direct method converged slowly as weakly amplified disturbances approached the neutral singular point. Therefore, a shooting method was used in addition to the direct method. Second, a spectral collocation method for the solution of the compressible Navier-Stokes equations for plane temporally-evolving compressible wakes was developed. The method combines Fourier expansions of spatial derivatives with an explicit time advancement algorithm. Mapped boundary conditions at infinity prevented imaging difficulties at the boundaries in x_2. Initial conditions for the simulations were provided by eigenfunctions of the least stable linear mode and a pair of oblique modes superimposed on a Gaussian laminar base flow. Third, an algorithm was developed whereby flow patterns computed from the simulations could be reduced to their basic elements, *i.e.* their critical points. These critical points were identified, and then classified using an existing three-dimensional critical point theory. With these tools the following problems concerning a compressible plane wake were investigated: (1) the effect of Mach number on the evolution of large-scale structures, (2) the sensitivity of the morphology to various initial conditions, and (3) the topology of the velocity, vorticity, and pressure gradient fields.

Effect of Mach Number. Linear stability theory not only predicts reduced growth rates at high Mach number, but also provides an explanation for why the growth rates are reduced. The reduction is caused by a misalignment of the pressure and density gradients in the flow as revealed by the structure of the linear eigenfunctions. At high Mach numbers this misalignment creates strong baroclinic torques, which together with dilatational effects in the saddle region, prevent spanwise vorticity from rolling-up. This explanation is supported by direct simulations which show that the same mechanisms present in the linear stage are also present in the nonlinear stage. However, it was found that once roll-up begins, the actual process of roll-up is similar to an incompressible wake. Linear theory also predicts that the fastest growing wave at any Mach number corresponds to a two-dimensional antisymmetric mode oriented in the streamwise direction. This result suggests that the first structures to appear from the initial instability will be predominantly two-dimensional for both low and high Mach numbers, with subsequent three-dimensional motions evolving from the strain field of the two-dimensional structures. Three-dimensional simulations of low and high Mach number wakes confirmed this hypothesis because the primary structures which emerged from the initial instability were spanwise rollers. Moreover, the fundamental mode is more energetic than the oblique modes in both the linear and nonlinear stages.

Sensitivity to Initial Conditions. Another major objective of this work was to determine the sensitivity of the topology of a compressible wake to various initial conditions. In two dimensions, by varying the phase angle between a fundamental and its subharmonic, pairing occurred on different sides of the wake. Regardless of the phase angle, the presence of a subharmonic resulted in a doubling of the width of the wake. Therefore, introducing a two-dimensional subharmonic in a wake may be an effective means of mixing fluid. From temperature contours alone, it would be very difficult to distinguish whether an increase in scale of the wake is due to pairing or to hydrodynamic instabilities. In three dimensions, an oblique subharmonic does not lead to pairing of the fundamental vortices, but rather leads to wavy spanwise vortices in a staggered "peak-valley-splitting" arrangement. The oblique subharmonic also develops asymmetrically on opposite sides of the wake, similar to the two-dimensional subharmonic.

Phase effects between a fundamental and a pair of oblique fundamental modes were also found to be important. The topology of the developed wake depends upon the initial presence of streamwise vorticity in the saddle region. If streamwise vorticity in the saddle region is initially in-phase with the pressure maxima, then vortex stretching mechanisms cause the streamwise vorticity to interact with the spanwise rollers to form vortex loops inclined along the principal axis of positive strain. If, on the other hand, the streamwise vorticity in the saddle region is initially out-of-phase with the pressure maxima, then the streamwise vorticity is advected into the cores creating wavy spanwise vortices which are in-phase with the preceding vortices.

Three-dimensional simulations suggest that the same vortex stretching mechanisms which are present in a wake may be universal to all free shear flows. For example, the vortex stretching mechanism in a wake near the saddle region is also well documented for a mixing layer (Corcos & Sherman [1984]). The vortex stretching in the saddle region is due to the strain field created by the spanwise rollers. The main distinction is that the saddle point in a wake connects vortices of opposite sign, while in a mixing layer it connects vortices of the same sign. The spanwise vortex stretching mechanism in a wake has also been documented for incompressible mixing layers (Rogers & Moser [1989]). This spanwise mechanism occurs inside the spanwise rollers at later stages in the development resulting in localized regions of vortex compression and vortex stretching near the centers of the rollers. The compression regions in a wake are stronger than the stretching regions, resulting in "hoop-shaped" spanwise structures.

Topology. The similarities of the vortical structures in wakes and mixing layers led us to believe that a systematic approach for reducing complicated three-dimensional flow patterns to their basic elements was needed, so that common features of different flows could be related. A recently developed three-dimensional critical point theory could provide such a framework. The topology of the velocity, vorticity, and pressure gradient fields was examined using this approach. From the topology of the velocity field, it was shown that the wake initially behaves as two independent mixing layers separated by an alleyway. As the disturbances grow, a bifurcation occurs wherein the saddles on opposite sides of the wake become connected. Saddle points and stable foci were found to be the basic elements in a two-dimensional compressible wake, while saddle points, contracting unstable foci, and stretching stable foci were found to be the basic elements in a three-dimensional wake. Saddle points are associated with regions of high strain rates and foci are associated with regions of rotational fluid. These critical points were found in the initial velocity field as well as in the developed velocity field suggesting that the developed wake is very sensitive to its initial disturbances. The spanwise vortex stretching mechanism in the rollers is topologically equivalent to the initial three-dimensional velocity field, *i.e.* contracting unstable foci are associated with regions of localized vortex compression, and stretching stable foci are associated with regions of localized vortex stretching.

The velocity, vorticity, and pressure gradient fields each have advantages and disadvantages. The critical points of the velocity field are relatively easy to find but are dependent upon the reference frame of the observer. In the present work, the reference frame was taken to move at the phase speed of the linear disturbances before the vortices have rolled up, and at the speed of the centroids of the vortices thereafter. The vorticity field is independent of the observer, and the critical points can be displayed on a Q-R phase plane since the first invariant of the vorticity gradient tensor is zero. However, the main disadvantage of the vorticity field is that, near pockets of irrotational fluid which border rotational fluid, it is impossible to distinguish critical points since the field is very degenerate. The pressure gradient field also is independent of the observer, and inside the wake has easily identifiable critical points with orthogonal eigenvectors. But it has the problem of degeneracy near the freestream since the pressure gradients decay there. Improvements in the current algorithm need to be made if all of the critical points of the vorticity and pressure gradient fields are to be identified.

7.2 Recommendations for Future Work

Many of the results presented in this work have implications for flow control in a wake. In particular, it was determined that both compressible and incompressible wakes are sensitive to (1) initial phase relationships between different modes and (2) frequencies of different modes. Further work is needed to determine if there is a preferred phase relationship between different modes, or a preferred frequency range which would offer the greatest mixing enhancement or drag reduction. Is it possible to enhance or suppress the streamwise vorticity in the saddle region? How sensitive are the large-scale structures to the relative initial strengths of the disturbances and to the shape of the initial mean velocity and temperature profiles? In this work the mean profiles were assumed to be Gaussian and shock waves never formed. Would a top-hat profile result in the formation of shock waves?

As simulations of three-dimensional flows become more common, the need for a systematic approach for extracting, summarizing, and relating salient features of the data arises. One such approach is to use a three-dimensional critical point theory to describe the topology of computed flow patterns. This work is a first attempt at using this approach to determine the topology of the velocity, vorticity, and pressure gradient fields for a compressible wake. Improvements need to be made if all of the critical points are to be identified and classified. Certain symmetry properties of the flow could be used as a diagnostic for resolution of the flow. For example, saddle points on either side of the wake should have identical invariants of the deformation tensor. Once the algorithm is improved, the temporal evolution of the critical points for the various fields could be determined and displayed in the space of invariants of the deformation tensor. The sensitivity of the trajectories of the critical points to various parameters of the initial conditions should be determined. Finally, further study is required to determine the extent to which linear theory can be used to deduce the topology of the structure in the developed wake.

The current study has concentrated on the effect of initial conditions on the evolution of large-scale structures in a wake. Only selected modes were initially forced. Turbulent wake simulations need to be performed in which random initial forcings are imposed. Turbulence statistics obtained from an ensemble of runs including Reynolds stresses and higher-order statistics need to be obtained for compressible free shear flows. These statistics are readily available from direct simulation data, but may be impossible to measure. These statistics would assist turbulence modelers in developing phenomenological models for compressible free shear flows.

There is considerable interest in high-speed combustion problems related to mixing in round jets and wakes. The numerical scheme presented here could be modified for such a geometry. The effect of compressibility on the large-scale structures of a round jet or wake should be determined and compared with the results of a plane wake or jet described here. Different mixing enhancement methods should also be tested.

REFERENCES

ANDERSON, D. TANNEHILL, J. & FLETCHER, R. 1984 *Computational Fluid Mechanics and Heat Transfer.* Hemisphere Publishing Company.

ANTONIA, R., BROWNE, L. & BISSET, D. 1987 A description of the organized motion in the turbulent far wake of a cylinder at low Reynolds number. *J. Fluid Mech.* **184**, 423–444.

BEHRENS, W. 1968 Far wake behind cylinders at hypersonic speeds: II–stability. *AIAA J. 6*, No. 2, 225–232.

BEHRENS, W. & KO, D. 1971 Experimental stability studies in wakes of two- dimensional slender bodies at hypersonic speeds. *AIAA J. 9*, No. 5, 851–857.

BEHRENS, W. & LEWIS, J. 1971 Transition and turbulence phenomena in supersonic wakes of wedges. *AIAA J. 9*, No. 10, 2083–2084.

BETCHOV, R. & CRIMINALIE, W. 1967 *Stability of Parallel Flows*, Academic Press Inc.

BLAISDELL, G. 1989 Personal communication.

BOGDANOFF, D. 1982 Compressibility effects in turbulent shear layers. *AIAA Paper No. 21*, No. 6, 926–927.

BREIDENTHAL, R. 1980 Response of plane shear layers and wakes to strong three-dimensional disturbances. *Phys. Fluids* **23**, 1929–1934.

BUELL, J. & MANSOUR, N. 1989 Near field structures in three-dimensional spatially-developing wakes. *Proceedings of the 10th Australasian Fluid Mechanics Conference, Melbourne.*

BUSEMANN, A. 1931 *Handbuch der Physik*, vol. 4, pt. 1, pp. 366, Akademische Verlagsgesellschaft experimentalischen, Geest & Portig, Leipzig.

CAIN, A., FERZIGER, J. & REYNOLDS, W. 1984 Discrete orthogonal function expansions for non-uniform grids using the fast Fourier transform. *J. Comp. Phys.* **56**, 272–286.

CAIN, A., REYNOLDS, W. & FERZIGER, J. 1981 A three-dimensional simulation of transition and early turbulence in a time-developing mixing layer. *Dept. Mech. Engng. Rep.* 14, Stanford University: Stanford, California.

CANTWELL, B. & COLES, D. 1983. An experimental study of entrainment and transport in the turbulent near wake of a circular cylinder. *J. Fluid Mech.* **136**, 321–374.

CANTWELL, B., LEWIS, G. & CHEN, J. 1989 Topology of three-dimensional variable density flows. *Proceedings of the 10th Australasian Fluid Mechanics Conference, Melbourne.*

CHEN, J., CANTWELL, B. & MANSOUR, N. 1989a The effect of mach number on the stability of a supersonic plane wake. *AIAA 89-0285.*

CHEN, J., MANSOUR, N. & CANTWELL, B. 1989b Direct numerical simulations of transition in a compressible wake. *Proceedings of Seventh Symposium on Turbulent Shear Flows, Stanford University.*

CHEN, J., CANTWELL B. & MANSOUR, N. 1989c The topology and vorticity dynamics of a three-dimensional plane compressible wake. *Proceedings of the 10th Australasian Fluid Mechanics Conference, Melbourne.*

CIMBALA, R., NAGIB, H. & ROSHKO, A. 1988 Large structure in the far wakes of two-dimensional bluff bodies. *J. Fluid Mech.* **190**, 265–298.

CHONG, M., PERRY, A. & CANTWELL, B. 1989 A general classification of three-dimensional flow patterns. *Phys. Fluids (to be published), also Stanford SUDAAR 572.*

COOLEY, J., LEWIS, P. & WELCH, P. 1970 The fast Fourier transform algorithm: programming considerations in the calculation of sine, cosine, and Laplace transforms. *J. Sound Vib*, **12**, 315–337.

COURANT, R., FRIEDRICHS, K. & LEWY, H. 1967 On the partial difference equations of mathematical physics. *IBM J. Res. Dev.***11**, 215–234.

CROCCO, L. 1932 *L'Aerotechnica*, vol. 12, 181–197.

GASPERAS, G. 1989 Transition prediction for two-dimensional viscous supersonic wakes. *AIAA 89-0284.*

GRANT, M. 1958 The large eddies of turbulent motion. *J. Fluid Mech.* **4**, 149–190.

GROPPENGIESSER, H. 1970 Study of the stability of boundary layers and compressible fluids. *NASA TT F-12, 786.*

HAMA, F. 1963 Progressive deformation of a perturbed line vortex filament. *Phys. Fluids* **6**, 526–534.

HERBERT, T. 1983 Secondary instability of plane channel fow to subharmonic three-dimensional disturbances. *Phys. Fluids* **26**, 871–874.

KENDALL, J. 1962 Experimental study of cylinder and sphere wakes at a Mach number of 3.7. *California Institute of Technology, Jet Propulsion Lab., TR 32-363.*

KENDALL, J. 1989 Personal communication.

LEES, L. & LIN, C. 1946 Investigation of the stability of a laminar boundary layer in a compressible fluid. *TN 1115 NACA.*

LEES, L. & GOLD, H. 1966 Stability of laminar boundary layers and wakes at hypersonic speeds. Part 1. Stability of laminar wakes. *Proceedings of International Symposium on Fundamental Phenomena in Hypersonic Flow, Cornell University Press, 1966.*

LEIBOVICH, S. & LELE, S. 1985 The influence of the horizontal component of the Earth's angular velocity on the instability of the Ekman layer. *J. Fluid Mech.* **150**, 41–87.

LELE, S. 1989 Direct numerical simulation of compressible free shear flows. *AIAA 89-0374.*

LIN, S. & CORCOS, G. 1984 The mixing layer: deterministic models of a turbulent flow. Part 3. The effect of plane strain on the dynamics of streamwise vortices. *J. Fluid Mech.* **141**, 139–177.

MACK, L. 1984 Boundary layer linear stability theory. *AGARD-R-709* .

MACK, L. 1988 Personal communication.

MACK, L. 1989 On the inviscid acoustic-mode instability of supersonic shear flows. *Fourth Symposium on Numerical and Physical Aspects of Aerodynamic Flows.*

MANSOUR, N., FERZIGER, J. & REYNOLDS, W. 1978 Large eddy simulation of a turbulent mixing layer. *Dept. Mech. Engng. Rep.* 11, Stanford University: Stanford, California.

MATTINGLY, G. & CRIMINALIE, W. 1972 The stability of an incompressible two-dimensional wake. *J. Fluid Mech.* **51**, 233–272.

MEIBURG, E. 1987 On the role of subharmonic perturbations in the far wake. *J. Fluid Mech.* **177**, 83–107.

MEIBURG, E. & LASHERAS, J. 1988 Experimental and numerical investigation of the three-dimensional transition in plane wakes. *J. Fluid Mech.* **190**, 1–37.

METCALFE, R., ORSZAG, S., BRACHET, M., MENON, S. & RILEY, J. 1987 Secondary instability of a temporally growing mixing layer. *J. Fluid Mech.* **184**, 207–243.

MUMFORD, J. 1983 The structure of the large eddies in fully turbulent shear flows. Part 2. The plane wake. *J. Fluid Mech.* **137**, 447–456.

PAPAMOSCHOU, D. & ROSHKO, A. 1986 Observations of supersonic free shear layers. *AIAA 86-0162.*

PATNAIK, P., SHERMAN, F. & CORCOS, G. 1976 A numerical simulation of Kelvin-Helmholtz waves of finite amplitude. *J. Fluid Mech.* **73**, 215–240.

PAYNE, F. & LUMLEY, J. 1967 Large eddy structure of the turbulent wake behind a circular cylinder. *Phys. of Fluids Supplement, S194–S196.*

PERRY, A. & LIM, T. 1978 Coherent structures in coflowing jets and wakes. *J. Fluid Mech.* **88**, 451–463.

PERRY, A., LIM, T. & CHONG, M. 1980 The instantaneous velocity fields of coherent structures in coflowing jets and wakes. *J. Fluid Mech.* **101**, 243–256.

PERRY, A. & CHONG, M. 1987 A description of eddying motions and flow patterns using critical point concepts. *Ann. Rev. Fluid Mech. 19*, 125–155.

PERRY, A. & STEINER, T. 1987a Large-scale structures in turbulent wakes behind bluff bodies. Part 1. Vortex formation processes. *J. Fluid Mech.* **174**, 233–270.

PERRY, A. & STEINER, T. 1987b Large-scale vortex structures in turbulent wakes behind bluff bodies. Part 2.Far wake structures. *J. Fluid Mech.* **174**, 271–298.

PERRY, A. & TAN, D. 1984 Simple three-dimensional vortex motions in coflowing jets and wakes. *J. Fluid Mech.* **141** 197–231.

PIERREHUMBERT R. & WIDNALL, S. 1982 The two- and three-dimensional instabilities of a spatially periodic shear layer. *J. Fluid Mech.* **114**, 59–82.

RILEY, J. & METCALFE, R. 1980 Direct numerical simulation of a perturbed, turbulent mixing layer. *AIAA Paper 80-0274.*

RILEY, J. & METCALFE, R. 1980 Direct numerical simulations of the turbulent wake of an axisymmetric body. *Turbulent Shear Flows 2*, 78–97.

RILEY, J., MOURAD, P., MOSER, R. & ROGERS, M. 1988 *Proceedings of the Summer Program, Center for Turbulence Research*, 91–116.

ROGALLO, R. 1981 Numerical experiments in homogeneous turbulence. *NASA TM 81315.*

ROGERS M. & MOSER, R. 1989 The development of three-dimensional temporally-evolving mixing layers. *Proceedings of Seventh Symposium on Turbulent Shear Flows, Stanford University.*

ROSHKO, A. 1976 Structure of turbulent shear flows: a new look. *AIAA J. 14*, 1349–1357.

ROSHKO, A. 1954 On the development of turbulent wakes from vortex streets. *NACA report 1191.*

SANDHAM, N. & REYNOLDS, W. 1989a The compressible mixing layer: linear theory and direct simulation. *AIAA Paper No. 89-0371.*

SANDHAM, N. & REYNOLDS, W. 1989b Growth of oblique waves in the mixing layer at high Mach number. *Proceedings of Seventh Symposium on Turbulent Shear Flows, Stanford University.*

SANDHAM, N. & REYNOLDS, W. 1989c A numerical investigation of the compressible mixing layer. *Dept. Mech. Engng. Rep.* 45, Stanford University: Stanford, California.

SATO, H. & KURIKI, K. 1961 The mechanism of transition in the wake of a thin flat plate placed parallel to a uniform flow. *J. Fluid Mech.* **11**, 321–352.

SATO, H. & ONDA, Y. 1970 Detailed measurements in the transition region of a two-dimensional wake. *Institute of Space and Aeronautical Science, University of Tokyo, Report No. 453.*

SATO, H. & SAITO H. 1975 Fine-structure of energy spectra of velocity fluctuations in the transition region of a two-dimensional wake. *J. Fluid Mech.* **67**, 539–559.

SMITH, A. 1956 Transition, pressure gradient, and stability theory. *IX International Congress for Applied Mechanics, Brussels.*

SQUIRE, H. 1933 *Proc. R. Soc., ser. A* **142**, 621–628.

TOWNSEND, A. 1956 *The Structure of Turbulent Shear Flow.* Cambridge University Press.

TOWNSEND, A. 1966 The mechanism of entrainment in free turbulent shear flows. *J. Fluid Mech.* **26**, 689–715.

TOWNSEND, A. 1979 Flow patterns of large eddies in a wake and in a boundary layer. *J. Fluid Mech.* **95**, 515–537.

VAN INGEN, J. 1965 A suggested semi-empirical method for the calculation of the boundary layer transition region. *University of Technology, Dept. of Aero. Eng., Report UTH-124, Delft, The Netherlands.*

WALATKA, P. & BUNING P. 1989 PLOT3D user's manual. *NASA TM 101067*

WHITE, F. 1974 *Viscous Fluid Flow.* McGraw-Hill, Inc.

WINANT, C. & BROWAND, F. 1974 Vortex pairing: the mechanism of turbulent mixing-layer growth at moderate Reynolds numbers. *J. Fluid Mech.* **63**, 237–255.

WRAY, A. 1984 VECTORAL for FORTRAN users. Available from the author, NASA-Ames Research Center.

WRAY, A. 1988 Minimal storage time-advancement schemes for spectral methods. *J. Comp. Phys. (submitted).*

APPENDIX

ODDBALL FILTERING ALGORITHM

For a well-resolved simulation, the energy at the high wave numbers is small, $O(10^{-12})$. However, due to round-off error associated with packing 64-bit words into two 32-bit words, energy accumulates in the terms of the right-hand side of the governing equations (3.1.14-3.1.18). For all other wave numbers besides the oddball, the energy due to round-off error, is eventually reduced by viscous dissipation. However, since there is no mechanism for removing the round-off error which accumulates in the oddball wave number, it builds up and aliases back into the lower wave numbers through the convective terms. The presence of the oddball manifests itself as two-delta wave oscillations in the solution which grow and affect the solution. Therefore, the contribution of the oddball wave number must be set to zero in all the dependent variables after each substep.

The dependent variables are represented by discrete Fourier transform pairs:

$$\phi(i,k) = \sum_{n_1=-N_1/2+1}^{N_1/2} \sum_{n_3=-N_3/2+1}^{N_3/2} \hat{\phi}(n_1,n_3) e^{i2\pi[(n_1/N_1)(i-1)+(n_3/N_3)(k-1)]} \tag{1}$$

$$\hat{\phi}(n_1,n_3) = \frac{1}{N_1 N_3} \sum_{i=1}^{N_1} \sum_{k=3}^{N_3} \phi(i,k) e^{-i2\pi[(n_1/N_1)(i-1)+(n_3/N_3)(k-1)]}. \tag{2}$$

We employ an algorithm written by Blaisdell [1989] which sets the contribution of the oddball wave number to zero:

$$\hat{\phi}(N_1/2, n_2, n_3) = 0, \quad \hat{\phi}(n_1, n_2, N_3/2) = 0. \tag{3}$$

This can also be achieved by transforming the dependent variables into wave space, setting to zero the appropriate Fourier coefficients, and transforming back to physical space. However, it is more efficient to perform the filtering in physical space since the solution is time-advanced in physical space.

Filtering is performed in the streamwise (x_1) and spanwise (x_3) directions. The Cain-mapped direction (x_2) is not filtered. In two dimensions, the desired filtered function is given by:

$$\phi^f = \phi - \sum_{n_1=-N_1/2+1}^{N_1/2} \hat{\phi}(n_1, N_3/2) e^{i2\pi[(n_1/N_1)(i-1)+(k-1)/2]}$$
$$- \sum_{n_3=-N_3/2+1}^{N_3/2-1} \hat{\phi}(N_1/2, n_3) e^{i2\pi[(i-1)/2+(n_3/N_3)(k-1)]} \qquad (4)$$

which through much algebraic manipulation is given in its final form:

$$\phi^f(x_{1i}, x_{3k}) = \phi_i - \frac{(-1)^k}{N_3} \sum_{k'=1}^{N_3} \phi(x_1, x_3)(-1)^{k'}$$
$$- \frac{(-1)^i}{N_1} \sum_{i'=1}^{N_1} \phi(x_1, x_3)(-1)^{i'}$$
$$+ \frac{(-1)^i(-1)^k}{N_1 N_3} \sum_{i'=1}^{N_1} \sum_{k'=1}^{N_3} \phi(x_1, x_3)(-1)^{i'}(-1)^{k'}. \qquad (5)$$

We have omitted the details of the derivation which are given in Blaisdell [1989]. After each substep, each of the dependent variables is filtered according to equation 5 at the beginning of PASS1.

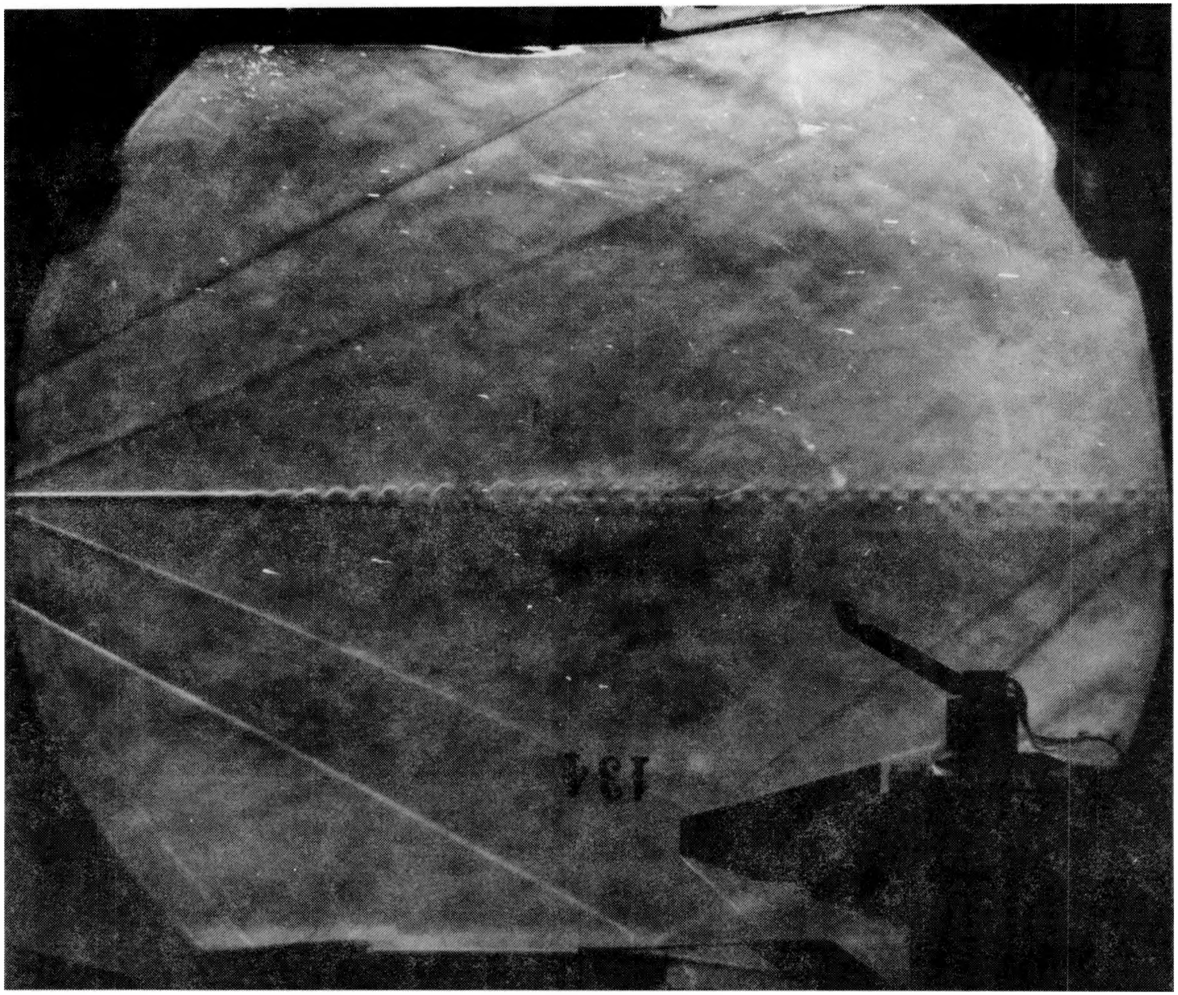

FIGURE 1-1. Schlieren of Mach 2.2 wake behind a flat plate forced at 34 kcps, *reproduced with permission from J. Kendall.*

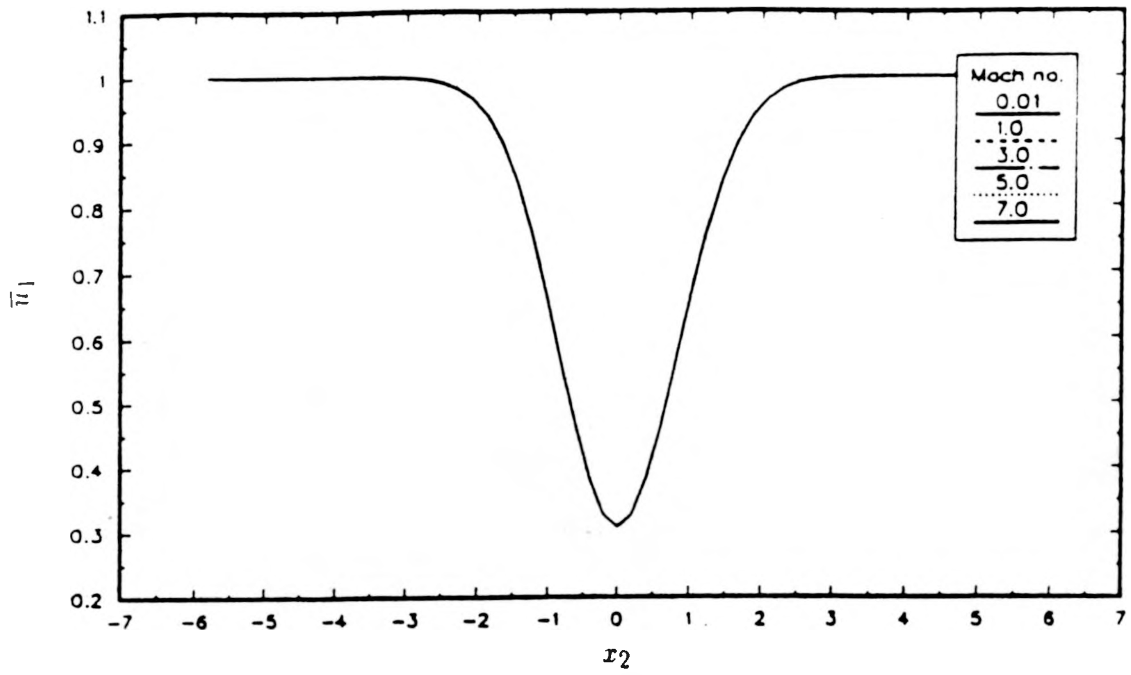

FIGURE 2-1. Gaussian mean velocity profile.

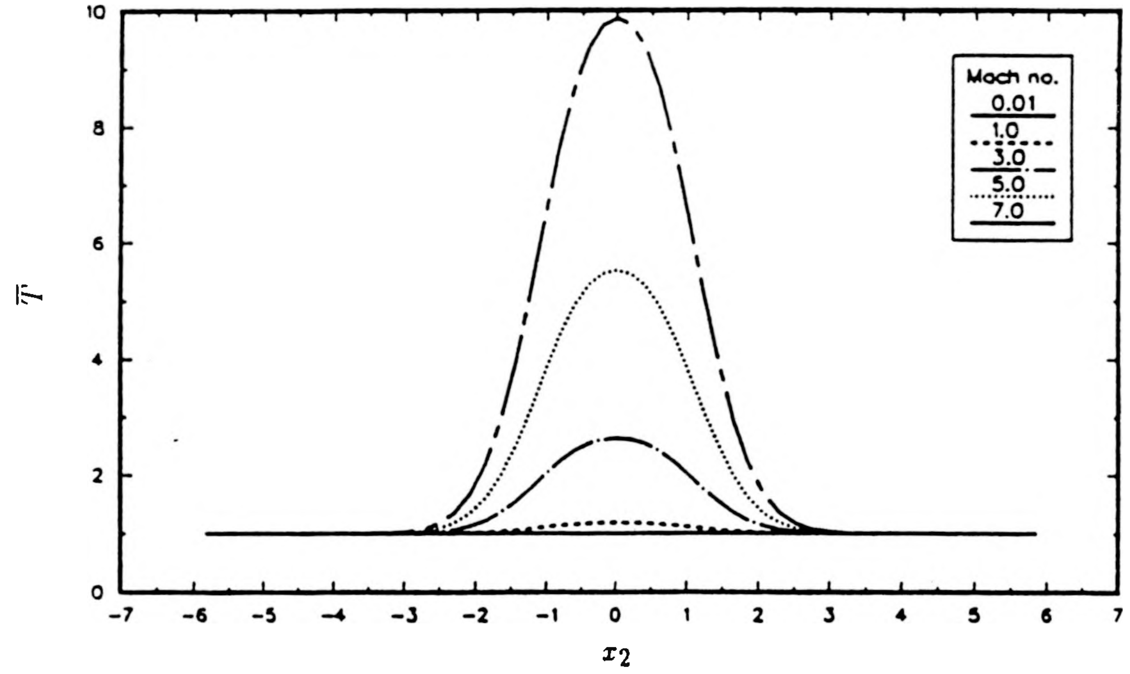

FIGURE 2-2. Mean temperature profile from Crocco-Busemann relation.

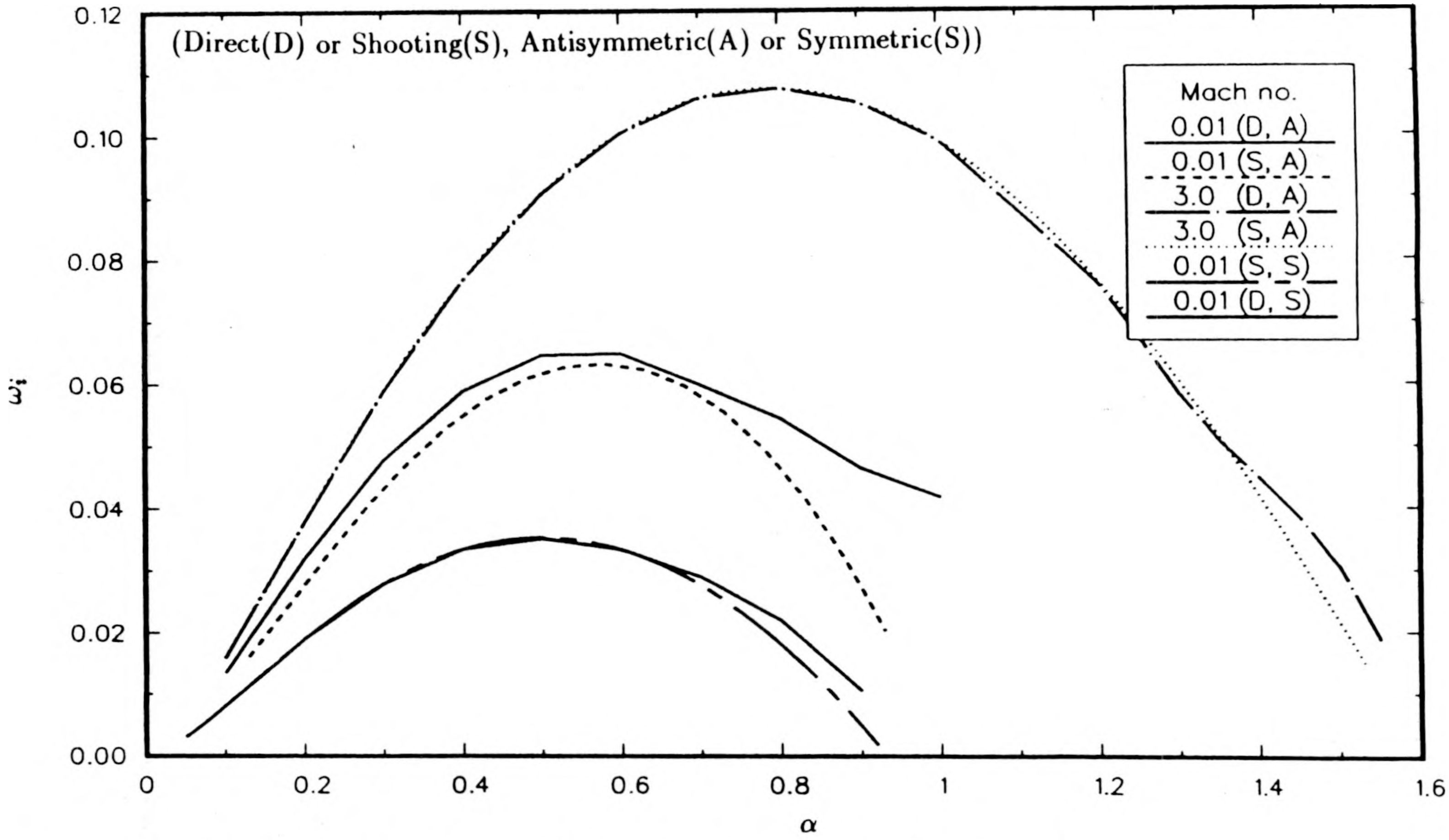

FIGURE 2-3. Comparison of linear growth rates for direct and shooting methods.

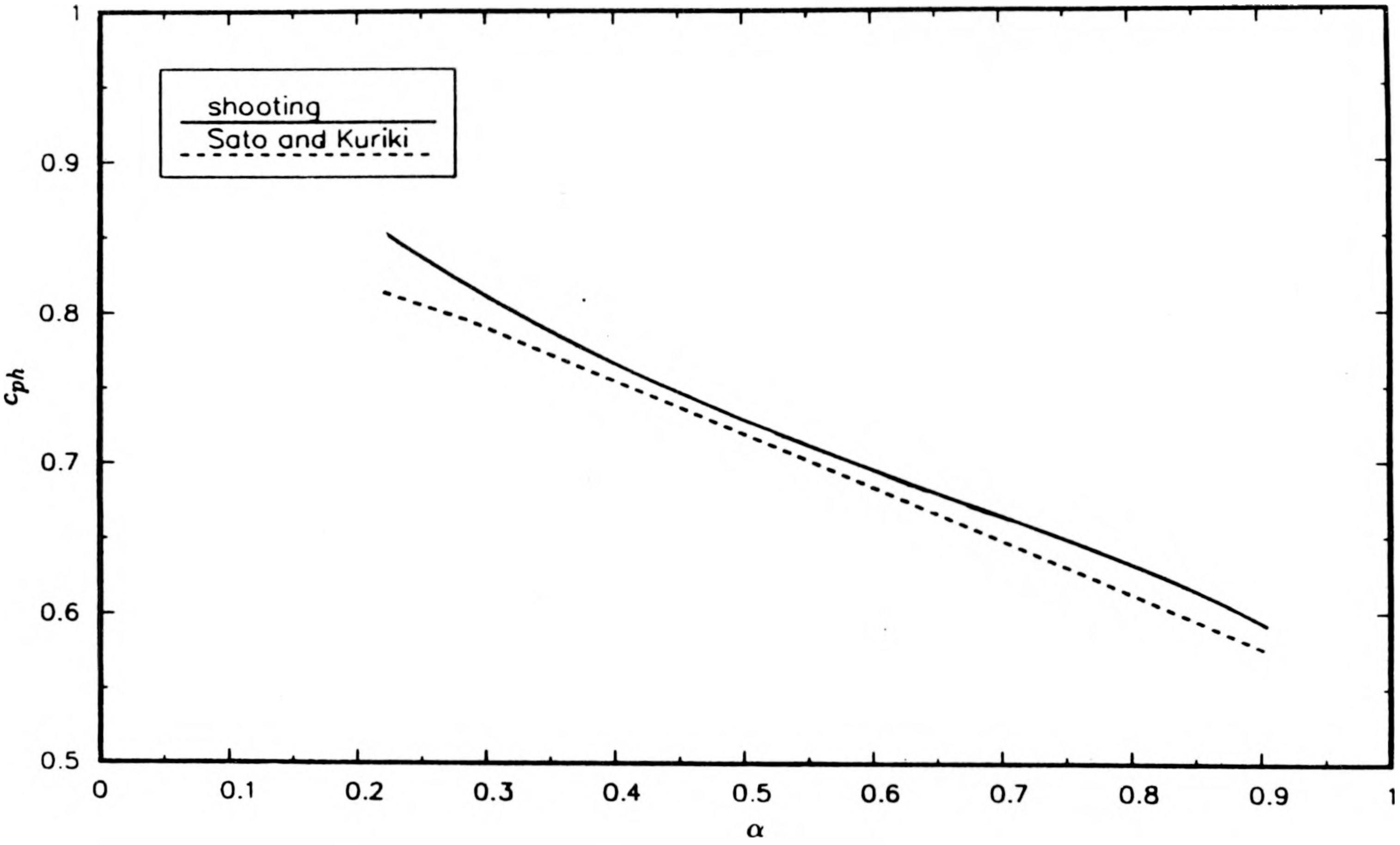

FIGURE 2-4. Comparison of phase speeds for an incompressible wake.

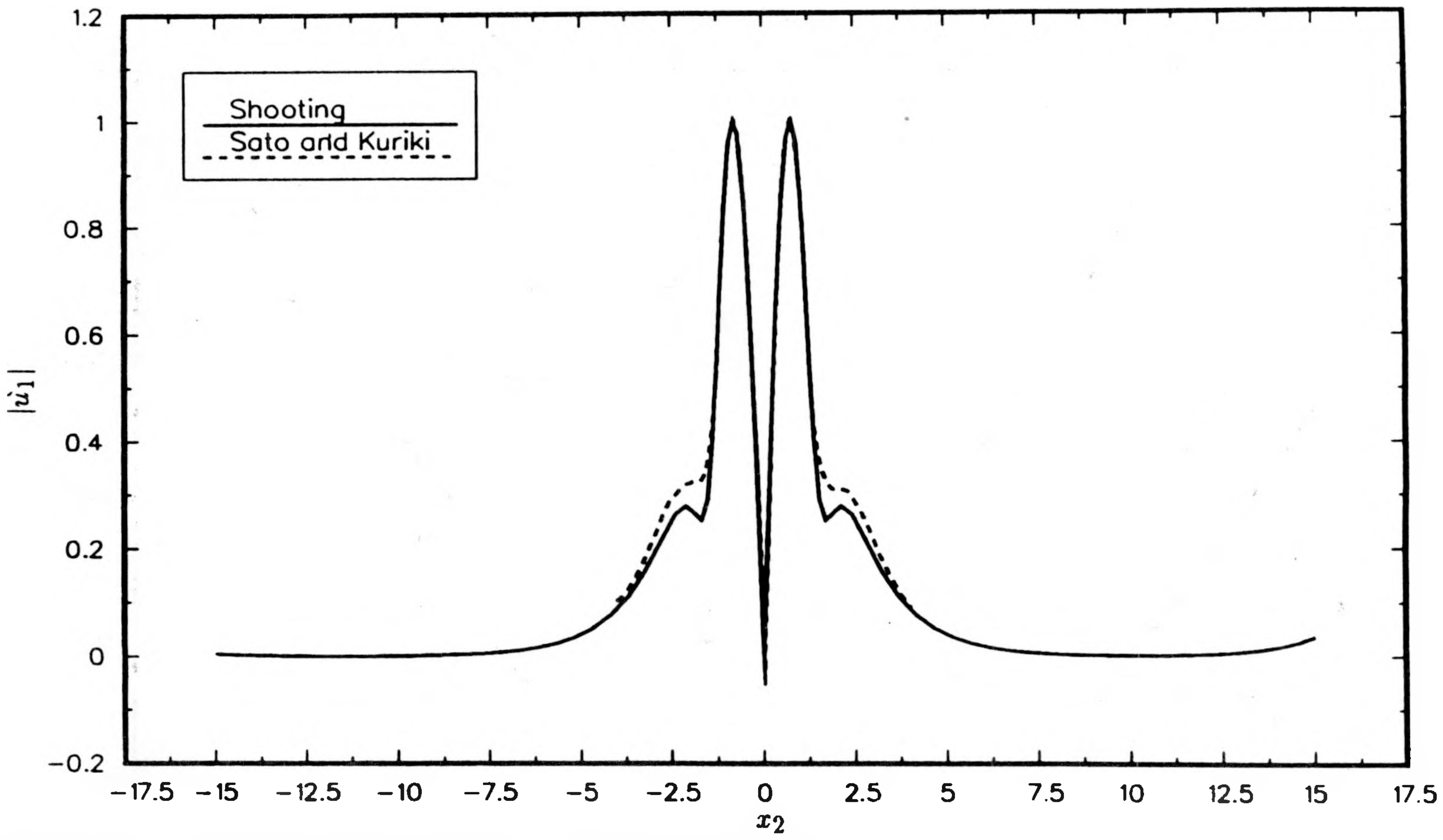

FIGURE 2-5. Comparison of streamwise velocity eigenfunctions.

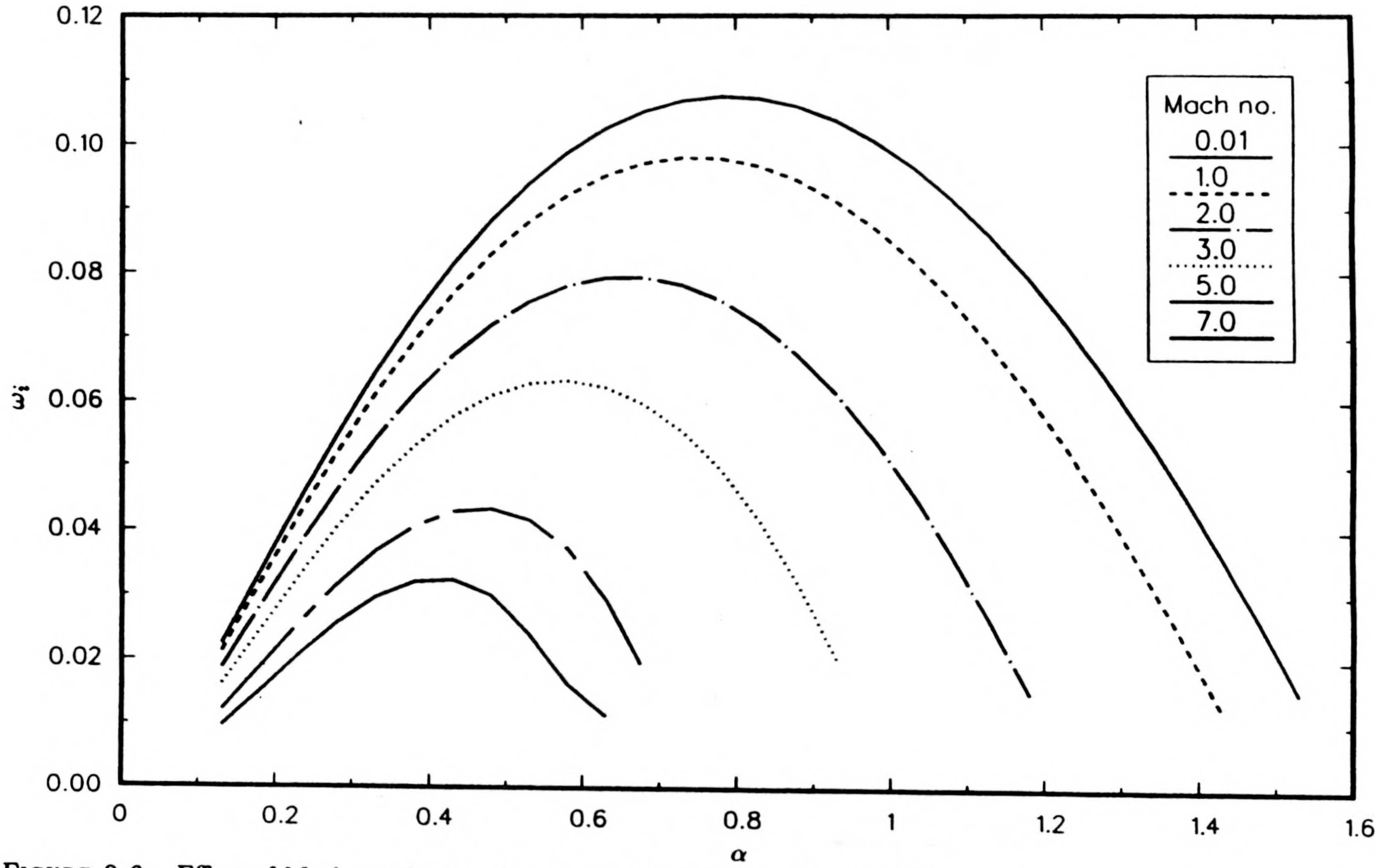

FIGURE 2-6. Effect of Mach number on the growth rate of the antisymmetric 2D mode.

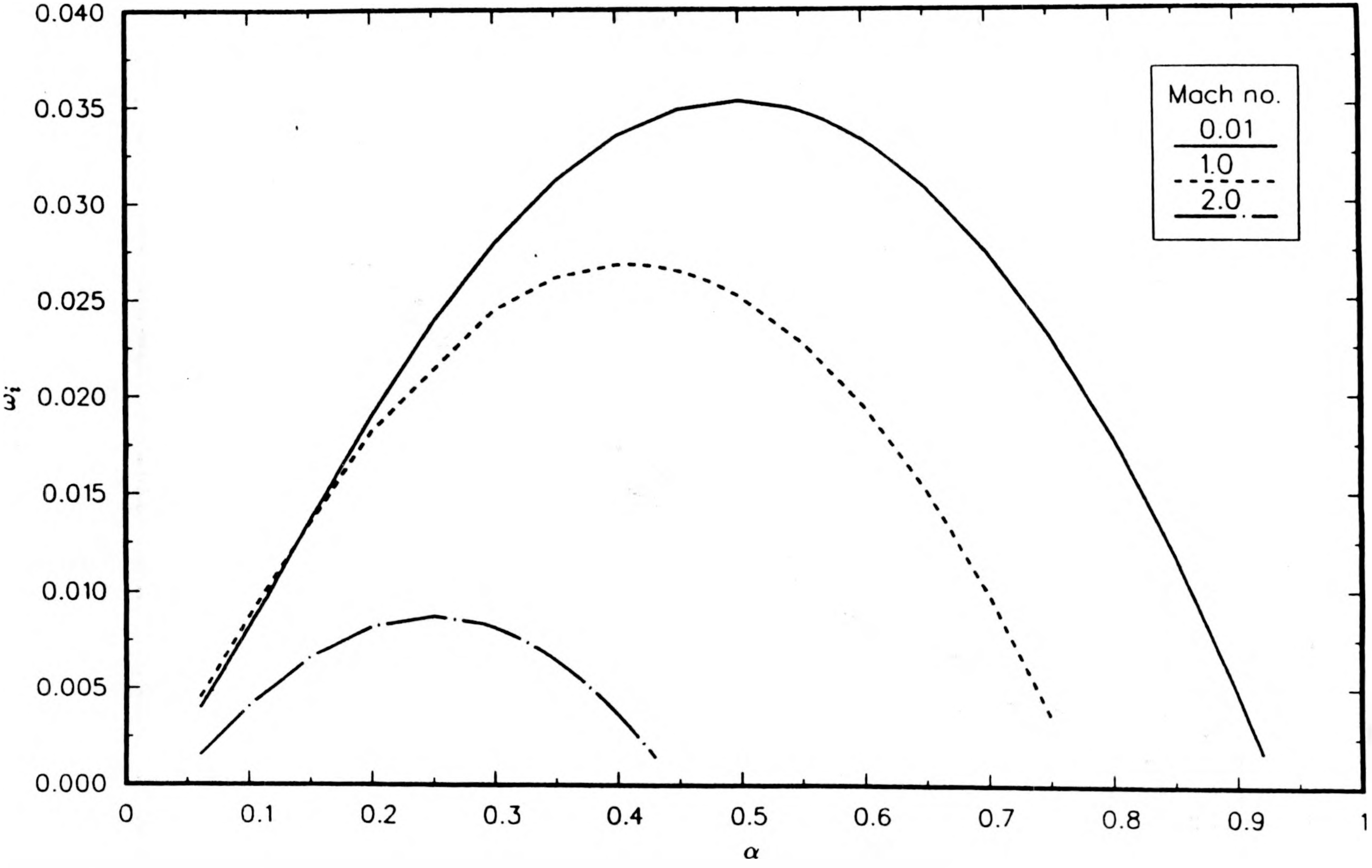

FIGURE 2-7. Effect of Mach number on the growth rate of the symmetric 2D mode.

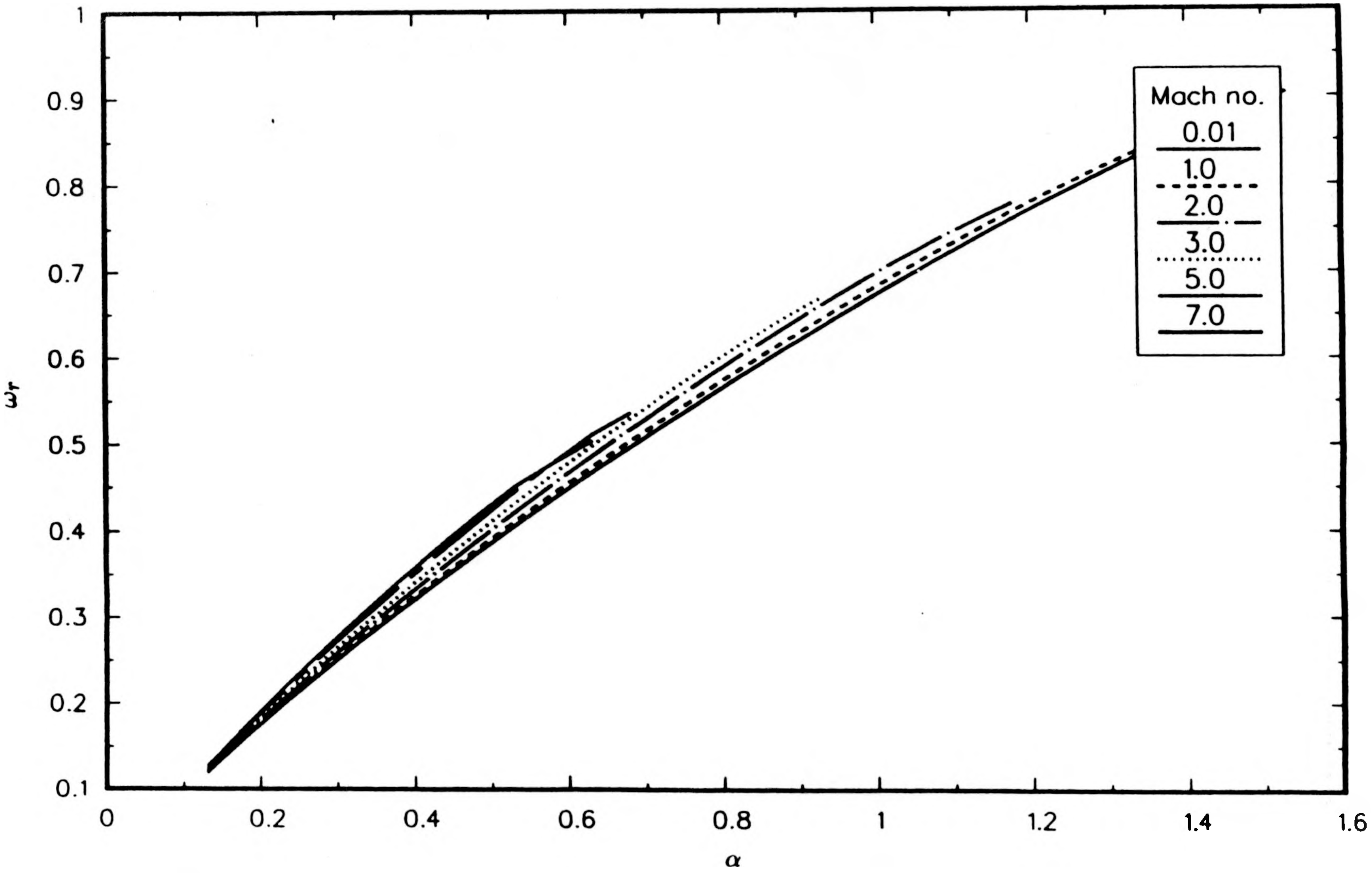

FIGURE 2-8. Effect of Mach number on the frequency of the antisymmetric 2D mode.

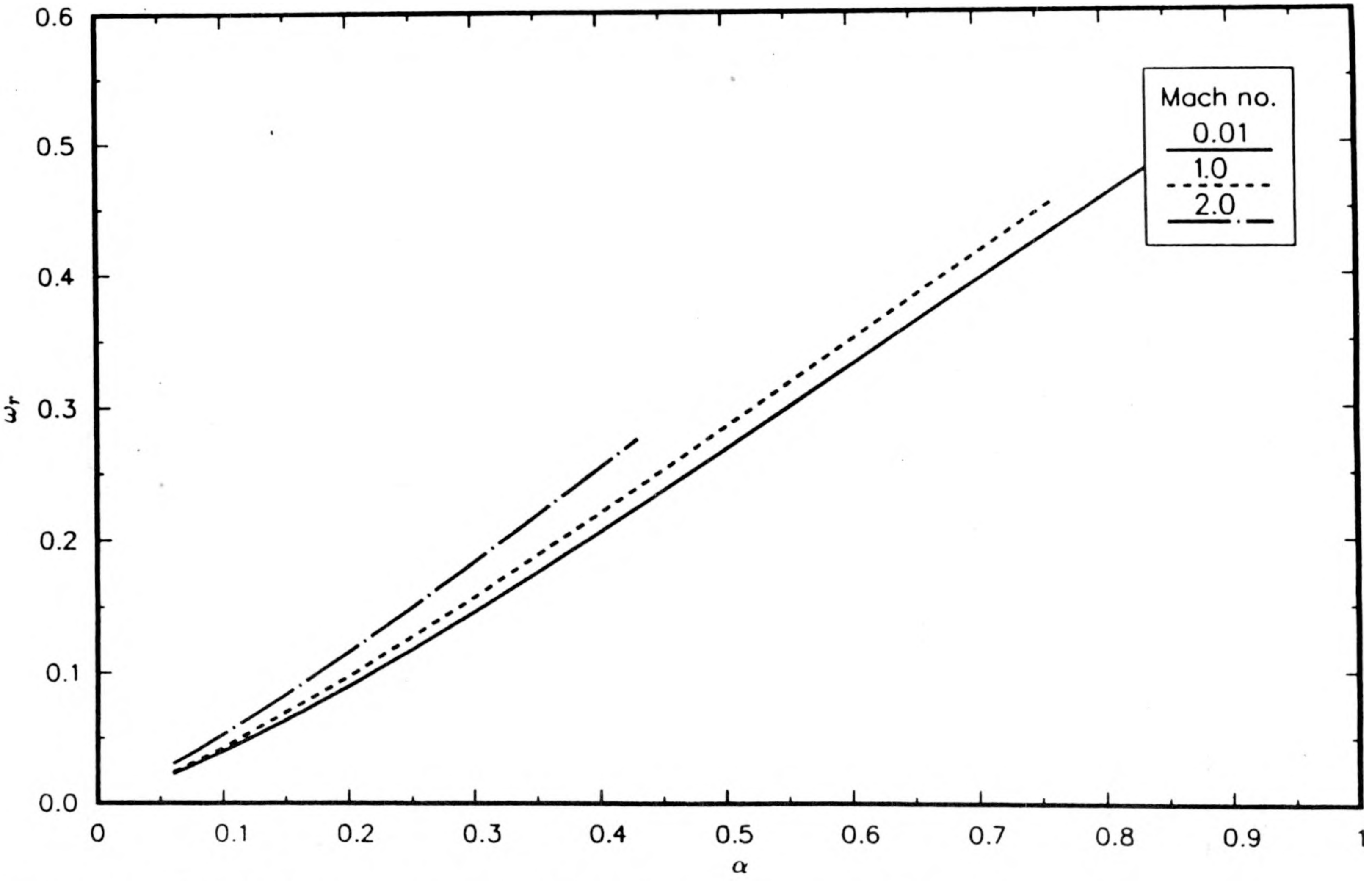

FIGURE 2-9. Effect of Mach number on the frequency of the symmetric 2D mode.

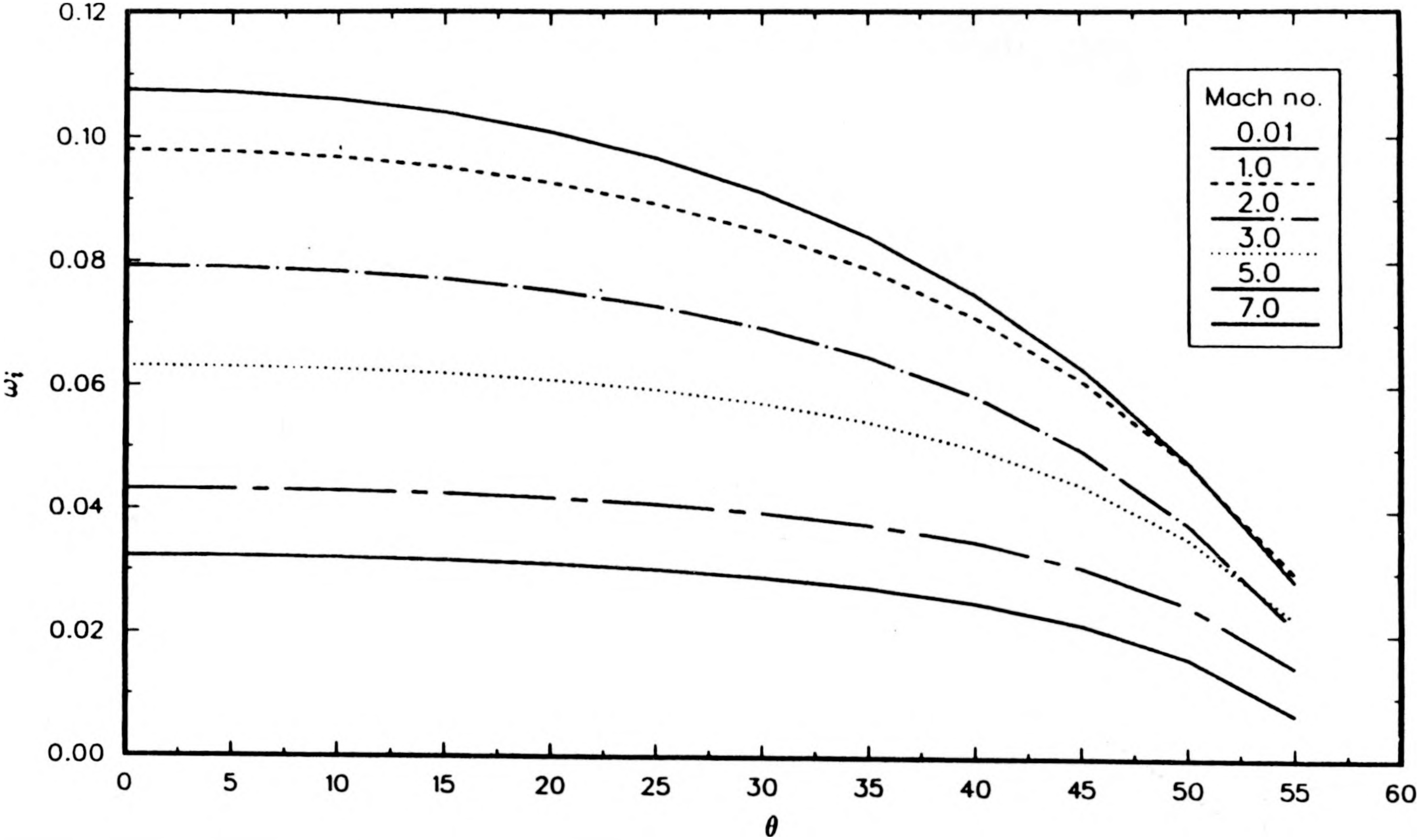

FIGURE 2-10. Effect of obliquity on the growth rate of the antisymmetric mode.

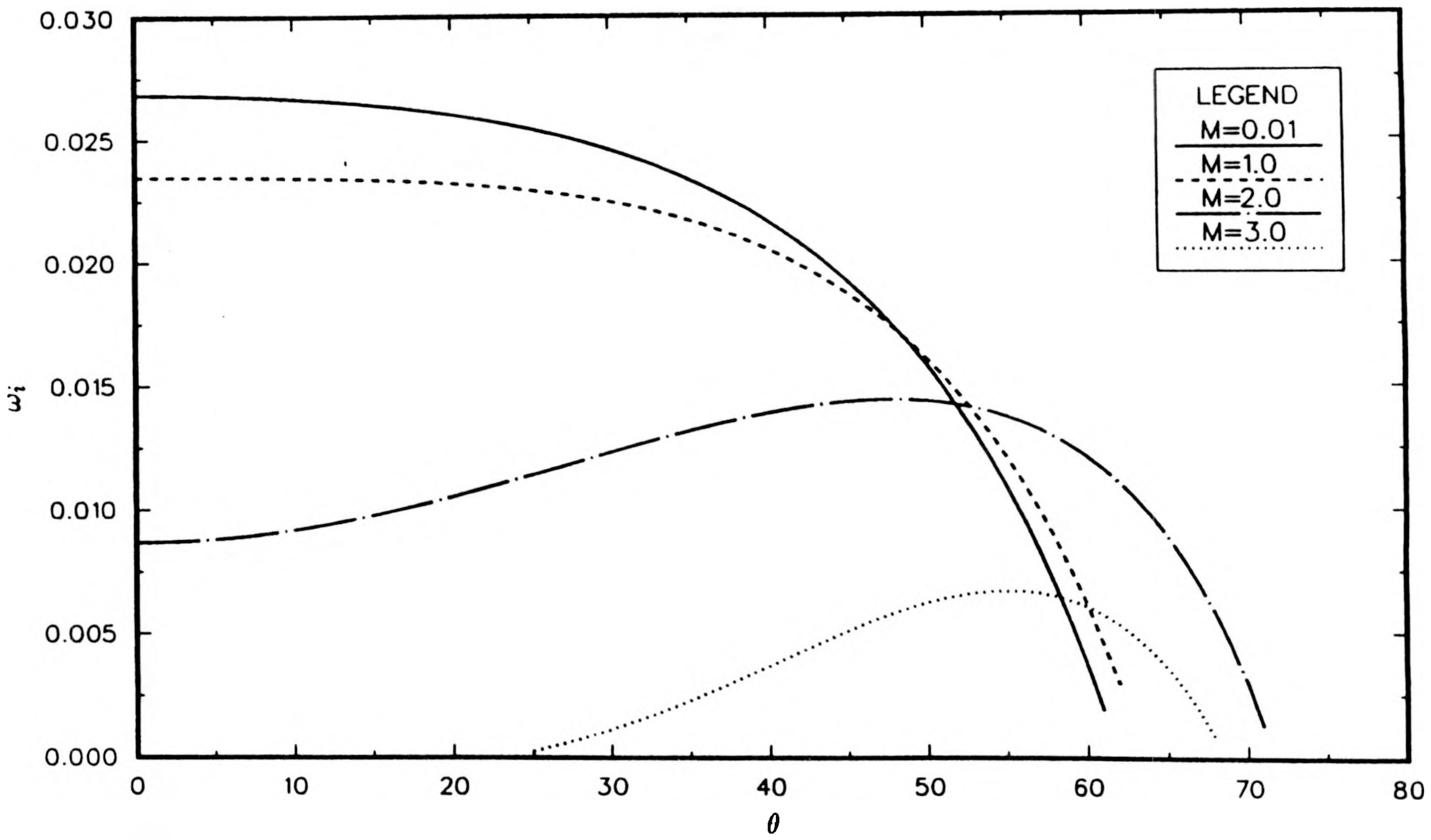

FIGURE 2-11. Effect of obliquity on the growth rate of the symmetric mode.

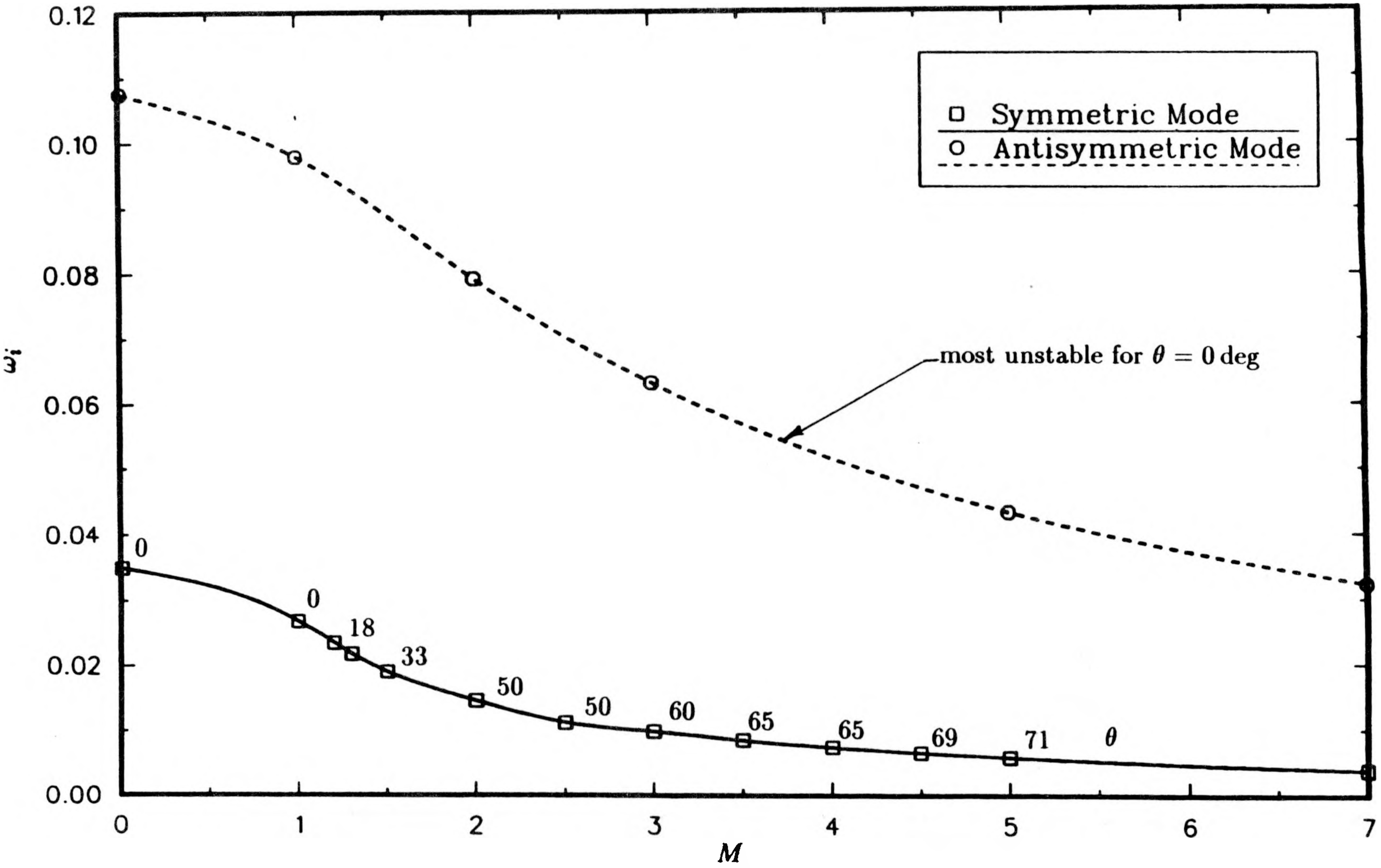

FIGURE 2-12. Most unstable three-dimensional antisymmetric and symmetric modes.

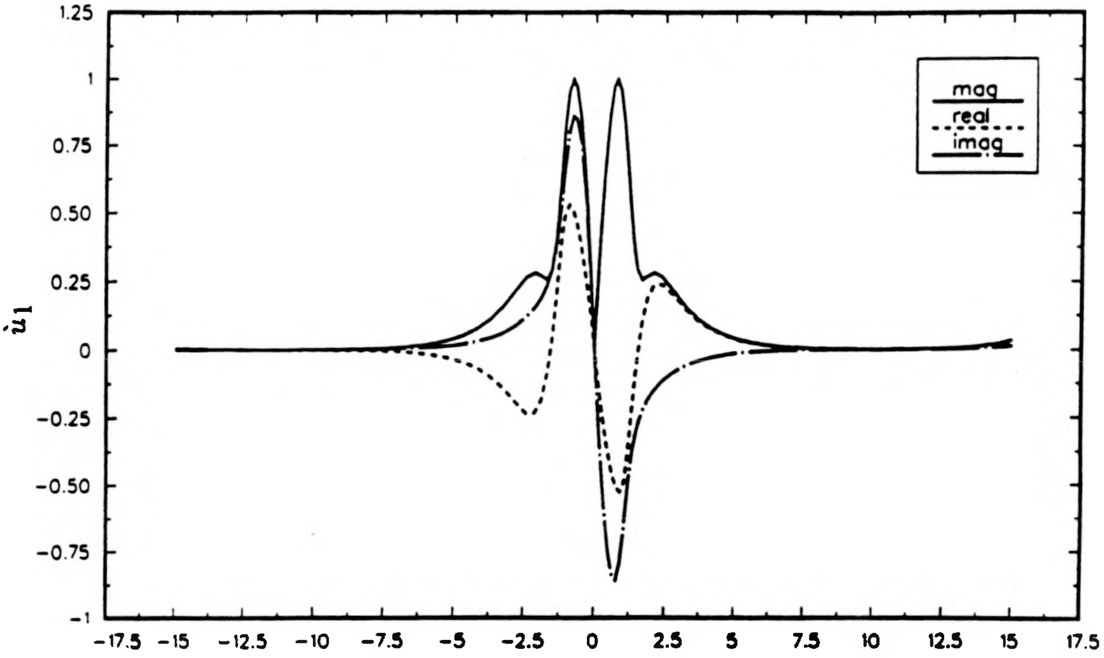
1.25
1
0.75
0.50
0.25
0
−0.25
−0.50
−0.75
−1
$\dot{u}_1$
−17.5 −15 −12.5 −10 −7.5 −5 −2.5 0 2.5 5 7.5 10 12.5 15 17.5
x_2
mag
real
imag

(a)

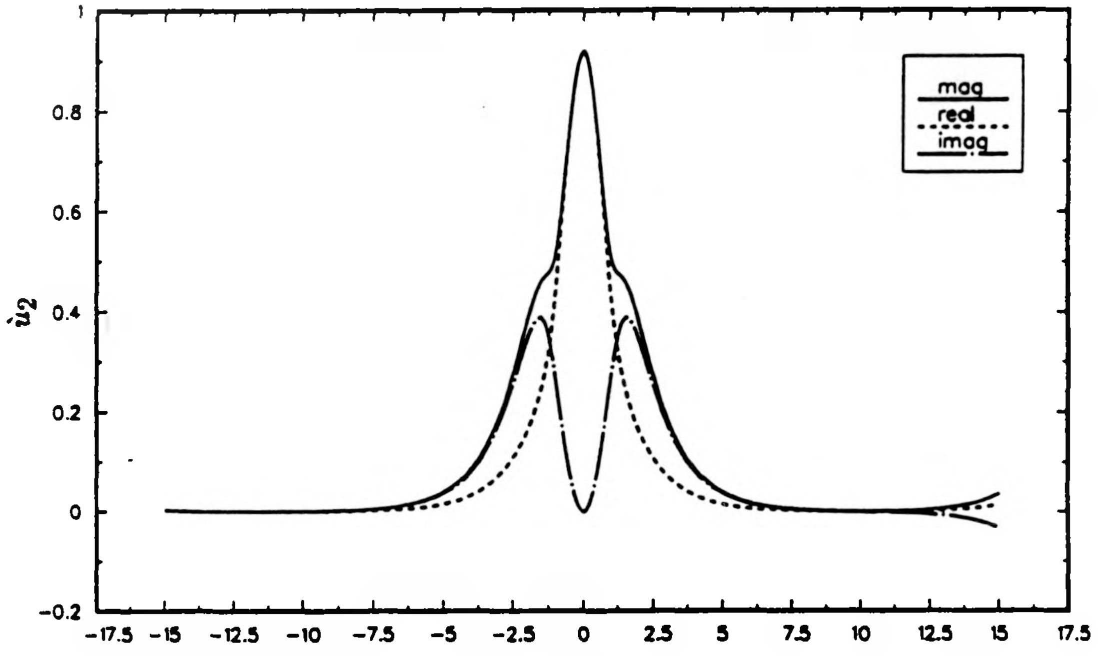
1
0.8
0.6
0.4
0.2
0
−0.2
$\dot{u}_2$
−17.5 −15 −12.5 −10 −7.5 −5 −2.5 0 2.5 5 7.5 10 12.5 15 17.5
x_2
mag
real
imag

(b)

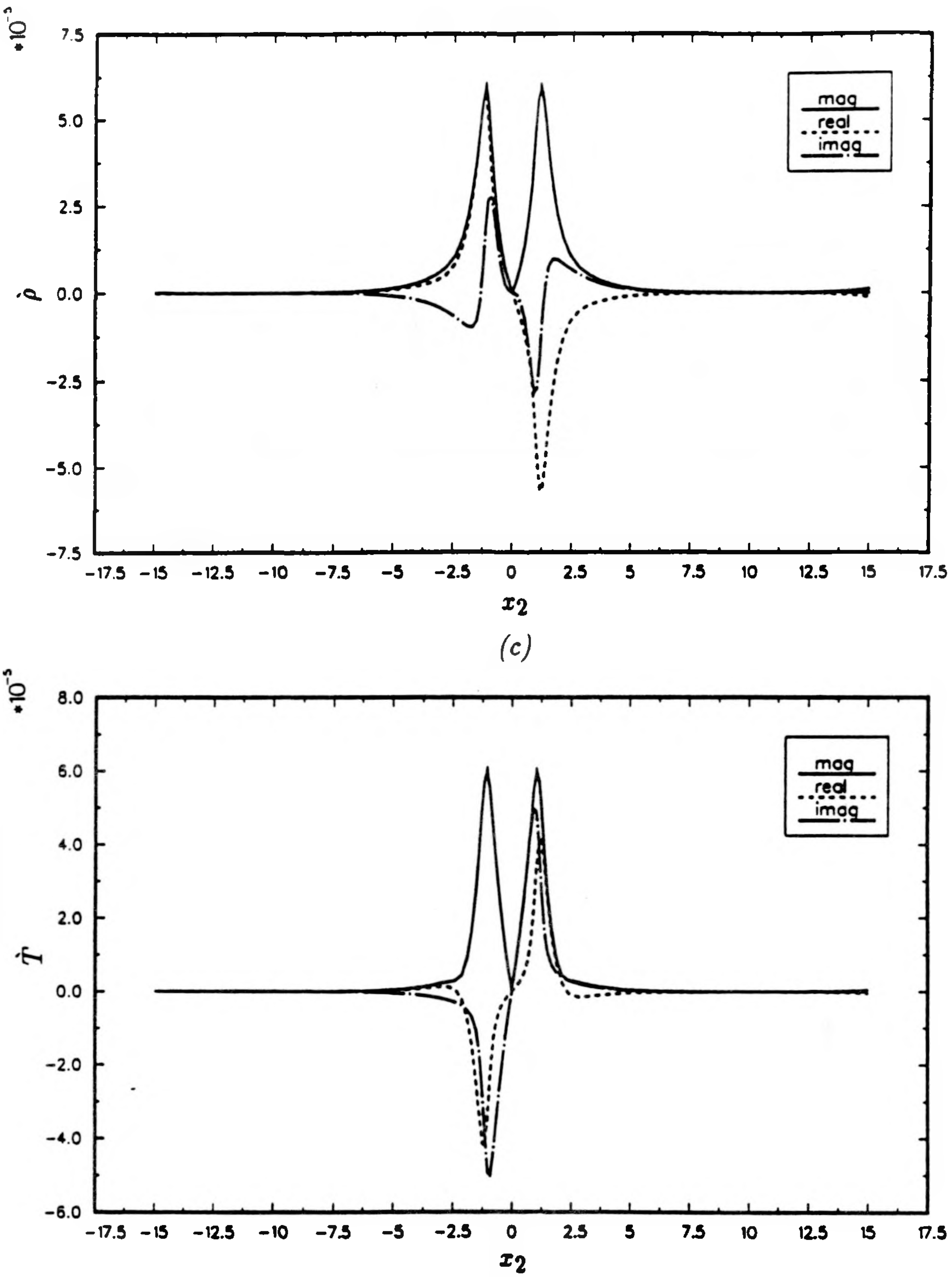

(c)

(d)

FIGURE 2-13. Inviscid linear eigenfunctions corresponding to most unstable antisymmetric mode for $M = 0.01$, $\Delta u_c = 0.692$, *(a)* $\grave{u}_1$, *(b)* $\grave{u}_2$, *(c)* $\grave{\rho}$, and *(d)* $\grave{T}$.

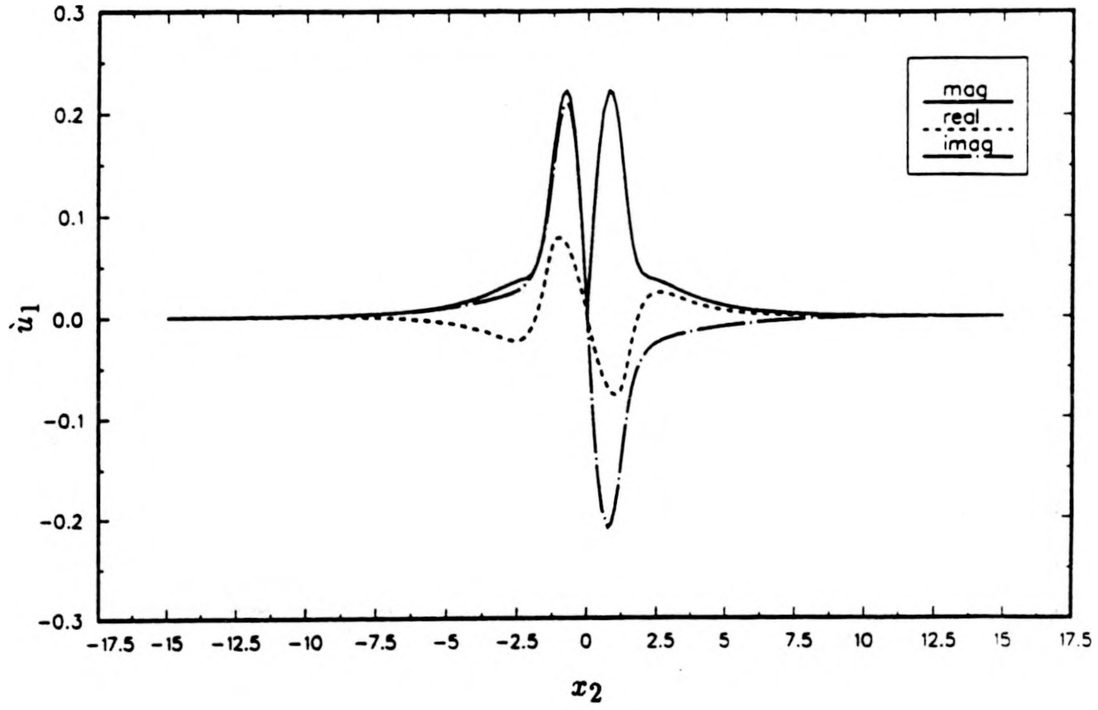
mag
real
imag
0.3
0.2
0.1
0.0
−0.1
−0.2
−0.3
$\grave{u}_1$
−17.5
−15
−12.5
−10
−7.5
−5
−2.5
0
2.5
5
7.5
10
12.5
15
17.5
x_2

(a)

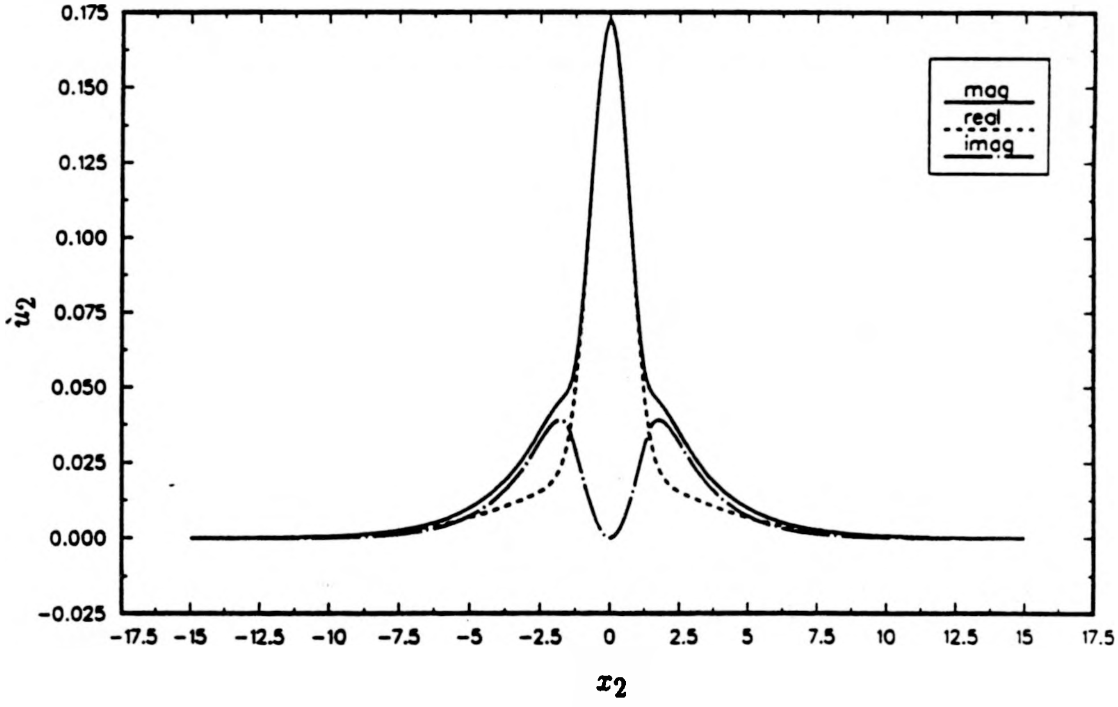
mag
real
imag
0.175
0.150
0.125
0.100
0.075
0.050
0.025
0.000
−0.025
$\grave{u}_2$
−17.5
−15
−12.5
−10
−7.5
−5
−2.5
0
2.5
5
7.5
10
12.5
15
17.5
x_2

(b)

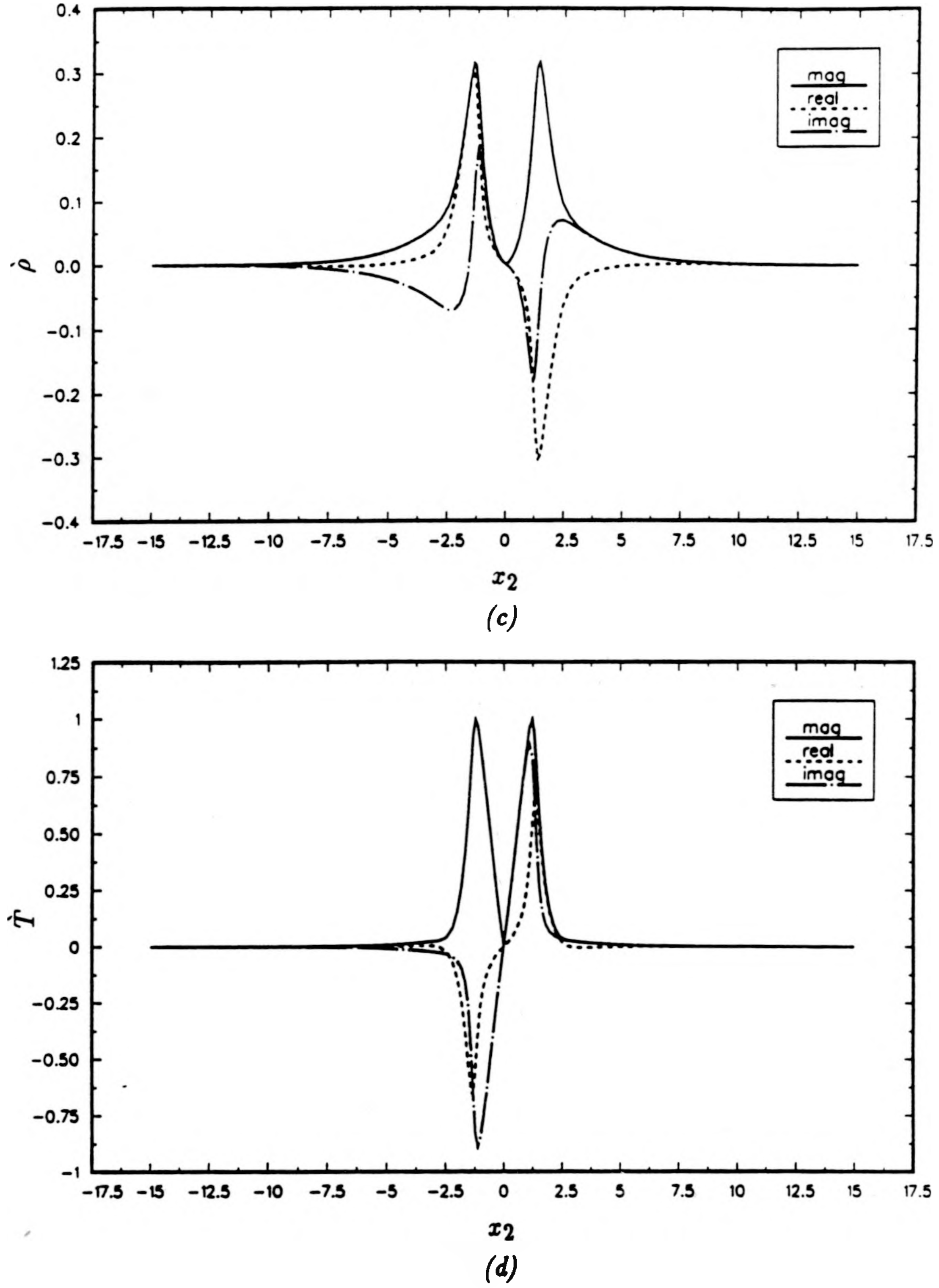

(c)

(d)

FIGURE 2-14. Inviscid linear eigenfunctions corresponding to most unstable antisymmetric mode for $M = 3$, $\Delta u_c = 0.692$, *(a)* $\grave{u}_1$, *(b)* $\grave{u}_2$, *(c)* $\grave{\rho}$, and *(d)* $\grave{T}$.

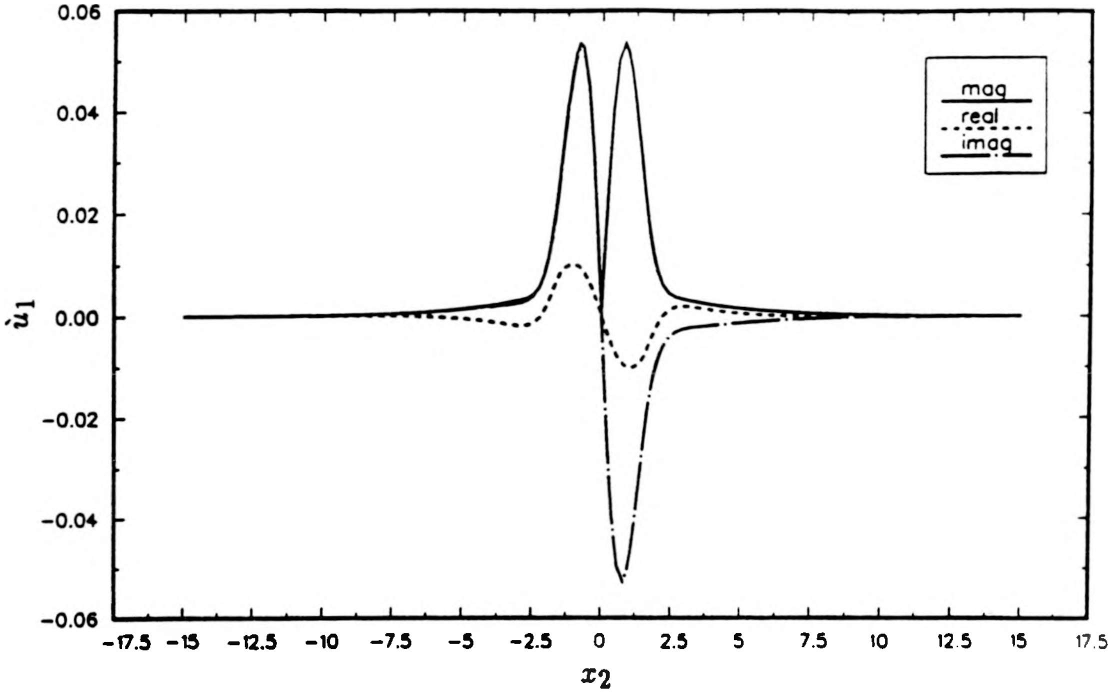

0.06
0.04
0.02
0.00
−0.02
−0.04
−0.06
$\grave{u}_1$
mag
real
imag
−17.5
−15
−12.5
−10
−7.5
−5
−2.5
0
2.5
5
7.5
10
12.5
15
17.5
x_2

(a)

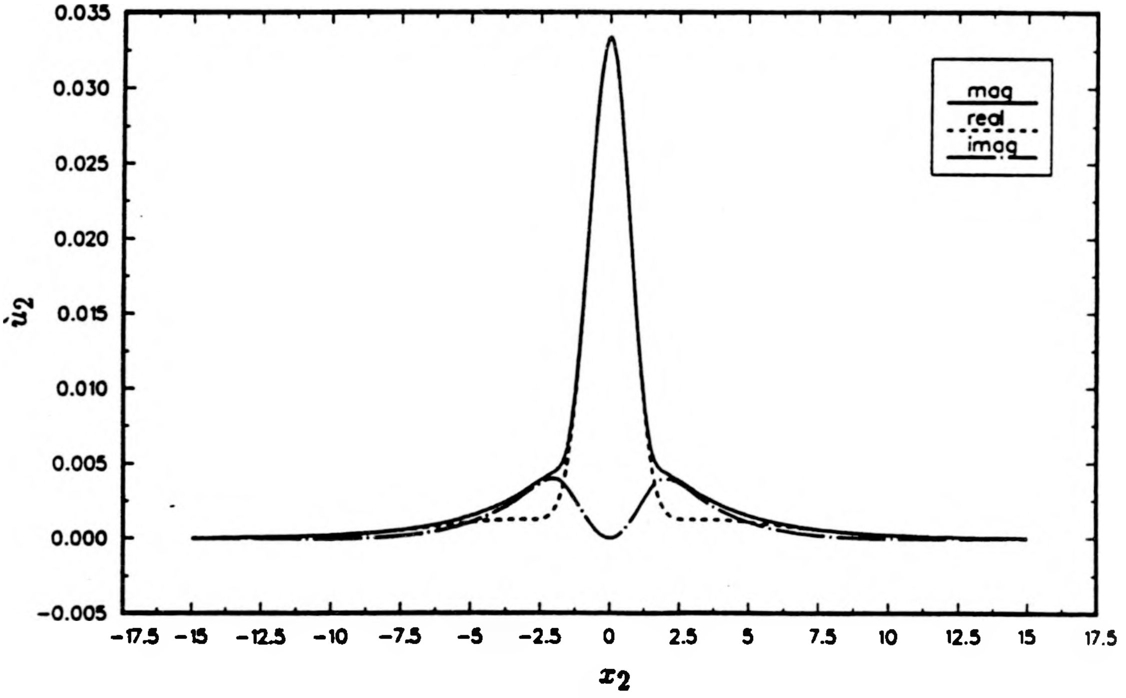

0.035
0.030
0.025
0.020
0.015
0.010
0.005
0.000
−0.005
$\grave{u}_2$
mag
real
imag
−17.5
−15
−12.5
−10
−7.5
−5
−2.5
0
2.5
5
7.5
10
12.5
15
17.5
x_2

(b)

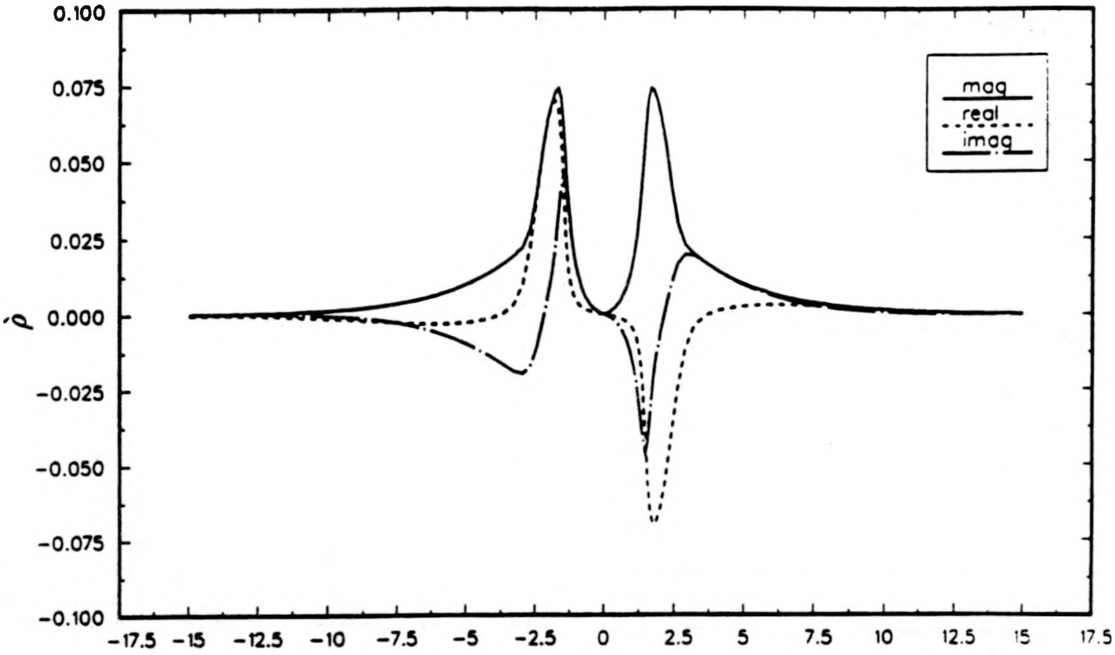

(c)

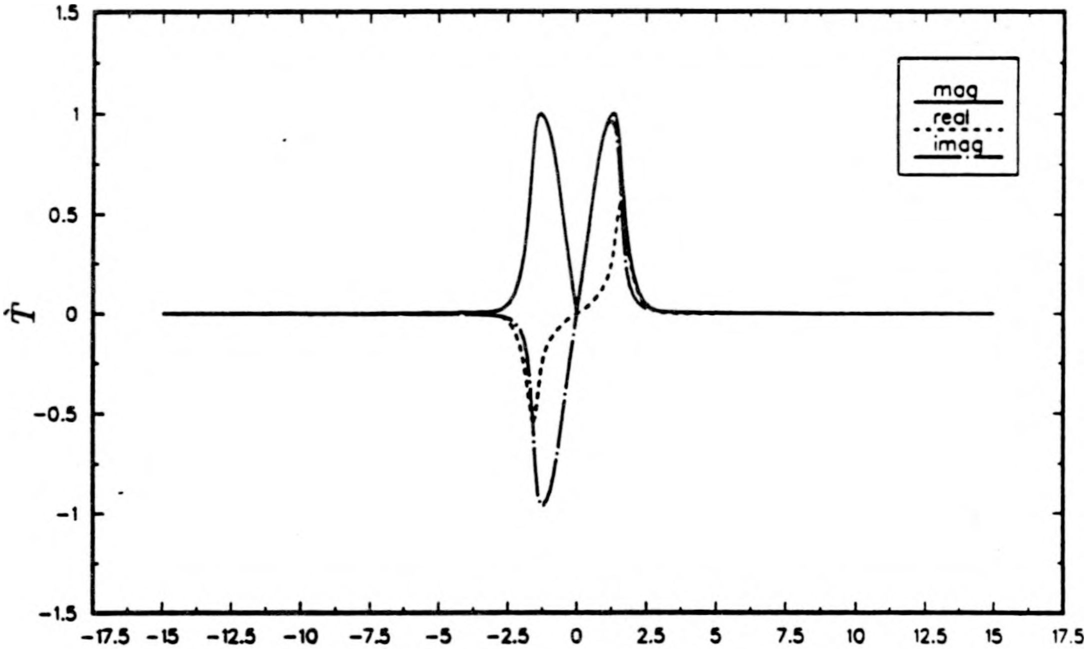

(d)

FIGURE 2-15. Inviscid linear eigenfunctions corresponding to most unstable antisymmetric mode for $M = 7$, $\Delta u_c = 0.692$, *(a)* $\grave{u}_1$, *(b)* $\grave{u}_2$, *(c)* $\grave{\rho}$, and *(d)* $\grave{T}$

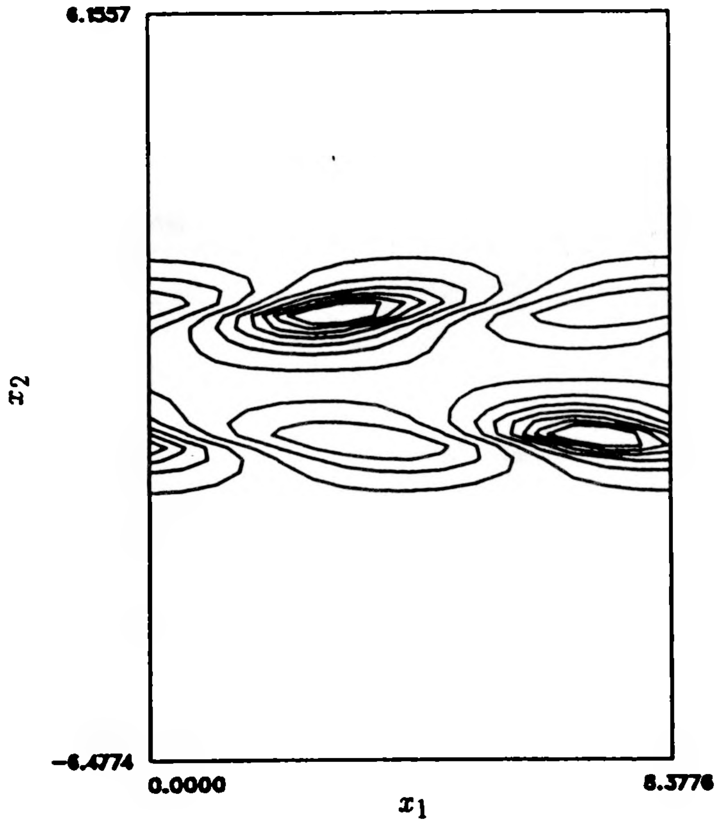

(a)

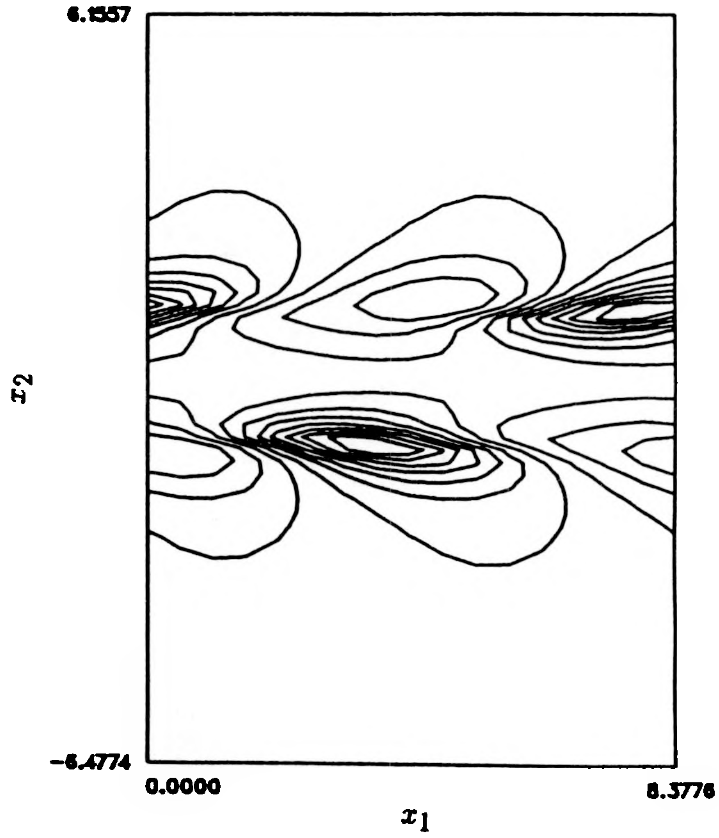

(b)

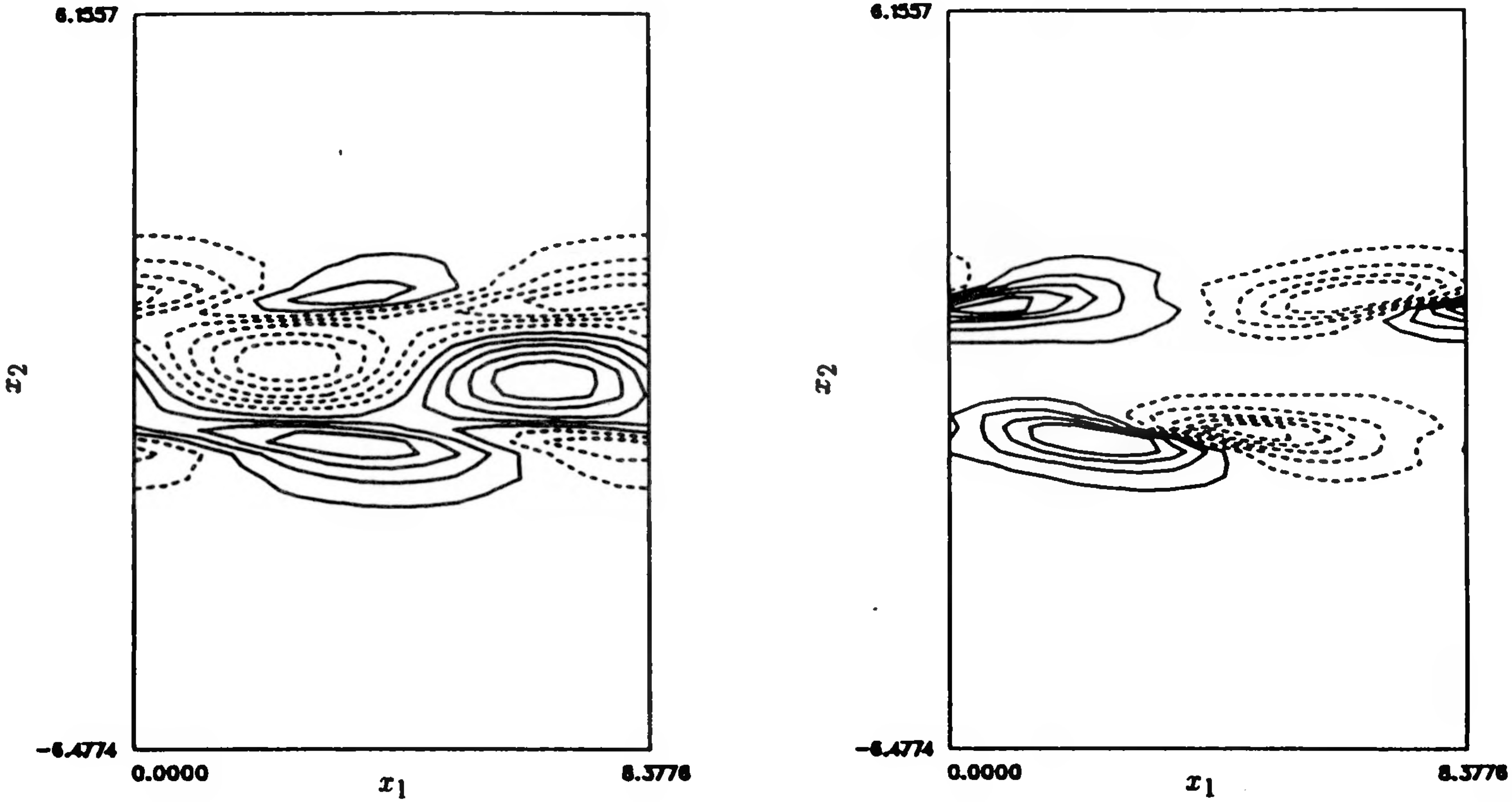

(c)

(d)

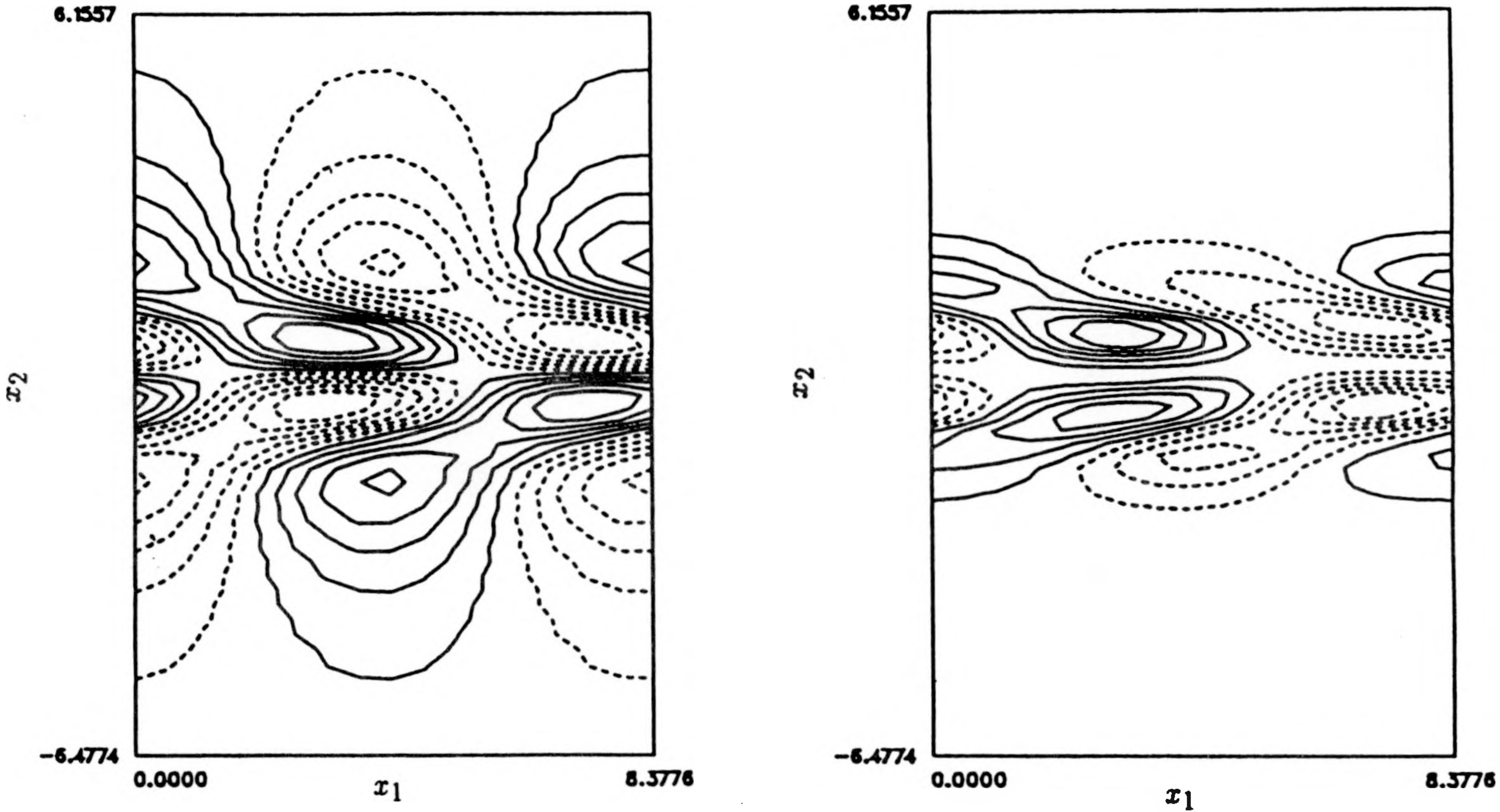

(e) *(f)*

FIGURE 2-16. Compressible vorticity source terms constructed from linear eigenfunctions for $M = 3$, $\Delta u_c = 0.692$, *(a)* pressure, *(b)* density, *(c)* spanwise vorticity, *(d)* baroclinic torque, *(e)* dilatation, and *(f)* negative of product of spanwise vorticity and dilatation

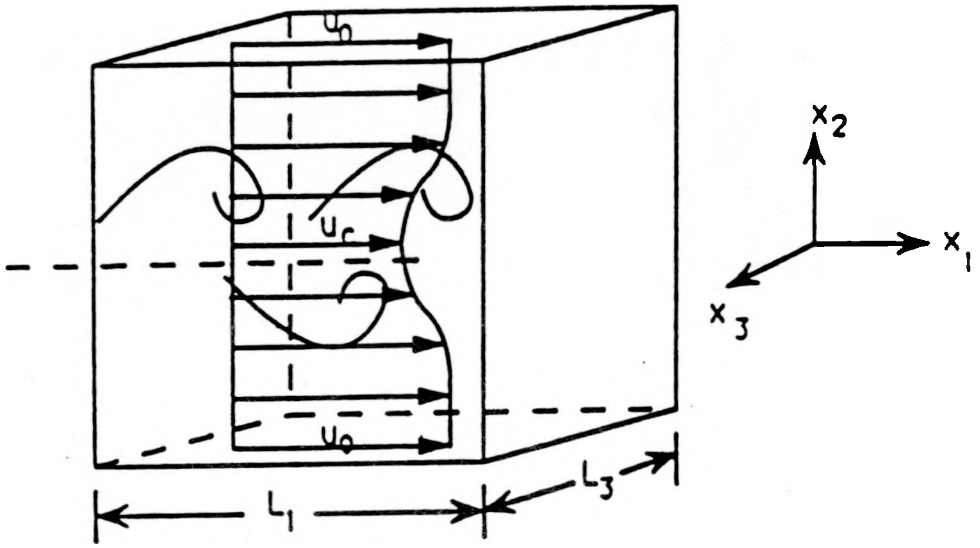

FIGURE 3-1. Computational domain for temporal wake.

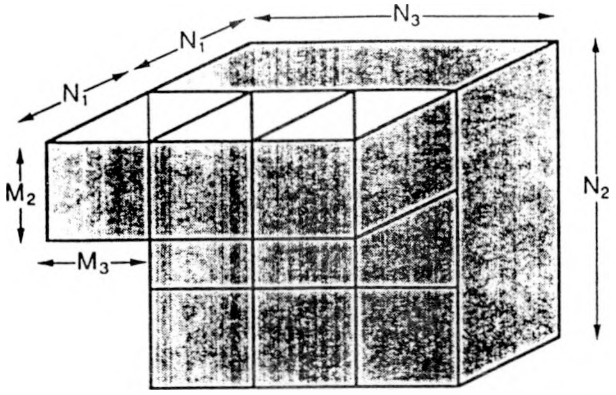

Horizontal Pass (Pass 1, Pass 3)
Fourier Transforms in x1 and x3

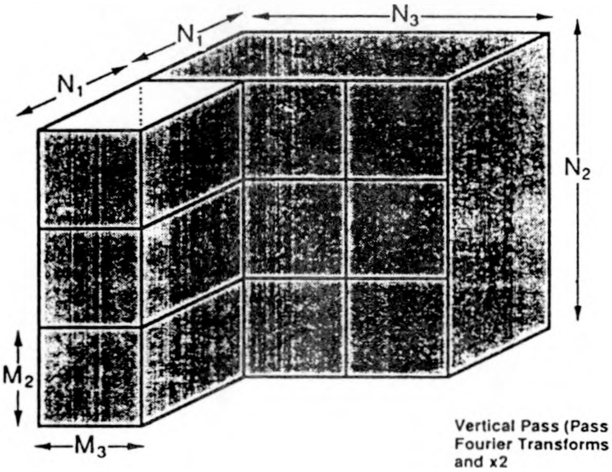

Vertical Pass (Pass 2)
Fourier Transforms in x1
and x2

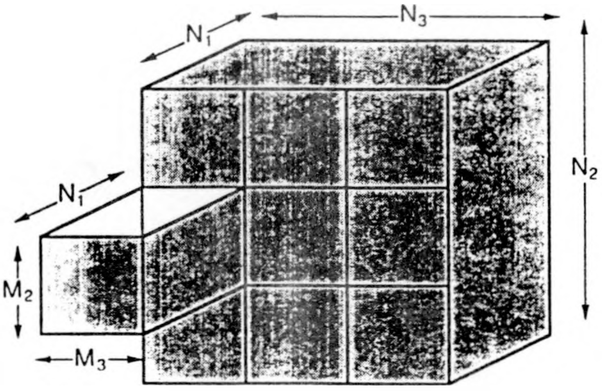

Temporal Pass

FIGURE 3-2. Data management "drawer" concept.

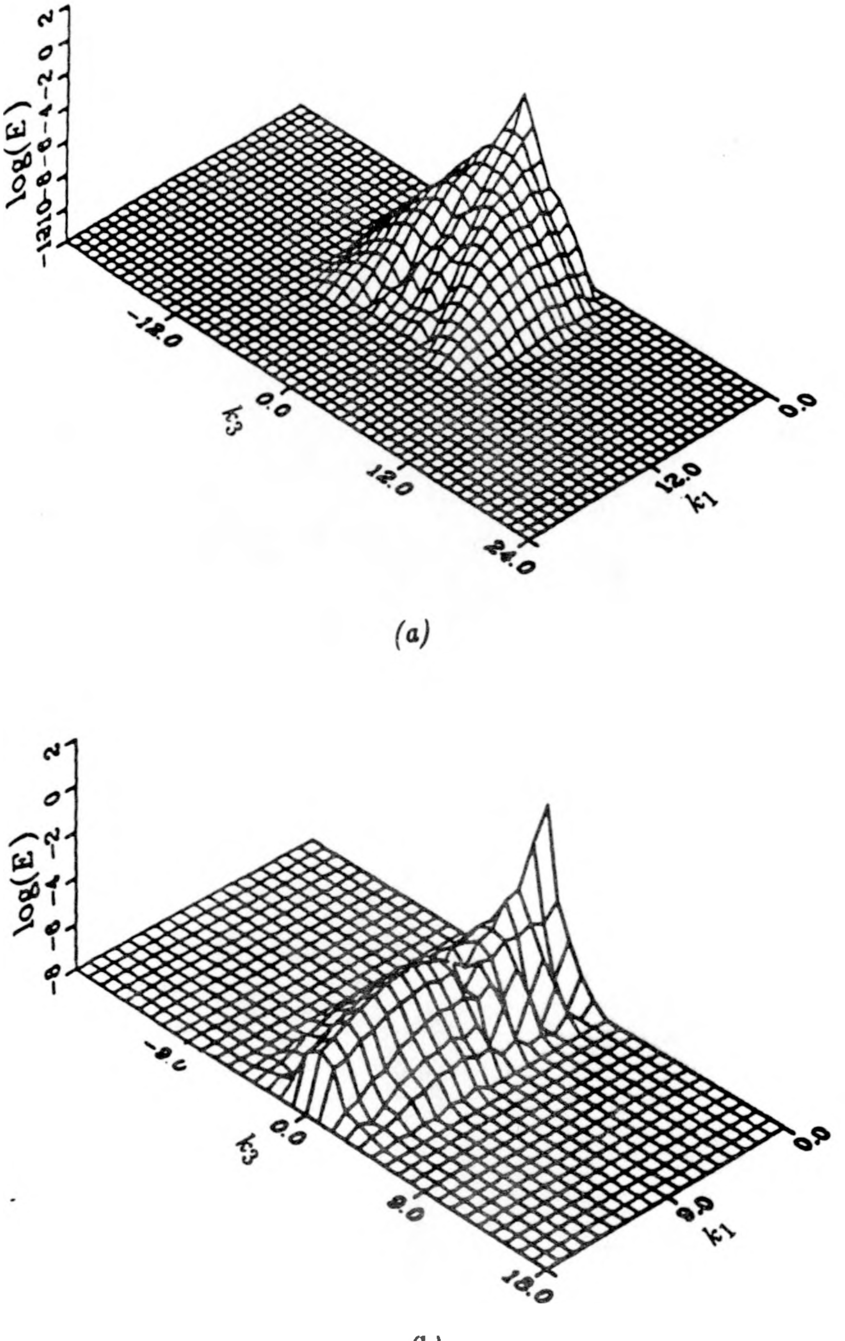

(a)

(b)

FIGURE 3-3. Two-dimensional energy spectra at $x_2 = 2.0$ for $M = 1.0$, $Re = 300$, *(a)* well resolved, and *(b)* poorly resolved with aliasing problems.

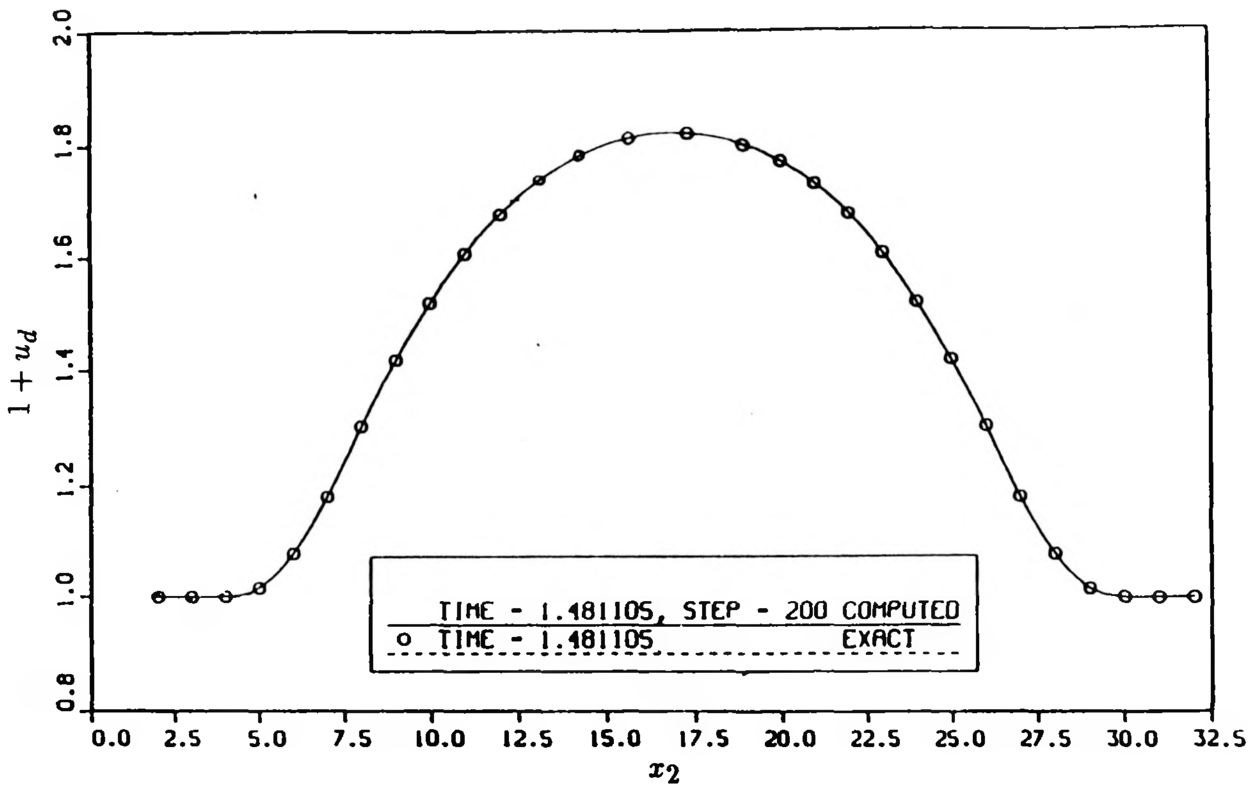

FIGURE 3-4. Comparison of laminar solution for far wake with direct simulation code.

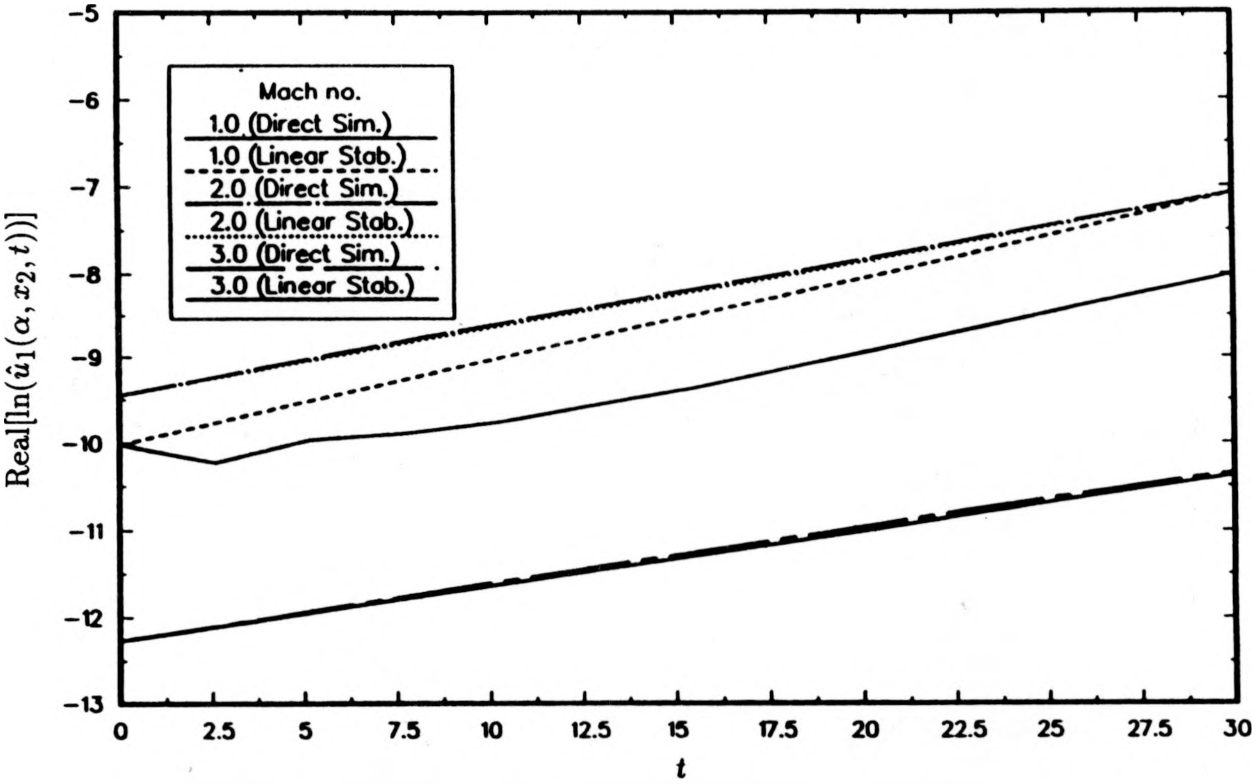

FIGURE 3-5. Comparison of linear growth rates between linear eigenvalue problem and direct simulation.

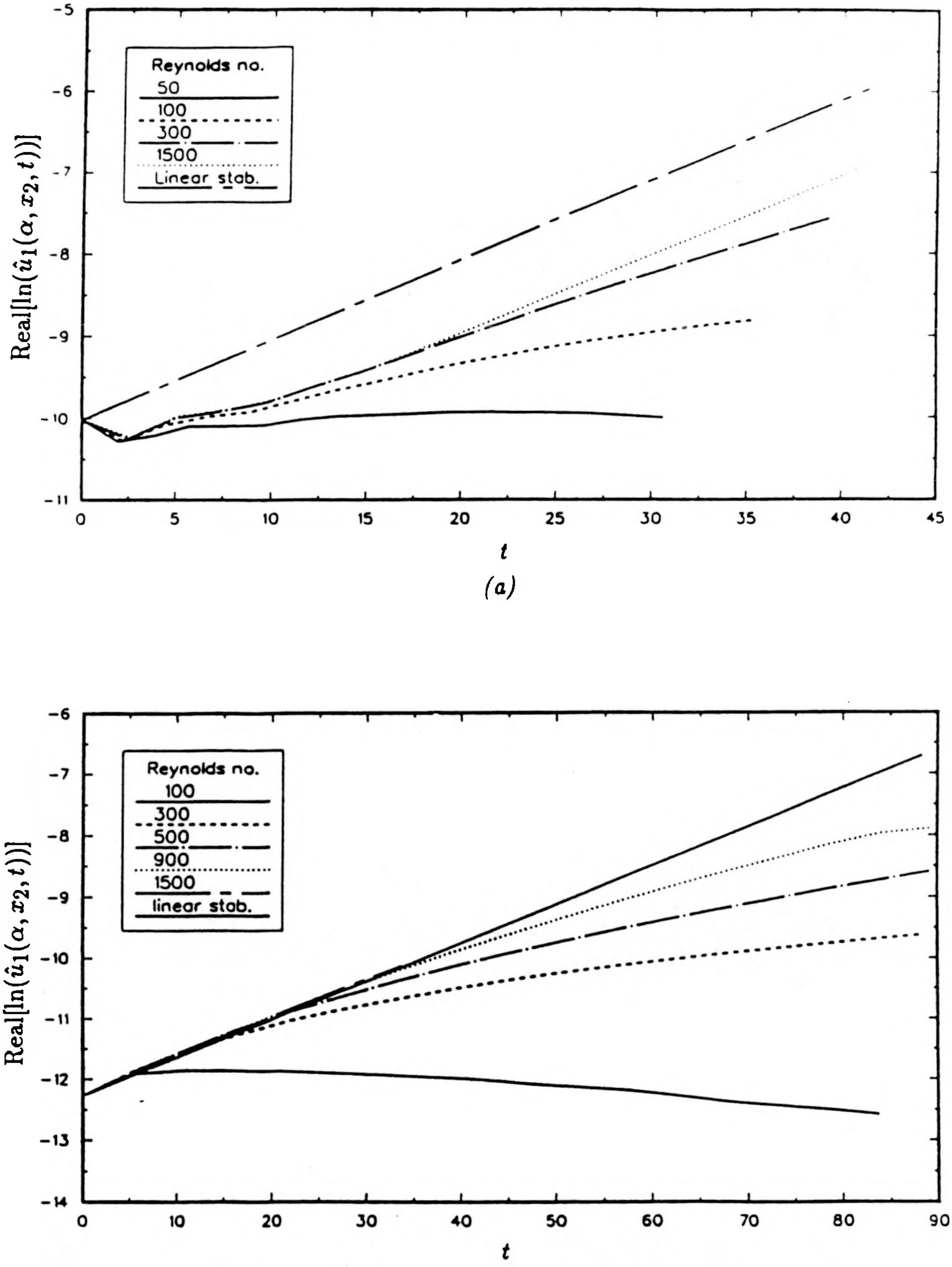

(a)

(b)

FIGURE 3-6. Effect of Reynolds number on linear growth rates *(a)* $M = 1$, and *(b)* $M = 3$.

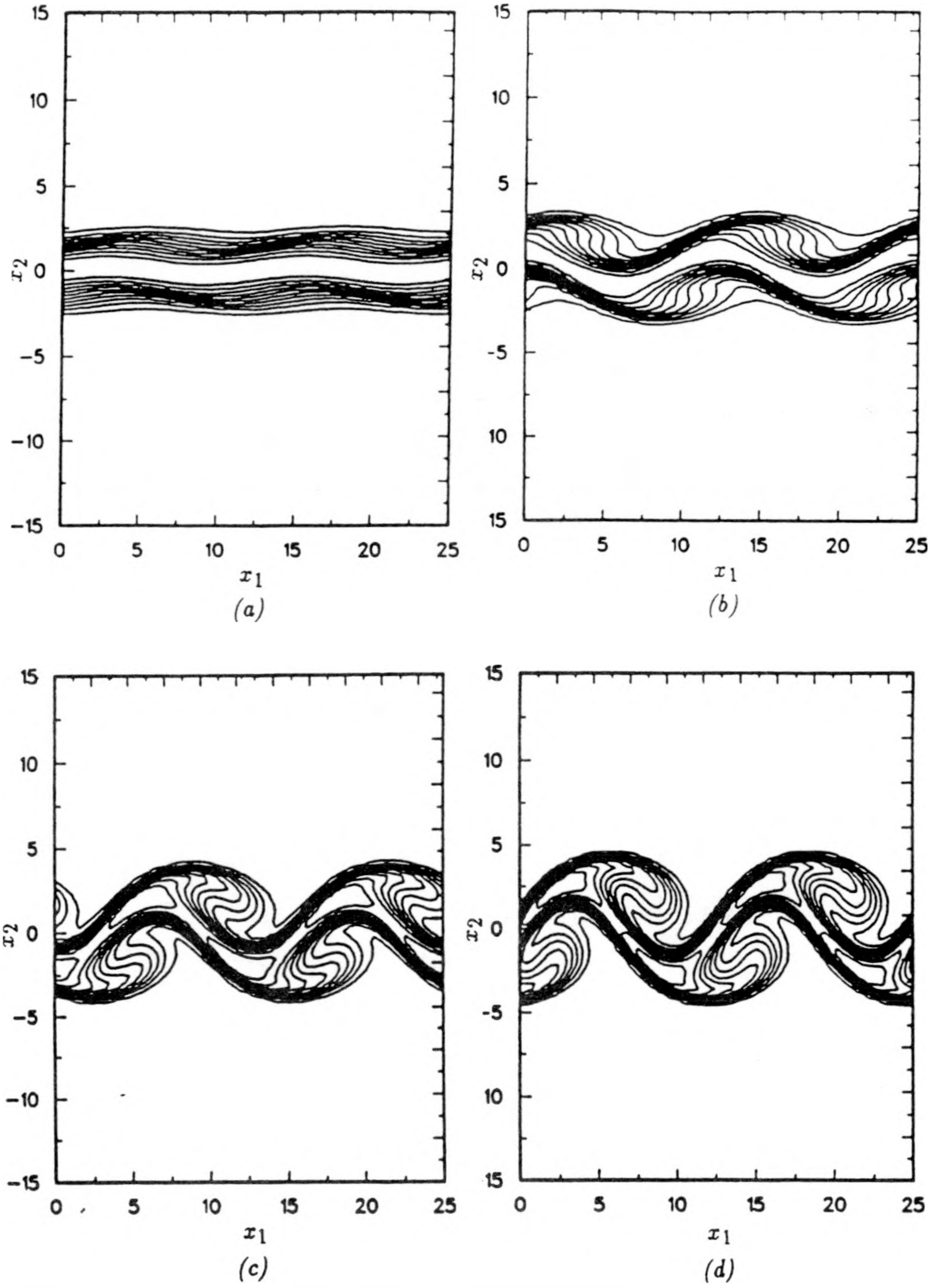

FIGURE 4-1. Contour plots showing the evolution of temperature field for $M = 1$, $\Delta u_c = 0.692$, $Re = 600$ at *(a)* $t = 0.$, *(b)* $t = 20.1$, *(c)* $t = 40.2$, and *(d)* $t = 50.2$.

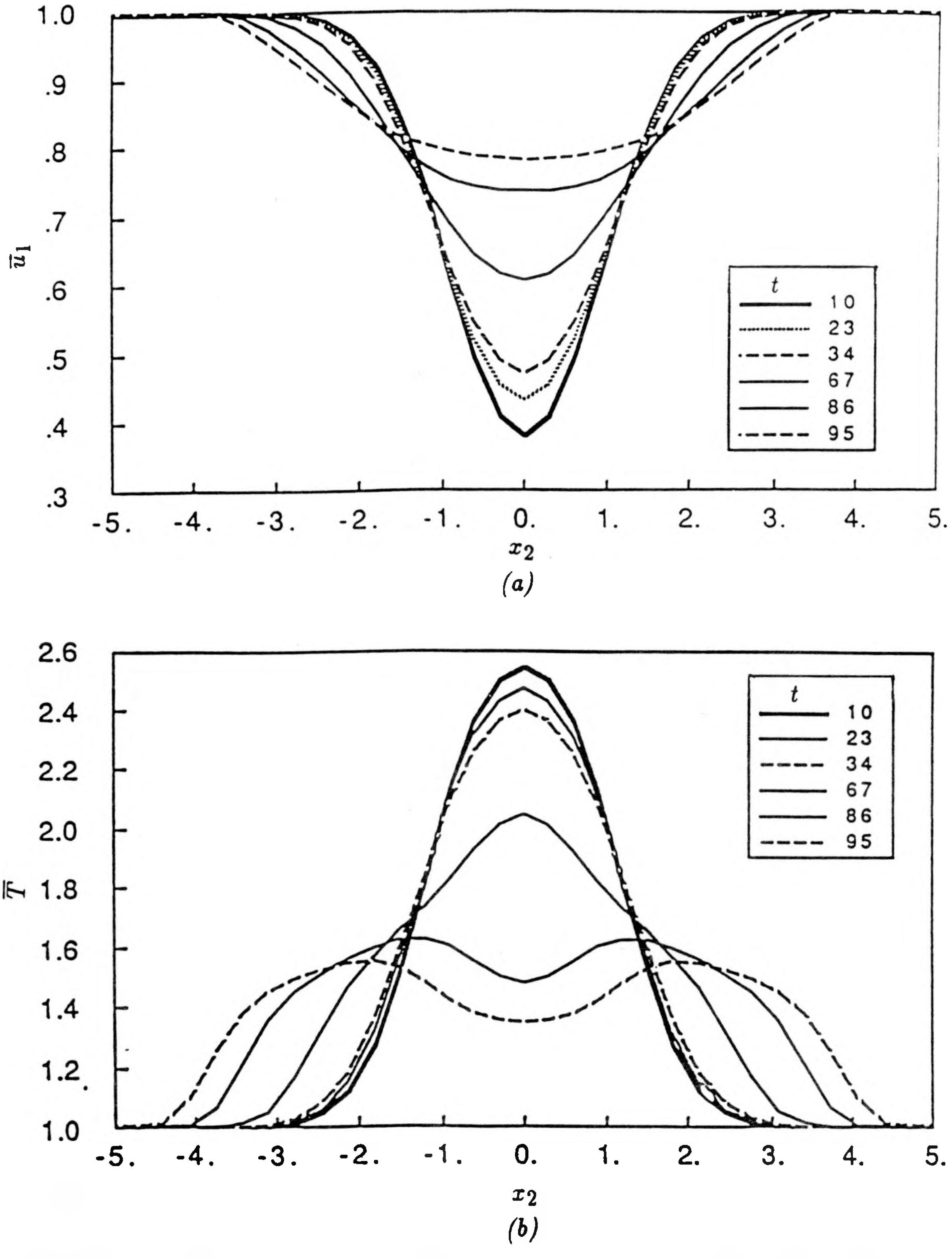

FIGURE 4-2. Evolution of mean profiles for $M = 3$, $Re = 600$, *(a)* $\overline{u}_1$, and *(b)* $\overline{T}$.

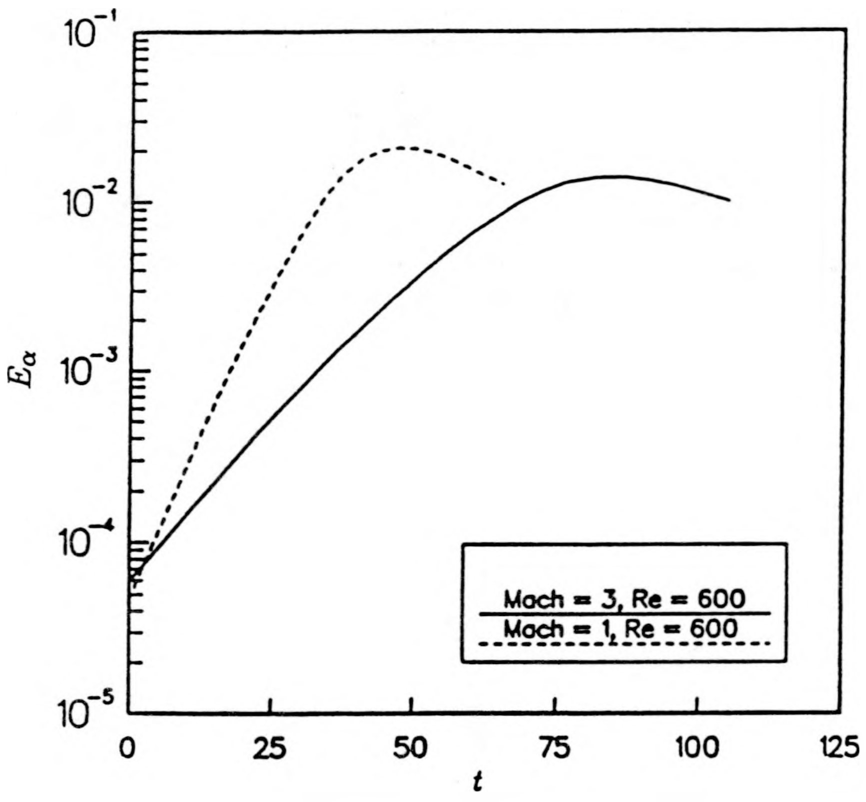

FIGURE 4-3. **Effect of Mach number on the kinetic energy of the fundamental mode.**

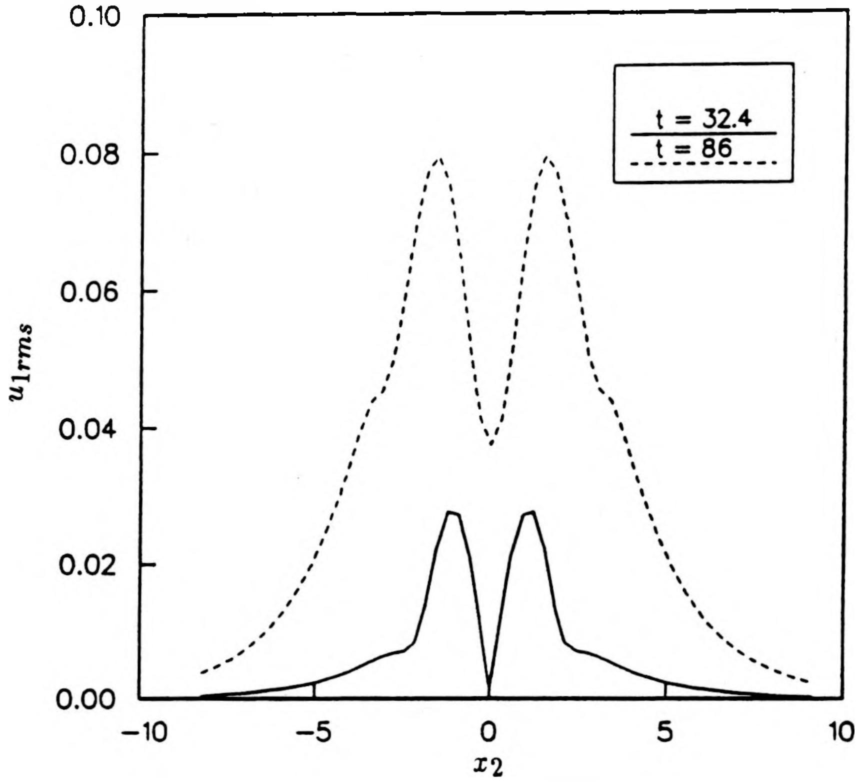

FIGURE 4-4. Intensity of the streamwise velocity fluctuation in linear (t = 32.4) and nonlinear (t = 86.0) regimes for M = 3, Δu_c = 0.692, $Re = 600$.

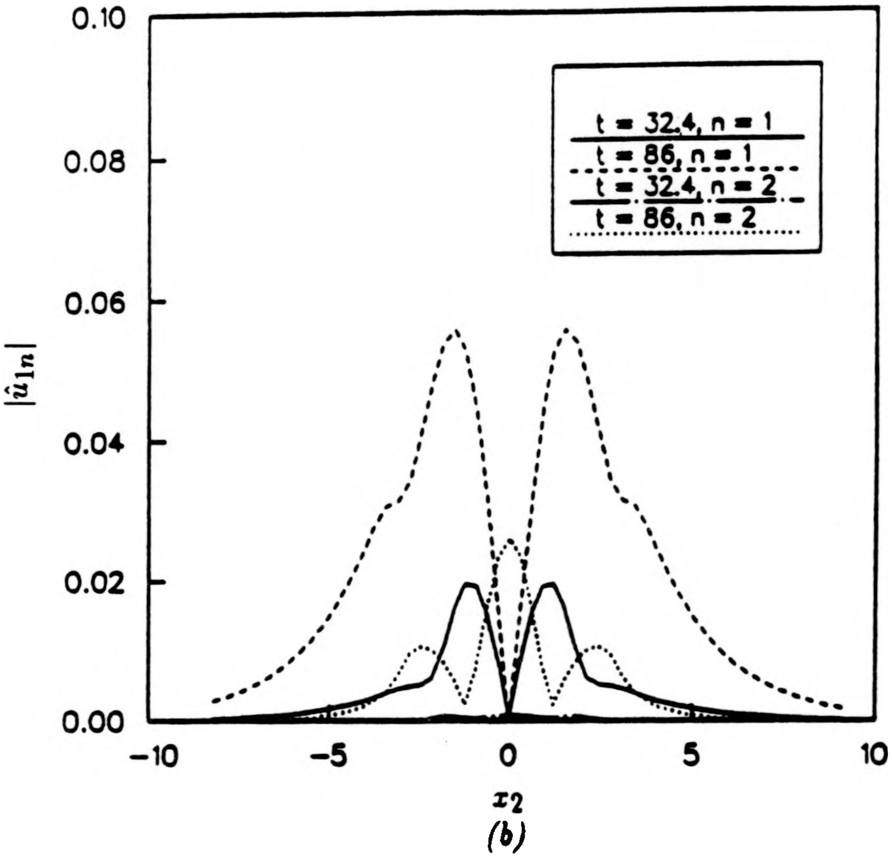

FIGURE 4-5. Distribution of fundamental ($n = 1$) and first harmonic ($n = 2$) modes in linear ($t = 32.4$) and nonlinear ($t = 86.0$) regimes for $M = 3$, $\Delta u_c = 0.692$, $Re = 600$.

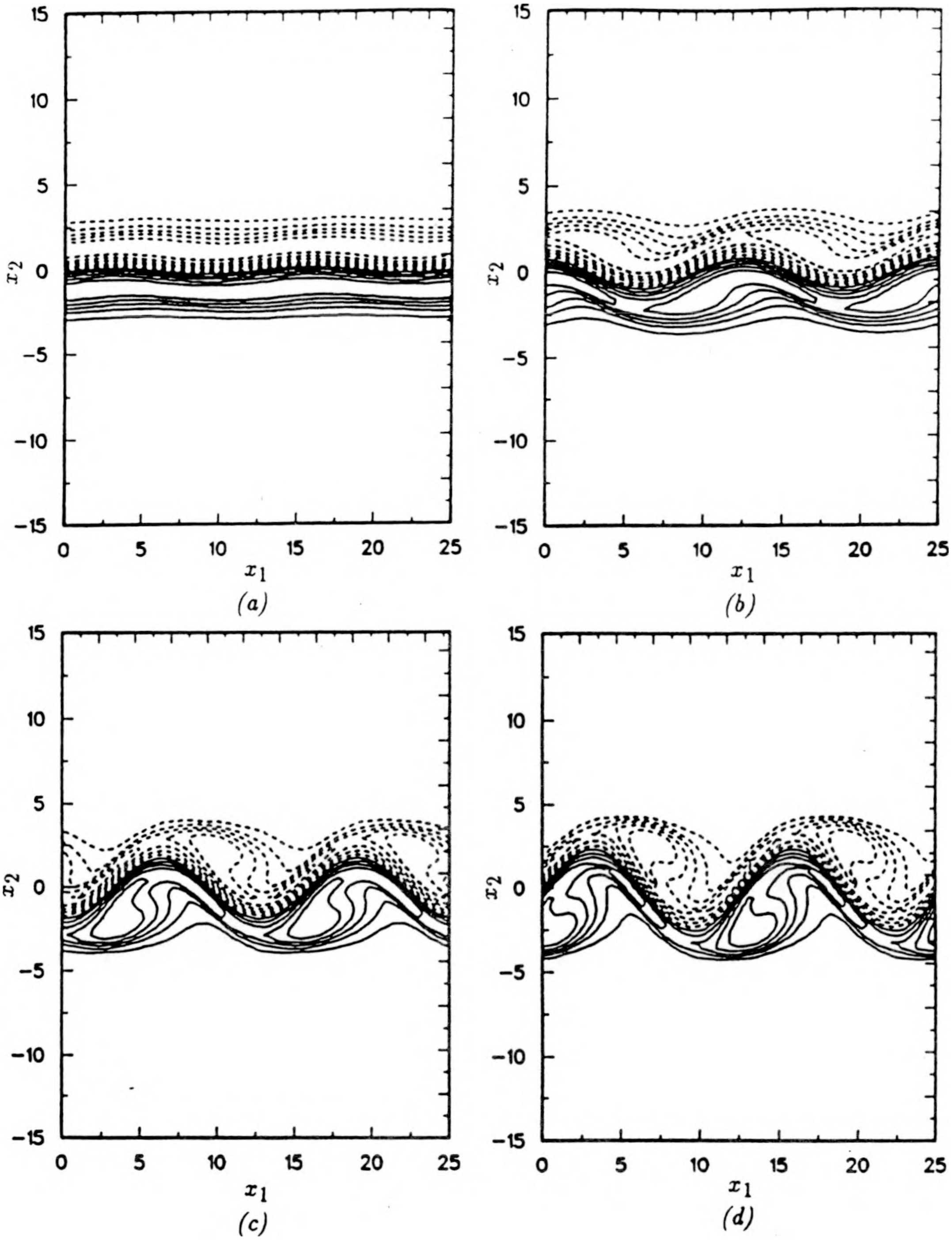

FIGURE 4-6. Contour plots of spanwise vorticity, ω_3, at *(a)* $t = 32$, *(b)* $t = 68$, *(c)* $t = 86$, and *(d)* $t = 96$ for $M = 3$, $\Delta u_c = 0.692$, $Re = 600$.

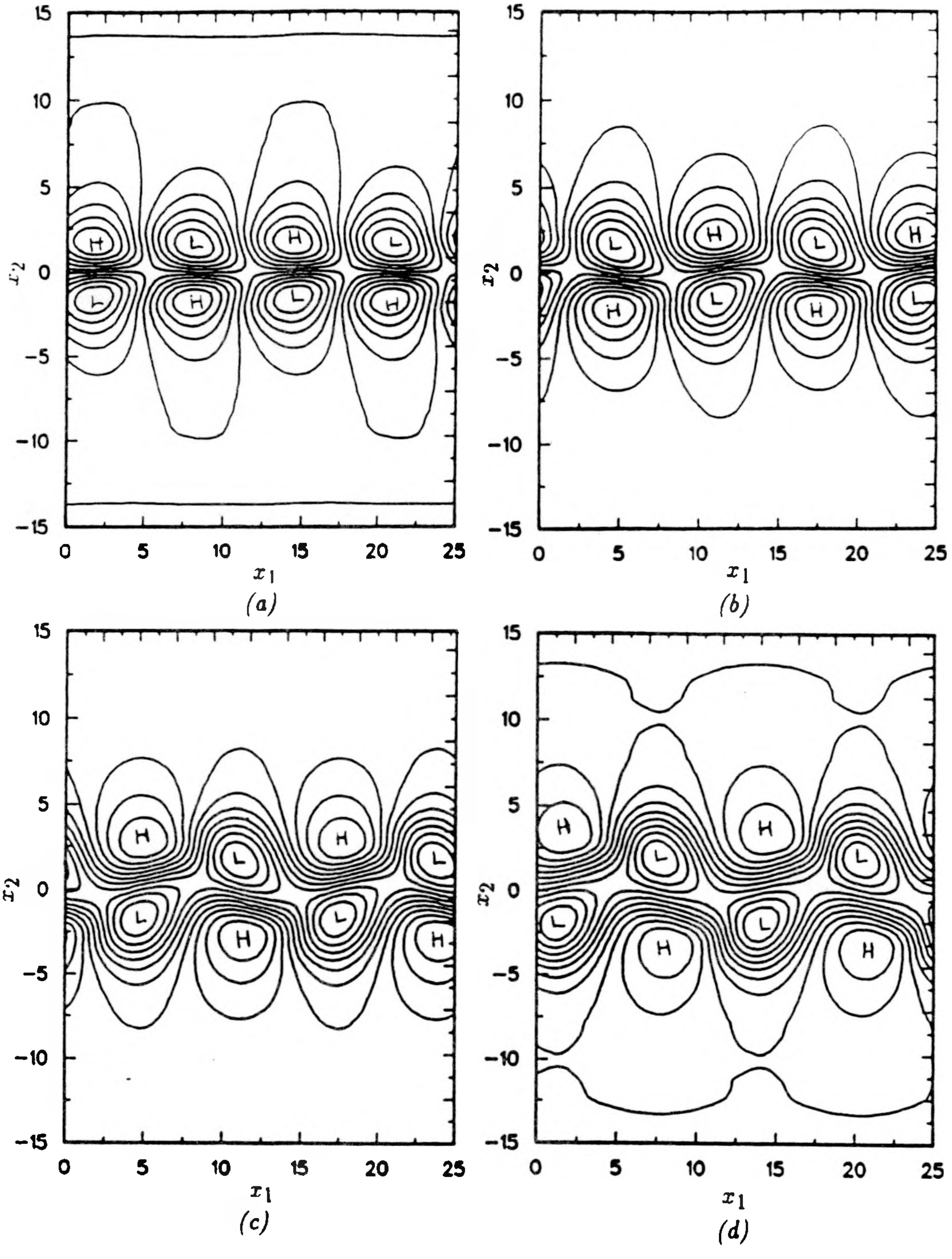

FIGURE 4-7. Contour plots of pressure, p, at *(a)* $t = 32$, *(b)* $t = 68$, *(c)* $t = 86$, and *(d)* $t = 96$ for $M = 3$, $\Delta u_c = 0.692$, $Re = 600$.

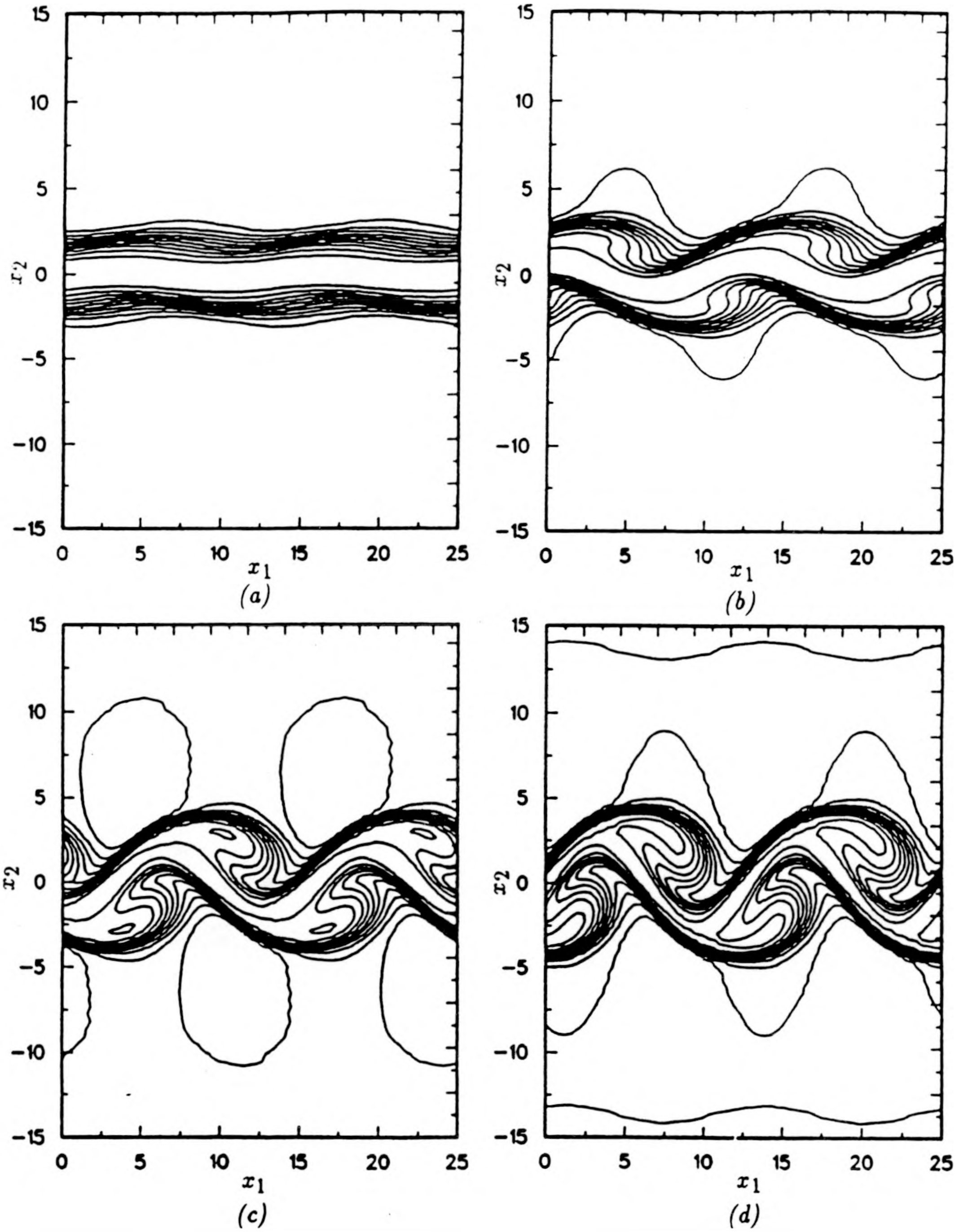

FIGURE 4-8. Contour plots of density, ρ, at *(a)* $t = 32$, *(b)* $t = 68$, *(c)* $t = 86$, and *(d)* $t = 96$ for $M = 3$, $\Delta u_c = 0.692$, $Re = 600$.

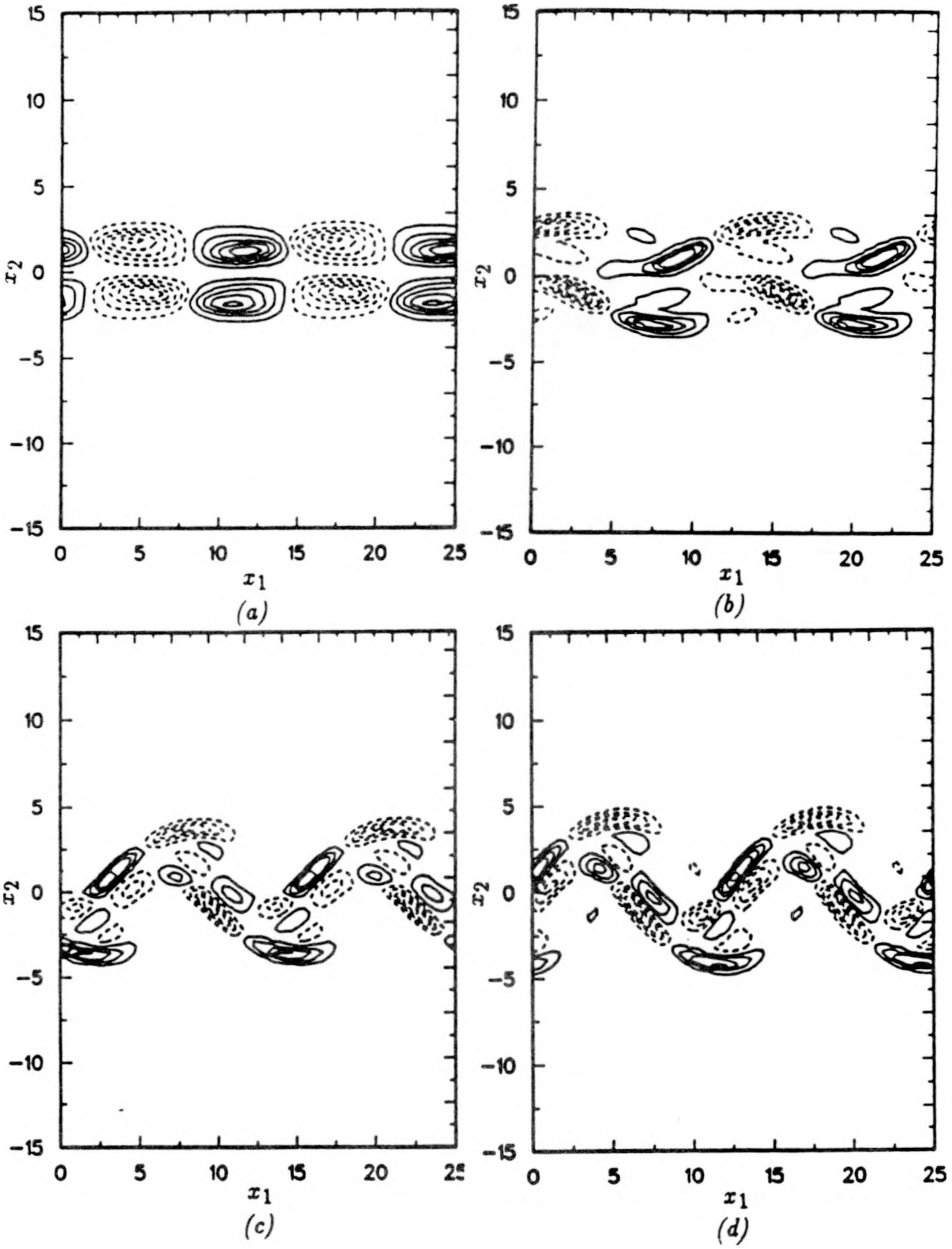

FIGURE 4-9. Contour plots of baroclinic torque at *(a)* $t = 32$, *(b)* $t = 68$, *(c)* $t = 86$, and *(d)* $t = 96$ for $M = 3$, $\Delta u_c = 0.692$, $Re = 600$.

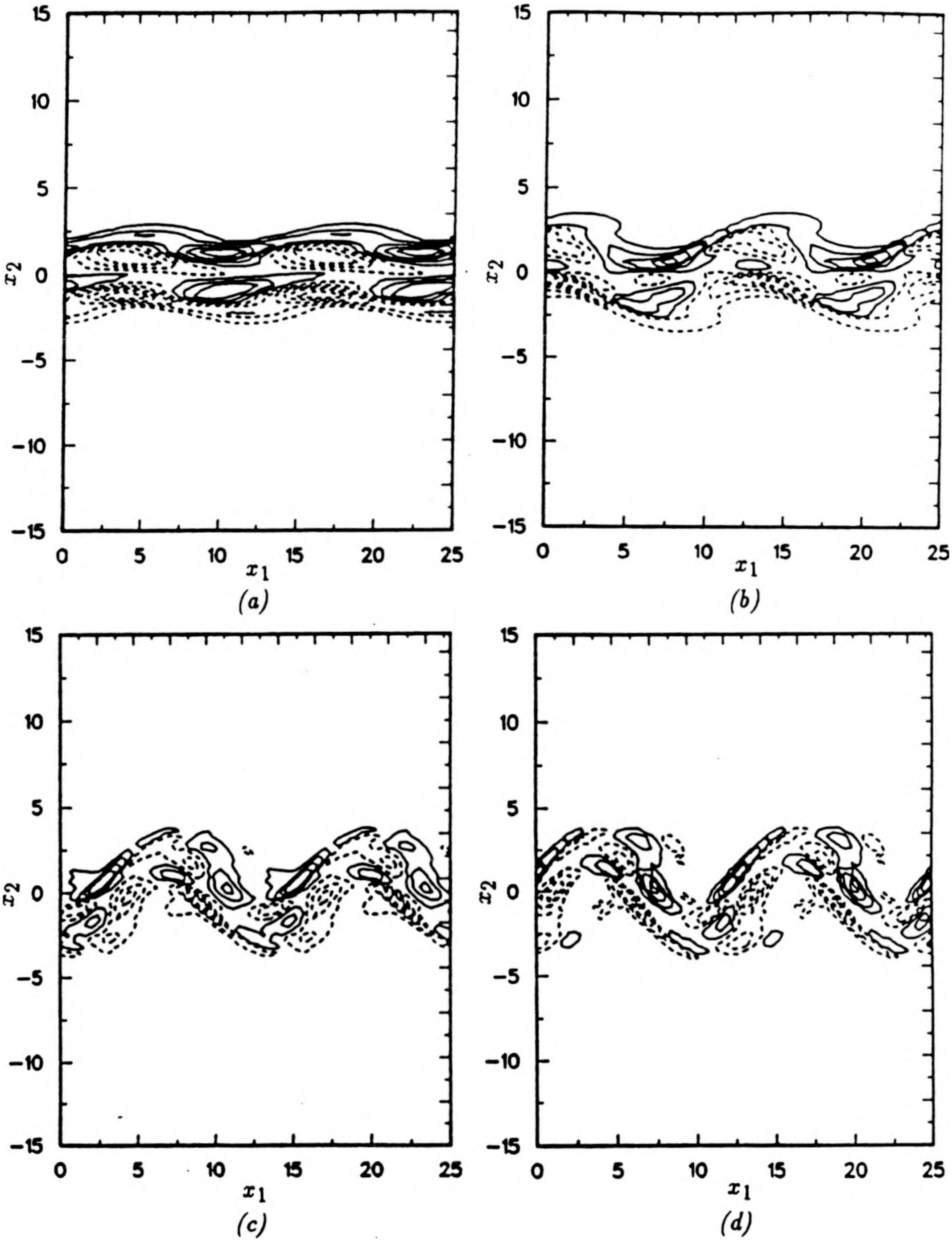

FIGURE 4-10. Contour plots of the negative of the product of the spanwise vorticity and dilatation at *(a)* $t = 32$, *(b)* $t = 68$, *(c)* $t = 86$, and *(d)* $t = 96$ for $M = 3$, $\Delta u_c = 0.692$, $Re = 600$.

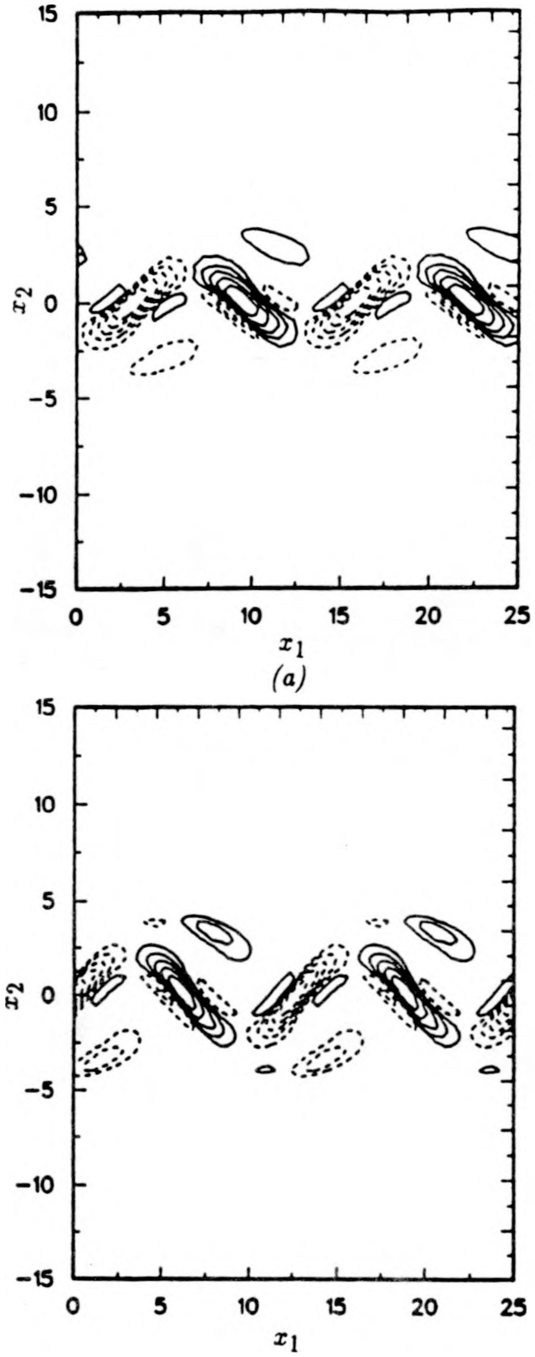

(a)

(b)

FIGURE 4-11. Contour plots of vorticity advection at *(a)* $t = 86$, and *(b)* $t = 96$ for $M = 3$, $\Delta u_c = 0.692$, $Re = 600$.

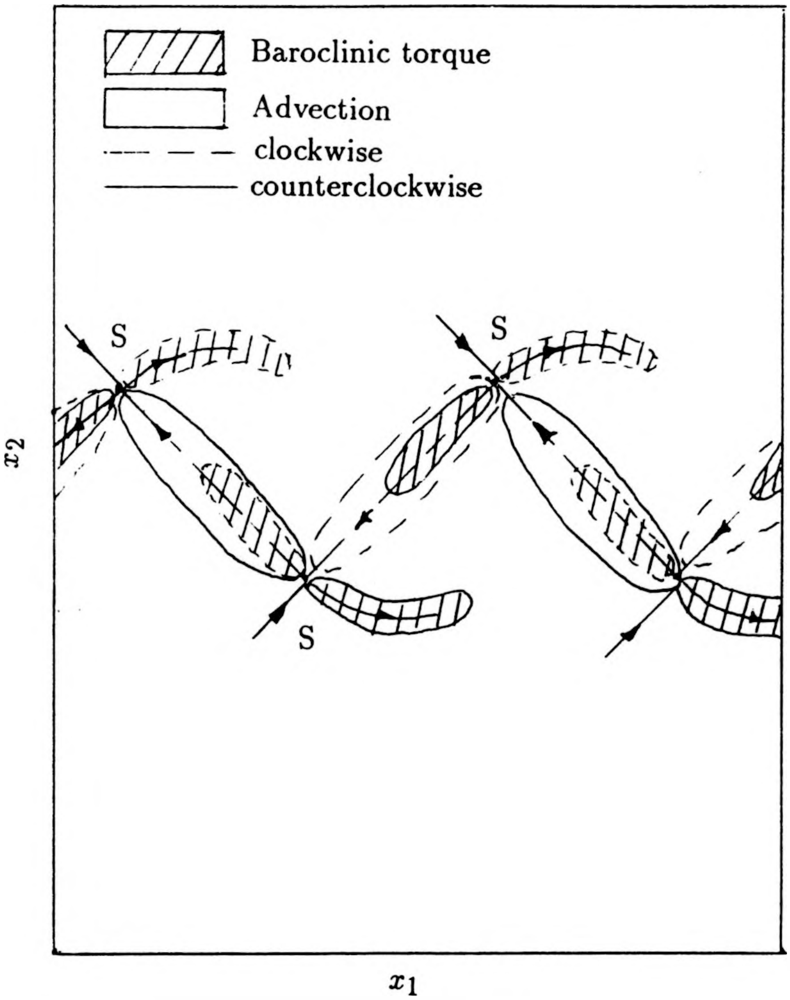

FIGURE 4-12. Superposition of baroclinic torque and advection terms in vorticity equation at $M = 3$, $Re = 600$.

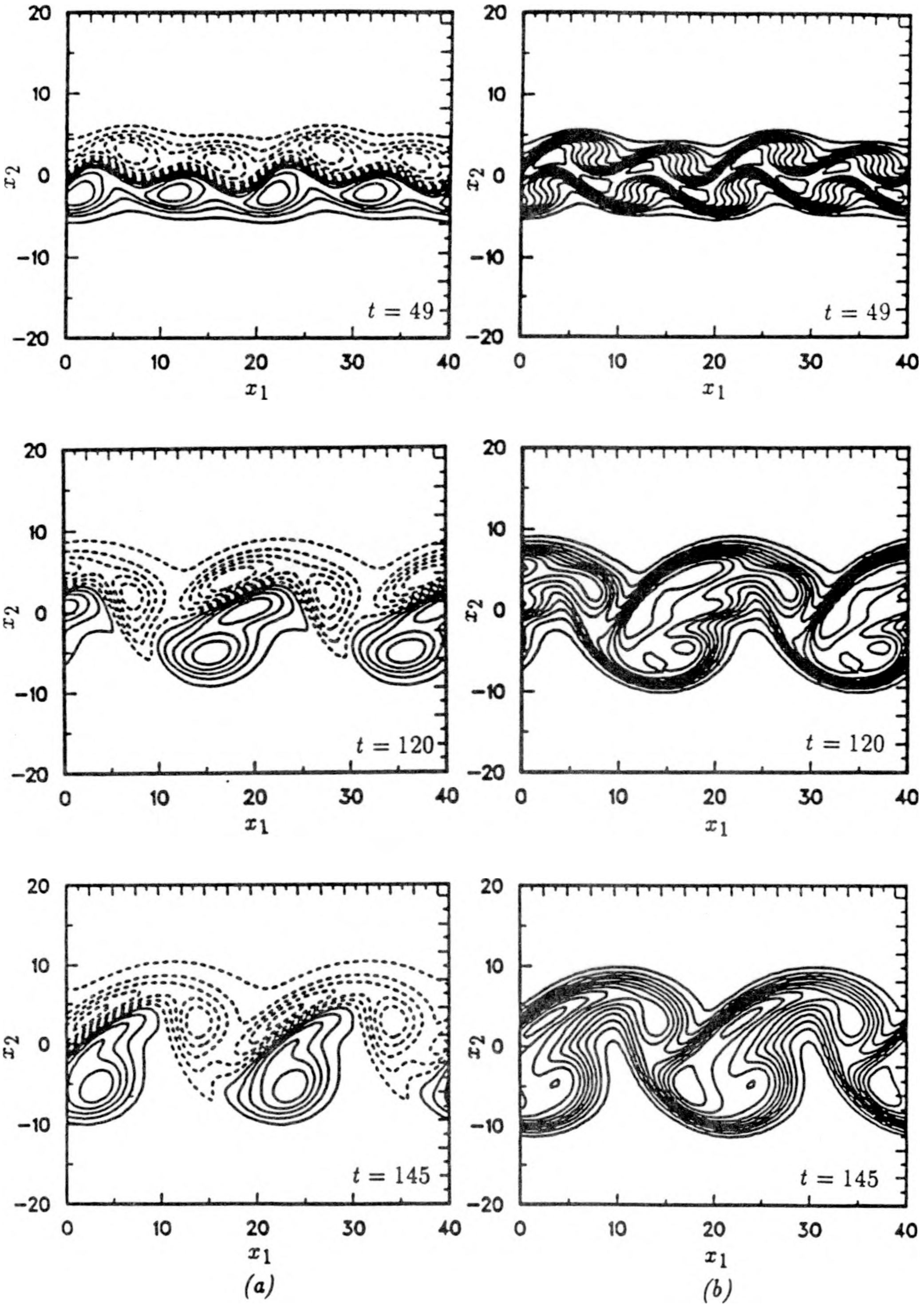

FIGURE 4-13. Phase effects on subharmonic evolution *(a)* ω_3, and *(b)* T for $\phi = 0$, $M = 1$, $\Delta u_c = 0.692$, $Re = 100$.

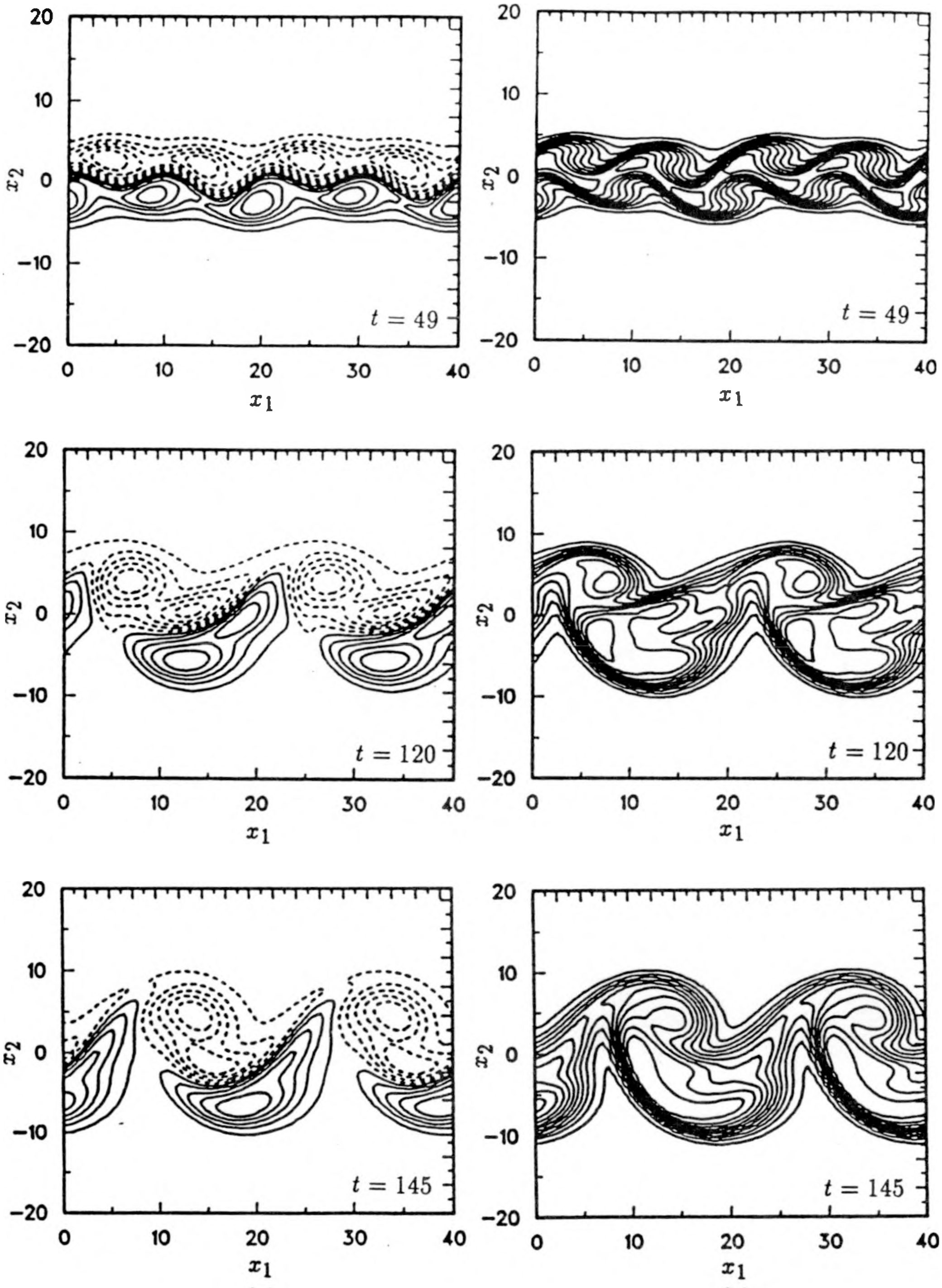

(a) *(b)*

FIGURE 4-14. Phase effects on subharmonic evolution *(a)* ω_3, and *(b)* T for $\phi = \pi/4$, $M = 1$, $\Delta u_c = 0.692$, $Re = 100$.

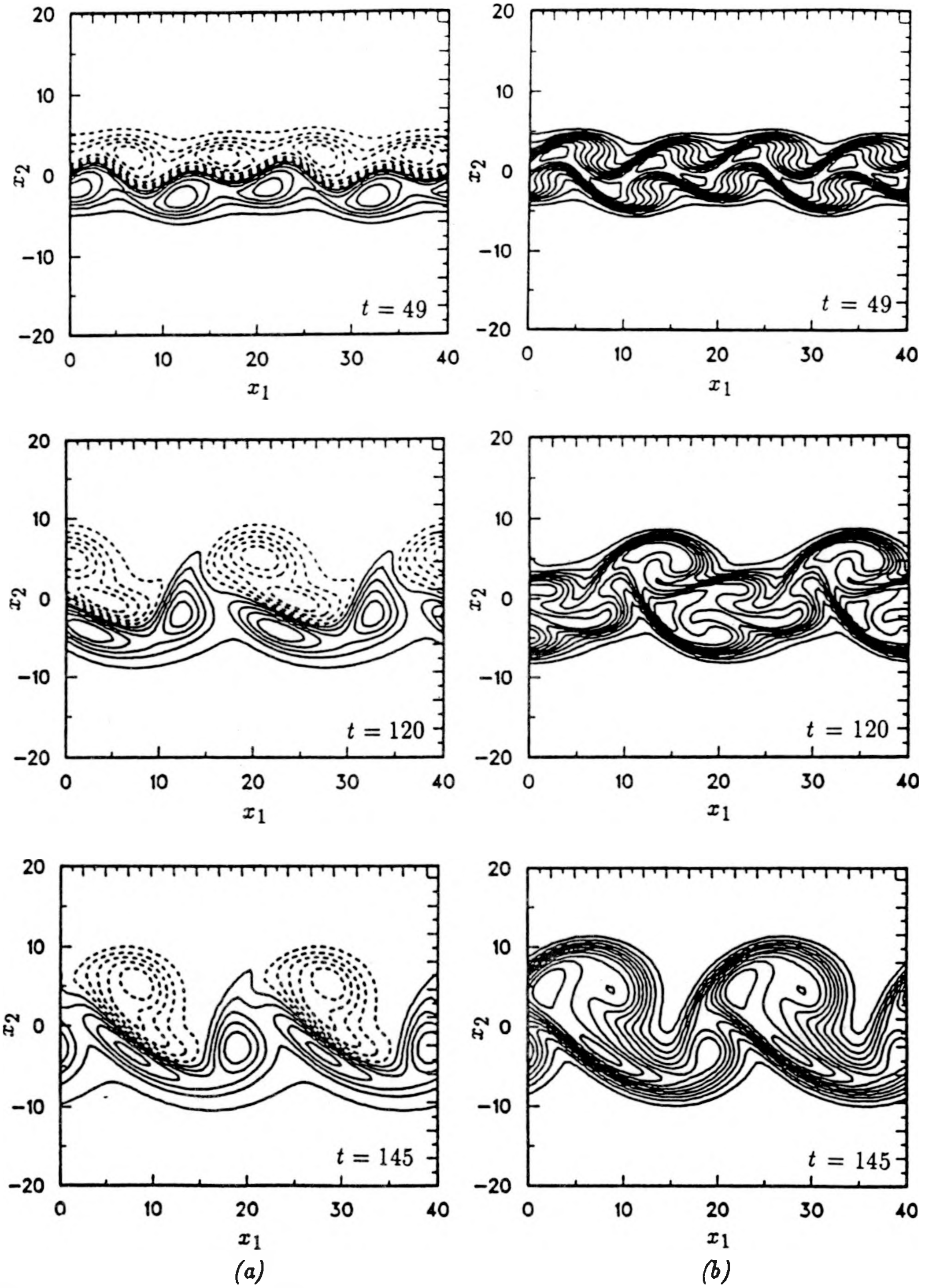

FIGURE 4-15. Phase effects on subharmonic evolution *(a)* ω_3, and *(b)* T for $\phi = \pi/2$, $M = 1$, $\Delta u_c = 0.692$, $Re = 100$.

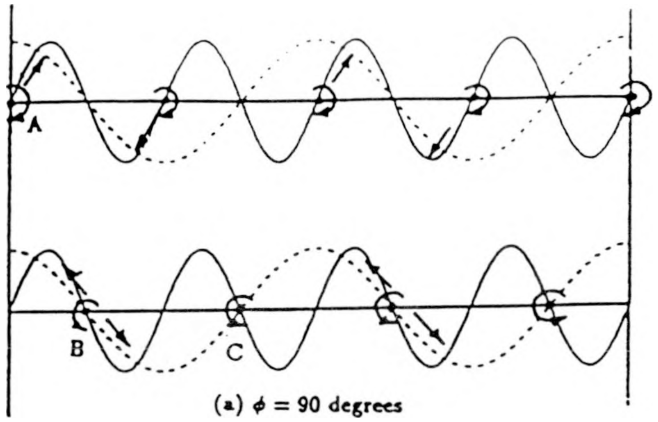

(a) ϕ = 90 degrees

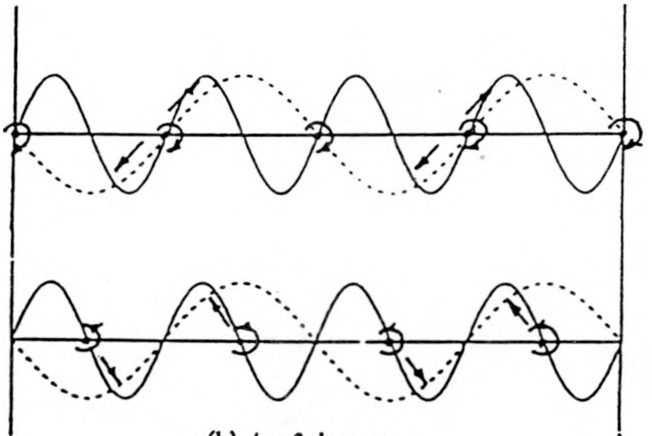

(b) ϕ = 0 degrees

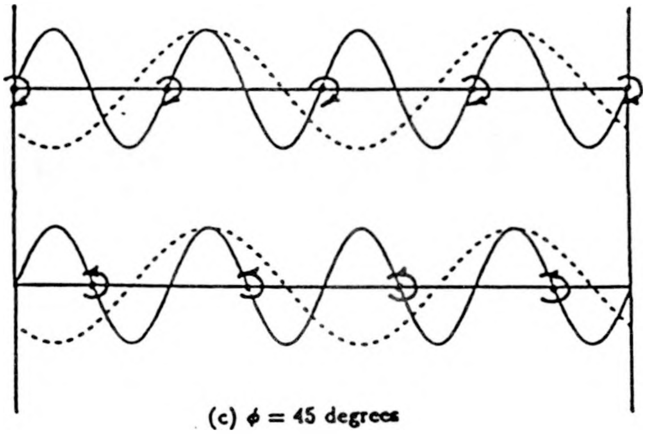

(c) ϕ = 45 degrees

FIGURE 4-16. Wave forms for u_2 corresponding to subharmonic and fundamental modes *(a)* $\phi = \pi/2$, and *(b)* $\phi = 0$, *(c)* $\phi = \pi/4$ for $M = 1$, $\Delta u_c = 0.692$, $Re = 100$.

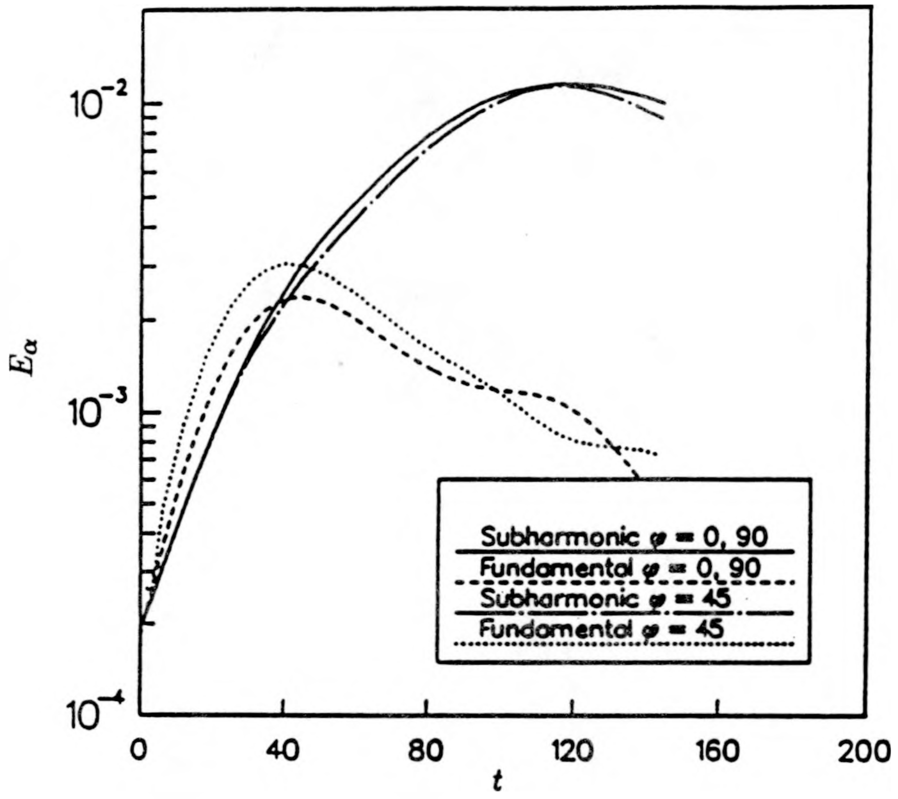

FIGURE 4-17. Streamwise kinetic energy history of subharmonic and fundamental for $M = 1$, $\Delta u_c = 0.692$, $Re = 100$.

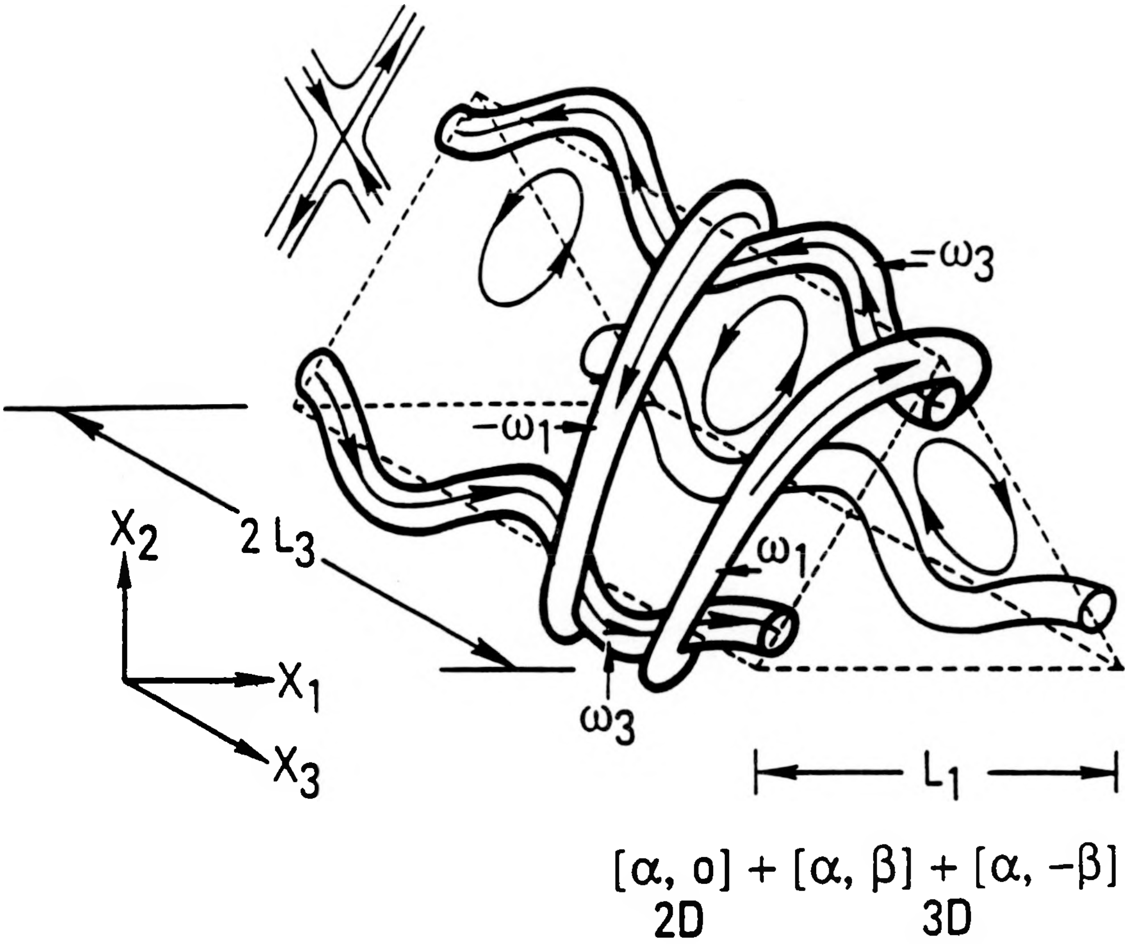

FIGURE 5-1. Cartoon illustrating interaction of streamwise vorticity ω_1 and spanwise vorticity ω_3 to form closed "vortex loops".

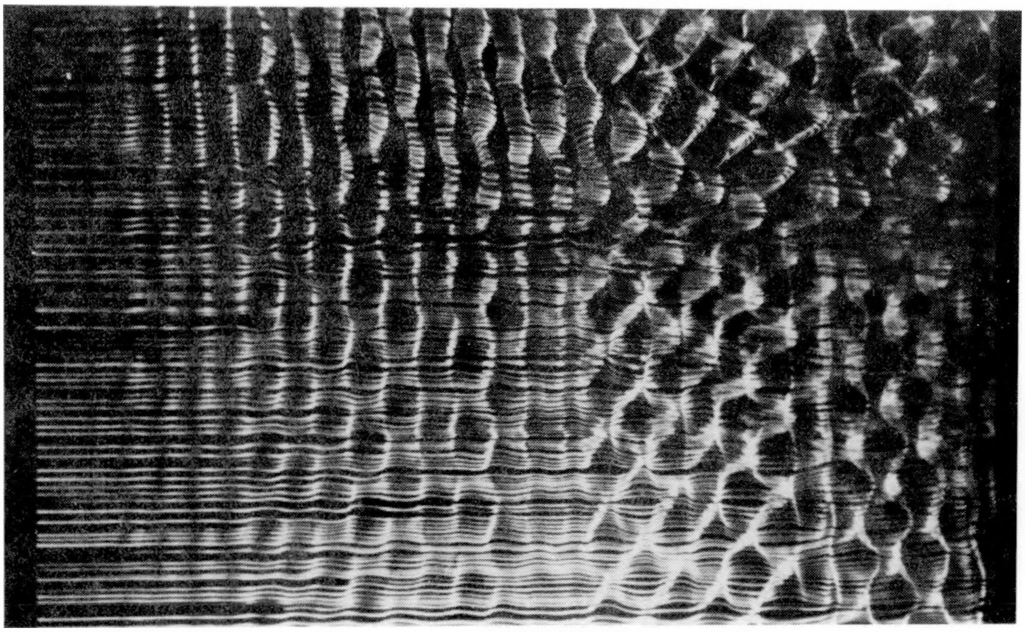

FIGURE 5-2. Plan view of a circular-cylinder wake at $Re = 150$; smoke-wire at $x_1/d = 2$, $x_2/d = 2$, corresponds to Fig. 20 of J. Fluid Mech. 1988, Vol. 190, pp. 291, *reproduced with permission from J. Cimbala.*

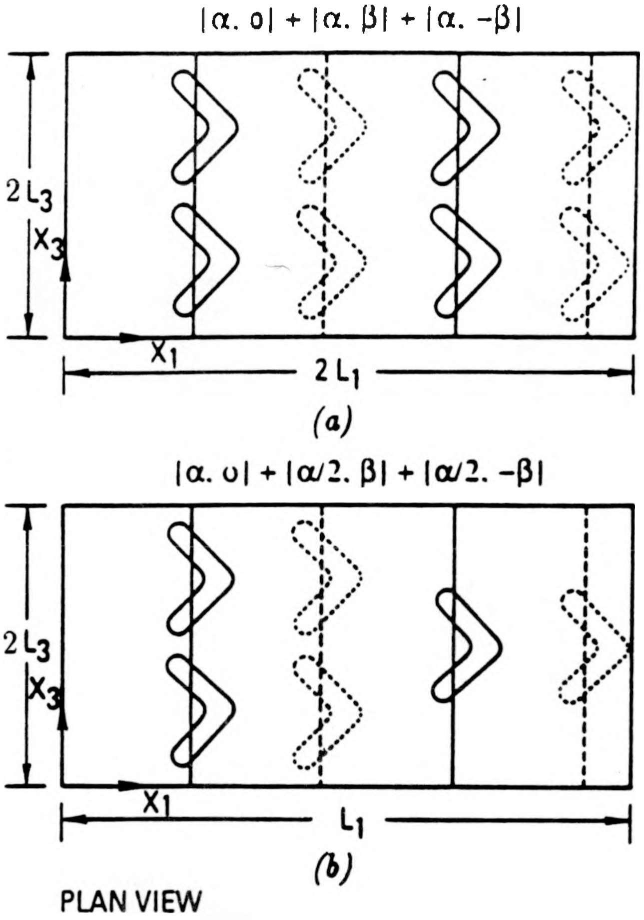

FIGURE 5-3. Cartoon illustrating orientation of spanwise vortices for *(a)* "peak-valley splitting" and *(b)* "staggered peak-valley-splitting" or "H-type" instability.

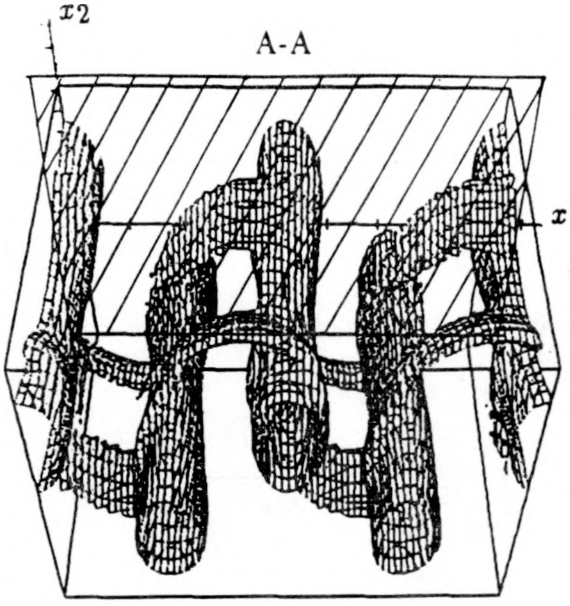

(a)

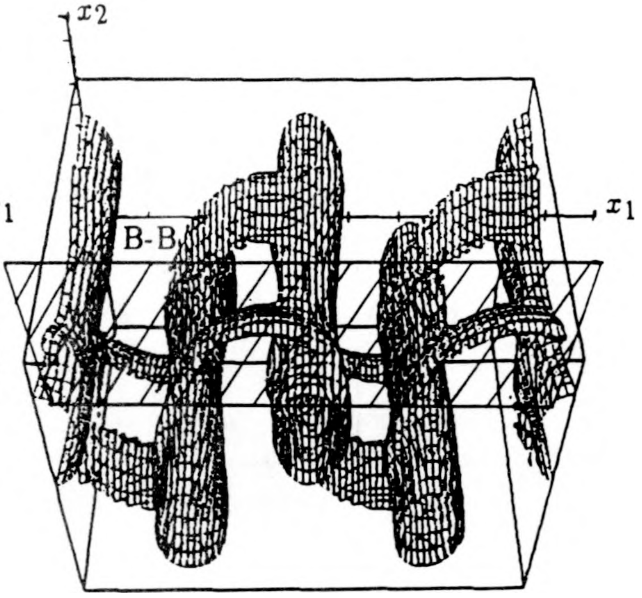

(b)

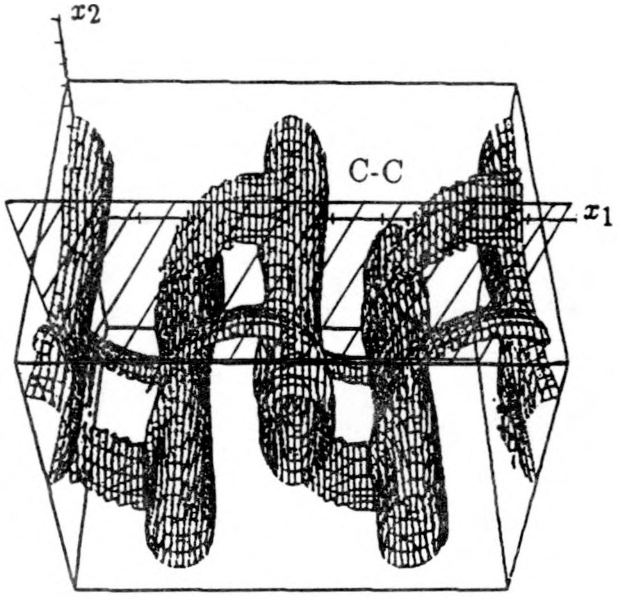

(c)

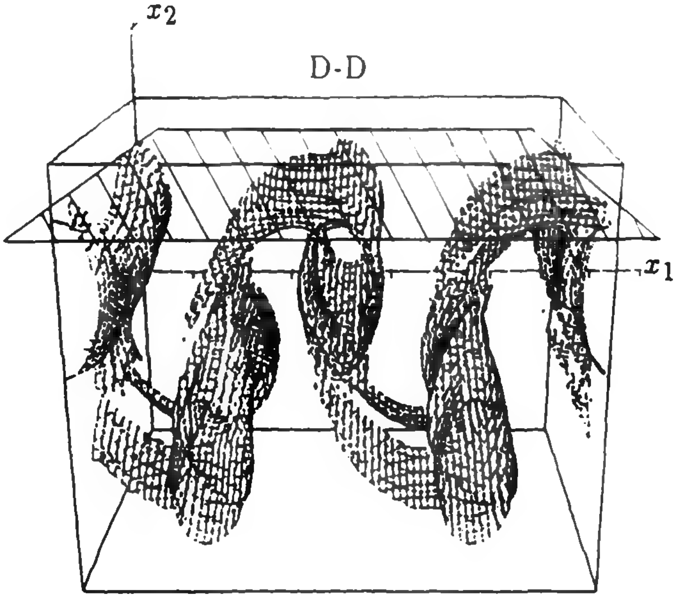

(d)

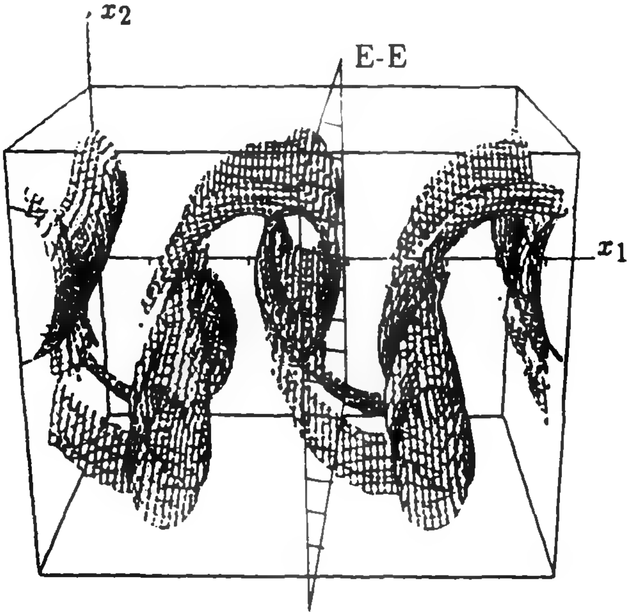

(e)

FIGURE 5-4. Perspective plots of vorticity norm for Case 1 after fundamental saturation ($t = 49$) illustrating planes of interest:*(a)* A-A, *(b)* B-B, *(c)* C-C, *(d)* D-D, and *(e)* E-E. Contour level chosen is 30% of peak value.

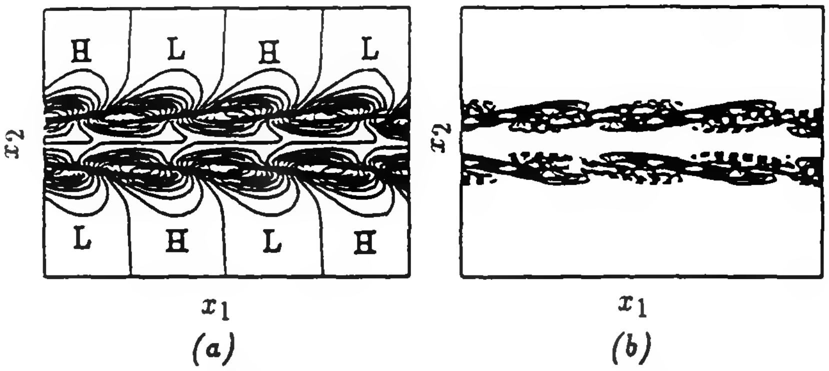

FIGURE 5-5. Side view (C-C) of *(a)* initial pressure and *(b)* initial streamwise vorticity. "H" and "L" denote maxima and minima in pressure.

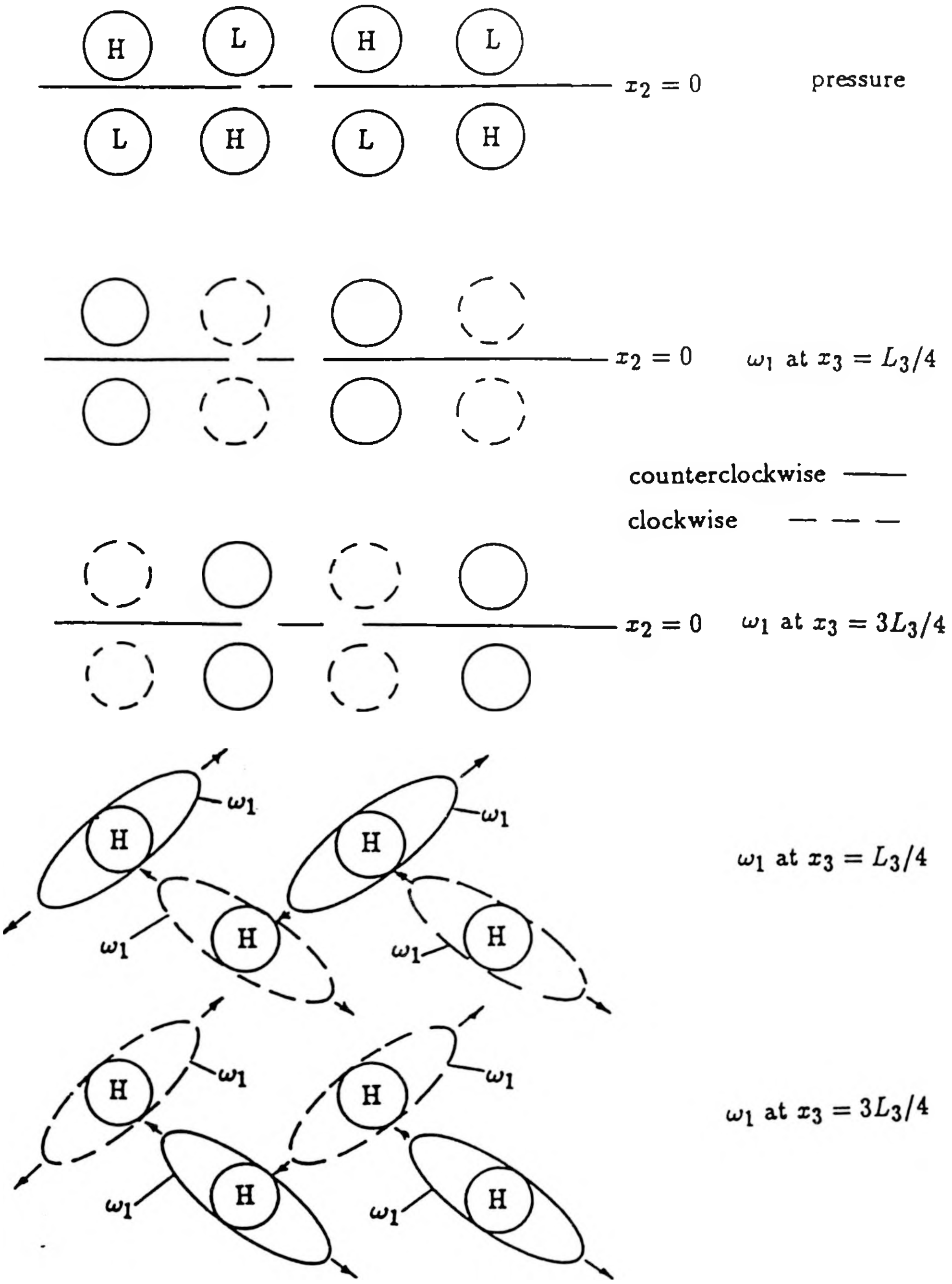

FIGURE 5-6. **Cartoon illustrating antisymmetric pressure eigenfunction and symmetric streamwise vorticity eigenfunction. Regions of high pressure denoted by "H" correspond to high strain rates where the streamwise vorticity will be stretched and intensified in the saddle region. Regions of low pressure denoted by "L" correspond to rotational regions in the spanwise vortex cores.**

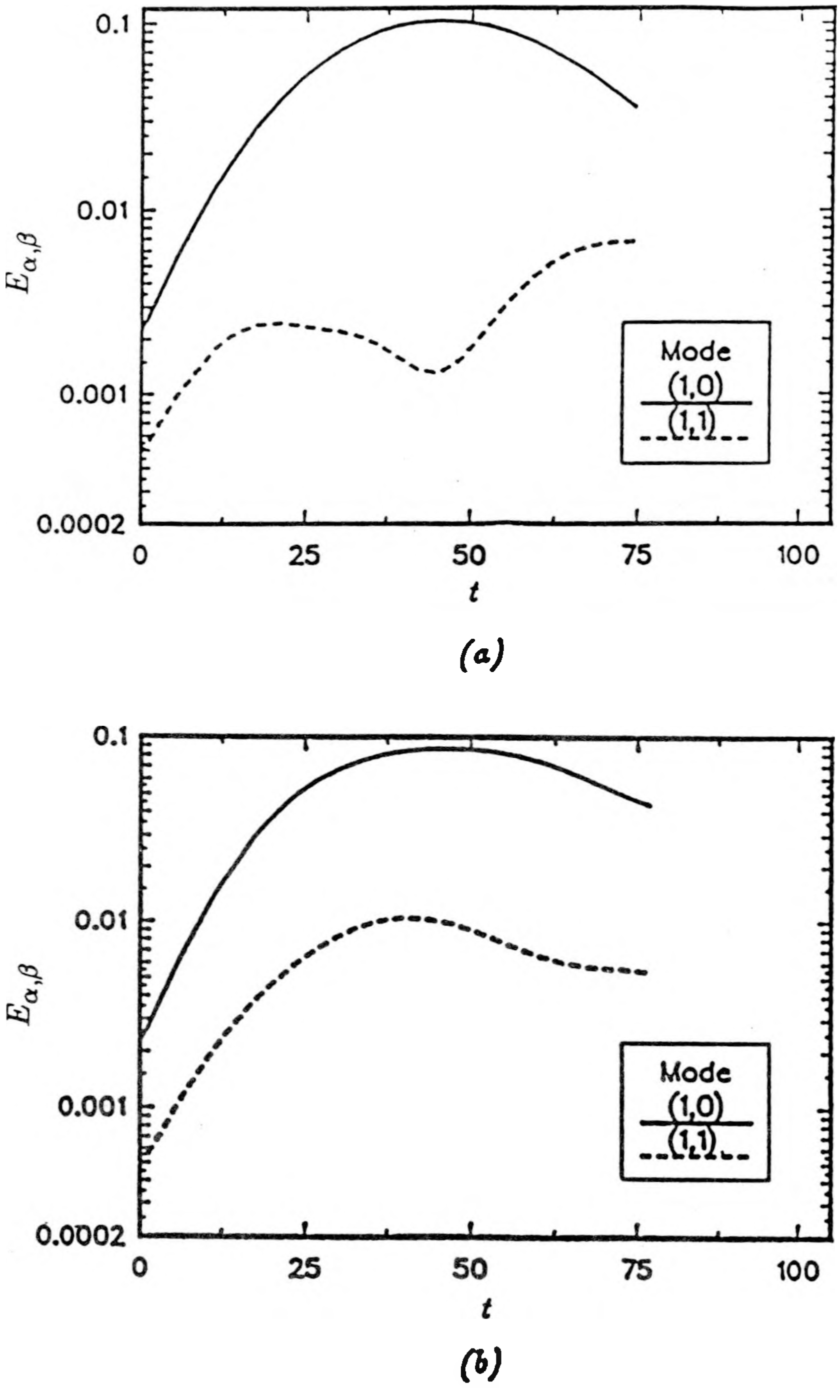

FIGURE 5-7. Evolution of modal energies for the fundamental $(1,0)$ and oblique $(1,\pm1)$ modes for *(a)* Case 1, $\Theta = 0$, *(b)* Case 2, $\Theta = \pi/2$.

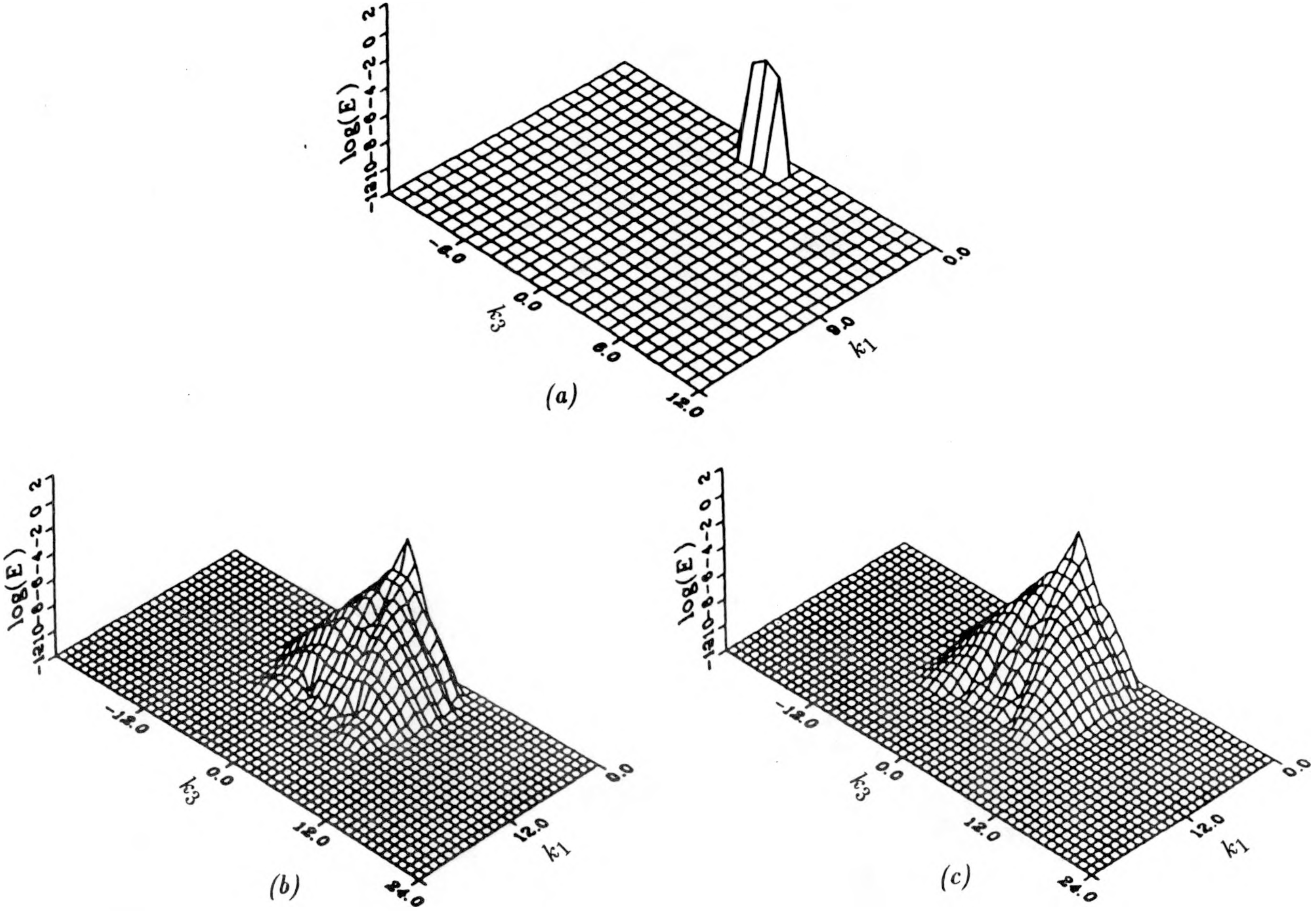

FIGURE 5-8. Two-dimensional energy spectra for Case 1 at *(a)* $t = 0$, $x_2 = 0$; *(b)* $t = 49$, $x_2 = 0$; and *(c)* $t = 49$, $x_2 = 2$.

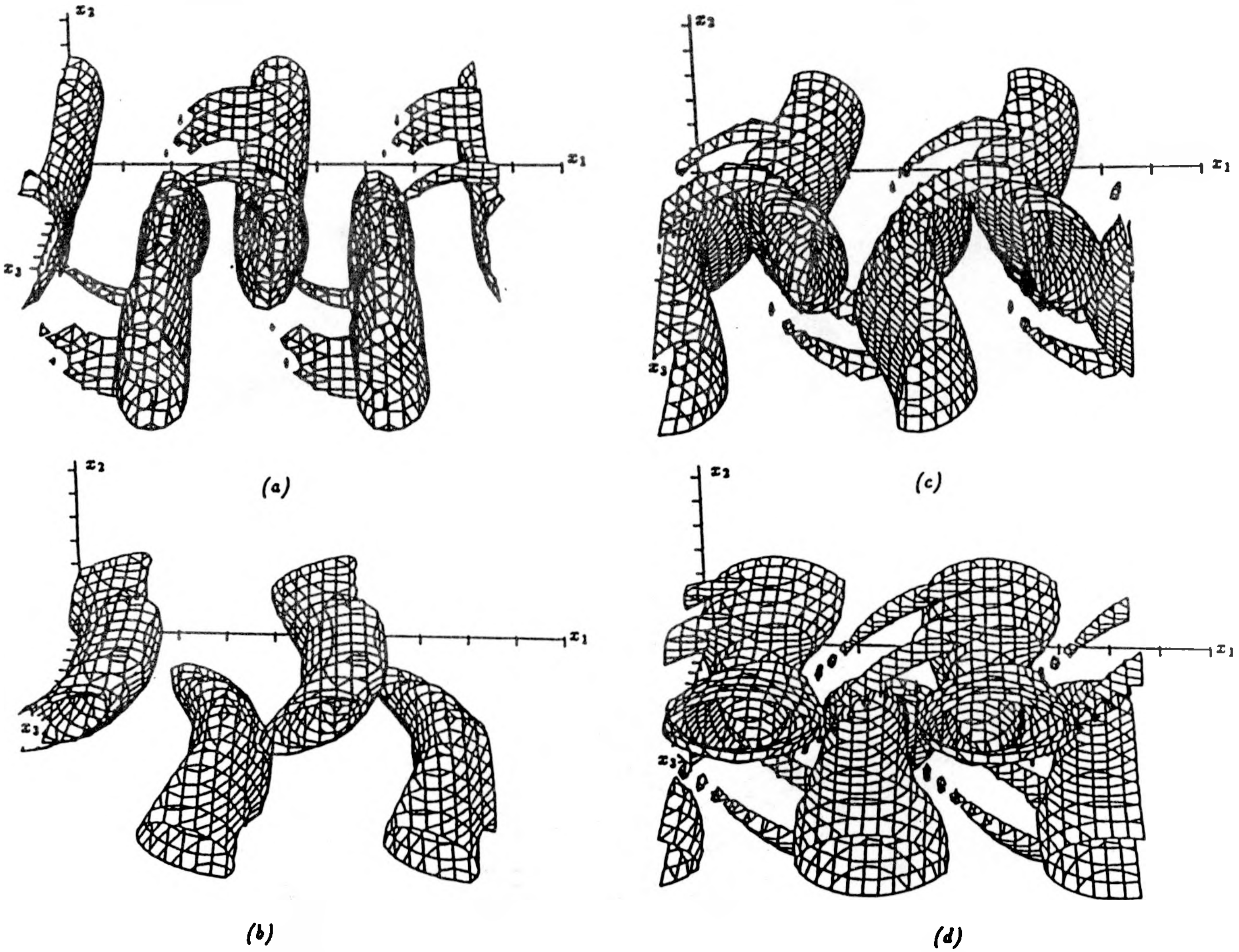

FIGURE 5-9. Iso-level surfaces of vorticity norm, $|\omega_i\omega_i|$, for a 3-D wake. Contour level is 40% of peak value. *(a)* Case 1 at $t = 49$, *(b)* Case 1 at $t = 64$, *(c)* Case 2 at $t = 49$, *(d)* Case 2 at $t = 64$.

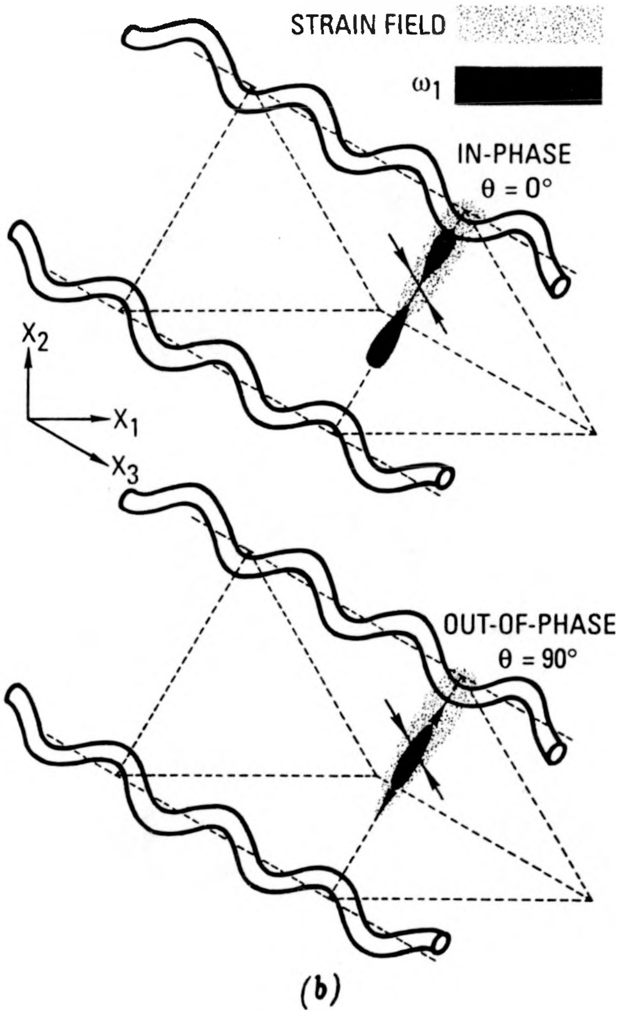

FIGURE 5-10. Cartoon illustrating relative location of maximum strain rate to initial streamwise vorticity peak in the saddle point region, *(a)* Case 1 and *(b)* Case 2.

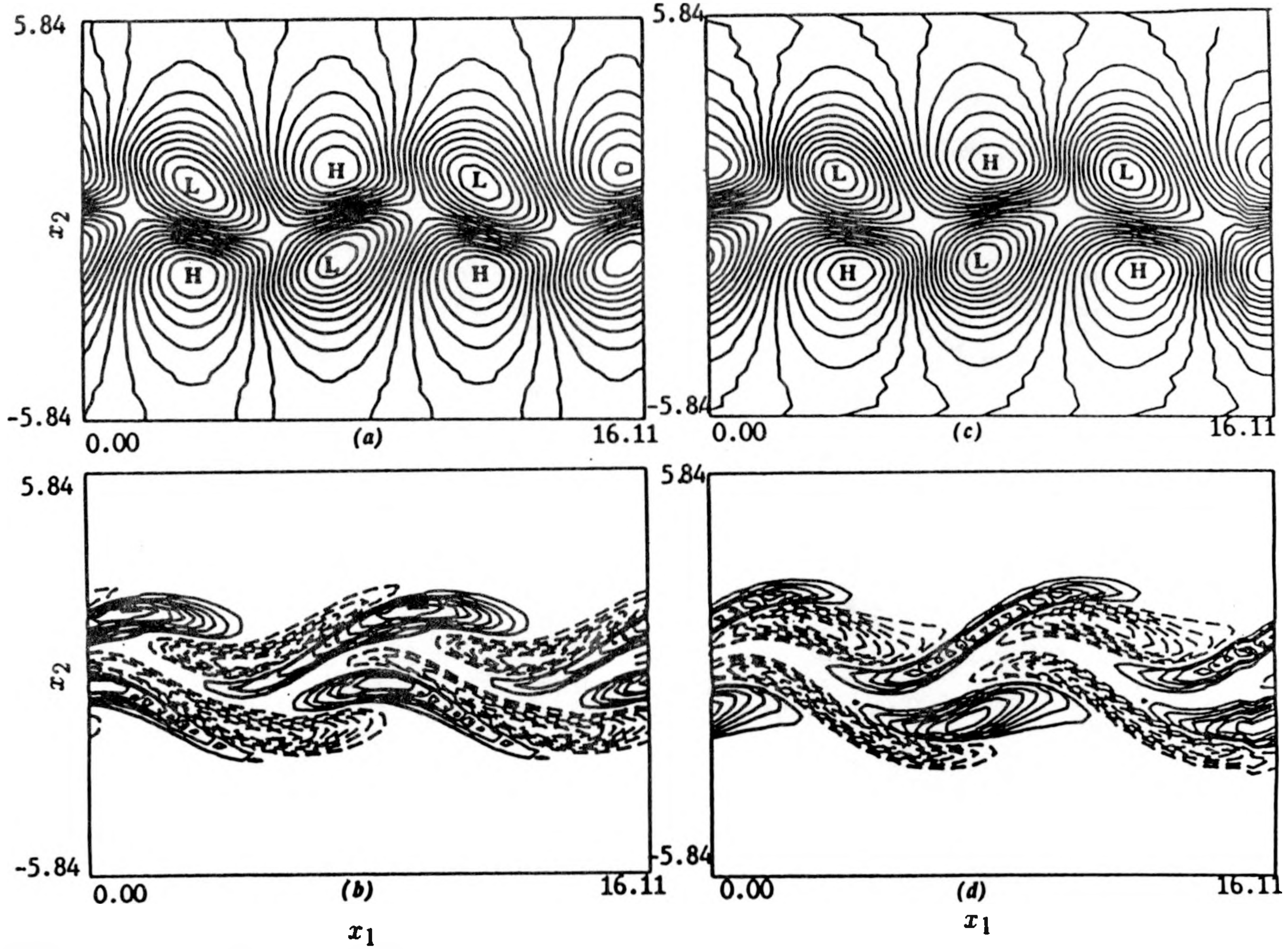

FIGURE 5-11. Side view (C-C) of *(a,c)* pressure and *(b,d)* streamwise vorticity for Case 1 and Case 2, respectively. "H" and "L" denote maxima and minima in pressure.

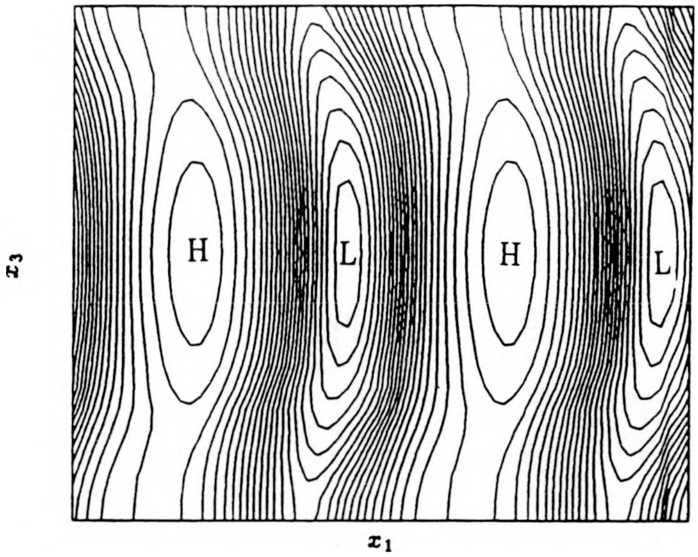

(a)

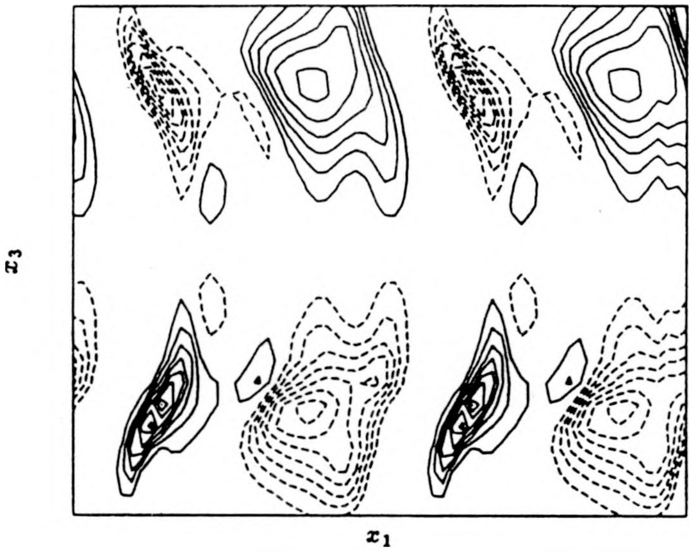

(b)

FIGURE 5-12. Plan view (D-D) of *(a)* pressure and *(b)* streamwise vorticity for Case 2. "H" and "L" denote maxima and minima in pressure.

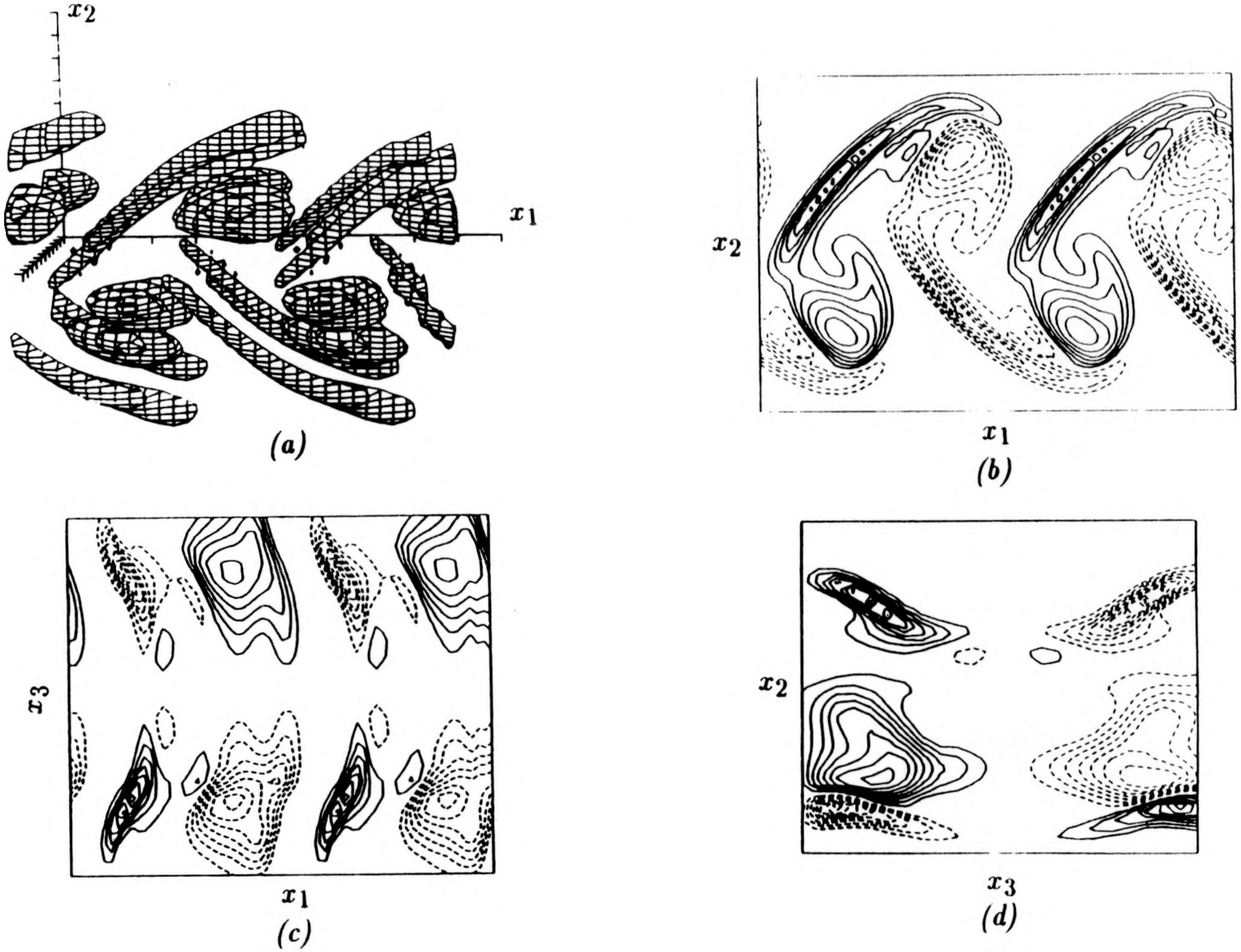

(a) (b) (c) (d)

FIGURE 5-13. Streamwise vorticity for Case 2 at $t = 49$, *(a)* perspective of streamwise vorticity at 50% of peak value, *(b)* side view (C-C), *(c)* plan view (D-D), and *(d)* end view (E-E).

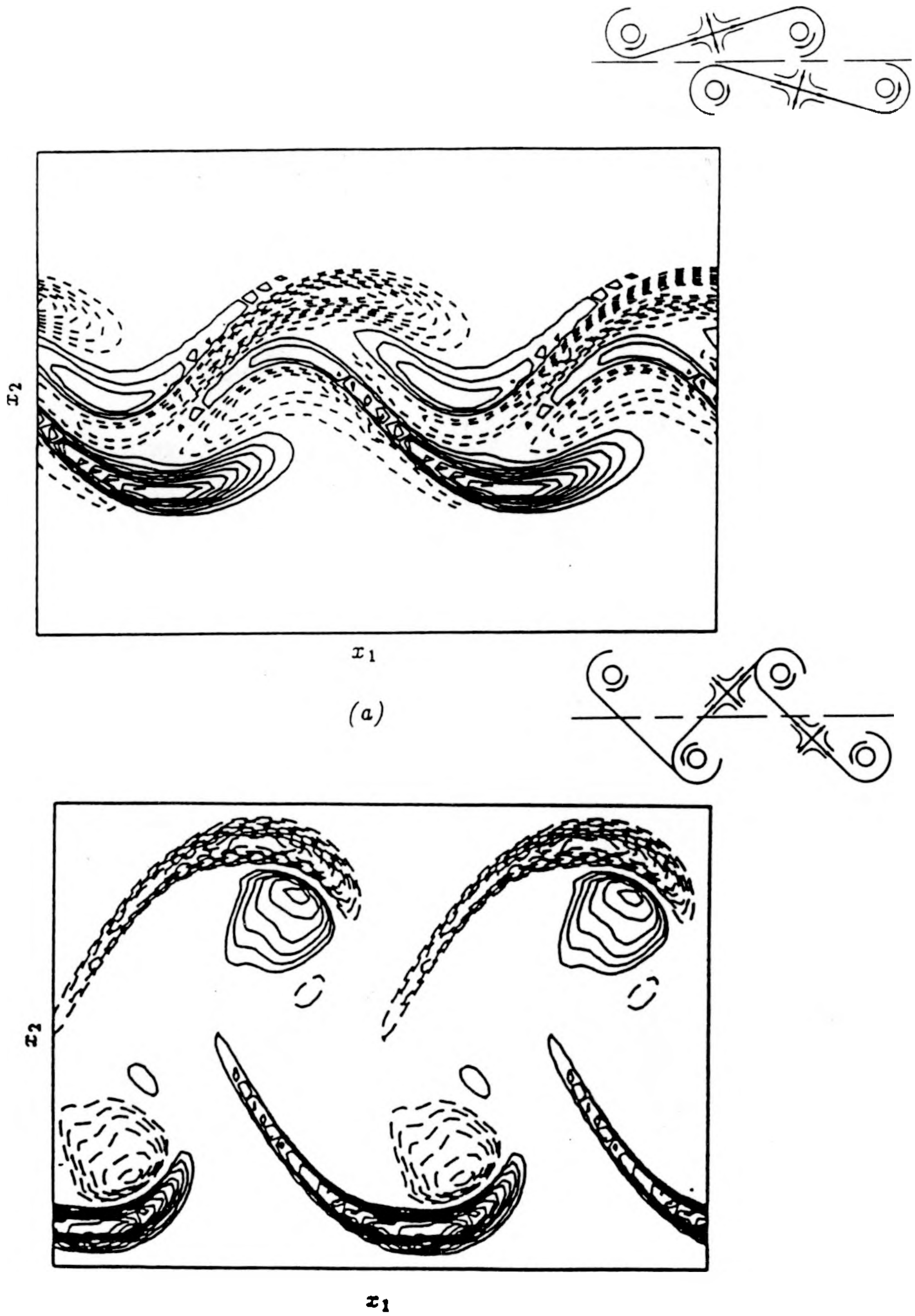

(a)

(b)

FIGURE 5-14. Side view (C-C) of streamwise vorticity for Case 1 at *(a)* $t = 18$, and *(b)* $t = 40$ illustrating different topology.

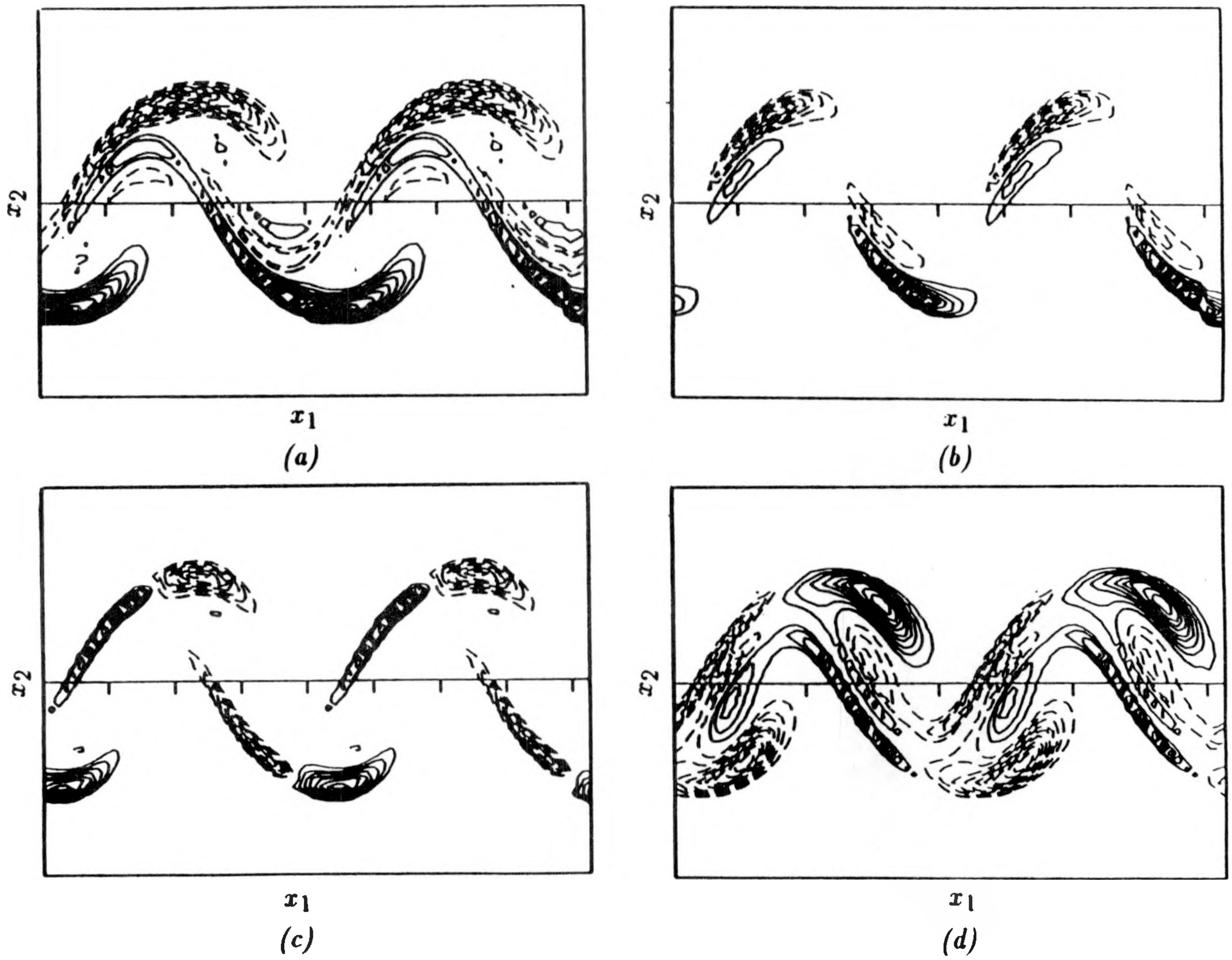

FIGURE 5-15. Vorticity stretching terms responsible for production of streamwise vorticity for Case 1 at $t = 30$, *(a)* ω_1, *(b)* $S_{11}\omega_1$, *(c)* $S_{12}\omega_2$, and *(d)* $S_{13}\omega_3$.

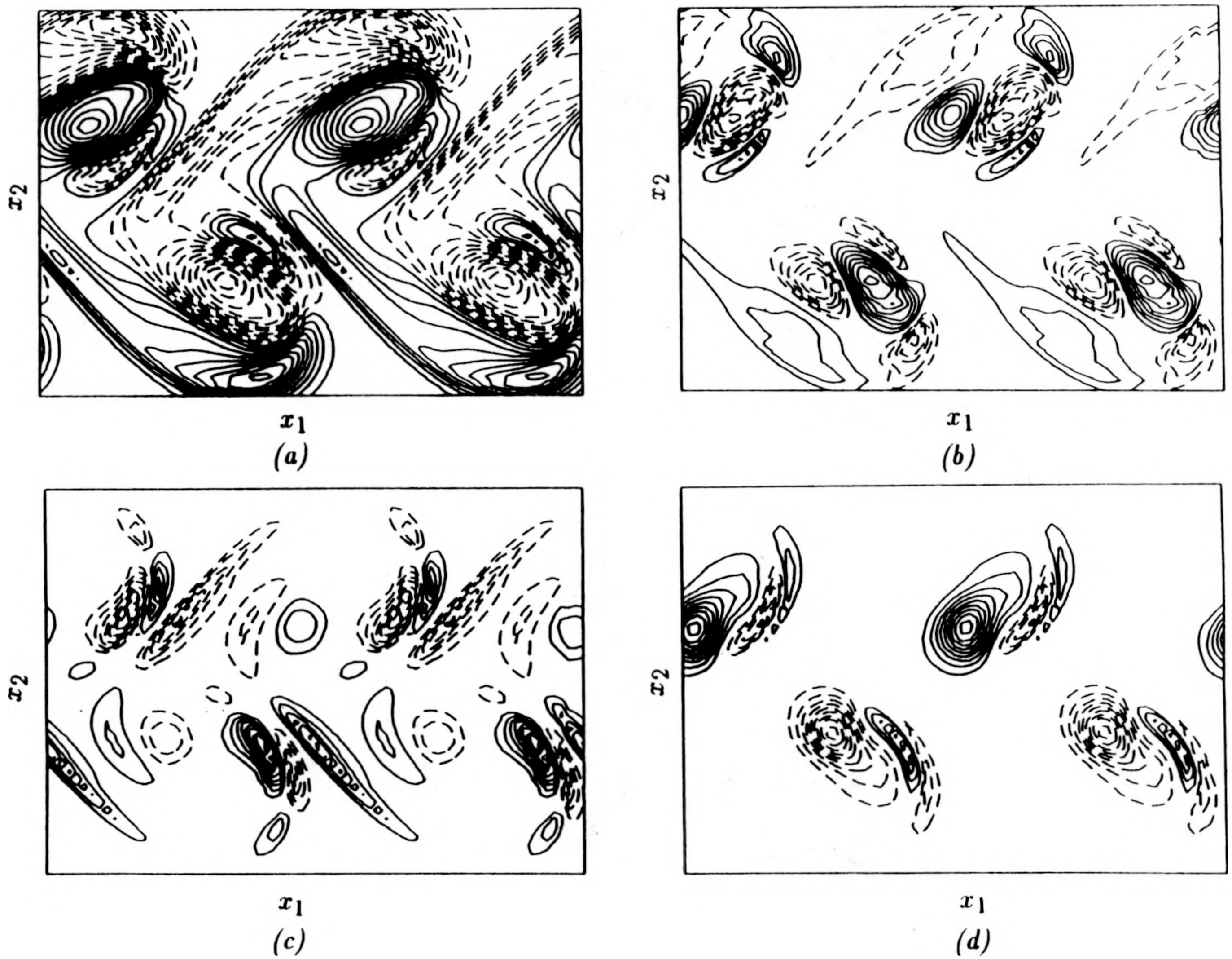

FIGURE 5-16. Vorticity stretching terms responsible for production of streamwise vorticity for Case 1 at $t = 64$, *(a)* ω_1, *(b)*$S_{11}\omega_1$, *(c)* $S_{12}\omega_2$, and *(d)* $S_{13}\omega_3$.

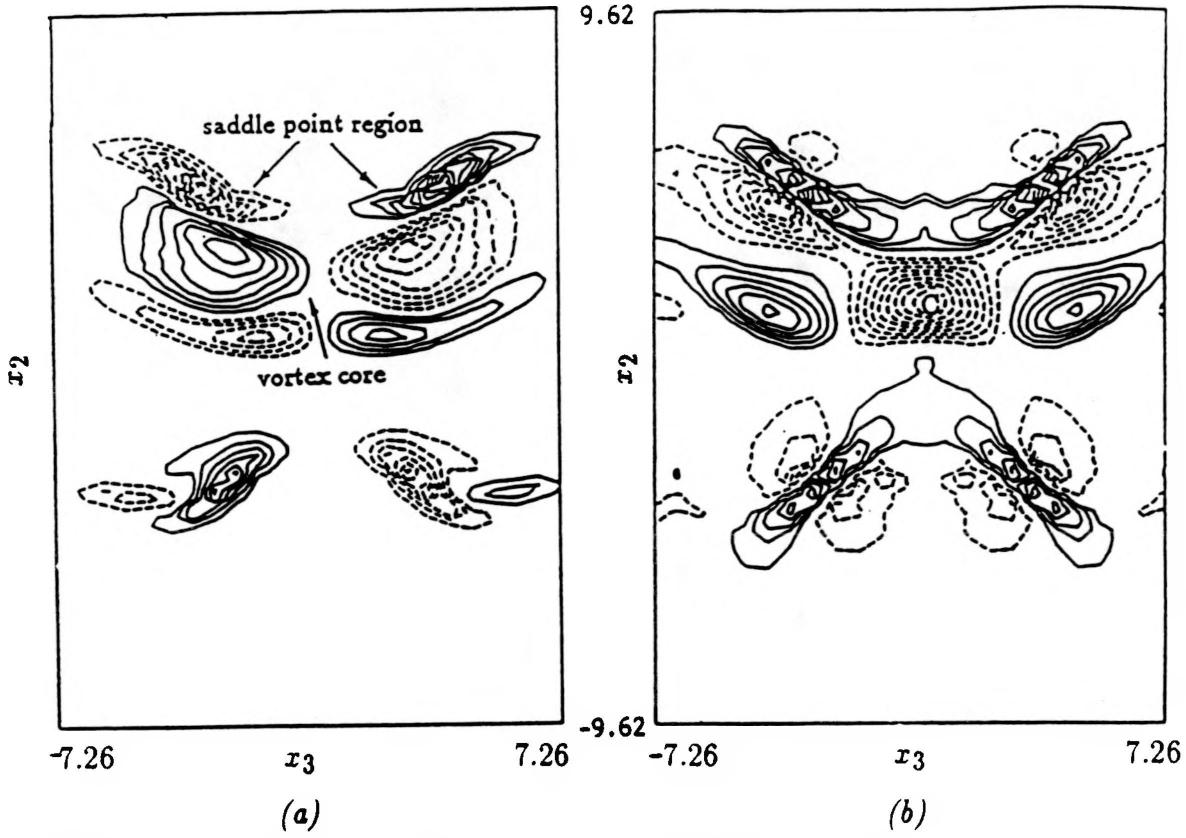

FIGURE 5-17. End view (E-E) of *(a)* ω_1 and *(b)* S_{33} for Case 1 at $t = 64$.

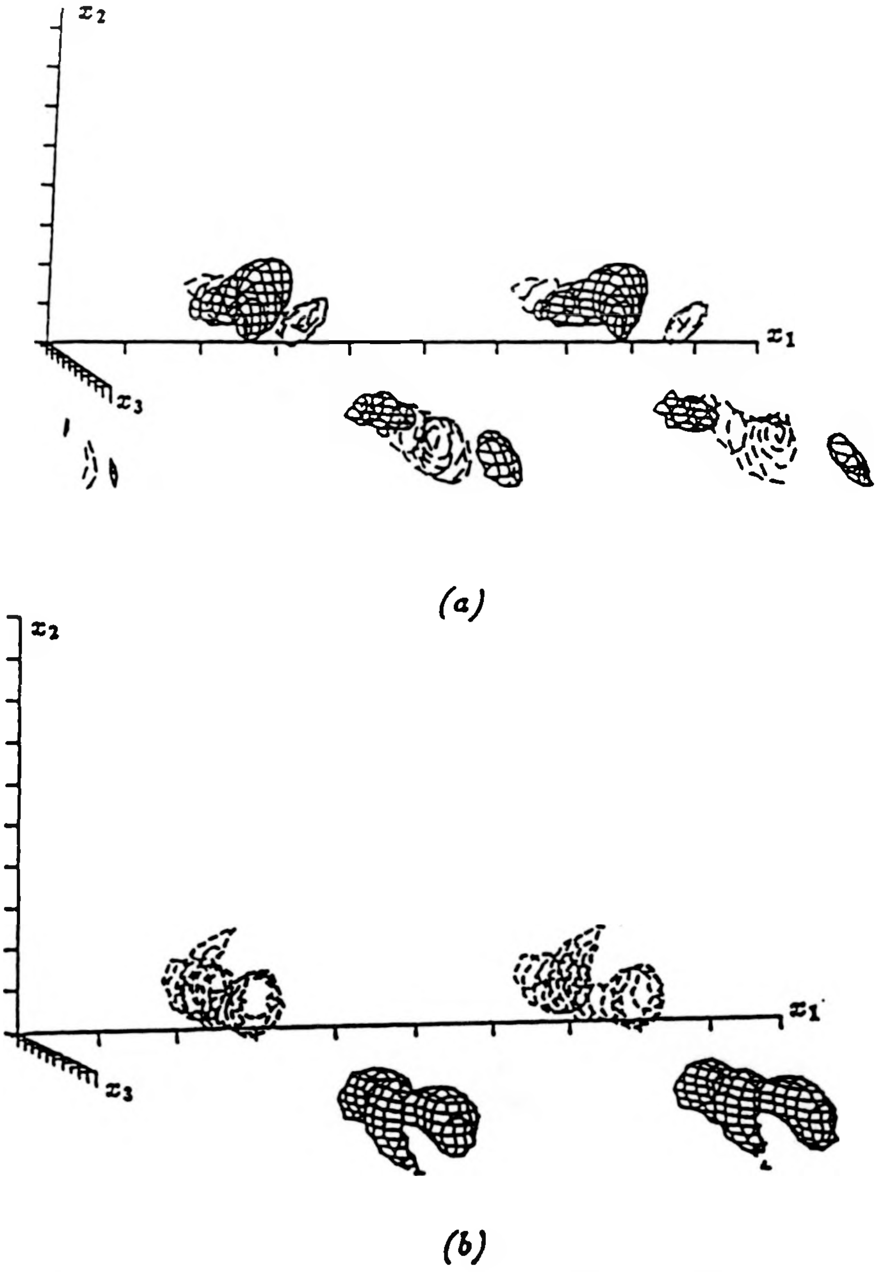

FIGURE 5-18. Iso-level surfaces of (a) $S_{33}\omega_3$ and (b) ω_3 for Case 1, $t = 64$. Contour levels are 70% of peak value 0.026 for (a) and 80% of peak value 0.45 for (b).

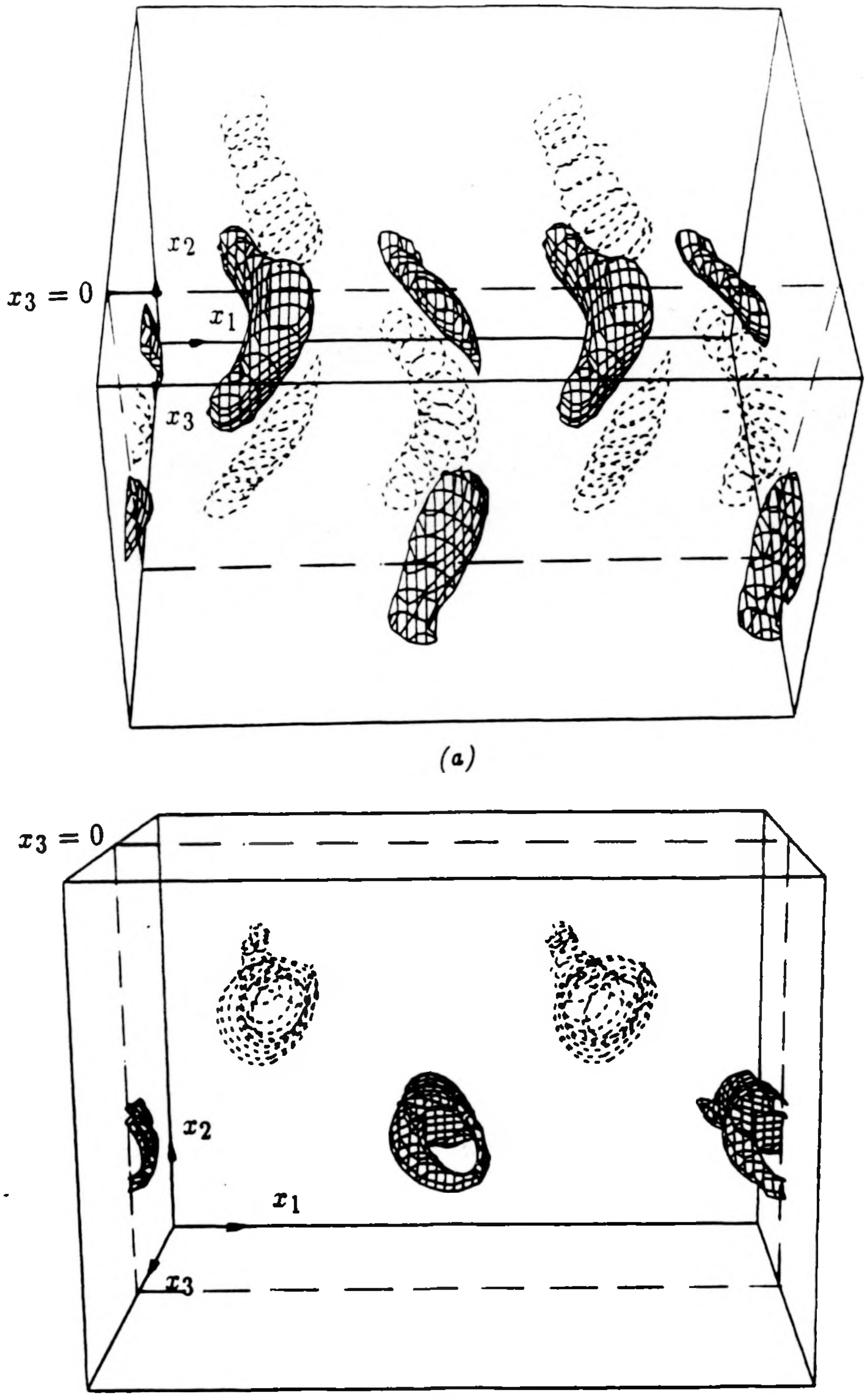

(a)

(b)

FIGURE 5-19. Iso-level surfaces of *(a)* $S_{33}\omega_3$ and *(b)* ω_3 for Case 1, $t = 64$. Contour levels are 40% of peak value 0.026 for *(a)* and 50% of peak value 0.45 for *(b)*.

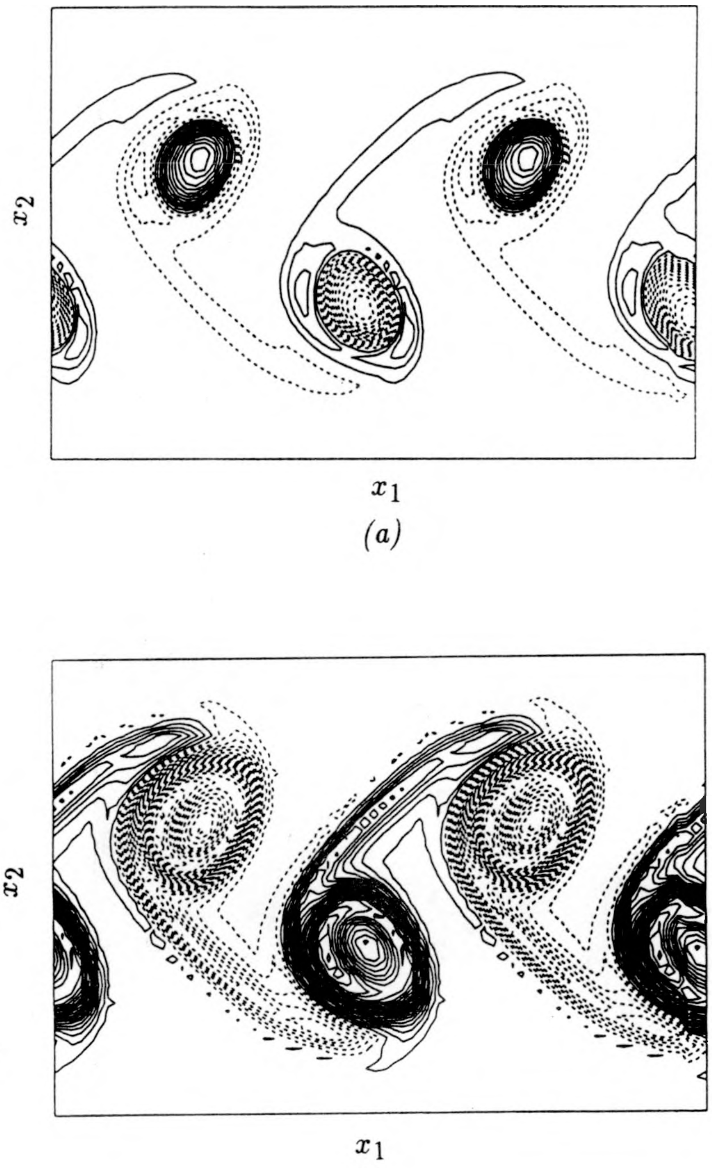

(a)

(b)

FIGURE 5-20. Side view (B-B) of *(a)* $S_{33}\omega_3$ and *(b)* ω_3 for Case 1, $t = 64$.

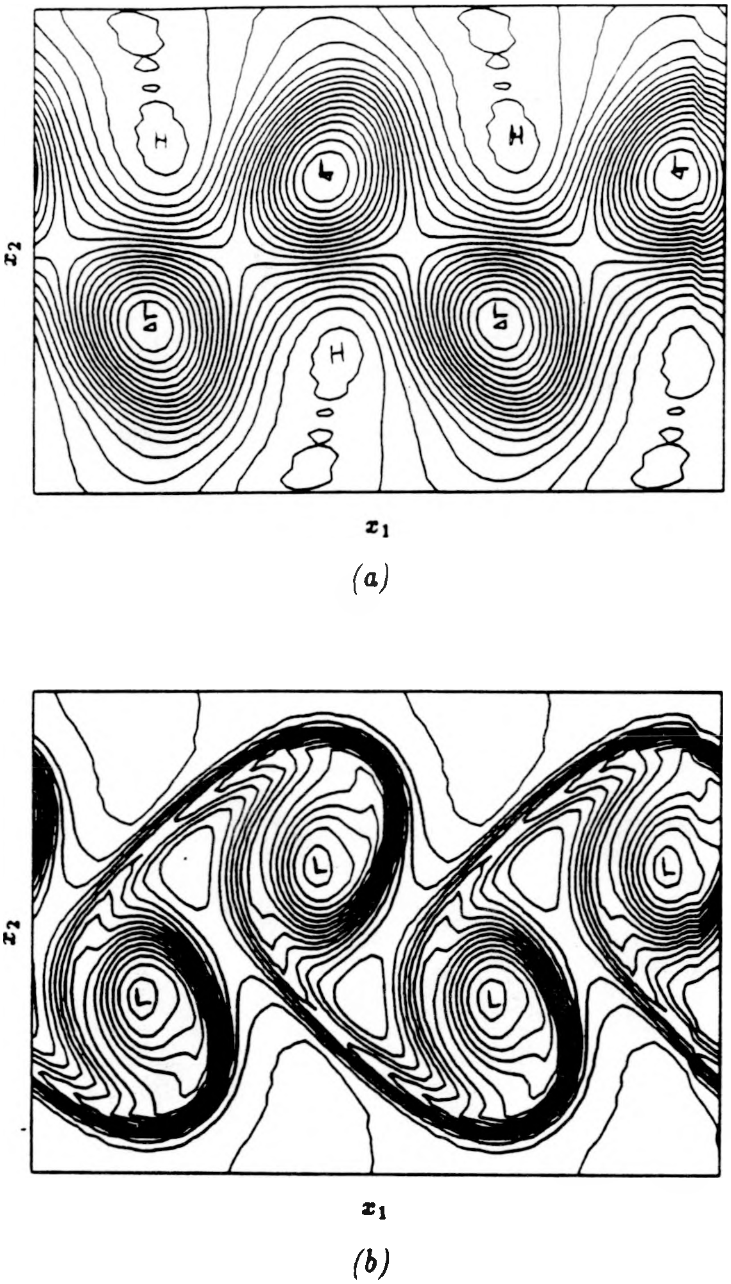

FIGURE 5-21. Side view of *(a)* pressure and *(b)* density for Case 1 at $t = 64$. "H" and "L" denote maxima and minima in pressure and density. Note that pressure and density minima coincide with spanwise vortex cores.

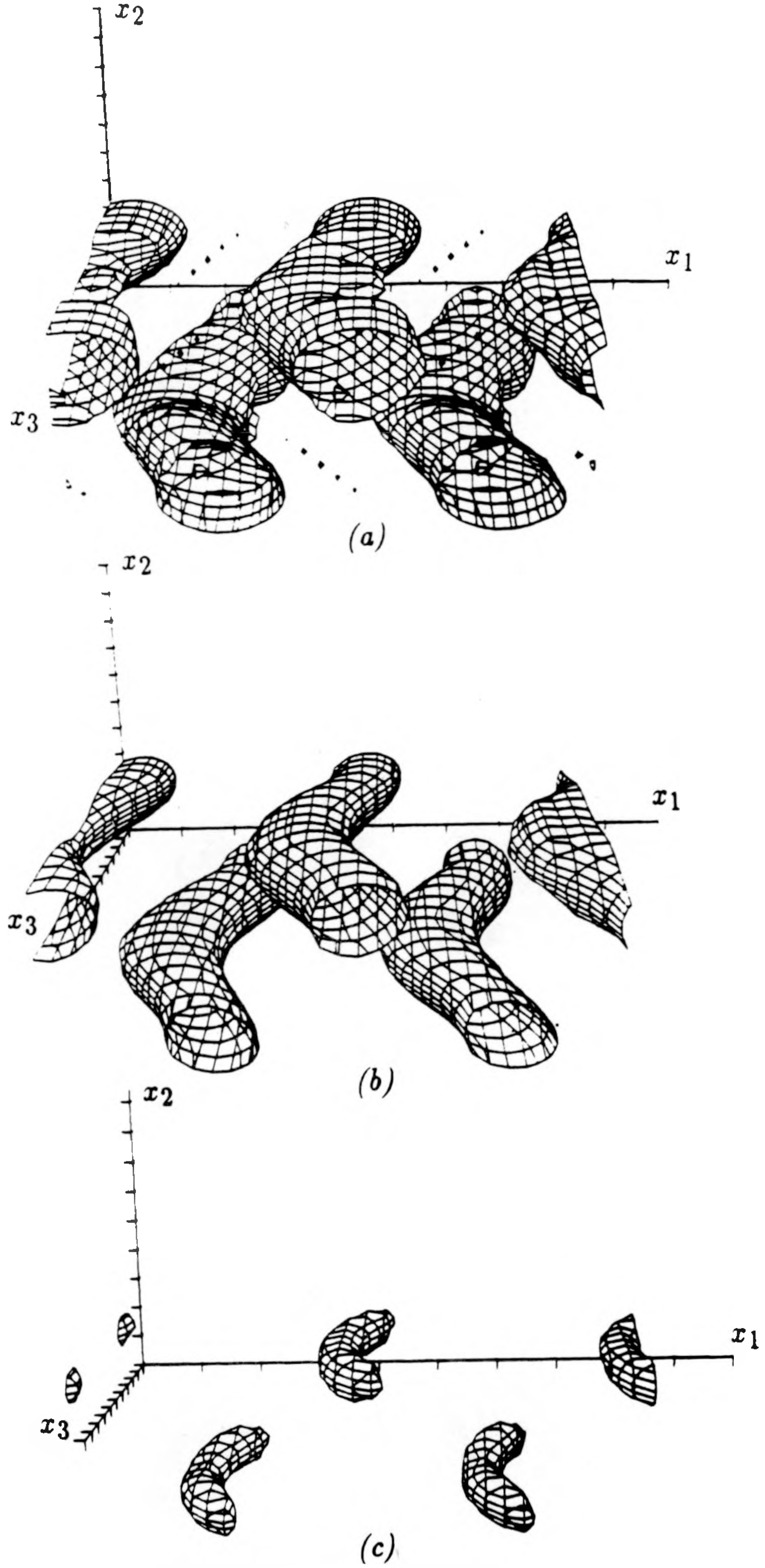

FIGURE 5-22. Iso-level surfaces of *(a)* vorticity norm, *(b)* pressure minima, and *(c)* density minima for Case 1 at $t = 64$.

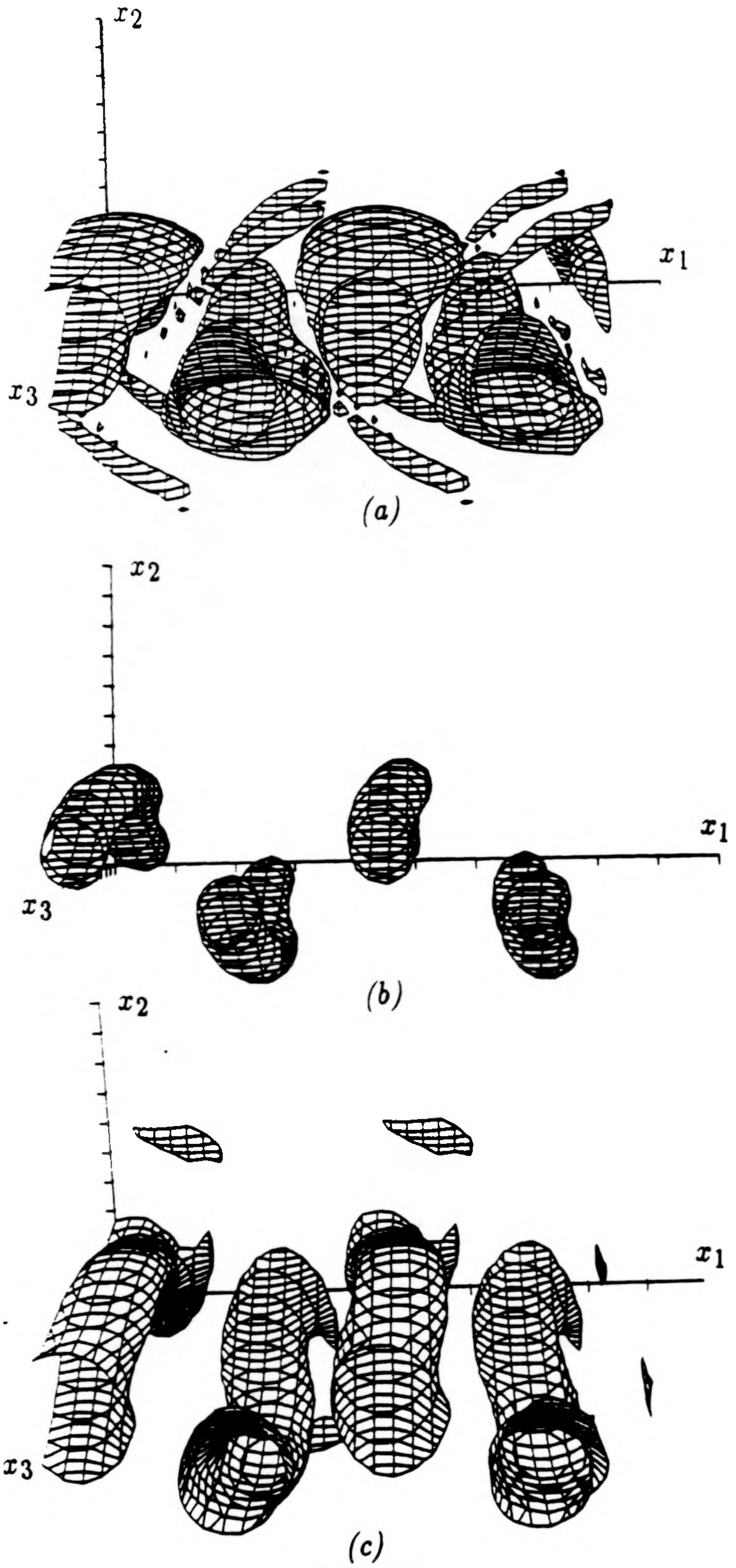

FIGURE 5-23. Iso-level surfaces of *(a)* vorticity norm, *(b)* pressure minima, and *(c)* density minima for Case 2 at $t = 64$.

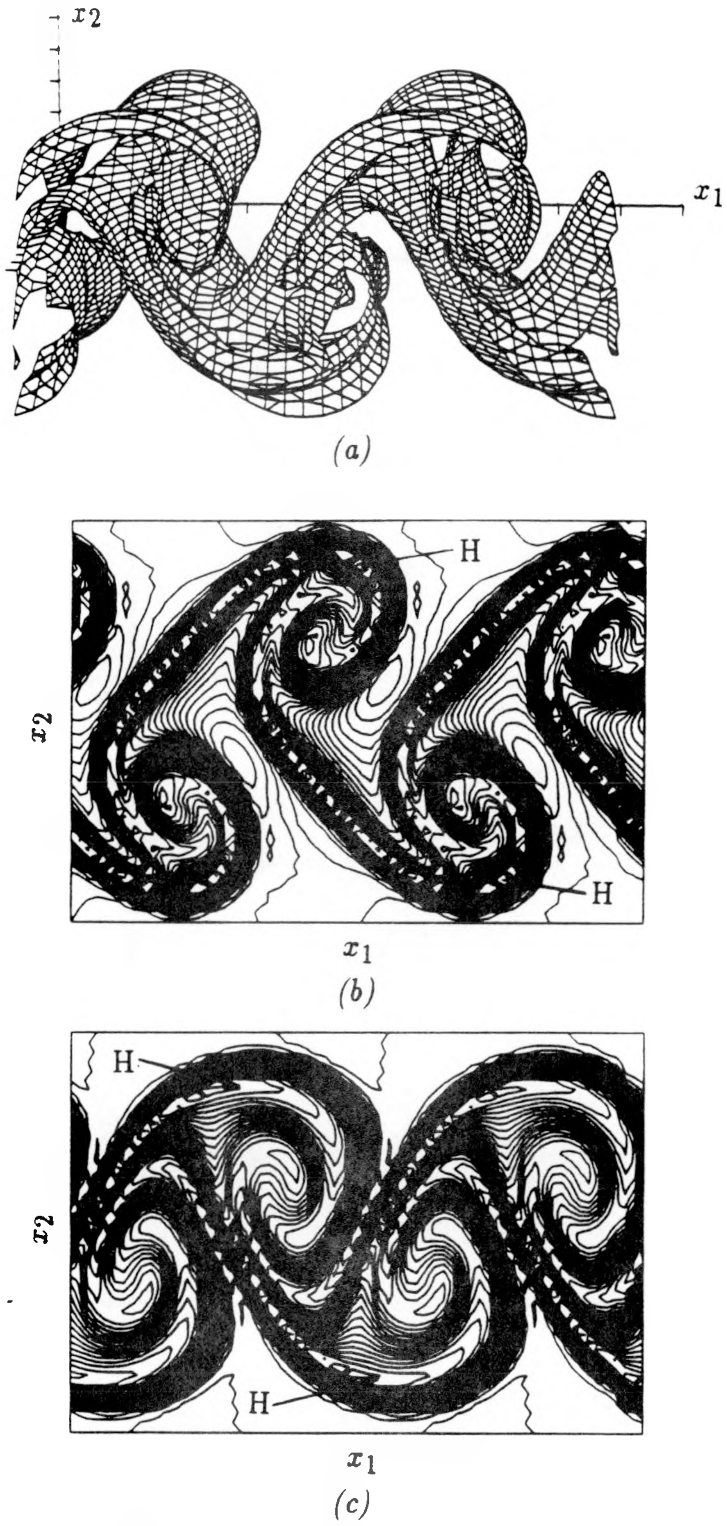

FIGURE 5-24. Temperature field for Case 2, $t = 64$ *(a)* iso-level surfaces of temperature at 20% of peak value, *(b)* side view (A-A), and *(c)* side view (B-B).

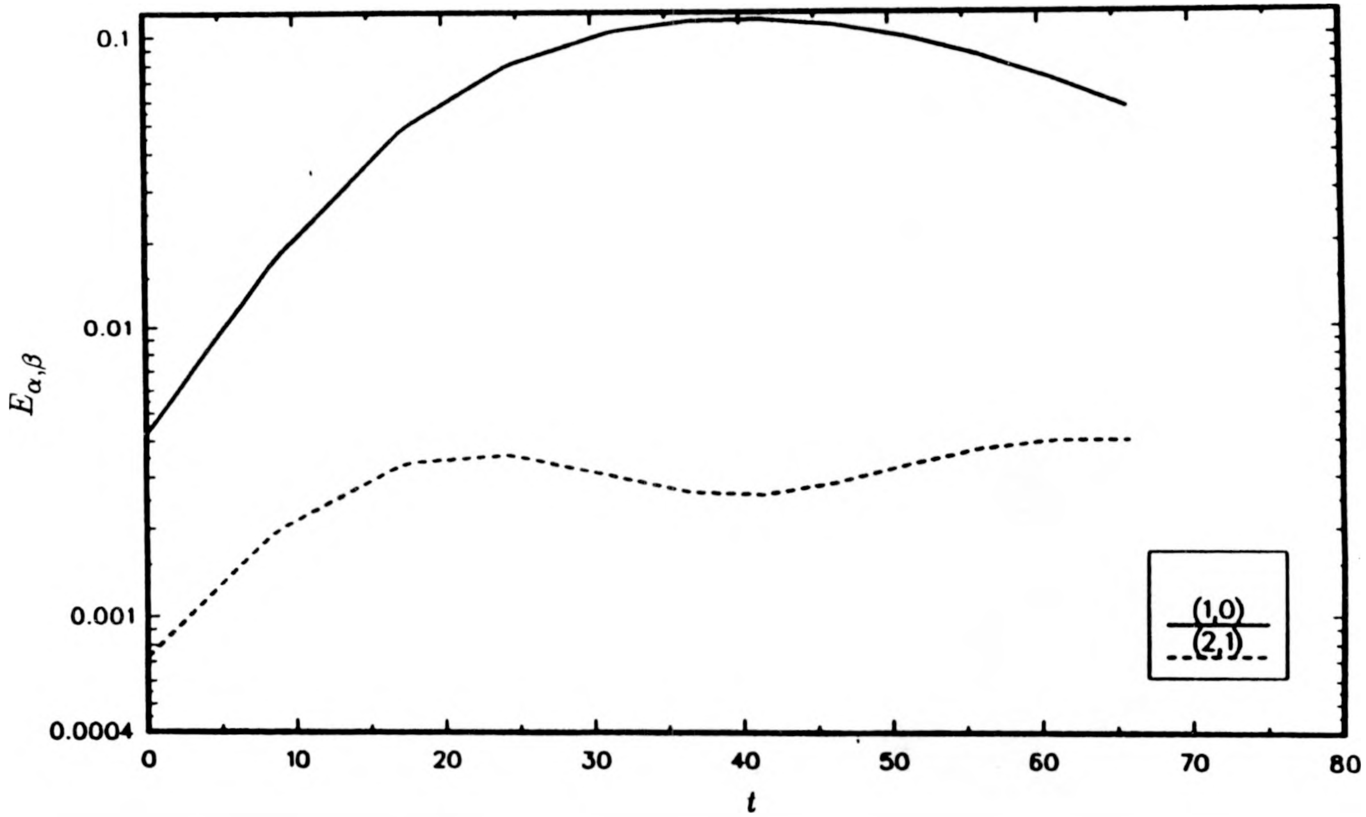

FIGURE 5-25. Evolution of modal energies for the fundamental $(1,0)$ and oblique subharmonic $(2,\pm 1)$ modes for Case 3.

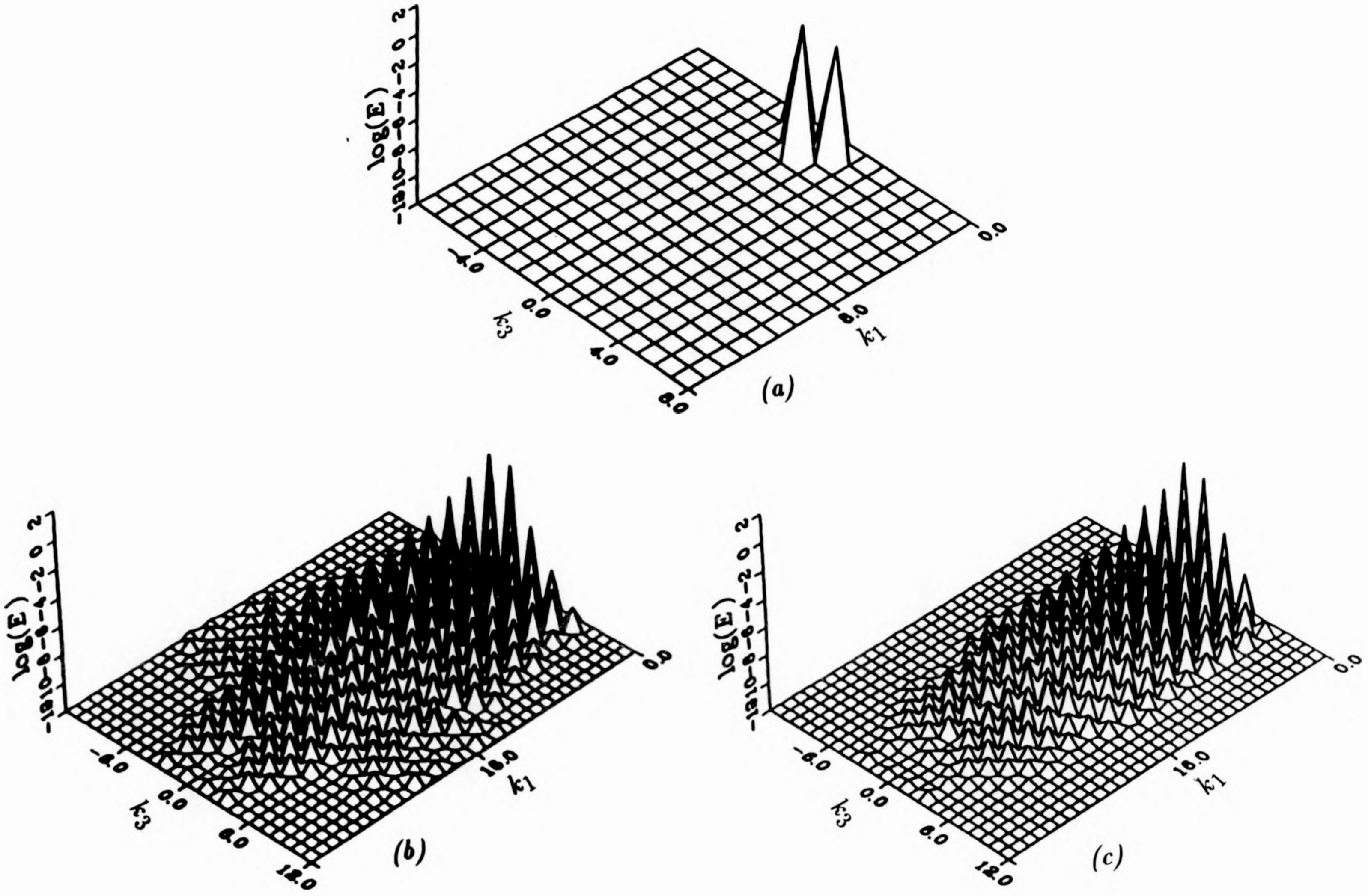

FIGURE 5-26. Two-dimensional energy spectra for Case 3 at *(a)* $t = 0$, $x_2 = 0$; *(b)* $t = 60$, $x_2 = 0$; and *(c)* $t = 60$, $x_2 = 2$.

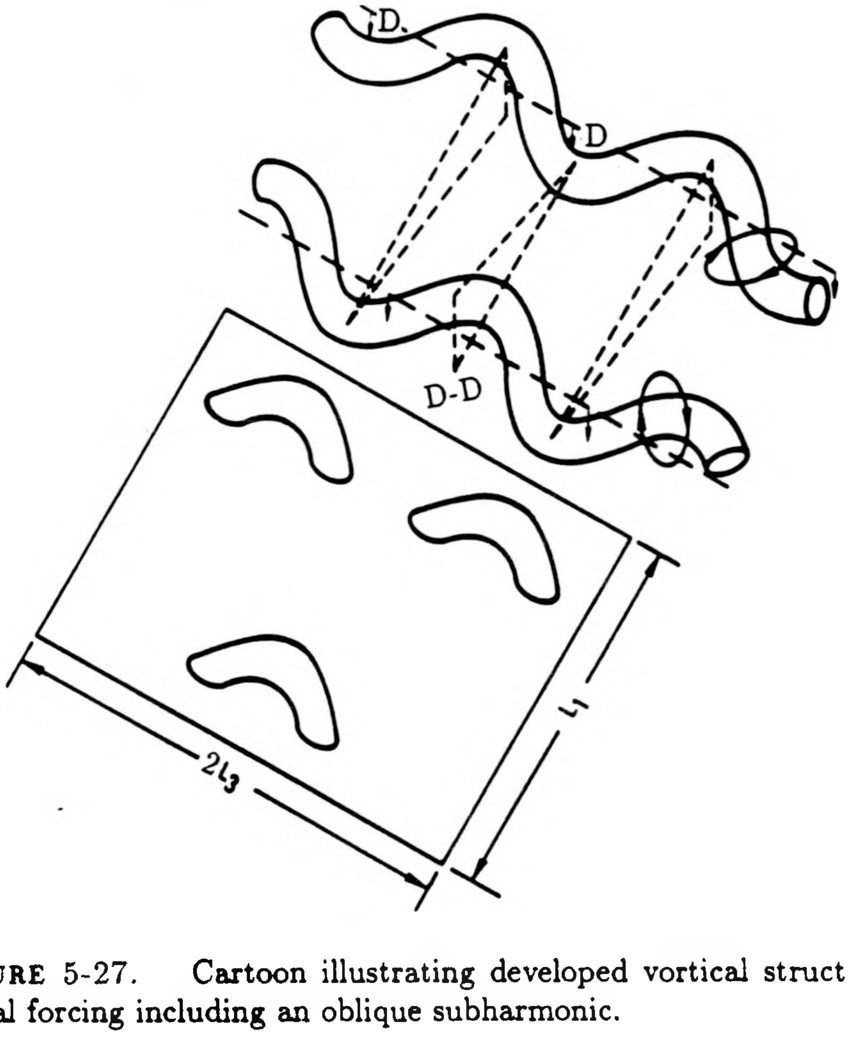

FIGURE 5-27. Cartoon illustrating developed vortical structures for an initial forcing including an oblique subharmonic.

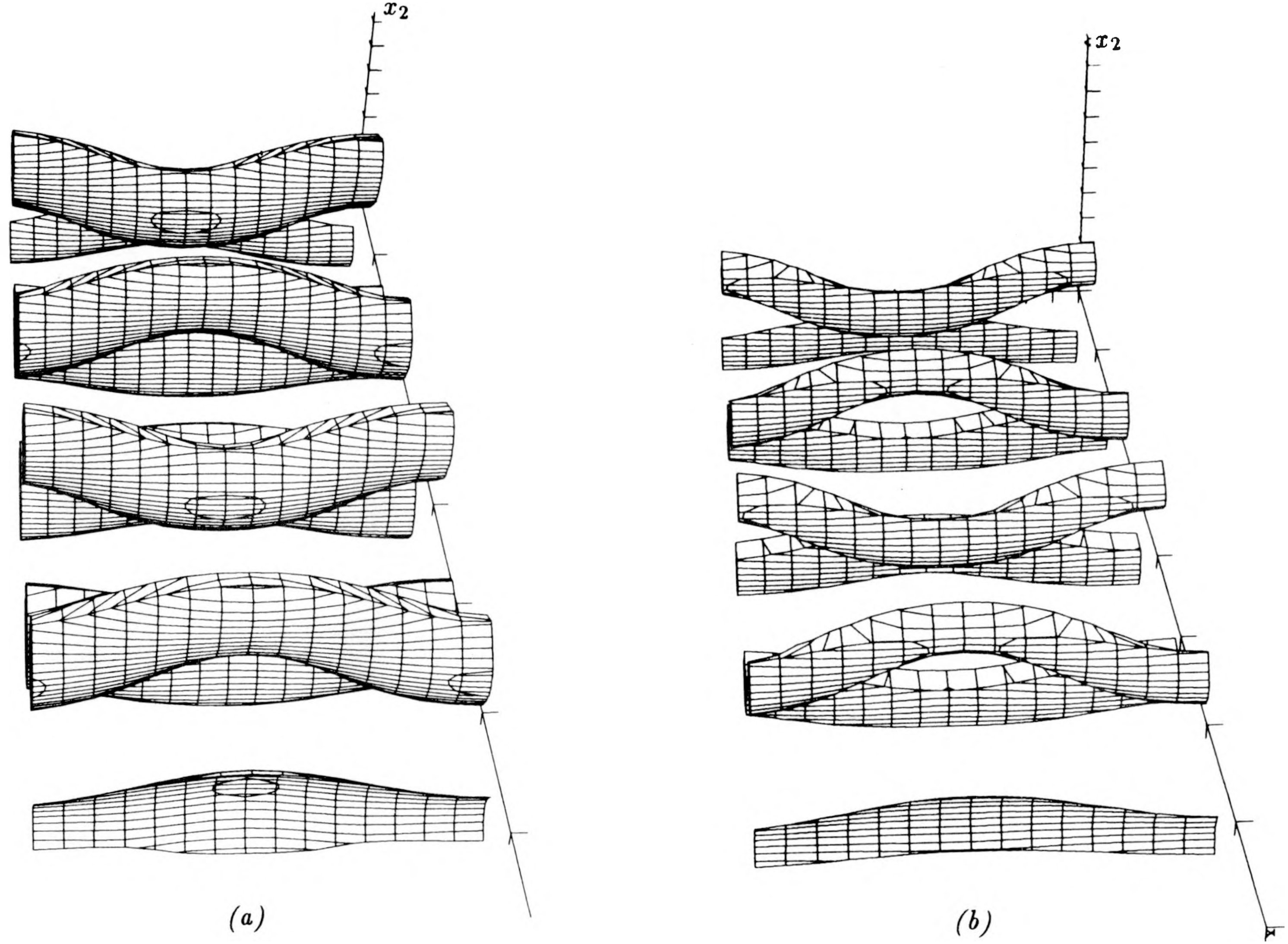

(a) (b)

FIGURE 5-28. Perspective view of *(a)* vorticity magnitude, and *(b)* pressure for Case 3 at $t = 60$. Contour level is chosen to be 50% of peak value.

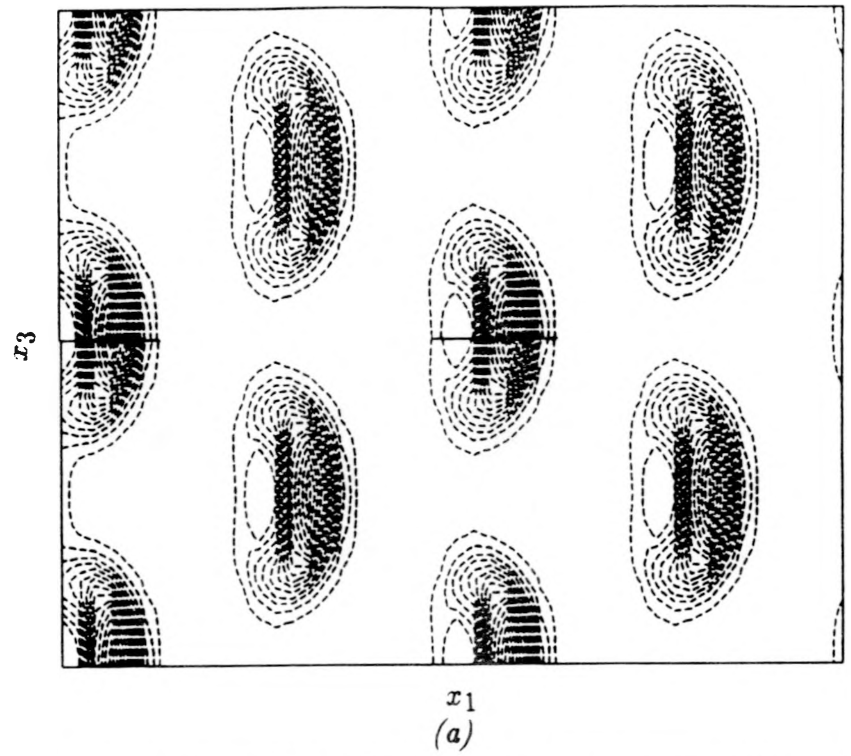

(a)

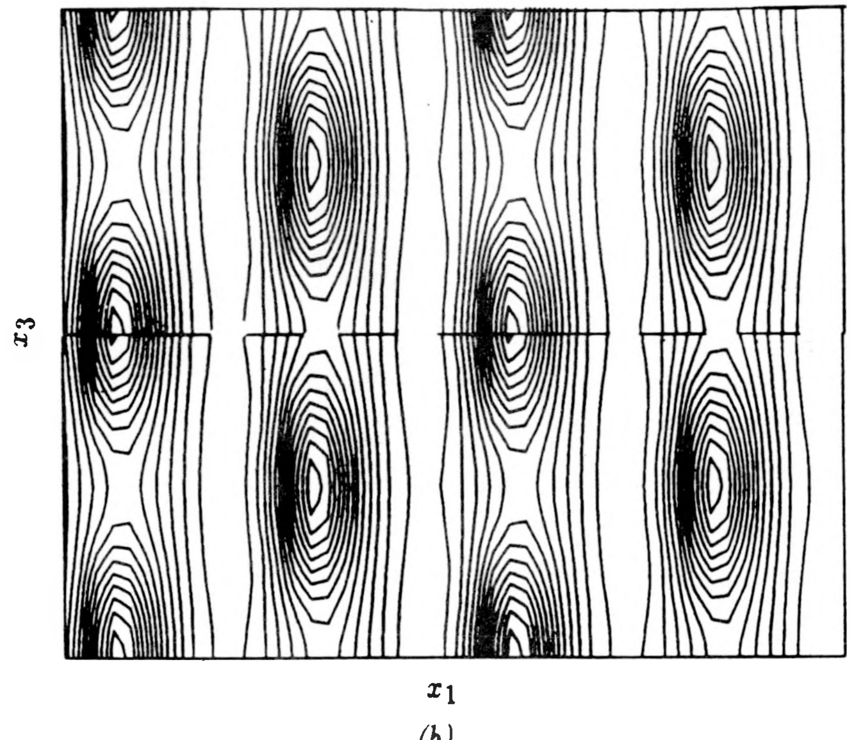

(b)

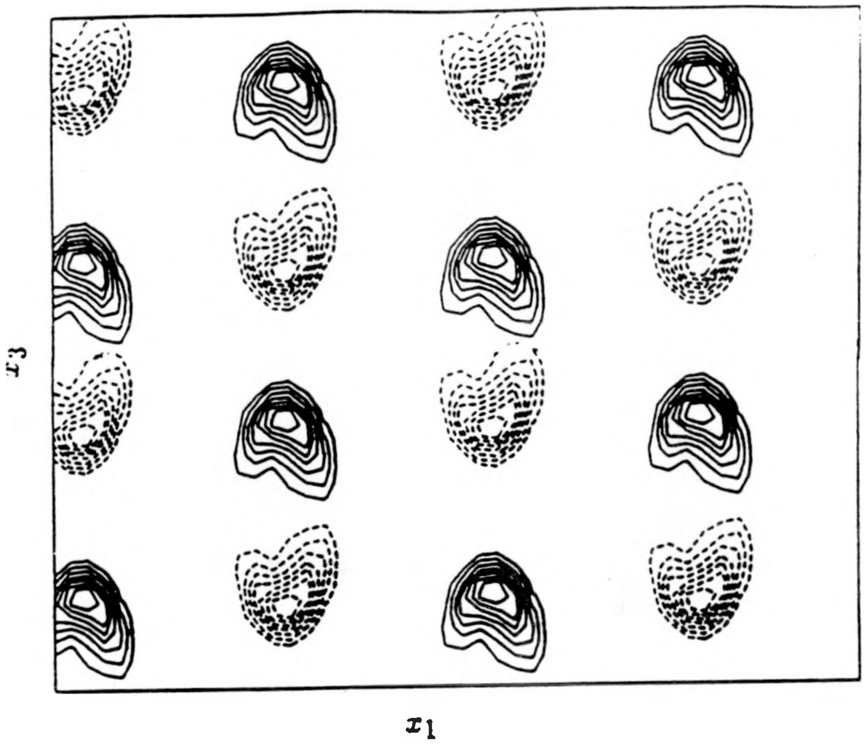

(c)

FIGURE 5-29. Plan view (D-D) of *(a)* spanwise vorticity, *(b)* pressure, and *(c)* streamwise vorticity corresponding to Case 3 at $t = 60$.

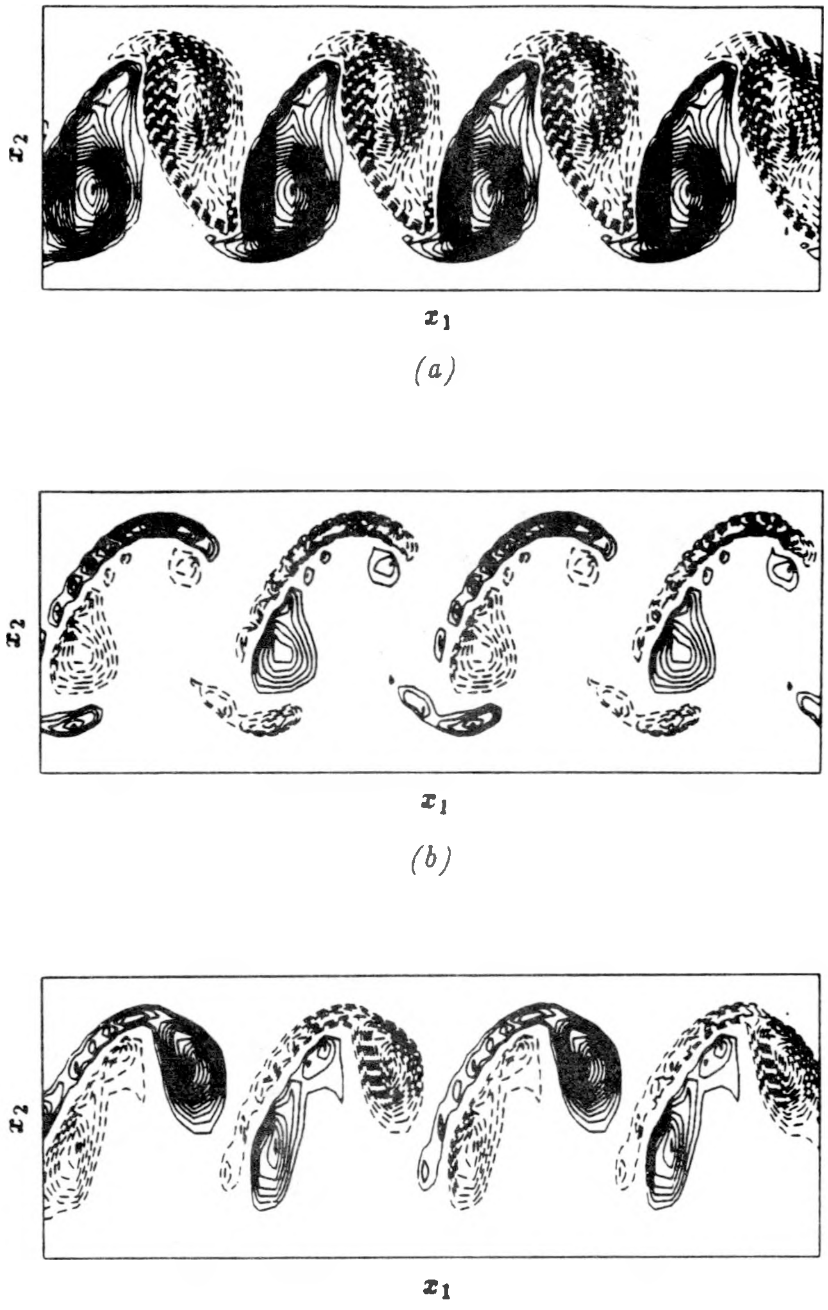

(a)

(b)

(c)

FIGURE 5-30. Side view (C-C) of *(a)* spanwise vorticity, *(b)* streamwise vorticity, and *(c)* transverse vorticity corresponding to Case 3 at $t = 45$.

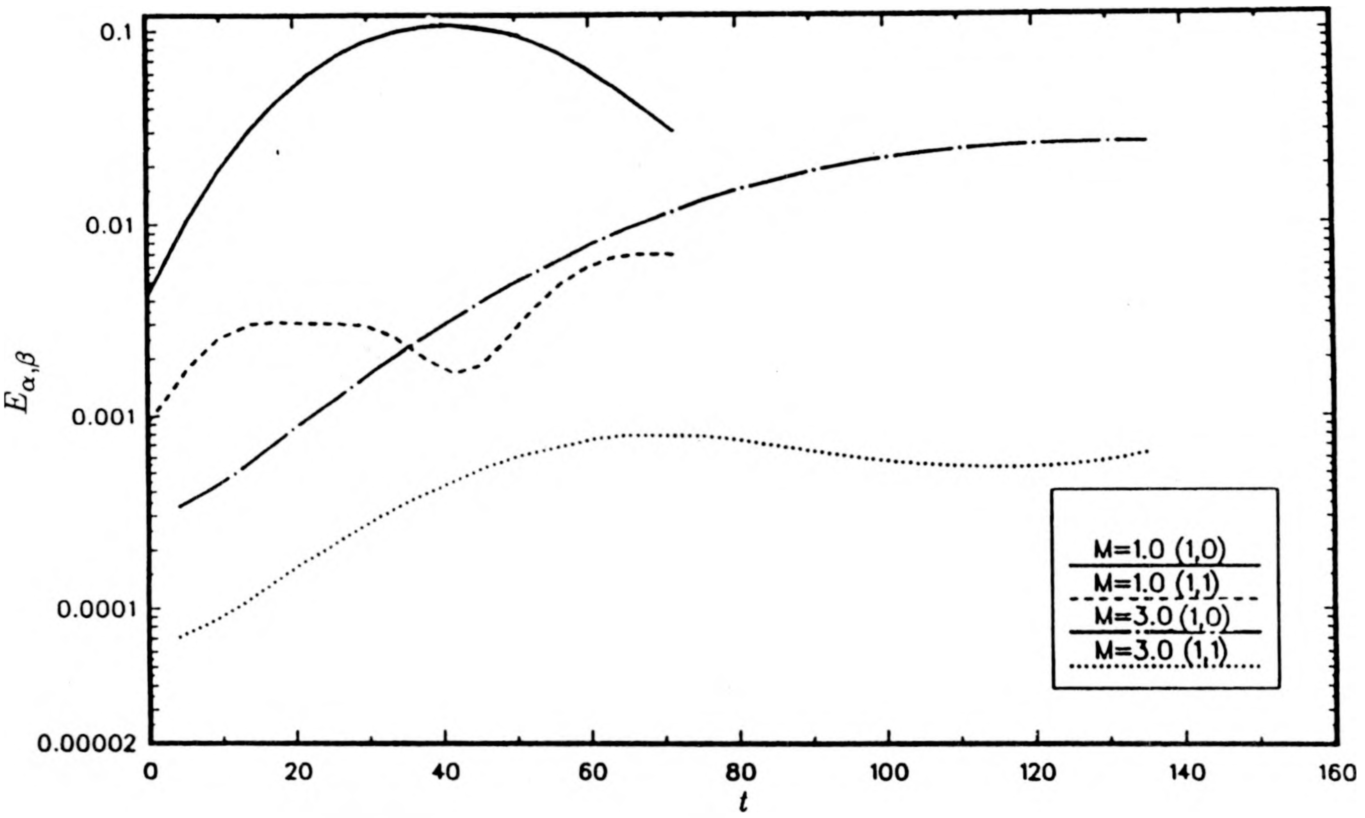

FIGURE 5-31. Effect of Mach number on the evolution of modal energies for the fundamental (1,0) and oblique (1, ±1) modes.

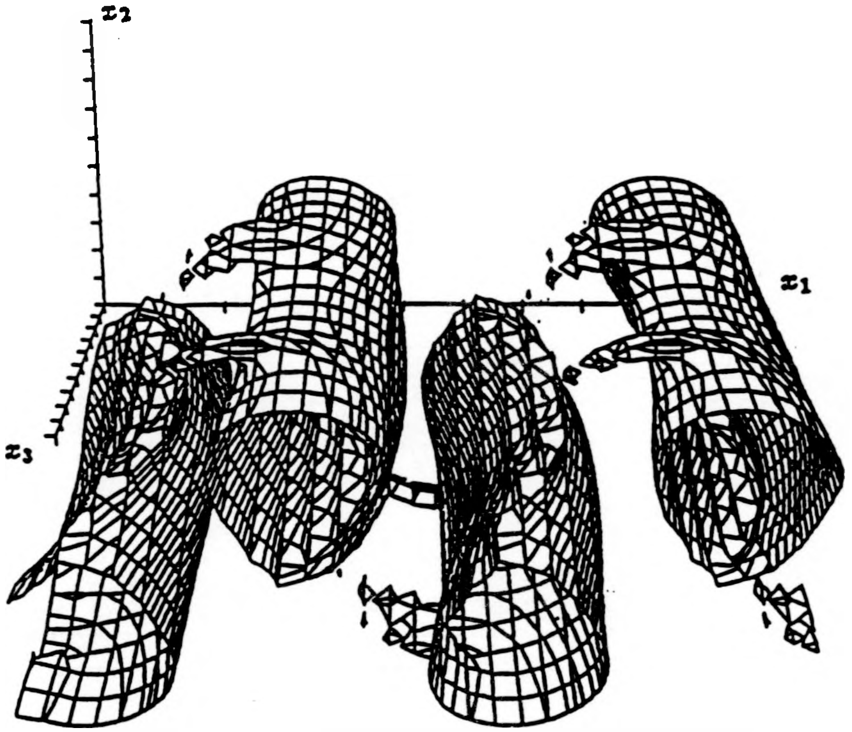

FIGURE 5-32. Iso-level surface of vorticity norm for Case 4 at $t = 130$. Contour level of 20% of peak value of 0.45.

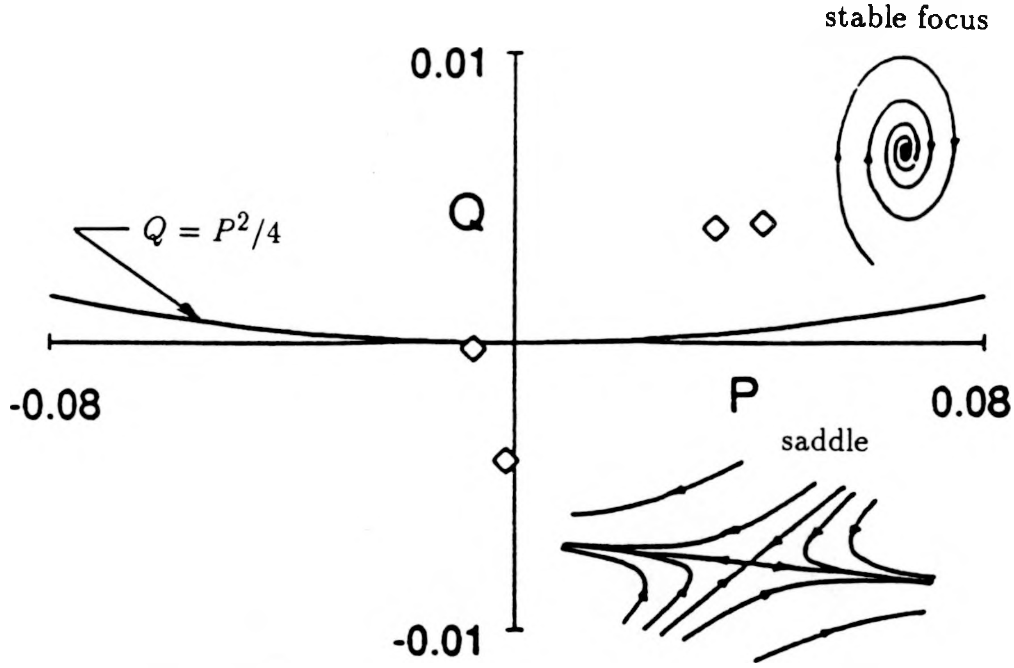

FIGURE 6-1. Classification of critical points on a P-Q diagram at $t = 0$ for a 2D wake at $Re = 300$, $M = 1.0$.

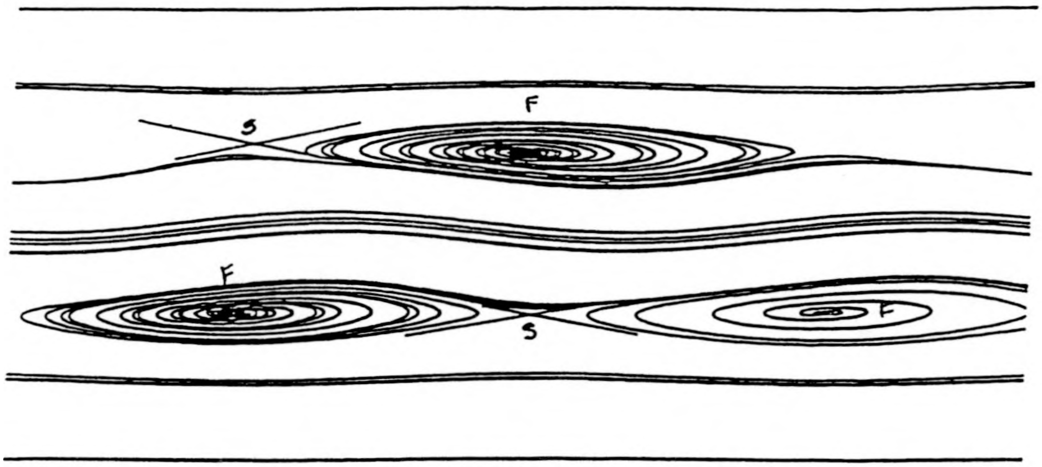

(a)

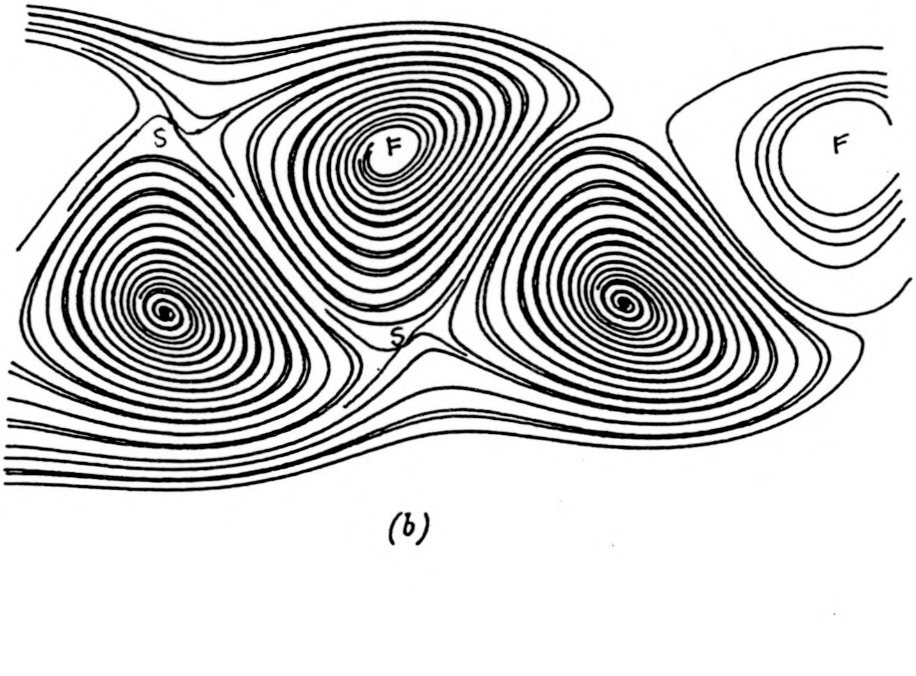

(b)

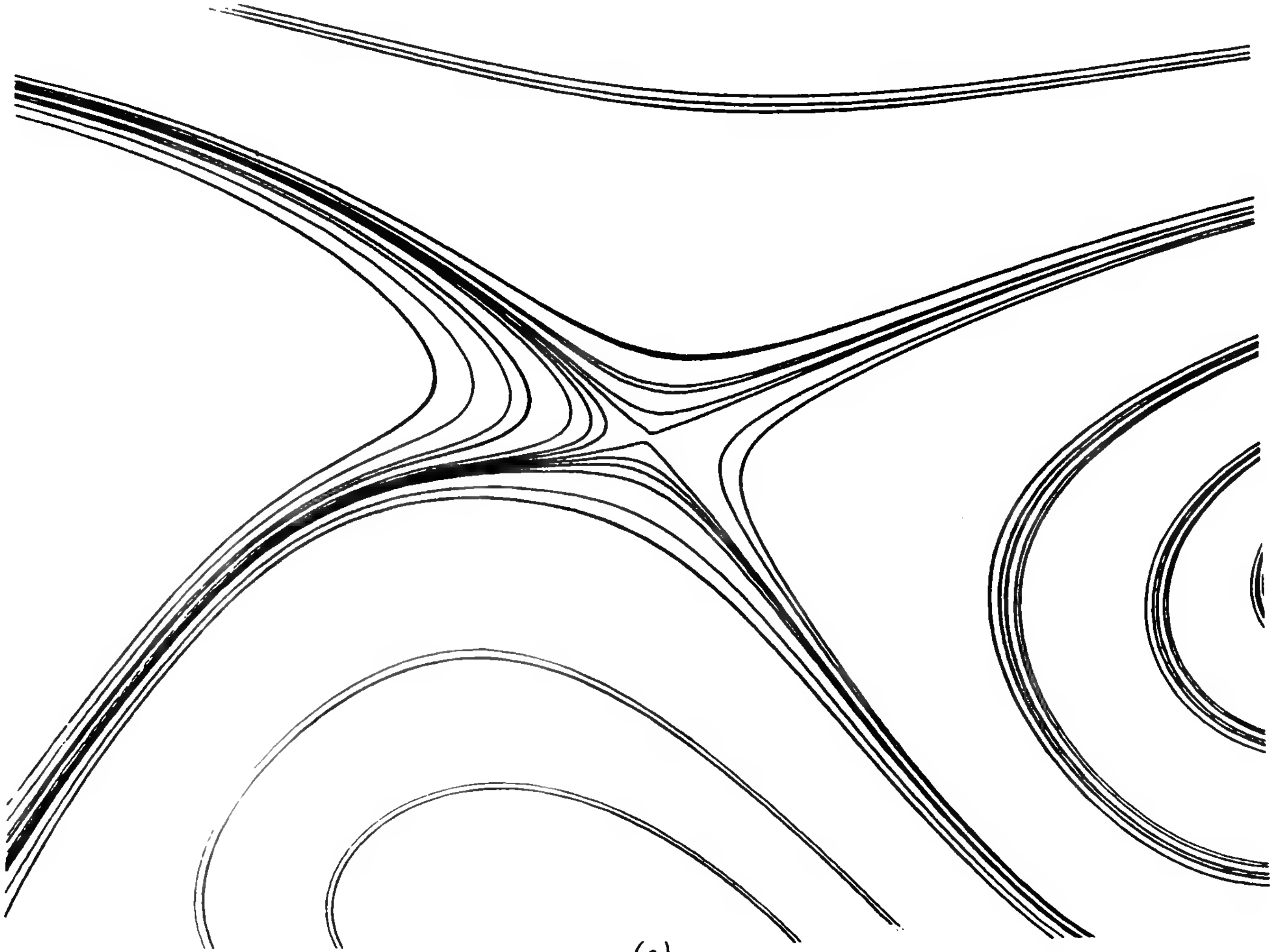

(c)

FIGURE 6-2. Two-dimensional instantaneous streamlines for $M = 1$, $Re = 300$ at *(a)* $t = 0$, *(b)* $t = 35$, and *(c)* $t = 35$ saddle point region enlarged. "S" denotes saddle point and "F" denotes focus point.

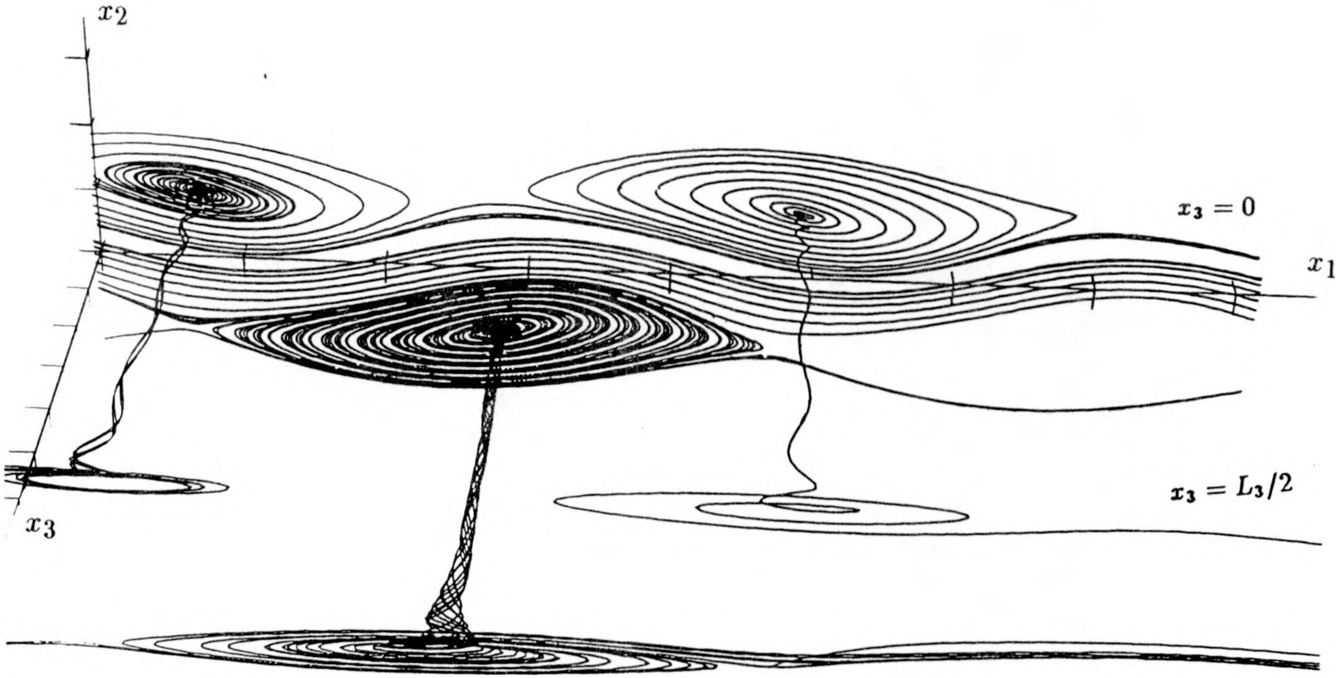

FIGURE 6-3. Three-dimensional instantaneous streamlines at $t = 0$ for Case 2.

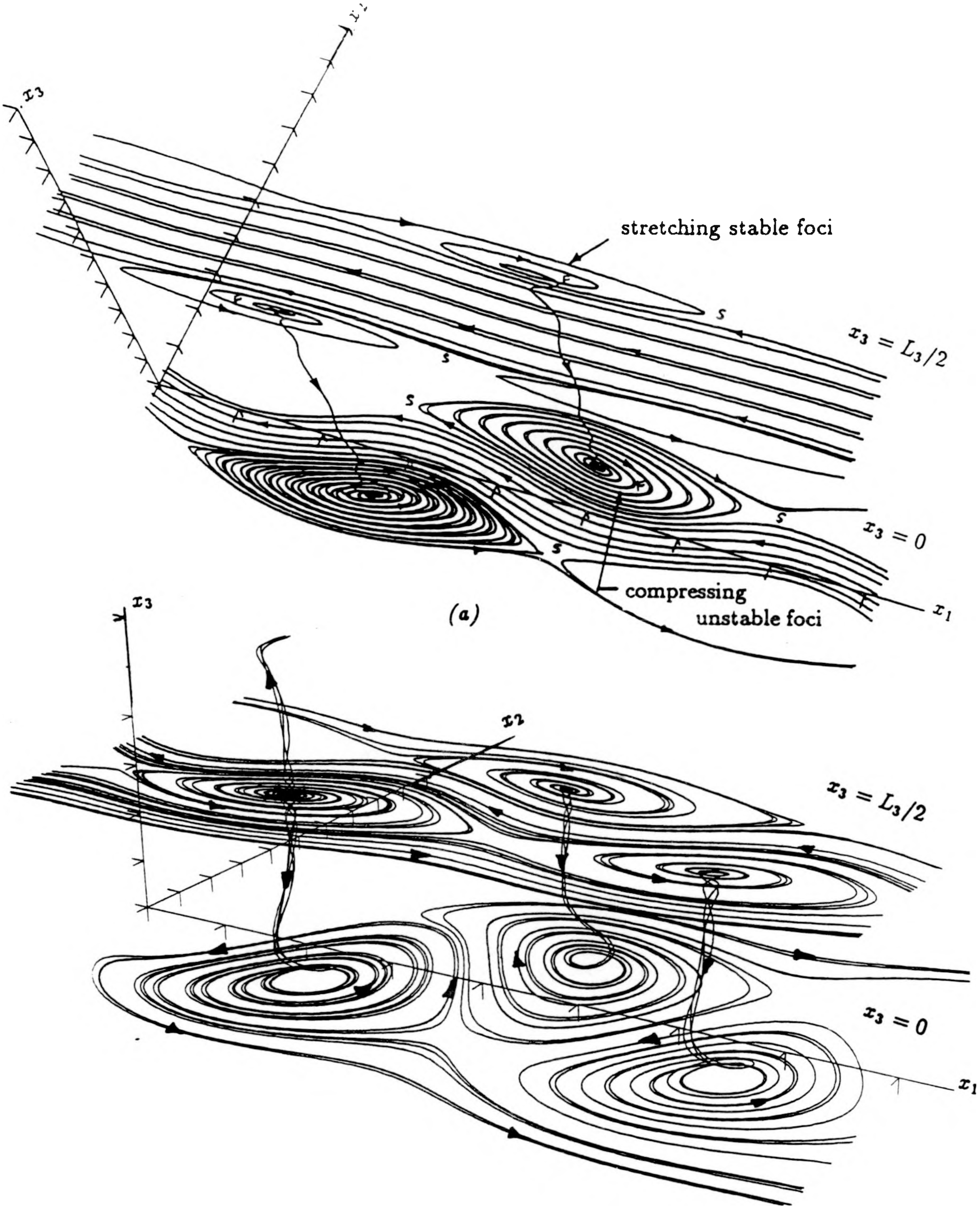

FIGURE 6-4. Instantaneous streamlines at *(a)* $t = 0$, and *(b)* $t = 25$ for Case 2. "S" denotes saddle point and "F" denotes focus point.

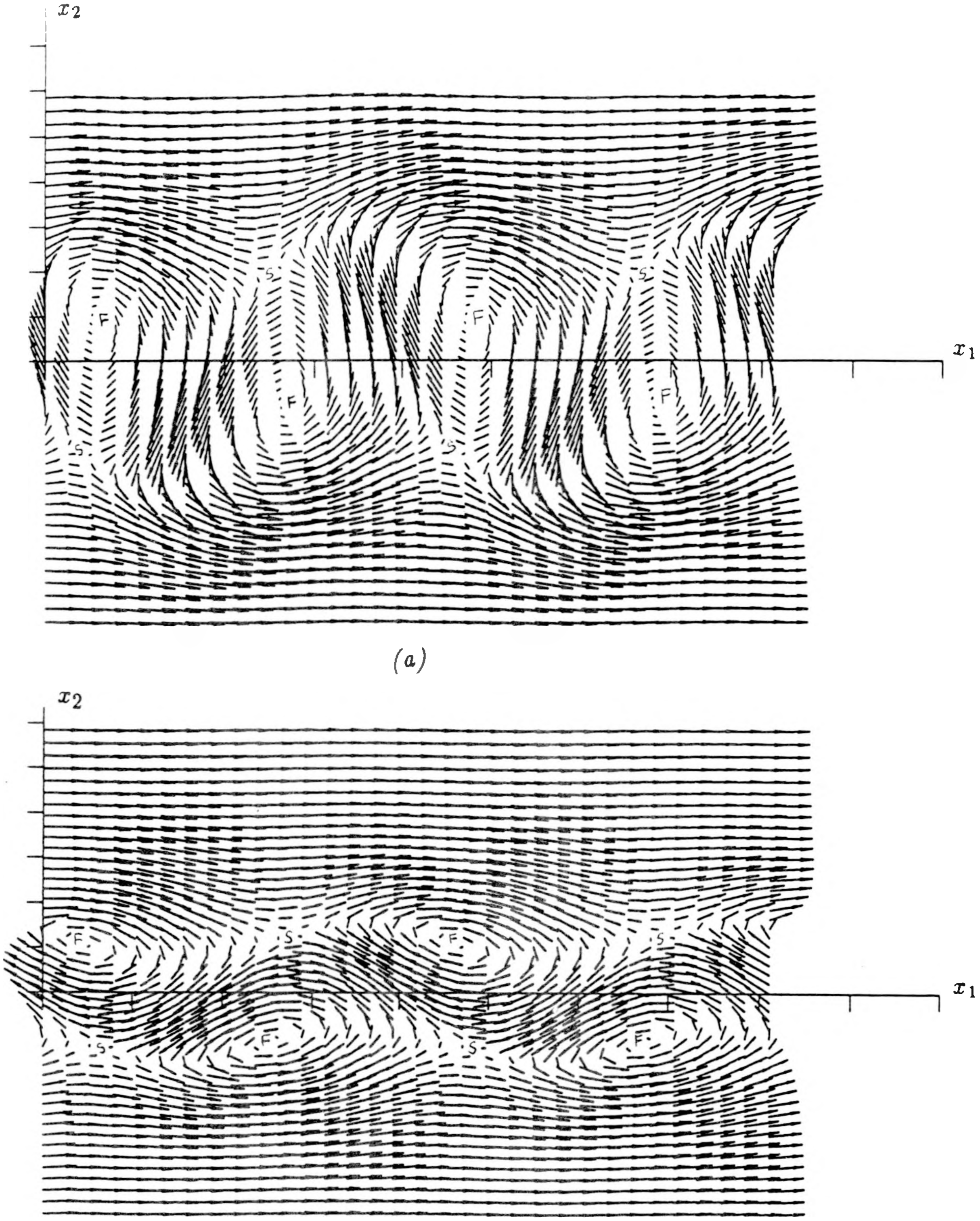

(a)

(b)

FIGURE 6-5. Projected velocity vectors at *(a)* $x_3 = 0$, and *(b)* $x_3 = L_3/2$ for Case 2 at $t = 25$. "S" denotes saddle point and "F" denotes focus point.

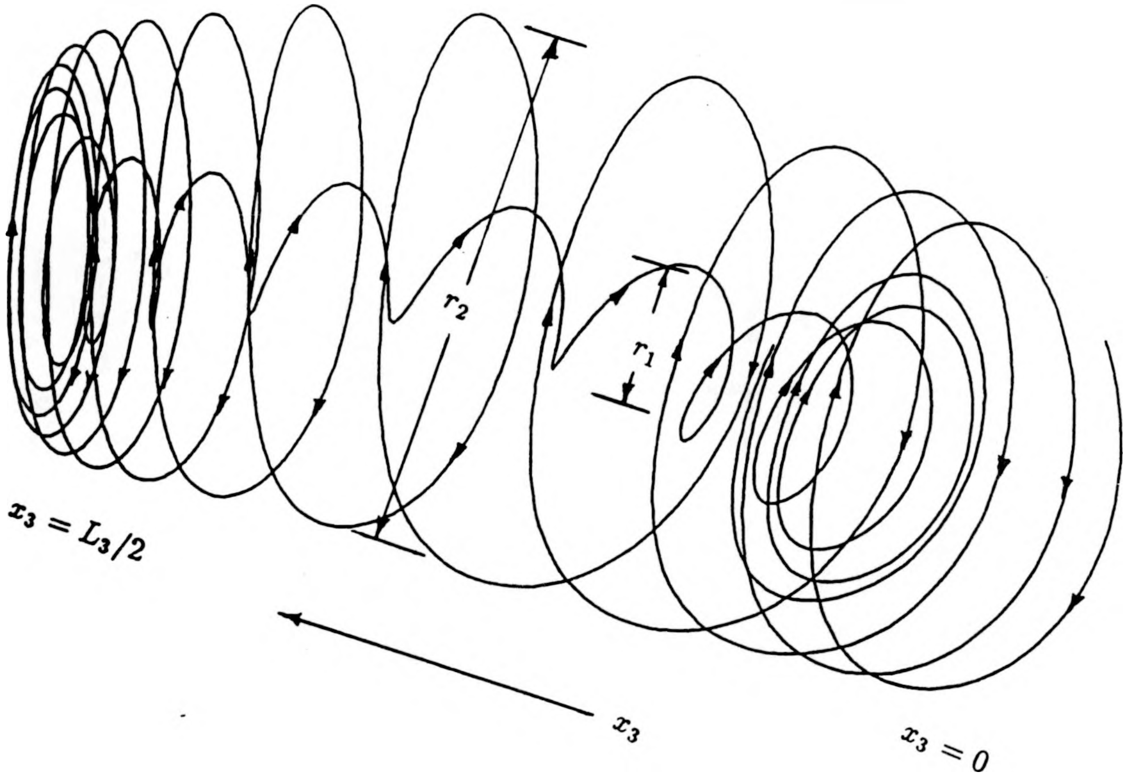

FIGURE 6-6. Instantaneous streamlines initialized at $x_3 = L_3/8$ illustrating "limit cycle" behavior for Case 2 at $t = 25$.

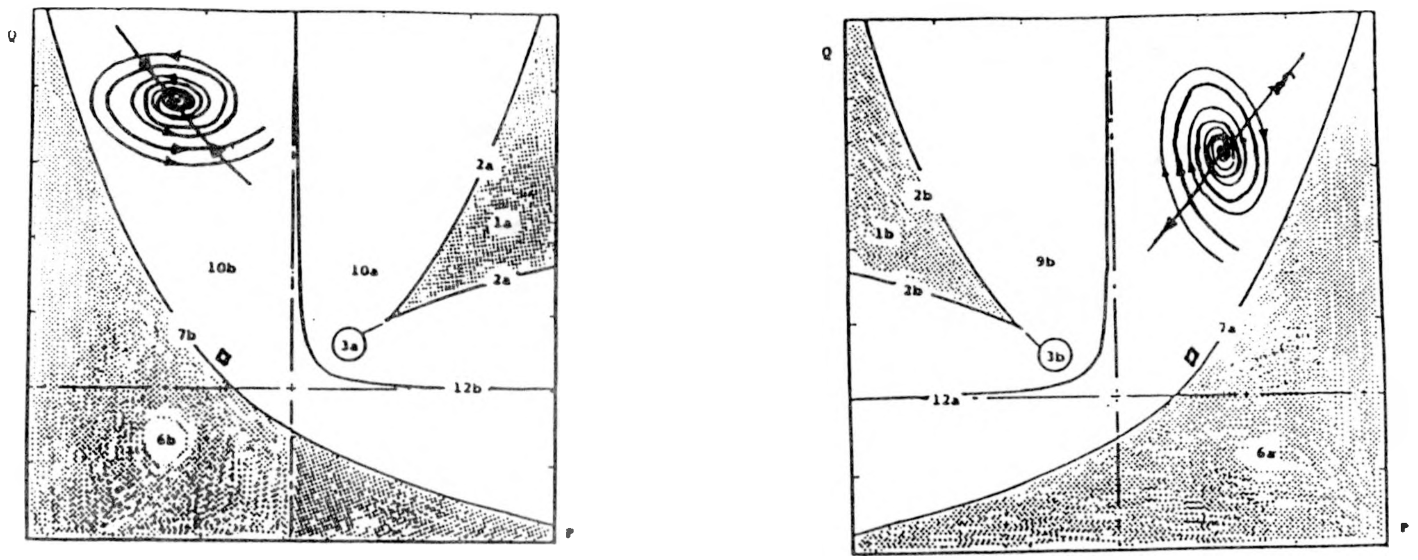

The P - Q plane ($R > 0$)

1a.	stable node / stable node / stable node
2a.	stable node / stable node / stable star node
3a.	stable star node / stable star node / stable star node
6b.	unstable node / saddle / saddle
7b.	unstable star node / saddle / saddle
10a.	stable focus / compressing ($b < 0$)
◆ 10b.	unstable focus / compressing ($b < 0$)
12b.	centre / compressing ($b < 0$)

The P - Q plane ($R < 0$)

1b.	unstable node / unstable node / unstable node
2b.	unstable node / unstable node / unstable star node
3b.	unstable star node / unstable star node / unstable star node
6a.	stable node / saddle / saddle
7a.	stable star node / saddle / saddle
◇ 9a.	stable focus / stretching ($b > 0$)
9b.	unstable focus / stretching ($b > 0$)
12a.	centre / stretching ($b > 0$)

FIGURE 6-7. Classification of critical points on a *(a)* P-Q diagram ($R > 0$), and *(b)* P-Q diagram for ($R < 0$) for Case 2.

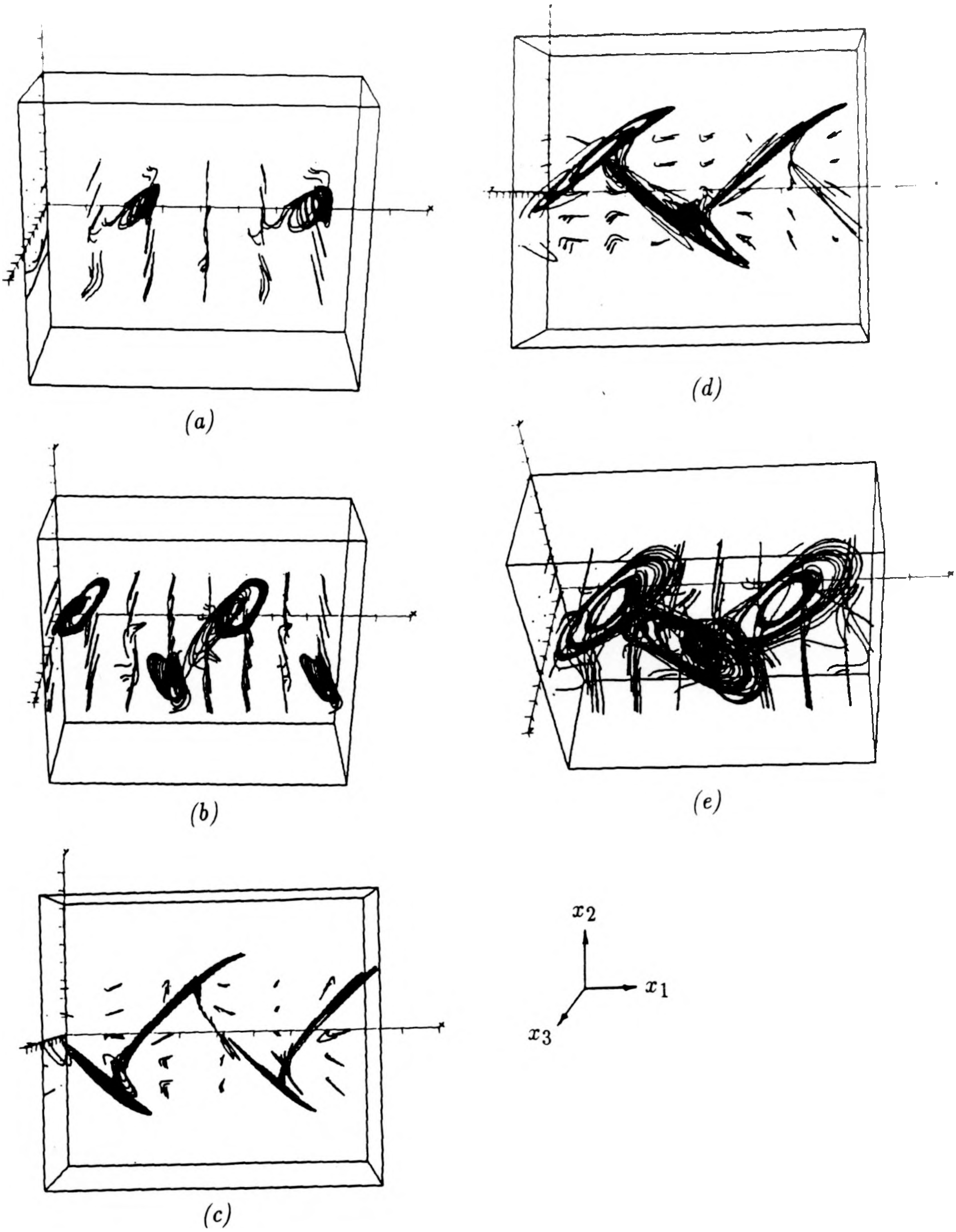

(a) (b) (c) (d) (e)

FIGURE 6-8. Evolution of three-dimensional vortex lines for $M = 1$, $Re = 100$ at *(a)* $t = 32$, *(b)* $t = 48$, *(c)* $t = 64$, *(d)* $t = 81$, and *(e)* $t = 81$.

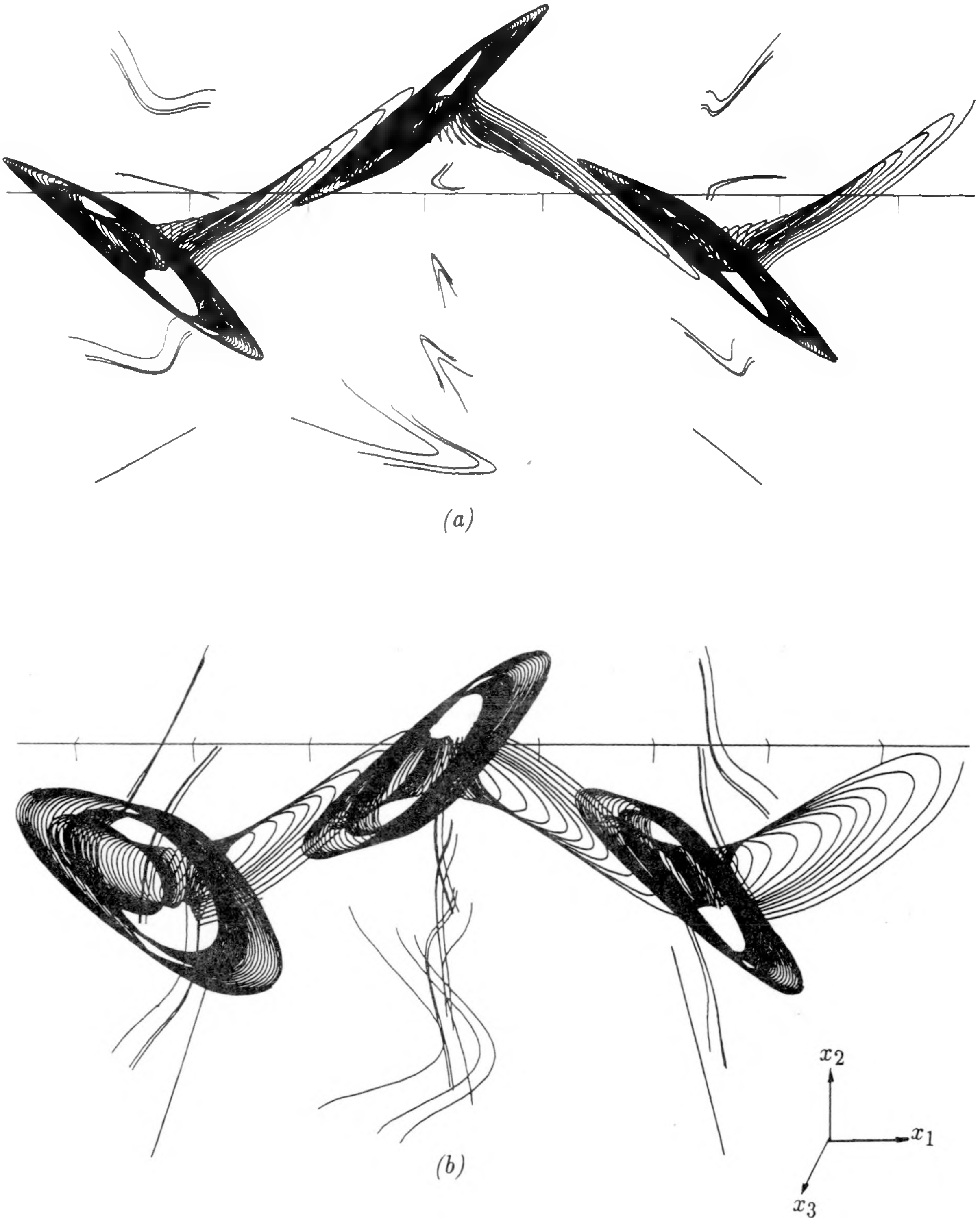

FIGURE 6-9. Vortex lines for Case 2 at $t = 77$ corresponding to *(a)* side view perspective, and *(b)* combination side-plan view perspective.

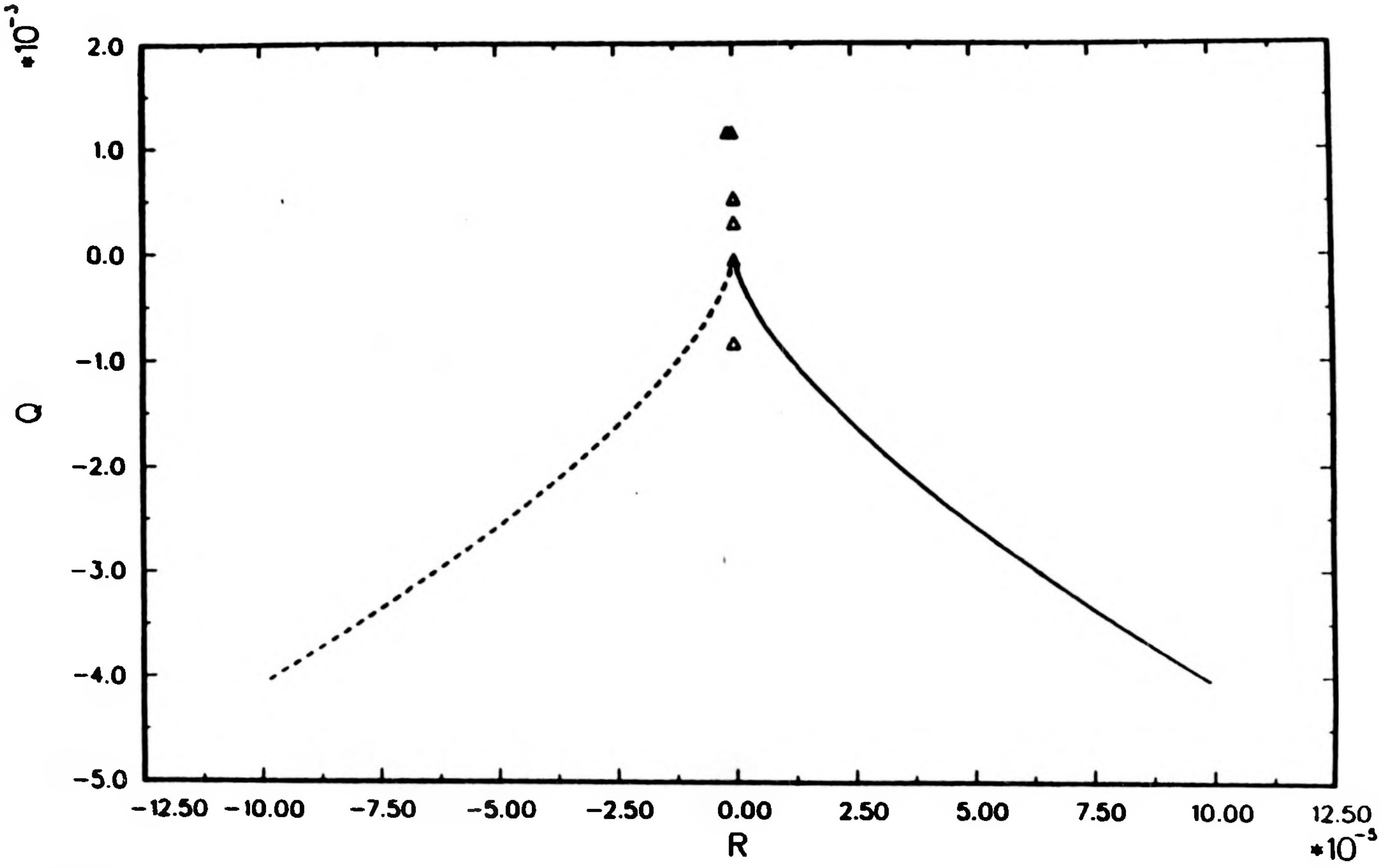

FIGURE 6-10. Critical points of the vorticity field for Case 2 at $t = 77$ displayed on a Q versus R diagram. The vortex loops consist of "no-flow through" centres connected by saddle points.

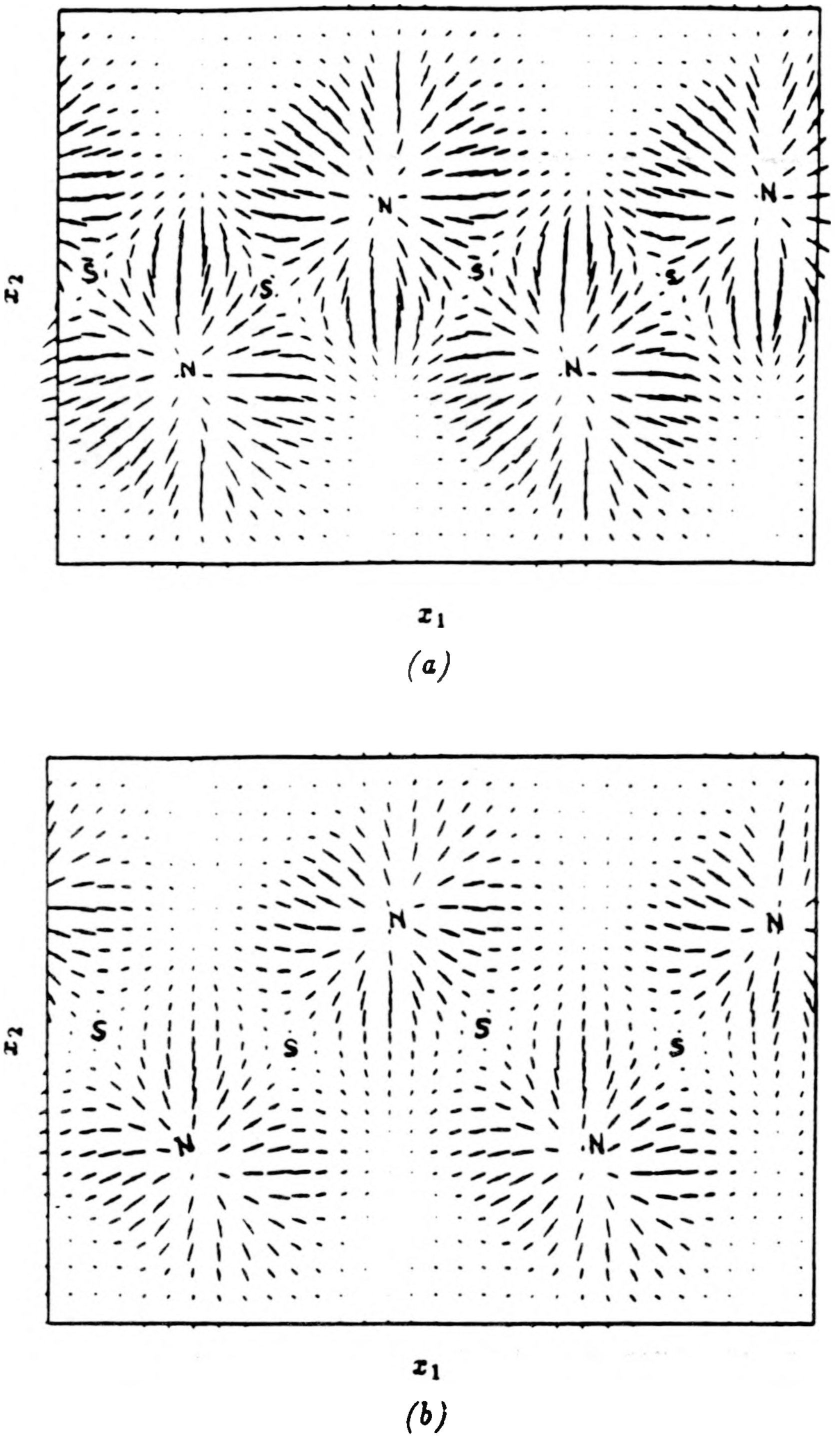

(a)

(b)

FIGURE 6-11. Pressure gradient vectors for Case 2 at $t = 64$ corresponding to *(a)* spanwise cut (C-C), and *(b)* spanwise cut (A-A). "S" denotes saddle point and "N" denotes either node or star-node.

END
12-18-90